TESIS DE LA UNIVERSIDAD DE ZARAGOZA

2019

10

Leyre Nogués Marcén

Constraints on Lorentz Invariance Violation through the study of energy-dependent photonic time dispersion utilizing observations from current gamma-ray instruments

Departamento

Física Teórica

Director/es

MARTÍNEZ RODRÍGUEZ, MANEL

GAUG, MARKUS

ISSN 2254-7606

Prensas de la Universidad Universidad Zaragoza

ISSN 2254-7606

Universidad Zaragoza
1542

Tesis Doctora

CONSTRAINTS ON LORENTZ INVARIANCE VIOLATION THROUGH THE STUDY OF ENERGY-DEPENDENT PHOTONIC TIME DISPERSION UTILIZING

Autor

Leyre Nogués Marcén

Director/es

MARTÍNEZ RODRÍGUEZ, MANEL
GAUG, MARKUS

UNIVERSIDAD DE ZARAGOZA

Física Teórica

2018

Institut de Física d'Altes Energies

EXCELENCIA SEVERO OCHOA

BIST Barcelona Institute of Science and Technology

Universidad Zaragoza

DOCTORAL THESIS

Constraints on Lorentz Invariance Violation through the study of energy-dependent photonic time dispersion utilizing observations from current gamma-ray instruments

Leyre Nogués

Departamento de Física Teórica
Universidad de Zaragoza

Supervised by

DIRECTOR: Dr. Manel Martinez
DIRECTOR: Dr. Markus Gaug
TUTOR: Dr. Eduardo García

A thesis submitted for the degree of
Doctor in Physics

November 2018

Contents

List of Figures

List of Tables

Resumen

La Gravedad Cuántica podría establecerse como el puente que conectase las leyes de la física que rigen los fenómenos a mayor y a menor escala en el universo − actualmente explicados por la Relatividad General y la Teoría Cuántica de campos, respectivamente − que desembocaría en la integración, dentro de una única teoría, de todos los fenómenos físicos: la llamada "Teoría del todo". Pese a que la Relatividad General y la Teoría Cuántica de Campos han sido intensamente probadas dentro de sus dominios de aplicabilidad, todavía presentan ciertas incompatibilidades fundamentales que han derivado en el continuo, aunque todavía inacabado, esfuerzo de definir teóricamente el comportamiento cuántico del campo gravitatorio, esfuerzo que comenzó en 1930. Desde ese momento y hasta hoy en día, han surgido un gran número de teorías de la Gravedad Cuántica, pero todavía no se ha alcanzado un marco teórico definitivo capaz de integrar simultáneamente todas las fuerzas fundamentales.

Un punto de partida para discriminar entre las diferentes teorías, así como para continuar impulsando el desarrollo teórico, es la búsqueda de las posibles consecuencias físicas que generaría el hecho de que el campo gravitatorio tuviese un comportamiento cuántico. Entre estas posibles consecuencias, se encuentra la modificación de simetrías asociadas al espacio-tiempo, en particular la desviación respecto de la simetría de Lorentz, cuyo estudio ha dado lugar a uno de los campo de investigación más activos dentro de la fenomenología asociada a la Gravedad Cuántica.

La escala de energía en la que los fenómenos asociados a un campo gravitatorio cuántico comenzarían a ser relevantes, se sitúa en torno a la escala de Planck. Dicha energía está varios órdenes de magnitud por encima del rango de sensibilidad de la generación actual de experimentos. Sin embargo, pequeñas desviaciones de la simetría de Lorentz integradas en largas distancias, fenómeno conocido como violación de la invarianza Lorentz, podrían producir efectos relevantes a energías más bajas, dentro del alcance experimental. Uno de los tests que tratan de medir estas pequeñas desviaciones se denomina "Tiempo de vuelo" ("Time-of-Flight" en inglés). Dicho test trata de buscar desviaciones dependientes de la energía en la velocidad de propagación de fotones, con respecto a su velocidad teórica, es decir, la velocidad de la luz en el vacío.

La presente tesis se centra en esta rama de la fenomenología de Gravedad Cuántica, estudiando las desviaciones mencionadas, mediante rayos gamma de muy alta energía, procedentes de fuentes lejanas. Los rayos gamma son ideales para este tipo de estudio, puesto que viajan a través del universo sin que les afecten los campos magnéticos. Además, han sido detectados procedentes de fuentes muy distantes ($z \sim 1$) y presentan energías muy altas, hasta varias decenas de TeV. Estos dos últimos factores están directamente relacionados con la intensidad del efecto que produce la ruptura de la invariancia Lorentz y, por tanto, con la capacidad de detectar estas pequeñas desviaciones de forma experimental.

En esta tesis se presentan resultados obtenidos usando el método de "Tiempo de vuelo" y haciendo uso de los rayos gamma procedentes de la galaxia lejana Mrk 421, detectados durante un periodo de muy alta actividad por los telescopios MAGIC en 2014. La emisión detectada está formada por cientos de eventos que alcanzan energías de hasta 30 TeV, convirtiéndola en una de las más energéticas jamás empleadas para tests de "Tiempo de vuelo" hasta la fecha. El análisis de esta emisión para detectar pequeñas desviaciones en la velocidad de los fotones se ha llevado a cabo con diversas técnicas, algunas de ellas desarrolladas como parte de este trabajo. Los resultados obtenidos se emplean para acotar la escala de energía esperada para Gravedad Cuántica.

Adicionalmente, se presentan los resultados del primer análisis combinado empleando la técnica de "Tiempo de vuelo". Este análisis ha sido desarrollado en colaboración entre todos los telescopios terrestres Cherenkov actualmente en funcionamiento (H.E.S.S., MAGIC y VERITAS) y hace uso simultáneo de datos de varias fuentes detectadas por los diferentes telescopios.

El hecho de combinar diferentes fuentes en un análisis, permite discriminar entre efectos temporales debidos a la ruptura de la invarianza Lorentz frente a otros efectos temporales relativos a las propias fuentes. Sin embargo, esta combinación también requiere un gran control de las incertidumbres asociadas a la forma de detección de cada experimento. La siguiente generación de telescopios terrestres Cherenkov, el observatorio llamado "Cherenkov Telescope Array", proveerá muchas nuevas fuentes con emisiones que permitan estudiar más en profundidad la ruptura de invariancia Lorentz. Asimismo, presentará avances técnicos tales como mejoras en la resolución angular y de energía de estos telescopios. Estos factores desembocarán en una disminución de las incertidumbres sistemáticas que de seguro llevará a una mejora en los resultados obtenidos hasta la fecha.

Esta tesis está dividida en 6 capítulos y un anexo. El capítulo 1 introduce el tema de Gravedad Cuántica, así como la evolución y los tipos de teorías propuestos a lo largo de la historia, centrándose especialmente en la ruptura de la invariancia Lorentz y los diferentes tests experimentales que tratan de estudiarla. El capítulo 2 presenta el campo de la astrofísica conocido como astronomía gamma. En él se tratan los mecanismos de producción de este tipo de radiación, las técnicas empleadas para su detección, así como los diferentes tipos de fuentes que la generan. El capítulo 3 se centra en los tests experimentales que buscan señales de ruptura de invariancia Lorentz y que son llevados a cabo por telescopios terrestres Cherenkov, con un énfasis especial en los tests de "Tiempo de vuelo". El capítulo 4 describe en detalle los telescopios terrestres Cherenkov llamados MAGIC, sus componentes físicos y el procedimiento seguido para la reducción sus datos. El capítulo 5 contiene los resultados originales de esta tesis, obtenidos mediante el método de "Tiempo de vuelo" y usando los datos de una emisión destacada de Mrk 421. El capítulo detalla cómo se seleccionó la fuente para el estudio, los datos sobre la observación y una descripción minuciosa de los diferentes métodos de análisis. Al final del capítulo, se presentan los resultados así como las conclusiones que se derivan de ellos. Por último, el capítulo 6 contiene los resultados del análisis de la ruptura de la invariacia Lorentz, realizado en colaboración por todos los telescopios terrestres Cherenkov activos en la actualidad. El capítulo muestra las diferentes fuentes empleadas, el método de análisis y su calibración, y termina con los resultados y los siguientes planes para la colaboración.

El anexo A contiene el trabajo desarrollado como contribución en la construcción del primer telescopio del nuevo observatorio "Cherenkov Telescope Array", basado en el diseño de las calibraciones del sistema de trigger de dicho telescopio. Puesto que el tema y los objetivos de dicho trabajo difieren

considerablemente del hilo conductor del resto de la tesis, se ha decidido separarlo del cuerpo principal y situarlo en un anexo. Sin embargo, esta tarea ha requerido una cantidad considerable del tiempo dedicado a esta tesis y ha supuesto una parte importante en la formación del autor, por lo que se considera que merece su lugar en este trabajo.

Introduction

Quantum gravity shall be the bridge linking the physics laws for the largest and the smallest objects in the universe − General Relativity (GR) and Quantum Field Theory (QFT) − and leading to a harmonious integration of all physical phenomena into a single theory: the Theory of Everything. Even though GR and QFT have been intensively confirmed in their respective applicability domains, they present several fundamental incompatibility aspects that have led to the continuous, but so far unsuccessful, theoretical effort of describing the quantum behaviour of the gravitational field since the 1930s. Until today, many candidate theories have been proposed to realize Quantum Gravity, but there is still a lack of a definitive theoretical framework capable of integrating all the fundamental forces.

In order to discard candidates and to orientate further theoretical development, a starting point is to look for the physical consequences of a quantized gravitational field. Among them, the departures from classical spacetime symmetries, specifically the Lorentz symmetry, has evolved into an active and productive research field within the phenomenology of Quantum Gravity.

The energy scale at which Quantum Gravity effects are expected to be relevant, the Planck scale, is out of reach by many orders of magnitude for current experiments. Nevertheless, small deviations from Lorentz symmetry − defined as Lorentz Invariance Violation (LIV) −, integrated over large distances, might produce measurable effects at lower energies. One of the experimental tests searching for such cumulative effects is called the Time-of-Flight method. It looks for energy-dependent deviations from the canonical value of the speed of light in vacuum.

This thesis focuses on this approach to Quantum Gravity phenomenology, looking for energy-dependent delays of photons due to LIV, using Very High Energy (VHE) gamma rays from distant sources. VHE gamma rays are particularly well suited for this study, since they travel unaffected by magnetic fields through the universe, have been detected up to very large distances, namely redshifts or the order of $z \sim$, and energies of tens of TeV. These two factors are directly related to the expected sensitivities to measure LIV through energy-dependent delays.

Here I present results from Time-of-Flight studies using an outstanding flare of the Mrk 421 blazar, detected by the MAGIC gamma-ray telescopes in 2014. The flare is composed of several thousands of events and reaches more than 30 TeV in energy, making this source the most energetic candidate used for Time-of-Flight studies up to date. The data are treated using different analysis techniques, some of them developed as part of this work. The results are later used to set constraints on the effective energy scale for Quantum Gravity.

Additionally, the first results from a combined Time-of-Flight study of a set of simulations of sources

detected by all currently active ground-based gamma-ray Cherenkov telescopes − H.E.S.S., VERITAS and MAGIC − using a dedicated analysis technique, is part of the work composing this thesis.

The combination of different sources allows to distinguish between possible LIV-induced time delays and other source-dependent effects. Nonetheless, combining the results of different experiments requires the control of a large number of uncertainties associated to the measurement technique of each instrument. The next generation of ground-based Cherenkov telescopes, the Cherenkov Telescope Array (CTA) observatory, already under construction, is expected to provide many more sources suitable to carry out such studies and technical improvements, allowing for an improved energy and angular resolution and a better the control of systematic uncertainties, that will certainly improve the current results.

The outline of this thesis can be summarized as follows:

- **Chapter 1** introduces the different approaches to Quantum Gravity, the evolution and types of theories as well as the Lorentz Invariance Violation effect and its possible experimental tests.
- **Chapter 2** presents the field of gamma-ray astrophysics, from the production mechanisms of this radiation and its production sites, to the different detection techniques.
- **Chapter 3** is devoted to tests of LIV performed with ground-based Cherenkov telescopes, with a special focus on Times-Of-Flight studies.
- **Chapter 4** describes the MAGIC telescopes, its hardware components, operation procedures and data analysis chain.
- **Chapter 5** contains the original results of this work, obtained from a LIV Time-of-Flight analysis of the MAGIC data of a Mrk 421 flare, detected in 2014. The chapter summarizes the selection of the source, the details of the observation and a profound description of the different analysis methods. At the end, the results and conclusions of the study are reported.
- **Chapter 6** presents the results of the first combined LIV analysis between the three collaborations active in the field of ground-based Cherenkov telescopes. The analysis methodology, calibration and results are described.

Appendix A hosts the work developed to contribute to the construction of the first telescope composing the CTA observatory's northern array, the Large-Sized Telescope (LST), based on the design of the calibrations for the trigger system. Since the topic does not fit the common topic the rest of this thesis, and the scientific goals differ from the other parts, it is presented separately from the main body. However, its elaboration has required a considerable amount of time and meant a large contribution to the formation of the author of this thesis and therefore it deserves its dedicated place.

Chapter 1

Quantum Gravity

The term *Quantum gravity* designates the goal to construct a theory that describes the quantum behaviour of the gravitational field and spacetime. The challenging task started during the 30s and is nowadays still insufficiently developed.

The quest for a quantum theory of gravitation has provided theories dealing with such abstract and contrived issues, that their connection to reality through observations or experiments seems nearly impossible and leave the frame with a lack of guidance to compare, corroborate, evaluate or discard a specific theory.

The expected energy scale at which Quantum Gravity (QG) effects become relevant, corresponds to energies well above the capabilities of any Earth-based or space-based experiments. However, some Quantum Gravity (QG) theories predict relic signatures that can be studied at lower energies and which get into the energy domain of current experiments.

QG is a very extensive field in continuous evolution that cannot be completely reviewed in one chapter, but we will provide a general idea about the theoretical backgrounds in order to understand the development of a QG phenomenology and the impact of possible experimental results.

This chapter gives a brief review of the history and current status of QG research, addressing briefly the most relevant theories and providing references for the rest. The focus is then drawn on the possible experimental signatures, especially one aspect of them, namely Lorentz Invariance Violation (LIV). The chapter ends with a summary of the experimental tests performed so far to search for LIV effects.

1.1 The necessity for a Quantum Gravity

GR and QFT compose the two main pillars of modern physics. They seem however not to belong to a same building. While at large scales phenomena are governed by gravitational interactions, and observational facts − from cosmological to millimeter distances − are well explained by GR [1]; at small scales the phenomena are dominated by strong and electroweak interactions, and observations − from fractions of millimeters down to distances of 10^{-19} m − are well-described by QFT [2]. At the moment, no known fundamental interaction falls out of these frameworks.

The two pillars seem very different: while GR has a dynamical spacetime and no preferred reference frame, QFT needs a fixed background and a preferred splitting of space and time. Unifying both pillars in a QG theory not only leads to profound technical problems, due to the complexity and non-linear character

of GR, that produces the failure of conventional techniques used in QFT [3] (like non-renormalizability, loss of unitarity, etc), but it requires also a quantization of spacetime itself, and at a fundamental level we do not know what that means.

The task of building a quantum theory of gravity seems so difficult to undertake, that one may wonder if gravity is just fundamentally different and must simply not be quantized. However, QG is definitively needed, not only on historical grounds − the historical trend of physics towards unity, from electromagnetism and electroweak models to gauge theories − but we can also appeal to two reasonings. Firstly, if gravity was not quantized, it would violate the uncertainty principle and the position and momentum of a particle could be determined to an arbitrary accuracy. This problem was studied by Eppley and Hana [4]. Secondly, if gravity is not quantized, but matter actually is, there must be a coupling between them. The simplest coupling between classical gravity and quantum theory was proposed by Moller [5] and Rosenfed [6] and led to non-linear Schrödinger equations, breaking the superposition principle and, with it, the foundations of QFT. This problem was discussed in detail by Kibble and Randjar-Daemin [7].

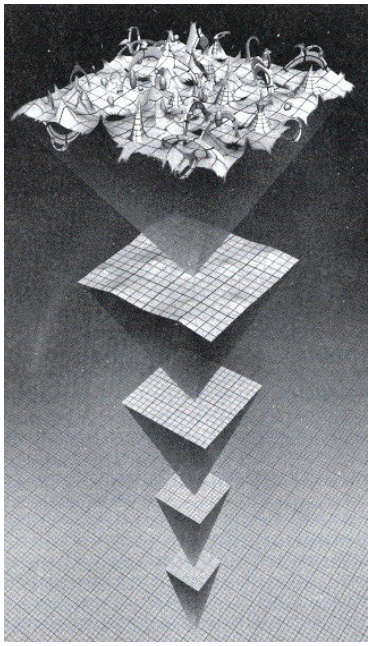

Figure 1.1: Artist's view of quantum space time, and its quantum fluctuations, appreciable at a close view.

While efforts to couple a quantum and a classical system continue, these arguments strongly suggest that a consistent model of the physical world requires either GR or QFT to be modified. The usual choice is to quantize gravity, however others such as Penrose [8] support modifications of QFT.

One more reason to quantize gravity is that both GR and QFT suffer serious limitations that QG might offer a cure for. In GR, the *"gravitational collapse"*, that requires a null pressure in order to explain the gravitational collapse of a large mass with Einstein's equations [9] or the lack of initial conditions for the universe. In QFT, the appearance of divergent integrals in the calculation of the second order correction to particles interaction, in some cases required to be coherent with measurements, known as *"QFT infinities"*[10]. A proper treatment of QG might determine the initial conditions of the Universe [11] or be the missing ingredient for QFT, that could provide an automatic energy cut-off at the Planck Energy [12].

The reason why the expected energy scale at which the effects of a theoretical QG start to be relevant, must be the Planck energy, is because it is exactly at this scale when the Compton wavelength ($\lambda_{Compton}$), the precision limit in QFT and the Schwarzschild radius (r_s), the radius defining the event horizon of a Schwarzschild black hole, achieve the same scale:

$$\begin{matrix}\lambda_{Compton} = 1/M \\ r_s = G \cdot M\end{matrix} \Leftrightarrow \begin{cases}\lambda_{Compton} = r_s \\ 1/M = G \cdot M\end{cases} \Leftrightarrow \begin{cases}M_{Pl} = \sqrt{1/G} \\ M = M_{Pl}\end{cases}$$

The same conclusion for the energy scale can be calculated by a more detailed theoretical treatment, taking into account that the merge of Quantum Mechanics (QM) and Special Relativity (SR) would

combine Heisenberg's uncertainty principle with the finiteness of the speed of light, transforming the spacetime into a dynamical entity that suffers external fluctuations and generates its own fluctuations (See Figure 1.1). Therefore, the uncertainty in the particle position implies not only an uncertainty in its momentum but also an extra uncertainty in geometry due to gravity-energy interaction. Using Einstein's equation, the scale of these quantum fluctuations have been calculated [13] leading to the conclusion that, independently of the way of measuring the position, the distance between two events will have a minimum uncertainty of the order of the Planck length. This conclusion tells us that beyond this scale, the concept of space and time loses its meaning in a similar way to the speed of light limit in SR. This leads to the idea that a quantum theory of gravity should be constructed at "Planck's border". [1]

1.2 Brief history of the Quantum Gravity search

Across more than 70 years, QG research was separated into three main lines. Even though these lines have changed along the years and there have been intersections and connections between them, they have maintained a distinct individuality. The starting point for these research lines appeared very early, in the thirties. At the end of the fifties, the different research programs were already very clearly formulated.

- **The covariant line of research:** This line attempts to build a QG theory as a QFT of the fluctuations of the metric over a flat Minkowski space or other specific background metric space. The research program was started by Rosenfeld [15], Fierz and Pauli [16] in the thirties. The Feynman rules for GR were found by Feynman and DeWitt [17, 18, 19] in the sixties while firm evidence of the non-renormalizability in the matter-GR coupling was discovered in the seventies by t'Hooft and Veltman among others [20, 21]. After that, the search for an extension of GR with a renormalizable or finite perturbation led to a modification of the theory, deriving in ideas as *Supergravity* [22] or higher derivative actions to GR, that finally converged successfully in String Theory (ST) in the late eighties.

- **The canonical line of research:** This attempt tries to construct a quantum theory in which the Hilbert space carries a representation of the operators corresponding to the full metric, without the necessity of a background metric. The program started in the fifties and was proposed by Bergmann and his group and by Dirac [23, 24, 25]. To unravel the canonical structure of GR was a hard work completed in the late fifties with contributions by Bergmann, Dirac, Peres and Misner, among others [26]. The formal equations for the quantum theory were derived by Wheeler and DeWitt [27], but later discovered to be too ill-defined [28, 29]. An improved version of the equations was successfully developed in the late eighties [30], giving birth to the theory of Loop Quantum Gravity (LQG)[31].

- **The sum over stories line of research:** This line tries to use some version of the Feynman's functional integral quantization to define the theory. In this line are included the discrete approaches (lattice-like, posets...), the spin foam models [32] or Hawking's Euclidean quantum gravity [33].

[1] However, there is still discussion about such energy scale since some authors support that, taking into account the possible variation ("*running*") of the gravity constant with energy $G(E)$, the expected energy scale could be shifted to much larger or smaller values [14].

- **Others**: There were other ideas to produce a quantum theory of gravity, even though none has been developed into large scale research program.
  - Twistor theory [34].
  - Non-commutative geometry [35].
  - Quantum state reduction [36].

After more than 70 years of research, we have well-developed theories as ST and LQG. There is still no consensus and no direct or indirect experimental support, so that logic has been the responsible for guiding these theories and they have overcome several difficulties: GR was discovered to be the low energy limit of the big theory of ST, and LQG was finally able to compute eigenvalues, a requirement for a canonical approach. Although the progress is undeniable, the search for a definitive QG theory is still ongoing.

This thesis is not intended to go into further details of the theoretical sector of QG, however it is important to understand the history and the reasons behind the development of a theory, now that many of them are developed before they achieve their corresponding experimental support. For a detailed review of the history of quantum gravity research, one can consult [37, 38, 39, 40].

1.3 Quantum Gravity phenomenology

Independently of the theory, if gravity is indeed quantum, its effects would be expected at the Planck energy, so far completely out of range of the sensitivity of current experiments. Nevertheless, during the past two decades, several experimental tests have been proposed based on the idea of detecting very small deviations from exact symmetries or very small collective effects that may be integrated over long distances or times.

This section shows a collection of possible classes of such effects. That collection comes from both the analysis of the general structure of the QG problem and the analysis of the proposed approaches to the solution.

- **Planck-scale departures from classical spacetime symmetries:** For a quantum-spacetime theory it is natural to expect some phenomenology departing from spacetime symmetries. If the Minkowski spacetime of current theories is quantized, it is logical to put under scrutiny the classical Minkowski spacetime and its symmetry group, the Poincaré group, defined by all the transformations that preserve the interval between events as invariant. An important subgroup of these transformations are the Lorentz transformations. The search for deviations from Lorentz symmetry is the most active topic in QG phenomenology, either with symmetry-breaking mechanisms that affect the symmetry itself or with deformations of it. Among the most popular QG models, there is theoretical support for the idea of for Lorentz symmetry departures. For example, LQG involves some intrinsic discretization of spacetime [41, 42] that may induce departures from classical Lorentz/Poincaré symmetry. Most hypotheses argue for symmetry violation [43, 44] but there are also methods to deform the symmetry [45, 46, 47]. The manifestations of this effect and possible options to test it experimentally are detailed in Section 1.4.

- **Planck-Scale departures from CPT symmetry:** There is a long tradition of arguments suggesting Charge Parity Time (CPT) violation in a QG scheme [48, 49, 50]. Since space quantization implies limitations to locality − as limitations to the localization of a spacetime event − and locality, unitarity and Lorentz invariance are the ensuring ingredients for CPT invariance, it is natural to put CPT symmetry under scrutiny. However, a proper analysis of CPT symmetry requires a level of understanding of the different theories (LQG, non-commutative spacetime, etc) beyond our present reach. Nevertheless there are several examples of QG approaches, as non-commutative scenarios, that deform parity (P) [51] − and therefore CPT − or predict CPT violation [52], e.g. for the noncritical Liouville String Model [53, 54].

- **Decoherence and modification of the Heisenberg principle:** The classical spacetime background has been instrumental to the successful tests of quantum mechanics so far performed. However, if spacetime is quantized, it might have associated departures from QM [55, 56]. Some of the theories to model spacetime quantization motivate such departures due to quantum gravity in the form of "decoherence" or loss of quantum coherence [57, 58, 59]. For example, a description of decoherence is inspired by the noncritical Liouville String Model [53, 54] and this feature is the core of the formalism developed by Percival and collaborators [60, 61, 62]. Other departures from traditional QM would be modifications of the Heisenberg principle or the de Broglie relation, that may need to be adapted to spacetime quantization, even though the modifications vary from one framework to another [63, 64, 65]. The de Broglie relation reflects the properties of the assumed spacetime − through the differential calculus on the spacetime manifold −, so that a quantum spacetime would require to adopt a new form of differential calculus [66, 67] and the reformulation of the relation [63, 64, 65, 68]. Modifications of the laws of quantum mechanics can be considered natural for the whole QG problem − even without assuming spacetime quantization − like in ST, where evidence of modifications to the Heisenberg principle are found in the so-called "Generalized Uncertainty Principle" [69].

- **Distance fuzziness and spacetime foam:** The term "spacetime foam", introduced by Wheeler, is used to provide some intuition for the effects induced by spacetime quantization, although it has no operative definition. Nevertheless, this description has motivated to look for a formalization of spacetime where the distance between two events can not be sharply determined, and the metric is correspondingly fuzzy. In contrast with the rest of effects, that describe departures from currently adopted laws, the "fuzziness" [70] would correspond to non-systematic effects guided by the idea that spacetime quantization might act as an environment inducing apparently random fluctuations on certain observables. During the past decades, there have been attempts to characterize the concept of spacetime foam and to introduce corresponding test theories [71, 72, 73, 42], usually centered on the fuzziness *per se* or associated decoherence. However, this effect has very little guidance from the most studied QG theories as LQG or spacetime non-commutativity.

- **Planck-scale departures from the Equivalence Principle:** Violations of the Equivalence principle have not been extensively studied from a quantum-spacetime perspective, even though being locality a key ingredient of the formulation of the Equivalence Principle and given the "delocalized point particles" that a quantum spacetime scenario would produce, the requirement of a modification of the Equivalence Principle would not be ruled out. In this direction, only few studies

have appeared, as violation of the Equivalence Principle due to quantum-spacetime decoherence [74], a study based on the non-critical Liouville String Theory [75] and a study based on metric fluctuations [76]. Other studies, even without quantization and based on ST, provide scrutiny of the Equivalence Principle [77, 78, 79, 80, 81]. There are analyses reporting the possibility that the violation of the Equivalence Principle might be a by-product of the violation of Lorentz symmetry [82].

1.4 Departures of Lorentz Invariance

In this thesis, the focus is cast on deviations from spacetime symmetries, specifically departures from Lorentz symmetry, that are in addition intimately related to violation of CPT. This and the next sections give a glimpse on both theory and experimental tests to study the phenomenology of LIV.

The theoretical point of view of LIV has been studied for many years [83, 84, 85] while investigation of its experimental consequences has been developed only within the past 20 years [86, 87, 88, 89], since the new effects were previously expected only in particle interactions at energies of the order of the Planck scale. Later, it was realized that there are special situations where effects could manifest also at much lower energies.

In recent years, attempts to detect deviations from Lorentz Invariance (LI) have mainly focused on modified dispersion relations for elementary particles (for a historical review, see [90]). Specific predictions of LIV arose in several approaches for QG, for example ST [91], spacetime foam [92], LQG [43], non-conmmutative geometry [93, 94, 95] or brane-world background [96].

In most QG approaches, LIV appears as a modification of the dispersion relation of particles that, in a general way $-$ preserving rotation invariance and considering that only boost invariance is affected at the Planck scale [90] $-$ can be expressed as

$$E^2 = p^2 + m^2 + f(E, p; \mu; E_{QG}), \tag{1.1}$$

where natural units have been used, E and p are the energy and momentum of the particle, μ is a mass-scale associated to the symmetry breaking and E_{QG} is the relevant QG energy scale, expected to be close to the Planck scale. At low energies, the function $f(E, p; \mu; E_{QG})$ can be expanded in powers of momentum and usually the lowest terms are considered (p, p^2, p^3, p^4) [97]. At first glance, it seems hopeless to look for effects suppressed by the Planck energy, nevertheless, even these tiny corrections can be magnified when dealing with high energies, long distances or peculiar reactions [97]. A short list of expected effects, detailed in Section 1.5, can be:

- Sideral variation of LIV coupling as the lab moves with respect to a preferred frame or direction.
- Cumulative long baseline dispersion or vacuum birefringence.
- Anomalous or forbidden threshold reactions (vacuum Cherenkov effect, etc).
- LIV induced decays (photon decay, photon splitting, neutrino splitting, helicity exchange decay, etc.)
- Shifts of threshold reactions.

- Dynamical effects of a LIV background field (gravitational coupling, additional wave modes, etc.)

The different tests depend on the underlying physical framework chosen to justify the use of modified dispersion relations as Equation 1.1 (Section 1.4.1). The cumulative effects use the power-law expanded form of the dispersion relation, but others effects depend on the underlying dynamics of the interacting particles and on the energy-momentum conservation law.

1.4.1 Lorentz Invariance Violation Parametrization

A simple approach to a phenomenological description of departures from LI consists of modified dispersion relations of particles.

The simplest possibility is to explicitly break LI, in the same sense as symmetries are broken in particle physics, provided by a tensor field with a vacuum expectation value [91].

An alternative possibility, is the one of deformed − rather than broken − spacetime symmetries, in the framework of the Doubly Special Relativity (DSR) proposal, put forward several years ago [98, 99].

This section illustrates briefly the differences between the broken-symmetry hypothesis and the DSR hypothesis and how both of them lead to modified dispersion relations. Even though these approaches to describe LIV are the ones with the strongest theoretical background, they are not the only ones, as shown in [97].

Lorentz Invariance Violation

The simplest kinematic framework breaking LI consists of modified dispersion relations while keeping the energy-momentum conservation laws.

It uses a preferred rest frame − that usually coincides with the one of the cosmic microwave background − in which the dispersion relations for particles are modified as shown in Equation 1.1. Since our world is LI at low energies, and we are nearly at rest with respect to the cosmic microwave background, the additional term in the dispersion relation should converge to the LI case at small energies and momenta, allowing a natural Taylor expansion around $p = 0$. After the simplifying assumption of rotational invariance, the expansion can be expressed as

$$E^2 = p^2 + m^2 + E_{Pl} f^{(1)}|p| + f^{(2)}p^2 + \frac{f^{(3)}}{E_{Pl}}|p|^3 + \frac{f^{(4)}}{E_{Pl}^2}p^4 + ..., \tag{1.2}$$

where E_{Pl} is the Planck energy scale, and $f^{(n)}$ are arbitrary dimensionless coefficients. There is no phenomenological reason to expect that the coefficients in Equation 1.2 are universal, so that they might depend on the particle species.

A complete physical theory should include dynamics in order to fully test LI. Purely kinematic frameworks forbid any test that relies on particle interactions, determined by the dynamics of the theory. Only few selected observational LIV tests, such as interferometry, vacuum birefringence, Doppler shifts, or Time-of-Flight are by construction insensitive to dynamics. However, for terrestrial tests one must recognize that different experiments can give different results when considering kinematic frameworks. The alternative strategy would be to embed the kinematics into a fully dynamical model. This a key point for the broken-symmetry approach, that can be embedded into an EFT[97].

EFT is the most conservative approach to study LIV, in which the Standard Model (SM) can be considered an EFT that can incorporate Lorentz violation via the introduction of extra Lorentz-violating

operators to the SM Lagrangian. EFT provides a sufficiently robust and general set of rules to describe LIV without requiring details of the QG model leading to such an effect. Indeed, many QG models can be reduced to EFTs [43, 100, 101]. When constructing an EFT of Planck-Scale LIV, one can introduce LIV terms in the SM Lagrangian that preserve renormalizability; or explicitly break LI by introducing non-renormalizable operators of mass dimension larger than four. The first group leads to contributions at low energies, and the second, to contributions at high energies which are naturally Planck-scale suppressed. Both possibilities are explored in the so called Standard Model Extension (SME).

- **SME with renormalizable operators:** This approach, carried out within the minimal SME [91] consists of the SM plus all the renormalizable LIV operators that do not change the field content or violate gauge symmetry. The terms can be classified according to their behaviour under CPT [97]. The modified dispersion relations for Quantum Electrodynamics (QED) sector look like

$$E_e^2 = p^2 + m_e^2 + f_e^{(1)}p + f_e^{(2)}p^2, \tag{1.3}$$

$$E_\gamma^2 = (1 + f_\gamma^{(2)})p^2, \tag{1.4}$$

  where the first equation is for electrons and the second one for photons. The coefficients $f_e^{(1)}$, $f_e^{(2)}$ and $f_\gamma^{(2)}$ depend in general on the helicity state of the particles and the coupling parameters of the LIV operators in the Lagrangian [97]. From these equations, we can appreciate that the typical energy at which new phenomenology should begin to appear is quite low, however the coefficients in Equations 1.3 and 1.4 may be much smaller than $O(1)$. A review of the tests used to set constraints on these Low Energy (LE) terms are explained in Section 1.5. All possible renormalizable Lorentz violating terms that can be added to the SM are summarized in [102].

- **SME with non-renormalizable operators:** This approach includes the non-renormalizable LIV operators that have mass dimension 5 or greater [103], that preserve rotation and gauge invariance but break local LI. Once added to the QED sector, they lead to modified dispersion relations as

$$E^2 = p^2 + m_e^2 + \frac{f_{e(R,L)}^{(3)}}{E_{Pl}}p^3 + \frac{f_e^{(4)}}{E_{Pl}^2}p^4 + ..., \tag{1.5}$$

$$E_\gamma^2 = p^2 \pm \frac{f_\gamma^{(3)}}{E_{Pl}}p^3 + \frac{f_\gamma^{(4)}}{E_{Pl}^2}p^4 + ..., \tag{1.6}$$

  where the cubic term violates CPT, giving place to different dispersion relations for positrons and electrons and for photons with different helicity states. In this case, as terms in Equations 1.5 and 1.6 are suppressed by the Planck energy, the expected energy scale for new phenomenology is much higher, out of reach of terrestrial experiments. Observations involving very high energies can thus potentially cast an $O(1)$ constraint on the coefficients. As we lack a definite QG model, usually the coefficients are considered to be $O(1)$ at the Planck scale and the strength of the constraints is judged with respect to this reference value.

Since the LE world has proven to be LI, it may make sense to create an EFT with only non-renormalizable LIV operators, of mass dimension 5 or higher. However, in QFT, radiative corrections generate LIV operators of dimension $(n-2)$ that become dominant, under the assumption that any coefficient ($f_e^{(n)}$ / $f_\gamma^{(n)}$) is of order $O(1)$ [104, 105] and given that the renormalizable terms are not Planck

suppressed. Thus, radiative corrections do not preserve dispersion relations like those in Equations 1.5 and 1.6, but lead to additional term as the ones shown in Equations 1.3 and 1.4.

A possible solution is SuperSymmetry (SUSY) [106, 107] that can be an exact symmetry in the presence of LIV. SUSY will prevent the lower order Lorentz-violating renormalizable operators from appearing in the Lagrangian. When SUSY is broken, as it is in the LE world, the renormalizable operators would appear again [106, 107].

Moreover, the terms with odd powers of p seem unnatural in the EFT frame, since they break CPT, include birefringence, and their coefficient values must be much smaller than the "natural" value of $O(1)$ in order to fit the current constraints [108]. There is however no clear argument accounting for why dimension five operators should not appear in the high energy theory. Some argue that the GR action is proportional to $G_M \simeq M_{Pl}^{-2}$ so the leading order contribution to LIV should have dimension six and be suppressed by two powers of M_{Pl}, while in the Liouville string theory model, the leading order LIV term have mass dimension five [109]. Nevertheless, if the theory assumes CPT invariance for the Planck scale theory, odd terms are forbidden.

Therefore, a combination of CPT and soft-broken SUSY would produce a viable LIV theory with all operators below dimension six forbidden.

Lorentz Invariance Deformation

The fact that EFT is formulated in a specific system of reference means that the relativistic principle no longer holds. There are many experiments sensitive to the existence of a preferred reference frame that imply very strong constraints on LIV [110].

Doubly Special Relativity (DSR) emerged as an alternative way to consider LIV, where the symmetry is *deformed* instead of broken, so that there is no preferred frame and it is still possible to formulate observer-independent laws of physics. In this case, it is much more difficult to find observable effects of the theory but the characteristic deformation of DSR can be encoded in an energy-momentum dispersion relation which depends on a high-energy scale E_{DSR}, usually of the order of the Planck energy, constructed to be invariant in the same sense as the speed of light is a relativistic invariant, together with deformed Lorentz transformations which preserve the form of that dispersion relation. The presence of a new energy scale does not require to deform rotations, so usually DSR considers a deformation only in the transformation laws under boosts.

The generators of the deformed Lorentz transformations satisfy the ordinary Lorentz algebra but are represented in a non-linear way in momentum space [111]. In DSR theories, when dealing with multiple particles, the total momenta cannot be defined as the addition of the individual momenta if it has to transform under boosts as the momentum of a single particle, leading to the introduction of a deformed composition law which depends on the new energy scale of the theory.

DSR cannot be embedded in EFT and is currently developed only as a kinematic formulation. Trials to include a dynamical formulation face major problems since the spacetime structure underlying the theory is expected to be non-trivial, for example by containing fundamental non-commutativity [112]. There are several DSR proposals − DSR1 [98], DSR2 [113, 114] and DSR3 [115] − but they all keep the rotational symmetry unaffected and the Lorentz group still generates spacetime symmetries that act in a non-linear way on the fields. DSR-like features appear in models of non-commutative geometry, as the κ-Minkowski framework [116, 14] or non-canonical non-commutative field theories [117].

DSR, once mathematically consistent, has a phenomenological advantage − it does not have a preferred frame − so that it evades most of the threshold constraints from astrophysics (See Section 1.5) as well as any terrestrial tests looking for sideral variations, while still modifying the Lorentz group action. Since these experiments provide almost all the tests of LIV we have so far, DSR entails the search for new LIV tests, becoming more phenomenologically attractive.

As a simple case example, the DSR2 boost transformations [98] are derived from the relations

$$E = \frac{\epsilon}{1 + \lambda_{DRS}\epsilon}, \tag{1.7}$$

$$p = \frac{\pi}{1 + \lambda_{DRS}\pi}, \tag{1.8}$$

where $\lambda_{DRS} = E_{DSR}^{-1}$. E and p are the physical energy and momentum with an induced non-linear Lorentz transformation and a modified composition law, while ϵ and π are the "pseudo-energy" and "pseudo-momentum", that transform in the usual way under Lorentz transformations, and the usual conservation laws hold for them. Given these rules and for any measured energy and momentum of a particle, we can solve for ϵ and π and calculate physical quantities, as interaction thresholds. In this case, the invariant dispersion relation for the DSR2 boosts is given by

$$E^2 - p^2 = \frac{m^2(1 - \lambda_{DRS}E^2)}{1 - \lambda_{DRS}m^2}. \tag{1.9}$$

Although the theory is appealing, it is still however riddled with many open problems. For example, it is incomplete since it is only formulated in momentum space, but also needs a DSR spacetime to relate momenta to position. In this latter endeavor there have been two approaches: one in commutative space coordinates, another relating the DSR feature to a non-commutative position space. In both approaches problems have appeared, like triviality [118] or internal consistency [119, 120] for the commutative case, or lack of understanding [121] in the non-commutative case, still under intense research [122].

Summarizing, the DSR approach is still a subject of active research and debate [123, 124] but it has not reached the level of maturity needed to make robust phenomenological predictions which can be tested experimentally. For this reason, starting in Section 1.5 and for the rest of this thesis the constraints and discussions are focused on the SME approach.

1.5 Lorentz Invariance Violation experimental tests

The development of a systematic EFT-based approach represented a milestone in searches for departures from exact LI. A large and assorted phenomenological toolkit was hence created to test LI, which can be separated into two subsets: terrestrial experiments that deal with lower energies and astrophysical observations looking for effects at the highest energies.

This section gives a short overview about the most relevant cases in both subgroups (a more detailed overview can be found in [97]). A deeper description of the tests that can be performed by Imaging Atmospheric Cherenkov Telescopes (IACTs) is found in Chapter 3.

1.5.1 Terrestrial experiments

Nature has proven to be LI to a very high degree. Therefore, looking for deviations from LI at low energies, described by the renormalizable terms in EFT-based approach, requires very high precision, and hence Earth-based experiments. Among the most relevant experiments, we can find:

- **Clock comparison experiments:** Considering as clocks two co-local atomic transitions and moving them in space, they pick out different components of the renormalizable LIV tensors. This fact yields to a sideral drift between the clocks that can be constrained by measuring the difference between their frequencies over long periods. The clocks should be made of different materials or have different orientations. This technique has put strong limits on some renormalizable EFT parameters (usually for protons and neutrons) [125, 126, 127].

- **Cavity experiments:** This technique constrains the variation of a resonance cavity frequency, with respect a to standard stationary frequency, as its orientation changes in space. Even though this experiment is similar to the clock comparison, this one allows to set constrains also on the electromagnetic sector. Bounds from cavity experiments are given in [128, 129, 130, 131, 132].

- **Neutral meson experiments:** An orientation-dependent change in the mass difference of neutral mesons, one of the most accurately measured quantities in the SM, affected by the SME LIV operators can be constrained by looking for sideral variations or other orientation effects. This mass difference has been extremely well measured in KTeV [133] or FNAL E773 at Fermilab [134]. Also lifetime directional dependence has been investigated [135].

- **Penning traps:** In a Penning trap [136], a charged particle is confined for a long time with a combination of static magnetic and electric fields. A deviation from LI can be measured by monitoring the particle cyclotron motion and the magnetic field and its Larmor precession due to the spin. These two frequencies are affected by the SME operators and Penning traps can be set up to be very sensitive to these changes. Two examples of these experiments can be found in [137, 138].

- **Spin polarized torsion balances:** This experiment appears as an effective technique to constrain the LIV tensors in the electron sector. An experimental setup consists of an octagonal pattern of magnets that have an overall spin polarization in one plane. Four octagons are suspended from a torsion fiber in a vacuum chamber and the whole apparatus located on a round table. As the round table rotates, looking for orientation dependent phenomena, the Lorentz breaking effect is measured. The best limits for the electron sector come from experiments in Washington [139] and in Taiwan [140]. Torsion experiments also allow to set constraints on mass dimension five operators in the absence of all lower dimension operators [103].

1.5.2 Astrophysical observations

In order to constrain higher mass dimension operators, much higher energies are required, unreachable for terrestrial experiments. High Energy (HE) and VHE gamma-ray astrophysics, widely introduced in next chapter, are the best fields to constrain these operators.

In this sector, the experiments set constraints on the dimensionless coefficients in Equations 1.5 and 1.6, considering the absence of lower mass dimension terms.

- **Vacuum birefringence:** In SME with mass dimension five operators, odd in CPT, particles with opposite helicities have slightly different group velocities, implying that the polarization vector of a linearly polarized wave during the wave propagation, rotates differently for different photon energies. Over long distances, this effect disrupts the amount of polarization in the wave. This method has been applied to several astrophysical sources as Gamma-ray Bursts (GRBs) [108, 141] or Pulsar Wind Nebulae (PWNe). This method has yielded the strongest constrain on $f_\gamma^{(3)}$ so far, orders of magnitude below 1.

- **Photon time of Flight:** A dispersion relation as in Equation 1.6 implies that photons with different energies travel at slightly different speeds. If no birefringence is assumed, after travelling a given cosmological distance, the energy-dependent speed would produce an energy and distance dependent time delay that can be constrained using astrophysical observations. The methodology, sources and results on these tests are shown in detail in Chapter 3.

- **Threshold reactions:** The extra terms in the SME approach can be considered as extra mass terms, that is the reason why LIV corrections are important for threshold processes. A rich phenomenology related to threshold reactions is introduced by LIV in EFT and threshold theorems can be generalized [142, 143]. The different aspects under study in threshold reaction experiments are

  - A shift of the energy threshold of existing reactions, leading to upper thresholds.
  - The possibility of pair production reaction with unequal outgoing momenta.
  - The viability of new, normally forbidden, reactions.

- **Synchrotron radiation:** Synchrotron radiation is affected by LIV [144, 109, 145, 146, 147], thus effective constraints can be obtained by comparing observed and expected synchrotron spectra from astrophysical sources. This technique allows to set strong constraints on mass dimension four and five LIV operators. Constraints on the lepton sector have been obtained with observations of the Crab Nebula [148].

Chapter 2

Gamma-ray Astronomy

The range of frequencies composing the Electromagnetic (EM) spectrum belongs to electromagnetic waves whose wavelengths vary from thousands of km to the size of an atomic nucleus and beyond. These frequencies are divided in ranges with a given name (radio, IR, visible, UV, X-rays, gamma rays) whose waves share some properties, like production or interaction mechanisms or practical applications. As humans, nature has provided us with the direct visible access to a tiny fraction of the EM spectrum − the so called visible range − composed by wavelengths between 400 and 700 nm. However, along history, humans have developed all kinds of instruments in order to access even the most remote edges of the spectrum.

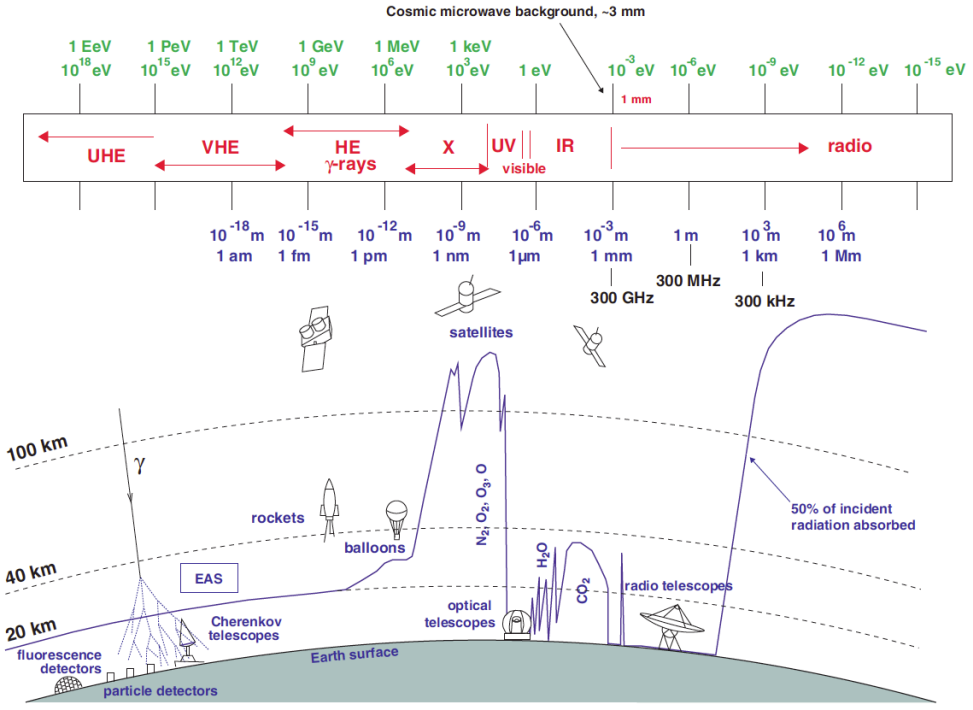

Figure 2.1: Above: Observable edges of the EM spectrum, the frequency ranges are indicated in red, the energy values in green and the wavelengths in blue. Below: atmospheric absorption altitudes and instruments in use for the different frequency ranges, a blue line indicates the atmospheric altitude at which the radiation is absorbed for the different energies. Credit: M.S. Longair [149]

Gamma-ray astronomy, the astronomy branch focused on EM waves with the smallest wavelengths produced in the universe, has opened the farthest limit in the window of the EM spectrum, resulting in the study of celestial phenomena in the highest energy domain. Nowadays, the study of gamma-ray cosmic radiation is a main stream in modern astrophysics, with hundreds of detected sources and reliable detection techniques with potential significant improvement in the future. Nevertheless, gamma-ray astronomy is still a very recent research field, born at the beginning of the 20th century, motivated by the discovery of Cosmic Rays (CRs).

CR is the name given to a steady rain of very energetic charged particles coming from outer space and moving close to the speed of light, that fall upon our planet at all times and whose origin and production mechanisms were unknown, since such high energies could not be explained by thermal processes.

CRs were discovered accidentally by Viktor Hess in 1912 [151] using a balloon that rose in Aussing, Austria, and ascended an altitude up to 5 km. The initial plan for Hess was to prove that the loss of charge in an electroscope [1] (Figure 2.2) due to the ionization of the gas inside the instrument, after discarding other hypotheses, was due to the radiation emitted by the radioactive materials in the Earth's crust. The expectation was that the discharge would be strongest near the Earth's surface, so increasing altitude and observing his electroscopes, Hess was expecting that the loss of charge would become progressively weaker with increasing altitude. Hess found that the ionization became somewhat weaker at first since the discharge rate was slower but, after 0.7 km altitude, the trend reversed itself and the ionization began to increase gradually until, at 5 km high, the discharge was about four times faster than on Earth. The only explanation to this phenomenon postulated by Hess was that there were some kind of ionizing radiation falling upon Earth coming from somewhere beyond the atmosphere. His striking statement had to wait many years and many experiments to be generally accepted. Final acceptation went hand in hand with the skeptical Robert A. Millikan after a series of remarkable experiments between 1923 and 1926, that convinced Millikan himself and the whole scientific community that the radiation discovered by Hess was coming for beyond the atmosphere. Millikan himself proposed the name of *Cosmic Rays*.

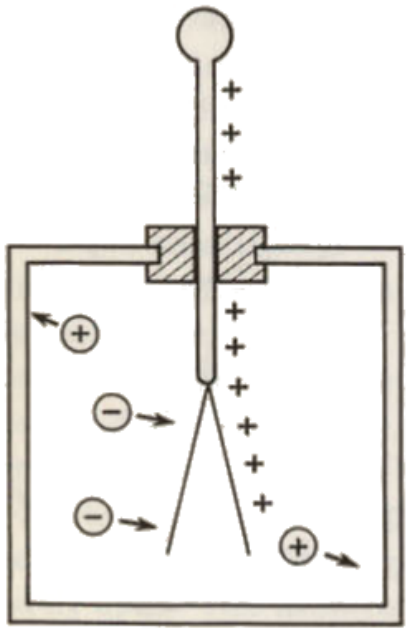

Figure 2.2: Graphical representation of an electroscope being discharged by gas ions. Credit: B. Rossi [150]

The presence of CRs made the scientific community wonder about the existence of *"factories"* in the universe capable of accelerating particles to such extreme energies. If that was the case, the acceleration of particles might possibly be accompanied by effective radiation processes, so that not only matter but very energetic radiation, would enter the game.

CRs, that are ordinary atomic nuclei stripped of their electrons, are the most energetic particles ever

[1] Electroscopes were early instruments to measure electrical charge. When in contact with a charged body, they had two leaves or wires that repel each other since they obtain the same charge. However, after some time, the leaves come back together, showing that the charge was somehow gone.

Unit	Electronvolts (eV)
eV	1
keV	10^3
MeV	10^6
GeV	10^9
TeV	10^{12}
PeV	10^{15}
EeV	10^{18}

Table 2.1: Electronvolt metric prefixes.

detected. Their study and interpretation can lead to a better understanding of the evolution and composition of the universe, today and in the past. Such study provides information about CRs composition and energy distribution, however their origin sites are not traceable from Earth since these charged particles are deflected by the presence of electromagnetic fields along their trajectories to Earth, loosing trace of the departing points. Nevertheless, analyzing the resulting radiation from their acceleration sites, that travels unaffected from the sources to Earth, we may obtain information about the location of these CR *"factories"* and their acceleration mechanisms.

Gamma-ray radiation refers to the most energetic electromagnetic waves, whose range covers at least 14 decades in frequency. This energy band spans from $E = h\nu \simeq 0.5 \cdot 10^6$ eV, the region of nuclear gamma-ray lines and the electron-positron annihilation line to more than 100 EeV, bound determined by the most energetic observed CRs, whose interactions should produce gamma rays of comparable energy. The enormous energy band is covered rather inhomogeneously, in the sense of very different instruments and detection techniques (see Figure 2.1), that allows us to sub-divide it in smaller observational energy bands,

- ***Low Energy (LE)*:** below 30 MeV.
- ***High Energy (HE)*:** 30 MeV - 30 GeV.
- ***Very High Energy (VHE)*:** 30 GeV - 30 TeV.
- ***Ultra High Energy (UHE)*:** 30 TeV - 30 PeV.
- ***Extremely High Energy (EHE)*:** above 30 PeV.

The electronvolt (eV) is an energy unit very common in gamma-ray astrophysics. It is equivalent to $1.6 \cdot 10^{-19}$ J, the energy gained by an electron crossing an electric potential difference of 1 volt. The symbols "MeV...PeV" are used to express very high energies and their relation to eVcan be found in Table 2.1.

The term "astronomy" is adequately applied to the activities in the LE, HE and VHE bands since no detection of gamma-ray sources in the UHE or EHE regime has been done so far. Only a limited fraction of the universe is available in the last three energy bands due to the so called gamma-ray horizon, determined by the interactions of gamma rays with the diffuse extragalactic photon fields, process with a strong energy dependence, that avoids the most energetic gamma rays to reach the Earth. As an example, the mean free path of TeV gamma rays is hundreds of Mpc, for PeV energies is reduced to few Kpc and down to few Mpc for EeV gamma rays .

Even though the study of gamma rays was at its origin very closely linked to CRs, now it can be considered a discipline in its own right. gamma rays reveal information about non-thermal[2] relativistic processes, usually proceeding under extreme physical conditions, in a wide variety of astrophysical environments, and involving a broad range of topics related to the acceleration, propagation and radiation of particles at all astronomical scales.

The study of VHE gamma rays can help us to to understand the physics of the relativistic cosmic flows, common in many astrophysical environments in form of jets or winds, and to expand our knowledge about cosmology, studying the gamma-ray energy-dependent absorption features, related with epochs of galaxy formation and evolution. Moreover, as proved by the main topic of this thesis, VHE gamma rays are ideal tools to investigate fundamental open questions in physics, as the nature of gravity itself, through the study of the consequences of a quantum gravity, namely LIV, that require to reach very high energies.

This chapter gives an overall review of the current status of gamma-ray astronomy. Firstly, we exposed the production and absorption mechanisms of gamma rays in Section 2.1. Later, we explain in detail the evolution and current status of all techniques developed to detect gamma rays in Section 2.2. Finally, the chapter ends with the different gamma-ray sources detected so far (Section 2.3), specially centered on the VHE band.

2.1 Gamma-ray production and absorption mechanisms

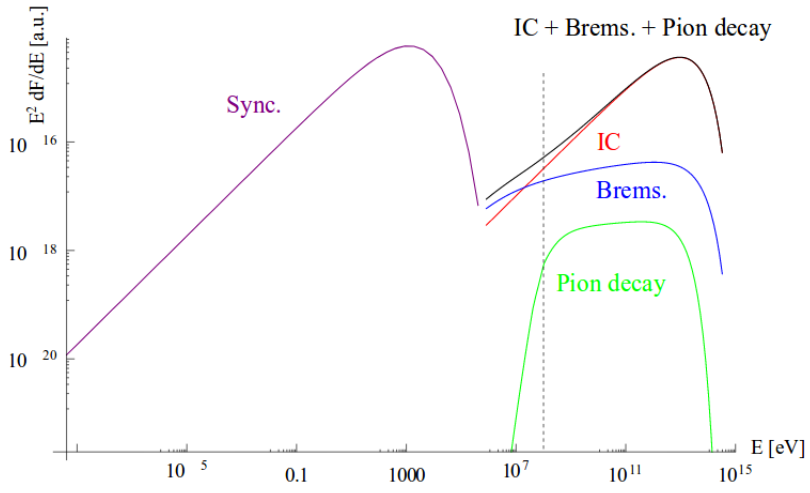

Figure 2.3: Broad band spectral energy distribution in arbitrary units produced by a power law distribution of index -2 of relativistic electrons and protons with an exponential cut-off at 10^{14} eV. The cut-off produced by pion decay is indicated with a dashed line. CMB photos are considered targets for IC. Credit: J. Krause [152]

.

For any interpretation of the results from gamma-ray observations is mandatory to have some knowledge about the principal radiation and absorption mechanisms that generate this non-thermal highly energetic light.

The gamma-ray wavelength band is characterized by a large number of competing radiation processes, that makes the theoretical study very challenging, specially when a experimental result can be equally explained by more than one radiation mechanism, that contribute comparably to an energy regime of the

[2]Radiation not produced by electrons changing positions in their orbital shells around atoms.

observed gamma-ray flux. Figure 2.3 shows the theoretical energy distribution of gamma rays , assuming a initial population or accelerated charged particles and their targets.

Most radiation processes imply the interaction of accelerated particles, as electrons, protons or nuclei, with ambient targets. A classification can be made through the character of the interactions – leptonic, hadronic, absorption or radiation – or through the target type, as matter, photon fields or magnetic fields [153]. In this section, the leptonic scenarios with their production and absorption cases will be treated first, followed by the hadronic scenarios.

The majority of the production mechanisms has a major "counterpart" or absorption mechanism with the same electromagnetic origin and similar cross section [3]. Different astrophysical scenarios favour one or another. This section exposes jointly the processes and their counterparts, for simplicity.

2.1.1 Leptonic scenarios

In these interactions, the accelerated charged particle is a lepton, usually an electron.

Electron Bremsstrahlung

Bremsstrahlung is a German term meaning *"Braking radiation"* and it refers to any radiation emitted by an accelerated charged particle in the electrostatic field of a nucleus. In gamma-ray astrophysics, the concept usually refers to the radiation from a relativistic electron due to its deflection in presence of an electric field, produced by the presence of another close-by charged particle, as shown in Figure 2.4.

The radiating power of bremsstrahlung is inversely proportional to the particle mass, so that electrons loose energy by bremsstrahlung much more efficiently than heavier charged particles (muons, protons, etc).

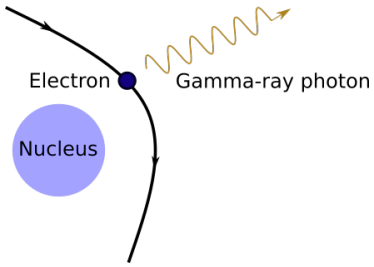

Figure 2.4: Graphical representation of the electron Bremsstrahlung process.

There are two important parameters in the bremsstrahlung mechanism: the radiation length and the critical energy. The radiation length (χ_0), is the distance at which the electron has travelled inside a medium and lost $1/e$ of its energy by bremsstrahlung. It depends on the target matter (nucleus charge and mass number of the nuclei). The critical energy is the energy below which the energy losses by ionization dominate over bremsstrahlung losses, so that the electrons stop producing gamma rays . A comprehensive analysis for bremsstrahlung features can be found in [154].

Considering a power-law electron spectrum – $f(E) = CE^{-\Gamma}$ – inside the relativistic regime ($E_e >> m_e c^2$) and assuming full screening effect [4], the electron energy loss due to bremsstrahlung [153] can be expressed as

$$-\left(\frac{dE_e}{dt}\right)_{Brems} \propto \frac{1}{\chi_0} E_e. \tag{2.1}$$

[3] The cross section of an interaction between two particles is the effective collision area transverse to the motion of the interacting particles. It is proportional to the probability of the interaction to occur. The cross section is typically denoted by σ and expressed in units of area. This concept is commonly used, instead of reaction rate, since it is instrument-independent.

[4] Depending on the energy of the accelerated particle, the Coulomb field of the nucleus can be more or less screened by the electron cloud. For the relativistic case, we have a full screening effect.

The relativistic bremsstrahlung energy losses are quite large for electrons and the energy of the emitted photons is $E_\gamma \sim E_e$, so that with these assumptions the energy spectrum of the radiated gamma rays follows the shape of the parent electrons, if bremsstrahlung is dominating.

Electron-positron annihilation and pair production

Electron-positron annihilation and pair production are counterpart processes of each other (see Figure 2.5).

Electron-positron annihilation refers to the radiation emitted when an electron collides with a positron, thus, its antiparticle. This mechanism can be an important source of gamma rays through the reaction

$$e^- + e^+ \longrightarrow 2\gamma. \tag{2.2}$$

When the two particles are at rest, the energy of the resulting photons is simply $E_\gamma = m_e c^2 = 0.511$ MeV, below the gamma-ray regime. However, if one of the leptons moves at high velocity when it collides with the other at rest, then one photon will have a high energy whereas the other will have an energy ~ 0.511 MeV. Electron-positron annihilation can also occur with the emission of a single photon, but in this case the electron must be bound to an atom. Three or more photons can be produced in the annihilation of free electron-positron pairs but the cross section of these processes are smaller [155].

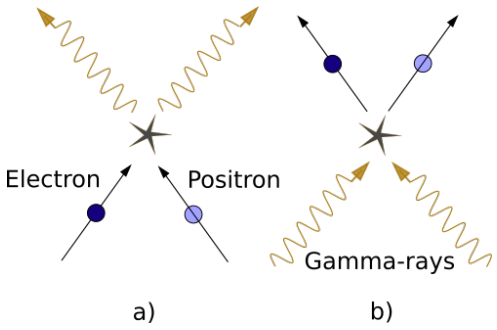

Figure 2.5: Graphical representation of electron-positron annihilation (a) and pair production (b).

Pair production is the inverse process. It defines the creation of an electron-positron pair by the interaction of two photons,

$$\gamma + \gamma \longrightarrow e^- + e^+, \tag{2.3}$$

typically a HE one and a LE one. Considering two photons of energies $E_{\gamma,1}$ and $E_{\gamma,2}$, they can produced a electron-positron pair above a given energy threshold

$$E_{\gamma,1} \cdot E_{\gamma,2} > (m_e\, c^2)^2, \tag{2.4}$$

whose value is at least the total rest mass energy of the two produced particles, in order to preserve energy and momentum.

The pair production reaction can occur in two different ways. The classical way, where the HE photon interacts with a virtual photon of a nucleus electric field, producing EM cascades that play the main role in the detection of gamma rays by ground-based instruments (Full description in Section 2.2.2). In the second case, the interaction occurs between a real HE photon with a LE photon from the ambient gas. This reaction is the responsible for the absorption of VHE gamma rays during their propagation towards Earth due to their interaction with the lower energy photons that compose the Extragalactic Background Light (EBL)[5].

[5]Diffuse radiation from ultraviolet to far infrared frequency produced by stellar nucleosynthesis and its re-emission by dust.

The pair creation cross section presents a peak at energy;

$$E_{\gamma,1} \cdot E_{\gamma,2}(1 - \cos\theta) \sim 2(m_e\, c^2)^2, \tag{2.5}$$

where θ is the collision angle between the photons. From Equation 2.5, we can see that photons with energies above 100 GeV will likely interact with photons in the IR or UV band, that is, the EBL band. The gamma rays absorption via pair production with the EBL photons explains why the VHE gamma-ray sources, can not be located at very large distances ($z > 1$), otherwise all the photons would be absorbed during their propagation to Earth, before reaching the ground-based telescopes.

Direct and Inverse Compton scattering

These two mechanisms are effectively the same, but they are named differently depending on how energy is exchanged between the particles.

Both mechanisms consist on the elastic interaction of a charged particle, here an electron, with a photon. The process can be expressed as

$$\gamma + e^- \longrightarrow \gamma + e^-. \tag{2.6}$$

The Compton scattering (CS) scattering denomination is used when, in the interaction, the electron gains energy from the photon (Figure 2.5, upper plot). If it happens the other way around and the electron looses energy while the photon gains it, then we called it Inverse Compton (IC) scattering (Figure 2.5, lower plot). In this case, we say that the photon is up-scattered by the electron and, if the energy exchange is effective enough, the photon can reach gamma-ray energies.

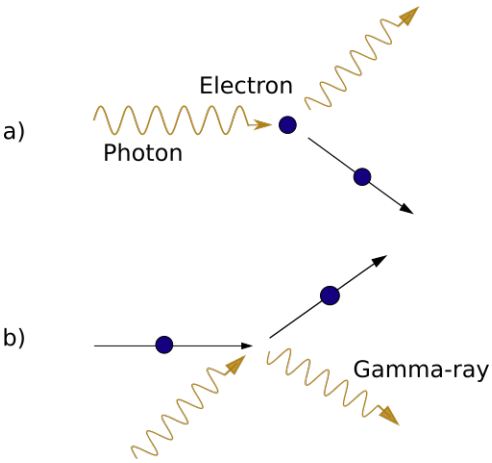

Figure 2.6: Graphical representation of direct (a) and inverse (b) Compton scattering.

The CS scattering can be an important source of energy loss for MeV photons and its cross section depends on the polarization of the photon. For unpolarized photons, and at low energy the cross section tents to the Thomson cross section [155][6].

The IC scattering is one of the most effective mechanisms for VHE gamma-ray production, where relativistic electrons scatter low energy photons up to GeV-TeV energies.

According to the initial energy of the interacting electron E_e and photon E_γ, we can distinguish two regimes [156],

- **Non relativistic regime** ($E_e E_\gamma \ll m_e^2 c^4$): The cross section in this case can be approximated by the Thomson cross section. In this regime only a fraction of the electron energy is released to the photon an the average energy of the emerging photon is

  $$\langle E_\gamma \rangle = \frac{4}{3}\langle E_{photon} \rangle \gamma^2 \tag{2.7}$$

  where the γ is the Lorentz factor[157, 155].

[6] J.J.Thomson derived the formula of the cross-section for absorption or radiation in matter when the photon energy is much smaller than the electron rest energy.

- **Ultrarelativistic regime** ($E_e E_\gamma \gg m_e^2 c^4$): This regime is also know as deep Klein-Nishina regime since cross-section tends to the Klein-Nishina one when $E_e E_\gamma \approx m_e^2 c^4$. Inside this regime, the electron gives most of its energy to the photon ($E_\gamma \sim E_e$) and one interaction is sufficient for it.

Synchrotron and curvature radiation

Synchrotron radiation refers to the radiation emitted by a relativistic charged particle in the presence of a magnetic field B. In the case of non-relativistic particles, the given name is Cyclotron radiation.

The accelerated particle, an electron in this case, follows a helical path with an angular frequency

$$\omega_B = \frac{eB}{m_e c^2}\frac{m_e c^2}{E_e}, \tag{2.8}$$

around the magnetic field lines and emits photons within an angle $\theta \sim mc^2/E_e$ of its direction of motion (see Figure 2.7).

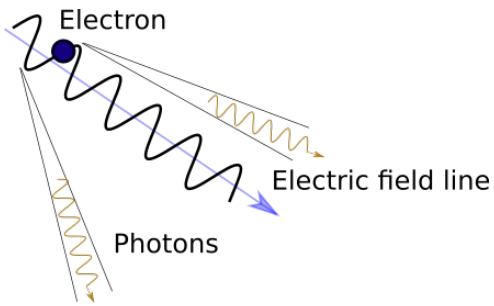

Figure 2.7: Graphical representation of synchrotron radiation mechanism.

Usually, the characteristic energy of the photons generated by this mechanism is much lower than the energy of the parent electrons[155],

$$E_{photon} = \frac{3h}{4\pi}\frac{eB_\perp}{m_e c}\left(\frac{E_e}{m_e c^2}\right)^2, \tag{2.9}$$

where $B_\perp = B\sin\theta$ is the pitch angle. Only for extremely energetic particles and strong magnetic fields we can get gamma-ray photons from synchrotron radiation, so that this is not the main process of gamma-ray production. However, some astrophysical environments like pulsar magnetospheres or magnetized accretion disks (See section 2.3), the VHE photons are produced via shychrotron. Synchrotron radiation is also relevant for producing gamma rays in a indirect way, by producing low energy photon targets for the IC scattering.

In the case of strong magnetic fields, charged particles tend to move along the field lines. In this situation, if the curvature radius of the field lines is small, particles will be accelerated and then they will radiate. This radiation of particles that follow the field lines is called curvature radiation. Usually the synchrotron regime ends in a curvature regime when the energy loss due to the radiation emission makes the pitch angle between the magnetic field and the electron velocity decrease, so that the radius of the helical movement shrinks and the particle ends following the field line. This transition speeds up as the magnetic field strength grows. A detailed description of this transition and its implications in the spectrum of the emitted radiation can be found in [158].

Synchrotron-self-Compton radiation

This process is not a new production mechanism but a combination of two of the processes mentioned previously. This case is given when the synchrotron emission is very efficient, the angle between the electron velocity and magnetic field is big [158], creating a radiation field. The synchrotron-produced photons become the targets of their own parent electrons that scatter them up via IC, making them reach higher energies. After some iterations between these two mechanisms, we might end up generating VHE gamma rays .

Estimating the electron and photon densities, we can compute the ratio between the two production methods and the expected energy distribution of the resulting radiation.

2.1.2 Hadronic scenarios

In the following scenarios a hadron, usually a proton, is the responsible of the produced or emitted radiation.

Neutral pion decay

Protons and nuclei moving at relativistic velocities suffer inelastic collisions with the ambient gas. As products of these collisions, secondary hadrons are produced. These secondary particles may produce high energy gamma rays as they decay.

In the case of proton-proton interactions leading to pion production, there can be different π-production channels [155], resulting in the production of the three types of pions π^+, π^- and π^0 with comparable probabilities, at high energies. Also electron-positron pairs can be created from these channel reactions and produce gamma rays through relativistic bremsstrahlung, IC and/or synchrotron processes depending on the environment.

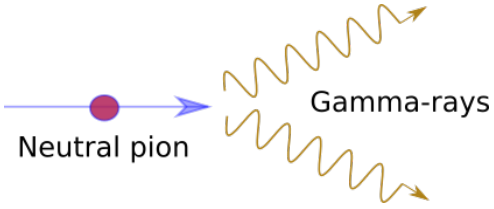

Figure 2.8: Graphical representation of pion decay gamma-ray production.

Among the resulting particles χ from the interaction, the neutral pions or π^0-mesons decay into gamma rays very rapidly since their mean lifetime, $8.4 \cdot 10^{-17}$s, is much shorter than the charged π mesons ($\approx 2.6 \cdot 10^{-8}$s). Therefore, shortly after their production, the π^0-mesons quickly decay into two gamma rays

$$pp \longrightarrow \chi + \pi^0 \longrightarrow \chi + \gamma + \gamma. \tag{2.10}$$

On the other hand, the charged pions decay into muons and neutrinos $\pi^{\pm} \rightarrow \mu^{\pm} + \nu$, and these muons decay into positrons or electrons, neutrinos and antineutrinos $\mu^{\pm} \rightarrow e^{\pm} + \nu + \nu + \bar{\nu}$, injecting leptons and neutrinos in the source.

Moreover, gamma rays can be also produced from neutral pion decay produced in proton-positron collisions [155].

Other processes

- Bremsstrahlung emission by hadrons can occur, however it is less efficient than in the electron case, due to the large mass of the proton. Moreover, the bremsstrahlung of UHE CRs is expected to lead to VHE gamma-ray photons production.

- Synchrotron emission can also be produced by protons, but this is considered an inefficient process. The reference of the developed theory for proton synchrotron radiation can be found in [159].

- Inverse Compton proton scattering $p + \gamma \longrightarrow p + \gamma'$ happens, but is has not relevant astrophysical implication since the energy loss rate is significantly slower than in the leptonic case.

2.2 Gamma-ray detection

The atmosphere is opaque to photons beyond the optical wavelength (Figure 2.1), forcing high-energy astrophysics to make use of space-based experiments. The first cosmic source detected by satellites was a X-ray source [160]. In the case of gamma-ray astronomy, there are more challenges to overcome since gamma rays with different energies require different detection techniques. Nowadays, gamma-ray astronomy has evolved to count with two detection strategies: direct detection using space-based instruments located outside the atmosphere, or ground-based detectors, located on Earth, that detect gamma rays indirectly, making the atmosphere become part of the detection process.

2.2.1 Evolution of gamma-ray detection techniques

After the discovery of the CRs, the interest in their nature and origin grew rapidly, and many experiments improved their detection techniques in order to carry out research on the topic. In the 20s, all CRs were believed to be produced by gamma rays , while Millikan defended that electrons reaching the Earth were produced by CS scattering of VHE gamma rays , Arthur Compton supported that CRs were simply charged particles, leading to a big debate in 1932 (see Figure 2.9). The situation changed when Pierre Auger discovered that CRs hitting the atmosphere produce Extensive Air Showers (EAS) [161]. CR physicists, after understanding better the shower development process, started to build balloons to study low energy CRs and air shower arrays for the more energetic CRs, providing a new detecting technique from ground.

Cherenkov radiation (Section 2.2.2) was studied by P.A.Cherenkov experimentally in 1934 [162] observing beta particles[7] crossing water and was finally explained theoretically by Frank and Tamm in 1937 [163]. Cherenkov, Frank and Tamm were awarded the Nobel Prize for this work in 1958. The link between this phenomenon and CRs was established in 1947 when Blackett pointed out that Cherenkov radiation should also be emitted when charged particles cross gases and proposed that CRs traversing the atmosphere must also produce Cherenkov light that would contribute to the night-sky luminosity [164]. This opened the door to a third detection option, measuring CRs indirectly from ground, by trying to detect the Cherenkov light produced by them when crossing the atmosphere. From that moment on and simultaneously, both detection branches were developed in parallel, space-based and ground-based CR detection.


The New York Times

VOL. LXXXII...No. 27,370. December 31,1932

MILLIKAN RETORTS HOTLY TO COMPTON IN COSMIC RAY CLASH

Debate of Rival Theorists Brings Drama to Session of Nation's Scientists.

THEIR DATA AT VARIANCE

New Findings of His Ex-Pupil Lead to Thrust by Millikan at 'Less Cautious' Work.

Figure 2.9: Front page of the New York times in 1932, indexing to the debate between Millikan and Compton.

On the ground-based side, Galbraith and Jelly built a simple detector and proved that EAS, produced in the interaction of CRs with the atmosphere, do indeed produce Cherenkov radiation [165], detected as fast light flashes visible in dark nights. The change of interest from CRs to gamma rays started with a conference of Cocconi in 1959 [166], stating that the Crab Nebula was expected to be a strong TeV gamma-ray source and, with an instrument with good angular resolution, it would be possible to distinguish between

[7] Very energetic electrons or positrons emitted in the radioactive beta decay of a nucleus.

isotropic CR EAS and the EAS produced by gamma rays interacting with the atmosphere that would be centered around the source position. Even if his model overestimated the fluxes and his proposed instrument was not appropriate, these predictions stimulated further work that led to the construction of the first Atmospheric Cherenkov Telescope designed to detect gamma rays in the early 60s. However there was a major drawback, the showers produced by gamma rays are a tiny fraction of the total amount of showers produced by ionizing radiation reaching the atmosphere and the first generation of instruments were not able to discriminate between different types of EAS. Therefore, the process advanced slowly with doubtful and inconsistent results until almost the 80s. Finally, in 1977, Weekes and Turver presented the first concepts for hadron and gamma-ray shower separation using computer simulations [167]. Then, the promising "*imaging technique*" proposed by Hillas in 1985 [168], that based the classification of the showers on the shape of the projected Cherenkov light image, finally encouraged the development of new instruments and analysis techniques which finished with the detection of the Crab Nebula by the Whipple telescope in 1989 [169]. These analysis techniques are still currently in use to analyze gamma-ray data and are presented in Section 2.2.2 and more in detail in Chapter 4.

On the space-based side, the first attempts to create instruments for gamma-ray detection were made with balloons in the early 70s. They were not very successful due to the high level of secondary gamma rays coming from interactions of CRs in the atmosphere, but they were able to see that the Galactic plane was bright for E>100 MeV [170] and to find evidence for pulsed gamma rays from the Crab Pulsar [171, 172, 173]. The OSO-3 satellite, flown in 1967-1968, was a sophisticated counter telescope and provided evidence that the Milky Way was bright in gamma rays above 50 MeV, although it did not image the pair production events [174]. The next space missions, with imaging technology of the 60s and 70s and using spark chambers, were two small satellites: the Second Small Astronomy Satellite (SAS-2), flown in 1972-1973, that mapped the galactic emission [175], found gamma rays coming from the Vela Pulsar [176] and measured an isotropic background radiation [177]; and the COS-B satellite (1975-1982), that already produced a catalog [178] of HE gamma-ray sources including an extragalactic one, namely 3C273 [179]. Because of the success and experience obtained with these pioneering small satellites, a major project by NASA, called the Compton Gamma Ray Observatory (CGRO), was launched with 4 instruments on board, one of them, EGRET, for HE gamma-ray detection. The CGRO mission ,from 1991 until 2000, released the first map of the entire HE gamma-ray sky and several catalogs, the most complete called the 3EG catalog [180]. A review of the EGRET results can be found in [181]. Finally, due to the early success of the CGRO, another project was proposed by the Stanford/SLAC group that, making profit of new advances in technology and modeling, resulted in the launch of the Fermi-LAT gamma-ray telescope [182] in 2008, on-board of the Gamma-ray Large Area Space Telescope (GLAST). Fermi-LAT continues nowadays surveying the gamma-ray sky and is presented in Section 2.2.3.

2.2.2 The physics of Extensive Air Showers

Types of Extensive Air Showers

VHE gamma rays or CRs entering the atmosphere interact with the nuclei present in the upper layers − around 20 - 25 km a.s.l., depending on the energy of the initial particle − and initiate an EAS, that are a series of chained interactions.

If the initial particle is energetic enough, the products of the interaction have a speed close to the speed of light in vacuum and interact themselves with more nuclei in their trajectory, producing more

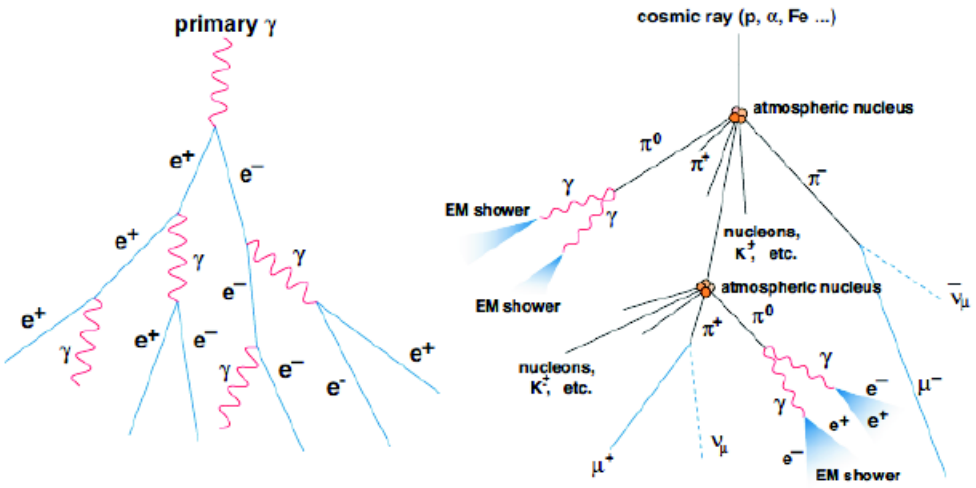

Figure 2.10: Schematic view of a EM shower (left) and a hadronic shower (right). Extracted from [183].

secondary particles. At the end, the cascade counts with thousands or even millions of particles. The development of the cascade continues until the particles' energy falls below a given threshold.

The particles of the cascade move almost in the direction of the initial parent particle (shower axis) with a small circular spread around it ($\sim$ 100 m). The part of the cascade where the density of particles is maximum is called the shower core.

These cascades can be divided in two types, electromagnetic or hadronic showers (see Figure 2.10), depending on the nature of the particle originating them:

- **Electromagnetic showers:** These showers can be initiated by gamma rays , electrons or positrons. During the cascade development, only the former particles are produced that is why the structure of these cascades is simpler than the ones initiated by hadrons. The cascades can be initiated in two ways: if the initial particle is a γ ray, it will create an electron-positron pair due the intense electric field. On the other hand, if the parent particle is an electron, it will radiate a γ ray via bremsstrahlung. The evolution of the cascade will then depend on the pair production of the photons and the bremsstrahlung or ionization energy losses of the charged particles. While the energy of the particles is high enough, the cascade will evolve while pair creating and bremsstrahlung processes take place alternatively. The development of this kind of cascades is well explained by the Heitler model [184]. It assumes that, in every iteration, the number of particles is doubled and their energy halved. The process will continue until the shower maximum when

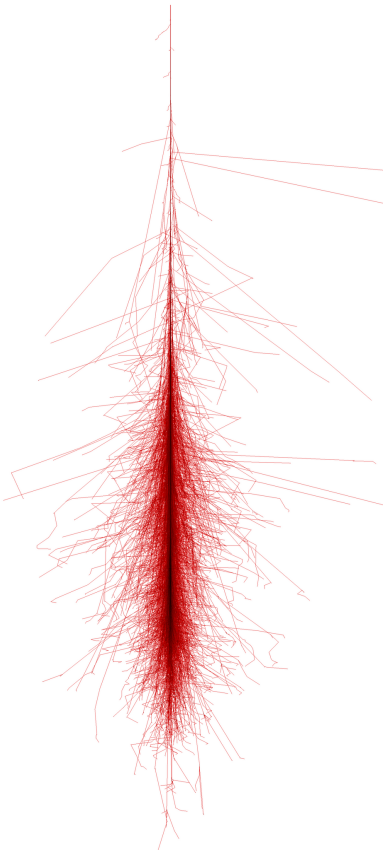

Figure 2.11: MC simulation of an EM cascade produced by a γ ray of 100 GeV.

the charged particles reach the critical energy and the ionization losses start to dominate. The EM showers are quite symmetric with respect to the shower axis (see Figure 2.11). The Heitler model predicts that the number of particles is proportional to the energy of the parent particle so that the energy of the parent particle can be deduced from the amount of Cherenkov radiation produced during the cascade development. Additionally, the altitude of the shower maximum is inversely proportional to the logarithm of the energy of the initial particle. This means that, the higher the energy of the initial particle, the deeper it will travel in the atmosphere before starting an EAS. The Heitler model does not take into account the Cherenkov light losses due to scattering (Rayleigh or Mie scattering) or absorption (by ozone, water or carbon dioxide molecules) during propagation, which need to be introduced separately by atmospheric models.

- **Hadronic showers:** The particle producing these showers is a hadron (hydrogen, helium or heavier nuclei). These showers are much more complex than EM showers since there are many more probable interactions and very different kinds of secondary particles. The first interaction is governed by the strong force and produces a pion in 90% of the cases (all three types π^+ π^- and π^0 in the same proportion), but also kaons (10%) and other baryons in smaller percentage. Charged pions, kaons and baryons usually suffer further collisions while neutral pions, whose life span is shorter (See section 2.1.2), decay in gamma rays that produce EM sub-showers. The shower develops until the nucleon energy falls below the pion production energy threshold ($\sim$1 GeV). Hadronic showers penetrate deeper in the atmosphere than EM showers and the variety of particles they contain makes them more irregular and wider (See figure 2.12). The particles that compose a hadronic shower can be divided in three groups:

  - Hadronic component: It involves nuclei and mesons, that transfer transversal momentum in the interactions. This contribution composes the core of the shower via decay or collisions that spread the shower.
  - EM component: Composed by the EM sub-showers produced by neutral pion decay. This component dominates at the end of the shower development.
  - Muonic component: It is comprised by the muons and neutrinos produced in the charged pion and kaon decays. Muons, due to their small radiation losses and their long lifetime, can travel long distances from their production position and reach the ground. Muons can produce enough Cherenkov light to be detected by IACTs, becoming a source of background.

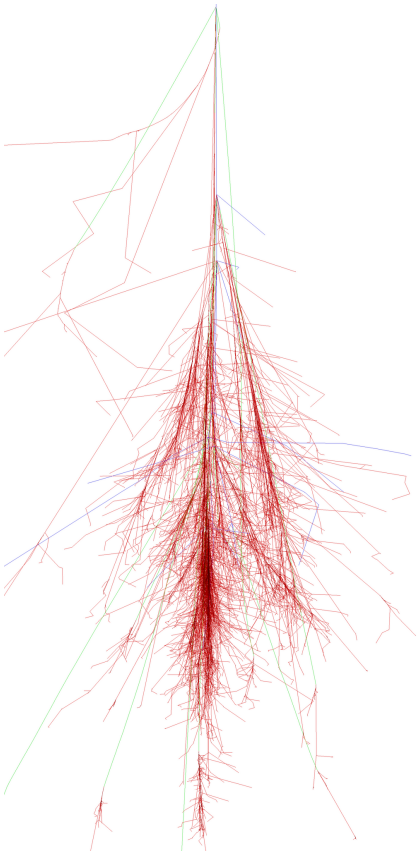

Figure 2.12: MC simulation of a 100 GeV hadron cascade.

Summarizing, the two kinds of EAS have different shapes and timing features that are exploited by background rejection techniques. On the timing side, the hadronic showers develop slightly slower (around 10 ns) than EM showers (around 3 ns). That is why, requiring the photons to arrive in a small time window can help to reject many hadronic showers. On the other hand, the difference in the showers' shape is reflected in the "picture" of the Cherenkov light pool that the Imaging Atmospheric Cherenkov Telescopes (IACTs) (Section 2.2.5) take (as reflected in Figure 2.21). Next section introduces the Cherenkov radiation produced by an EAS, the light pool and the corresponding camera images.

Cherenkov light

Cherenkov radiation, whose name comes from the first person detecting it experimentally, Pavel Cherenkov [165], is an electromagnetic emission produced when a charged particle crosses a dielectric medium at a speed greater than the speed of light in that medium.

As the charged particle travels through the medium, its electric field affects the medium that gets electrically polarized, losing its electromagnetic equilibrium. If the particle travels at low speed, the medium has time to recover the equilibrium by removing the disturbance via electrical relaxation. However, if the particle travels faster than the speed of light in that medium, the medium cannot relax quickly enough, and the disturbance remains after the particle has passed, so that the energy contained in the disturbance is radiated as a coherent shock wave (see Figure 2.13). The Cherenkov radiation spectrum is continuous, above a minimum wavelength, and its density is inversely related to the wavelength squared. Therefore, the number of photons increases as the wavelength decreases. That explains why most of the Cherenkov radiation gets emitted in the blue to UV range. When Cherenkov radiation is produced by an EAS in the atmosphere, the atmospheric extinction makes that the Cherenkov photons reaching the ground belong mostly to the visible range.

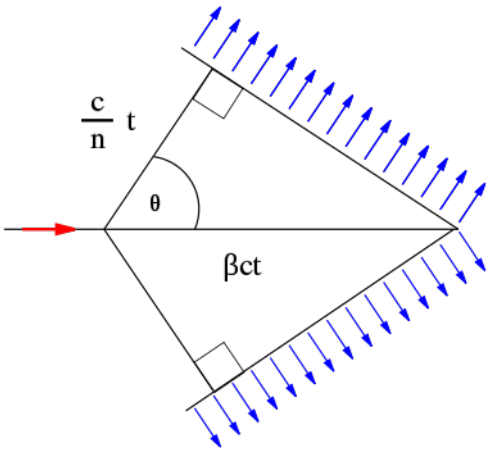

Figure 2.13: Geometrical scheme of the Cherenkov radiation emission.

In Figure 2.13, the left edge of the triangle where the red arrow points, indicates the initial position of the charged particle for an initial time $t = 0$. After a given time t, if the particle speed is v and the ratio between v and the speed of light c is defined as β, the travelled distance d is

$$d = v \cdot t = \beta \cdot c \cdot t. \tag{2.11}$$

For the emitted radiation, whose speed $v_r = c/n$ depends on the refraction index n of the medium, the travelled distance d_r during the same time is given by

$$d_r = \frac{c}{n} \cdot t. \tag{2.12}$$

The angle between the charged particle direction and the Cherenkov radiation is given by

$$\cos(\theta) = \frac{1}{n \cdot \beta}. \tag{2.13}$$

It can be concluded that,

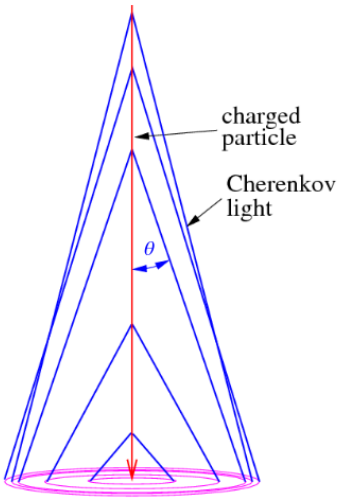

Figure 2.14: Cherenkov light pool projected on the ground produced by a charged particle travelling vertically.

- In media with higher refraction index n, the Cherenkov light cone will be wider, as happens in water (see Section 2.2.4).

- During the development of an EAS, the particles lose energy and the refraction index of air grows so that the light cone will get wider with time and the shower will reach a maximum width. There will be a point at which the charged particles have no more the ability to generate Cherenkov light ($v \ll c$) so that the cone will get thinner until the end of the shower development.

The light pool (Figure 2.14) is the density of Cherenkov photons produced by an EAS on ground and depends on the primary particle and its energy. Cherenkov photons emitted at different altitudes have different angles with respect to the shower axis, determined mostly by the Coulomb scattering of the particles and the refraction index of air. The illuminated area on the ground is very extended ($\sim$ 40000 m ^{2}), however, the energy of the primary particle originating the EAS have a large correlation with the density of Cherenkov photons in the light pool, not with the size of the light pool itself. All the Cherenkov photons of an EAS arrive in a very narrow time interval, between 3 and 10 ns.

If an IACT telescope resides inside the light pool generated by the EAS, the light is reflected by the mirrors and the camera records a projection of the shower (See Figure 2.21). These pictures are different for different parent particles. If an isolated muon from a hadronic shower reaches the ground and is detected, the picture shows a circle that corresponds to the Cherenkov light cone emitted by the muon (Figure 2.15, left image). On the contrary, if the image comes from an EAS, the shape is more elliptical. For the hadronic case, the image is wider and points to an arbitrary direction (Figure 2.15, central image), while in the case of a gamma-ray shower the image is more compact and points towards the source position (in the Figure 2.15 right image).

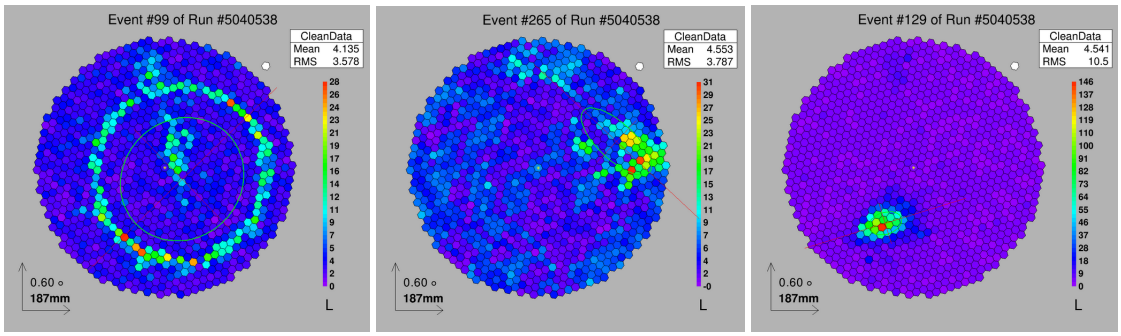

Figure 2.15: Recorded real MAGIC camera images produced by different types of EAS. Left: isolated muon. Center: hadronic shower. Right: gamma rays shower. Credit: MAGIC.

2.2.3 Space-based gamma-ray telescopes: Direct detection.

Gamma rays cannot be focused such that the effective detection area for direct detection is restricted to the area of the detector itself. This area hardly surpasses 1 m^2 if the instrument has to fit into a launcher to be put into orbit. Moreover, gamma-ray fluxes quickly decrease with increasing energy and, due their restricted size, satellites can hence only explore the gamma-ray energy band below 100 GeV, the HE domain (Section 2.2.3). In this energy region, gamma rays are detected via their conversion into electron-positron pairs when interacting with the instrument. Following these charged particle tracks we can estimate the incident gamma-ray direction. Inside the instrument, the electron-positron pair and the possible gamma rays produced by them via bremsstrahlung are absorbed by a calorimeter to estimate the initial gamma-ray energy. For these tasks, the space-based instruments count with several parts:

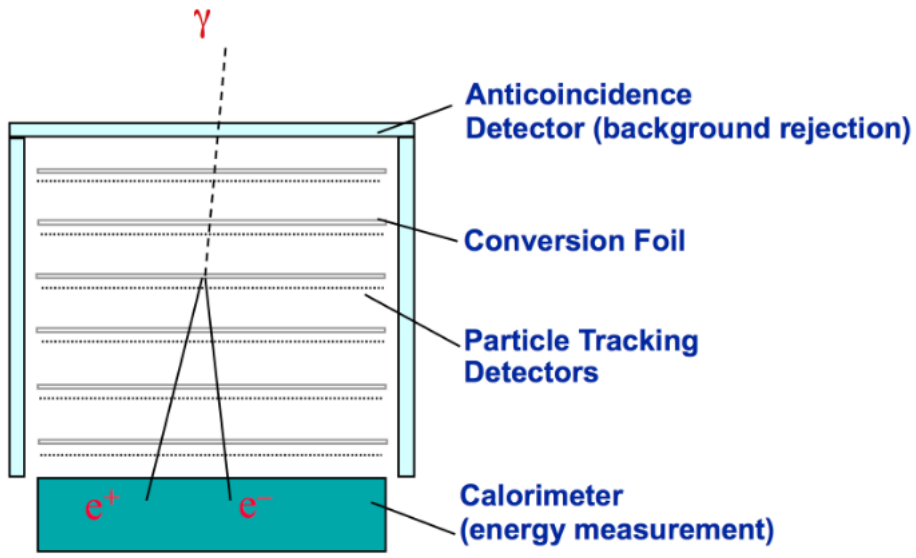

Figure 2.16: Generic space gamma-ray detector. Credit: D.J. Thompson [185].

- **Conversion foil:** Pair production needs an atomic nucleus that will absorb some momentum but not much energy from the initial photon so that the produced pair can be used later to predict the energy of the initial γ ray. In order to increment the probability of the gamma rays to interact with the detector conversion foil, it is recommendable to choose materials whose radiation lengths are short, thus with a higher atomic number, so that the mass of material needed for the instrument is minimum [186]. The conversion foil material shape and distribution in space-based instruments is intimately related to the particle tracker.

- **Particle tracker:** This part of the instrument deals with the most challenging goal, to determine the arrival direction of the initial γ ray from the paths of the electron and positron after the conversion point. The angle between the pair decreases with increasing energy of the incident γ ray. However, these charged particles interact with the converter and any other materials on their trajectory so that the initial information about their direction is degraded, and the high atomic number of the converter material worsens the situation. Usually the solution is to break the converter in various thin layers with tracking detectors between them, as shown in Figure 2.16.

- **Anti-coincidence scintillator:** The scintillator is a material that presents fast luminescence when it is hit by ionizing radiation, as CRs. The luminescence light is detected usually by photomultipliers (PMTs). This kind of material is very useful for background rejection purposes since, while the gamma rays pass freely through it, the CRs will create a flash of light, that allows to tag the background events.

- **Calorimeter:** The calorimeter permits to measure the energy of the resulting particles to know approximately the energy of the initial γ ray, taking into account energy losses as the particles cross the instrument. When particles enter the calorimeter, they produce secondary particle showers whose energy can be measured.

Space-based instruments have a much larger duty cycle than ground-based experiments. They can work in survey mode, surveying the full sky as they orbit, or in pointing mode, when they can be relocated to point to a specific source. There are currently two space-based HE gamma-ray instruments active, the Fermi-LAT and AGILE telescopes, described briefly below.

Fermi LAT

The Fermi Gamma-ray telescope (formerly GLAST) was a project motivated by the results of EGRET. It is an international multi-agency space mission that counts with more than 150 members and studies gamma rays in the energy range from 10 keV to 300 GeV. The satellite counts with two instruments on board,

- The imaging gamma-ray telescope LAT: It is the main instrument and, because of its large area, angular resolution, field of view (FoV) and low deadtime, provides a 30 times improvement in sensitivity versus previous satellite experiments. The LAT is modular, composed by a 4x4 array of identical towers (as seen in Figure 2.17). Each tower contains a tracker formed by strips of silicon detectors, a calorimeter in layers read by photodiodes and its own trigger system. The whole array is covered with an anticoincidence shield, whose luminescence is read by fibers and miniature phototubes.

- Gamma-ray Bursts Monitor (GBM): This instrument compliments the LAT in its observations of transient sources and is sensitive to X-rays and gamma rays with energies between 8 keV and 40 MeV. It counts with two types of scintillators that try to detect relevant changes in the flux. When an event is triggered, the instrument collects rapidly preliminary information about source position to send an alert to the ground-based telescopes and to repoint the LAT. The GBM detects around 200 Gamma-ray Bursts (GRBs) (Section 2.3.2) per year.

Fermi was launched in June 2008 and describes an orbit around the Earth every 96 minutes. The LAT points upwards all the time so that the Earth does not block observations. In every orbit, the telescope turns right and left allowing the LAT to cover the whole sky in two orbits. Usually, it operates in this survey mode, however, it can also point to a given source, e.g. if a burst happens.

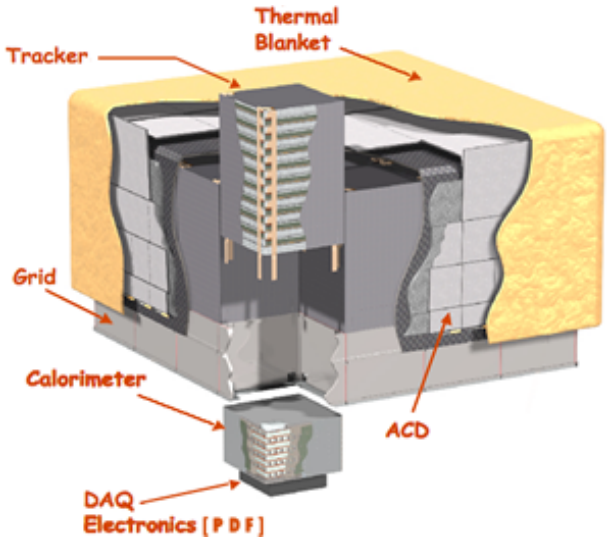

Figure 2.17: Schematic diagram of one of the towers of Fermi LAT. Credit: W.B. Atwood [187]

AGILE

AGILE (Astro-rivelatore Gamma a Immagini Legero) is a small Italian space mission dedicated to HE astrophysics that covers two energy bands, 30 MeV - 50 GeV and 10 - 40 keV. It is composed of three detectors with imaging capability and broad-band detection.

- Gamma-ray Imaging Detector (GRID) works in the gamma-ray domain and counts with a silicon-tungsten tracker, a mini calorimeter, an anticoincidence system with scintillators and fast readout electronics.
- The Super-AGILE detector focuses on the hard X-rays band (10-40 keV), and is composed of an extra plane of silicon detectors on top of GRID that try to achieve the simultaneous detection of sources in X-rays and gamma rays .
- The Mini-Calorimeter (MC) can detect and collect events independently of the GRID. It is very useful to provide spectral and timing information of transient events.

AGILE was launched on April 2007 and follows a quasi-equatorial orbit of 96 minutes duration. It works in pointing mode, that are fixed positions towards sources with a small drift. AGILE also provides an alert system to allow monitoring and follow-up observation in other energy bands. More information about the alert system can be found in [188].

2.2.4 High altitude arrays: Water Cherenkov technique.

To detect gamma rays beyond 100 GeV, we need larger instruments, hence the detection must be achieved from ground. In this case, gamma rays interact with the atmosphere, producing EM EAS. Locating intruments at high altitudes and when the initial gamma rays are very energetic, it is possible to collect directly the charged particles that compose the EAS and that reach the ground using the water Cherenkov technique.

The lowest energies detectable by this kind of instruments are given by the necessity of gamma rays to be energetic enough to produce showers that reach the ground and trigger the detector. This requirement

makes these detectors work at a higher energy threshold than the IACTs (Section 2.2.5). In order to reduce this energy limit, the detectors are located at very high altitudes. The water Cherenkov arrays are composed of densely populated tank arrays, with high efficiency for particle detection over a large area.

Water Cherenkov detectors are complementary to IACTs. While they are less sensitive to point-like sources due to the higher energy threshold, worse energy resolution and poorer hadron rejection, they have the advantages of a continuous duty cycle − compared to the 20% duty cycle for IACTs − and a much wider FoV,

$$\Omega = 4\pi \cos(l) \sin(\Theta_{max}), \tag{2.14}$$

where Ω is the solid angle of the detector, l is the latitude and Θ_{max} is the maximum zenith angle of the observation. These characteristics allow this type of detectors to perform full sky surveys at TeV energies, leading to the detection of unexpected transients and providing alerts to pointed instruments. In addition, for very extended sources ($> 1°$), Water Cherenkov instruments are often better suited than IACTs.

Figure 2.18: Generic Water Cherenkov detector.

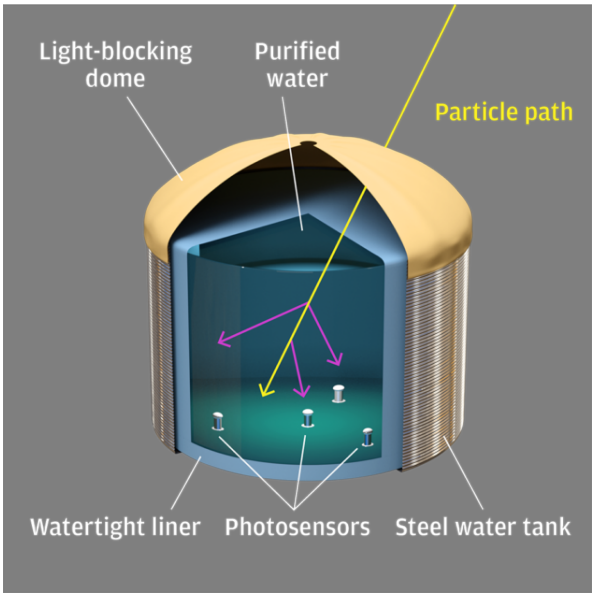

The Water Cherenkov technique consists of measuring the Cherenkov light of the shower particles as they cross the water tanks that compose the instrument (See Figure 2.18). In order to reject background, the detector must act as a calorimeter such that the collected energy from the crossing particles is proportional to the amount of Cherenkov light measured by the PMTs. For this reason, the PMTs should be deep inside the tank to avoid other light pulses created by other particles passing close to the detector.

So far, there have been only two experiments using this technique to detect VHE gamma rays , although only one of them is still active. MILAGRO [189] (1999-2008) and the currently operational HAWC observatory, presented below. However, the biggest observatory using Water Cherenkov technique is the AUGER Surface Detector (AUGER SD), a hybrid detector composed partially by 1,660 water tank detectors that cover about 3,000 km^2. However, this observatory is devoted to the detection of CRs, so it will not be treated in this section. An AUGER SD review can be found in [190].

HAWC

The High Altitude Water Cherenkov (HAWC) observatory consists of 300 steel tanks of 4 m height and 7.3 m diameter. Each tank contains 188000 litres of purified water. The HAWC observatory is located on the flanks of the Sierra Negra volcano near Puebla, Mexico, at 4100 meters altitude. It studies gamma rays and CRs between 100 GeV and 100 TeV with a FoV that covers 15% of the sky. In 24 hours, HAWC observes two-thirds of the sky.

Figure 2.19: The HAWC Observatory (J. Goodman, Nov. 2016).

Each tank is covered by a watertight liner and contains four PMTs, sensitive in the ultraviolet band (Figure 2.18). Three of used to belong to the old observatory MILAGRO and are located at the bottom of the tanks, separated from the center, looking upwards. The last PMT is allocated at the center and is a high quantum-efficiency PMT that helps to improve the sensitivity at lower energies.

These PMTs measure the Cherenkov light when a charged particle crosses the tank. The emission of Cherenkov light is very efficient in water due to its high index of refraction. The light is emitted inside a cone that surrounds the direction of the particle, whose large aperture angle ($\sim 43°$) assures that all particles entering the tank are detected by at least one PMT. The tanks are suitable to detect not only charged particles, but also secondary gamma rays generated inside the shower, since they produce new electron-positron pairs, that emit Cherenkov light inside the tank.

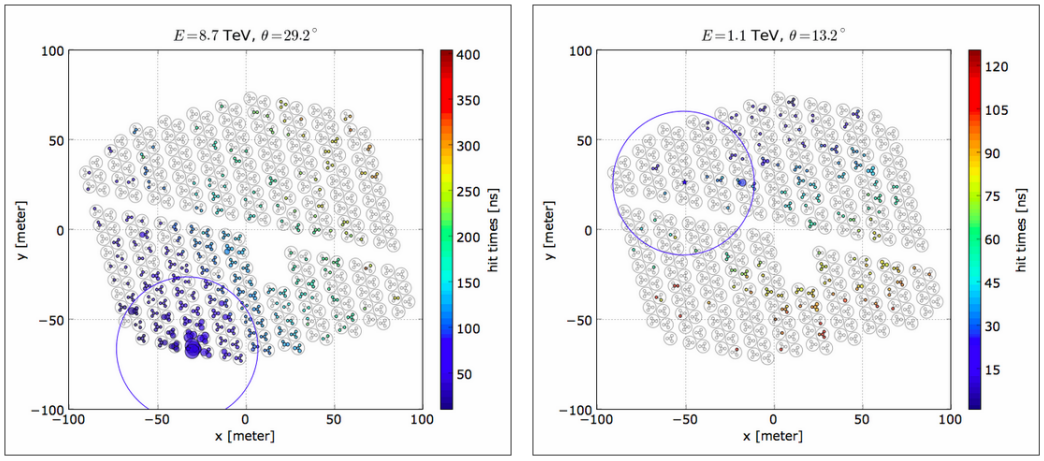

Figure 2.20: Simulated gamma-ray event (left plot) and proton event (right plot) in the HAWC tank array. Credit: HAWC.

HAWC discriminates air showers from gamma rays and CR by studying the spatial pattern of the "hits" observed by the detector when the showers reach ground level. In gamma-ray showers, most of the signal at ground level is located near the shower axis, i.e., along the direction of the initial gamma-ray. In contrast, charged CRs tend to have much more asymmetric showers in the atmosphere (Section 2.2.2), creating much messier signals at ground level. Figure 2.20 shows a graphical simulation of the "hits" distribution and intensity of showers produced by a gamma-ray and a CR.

2.2.5 Ground-based telescopes: IACT technique.

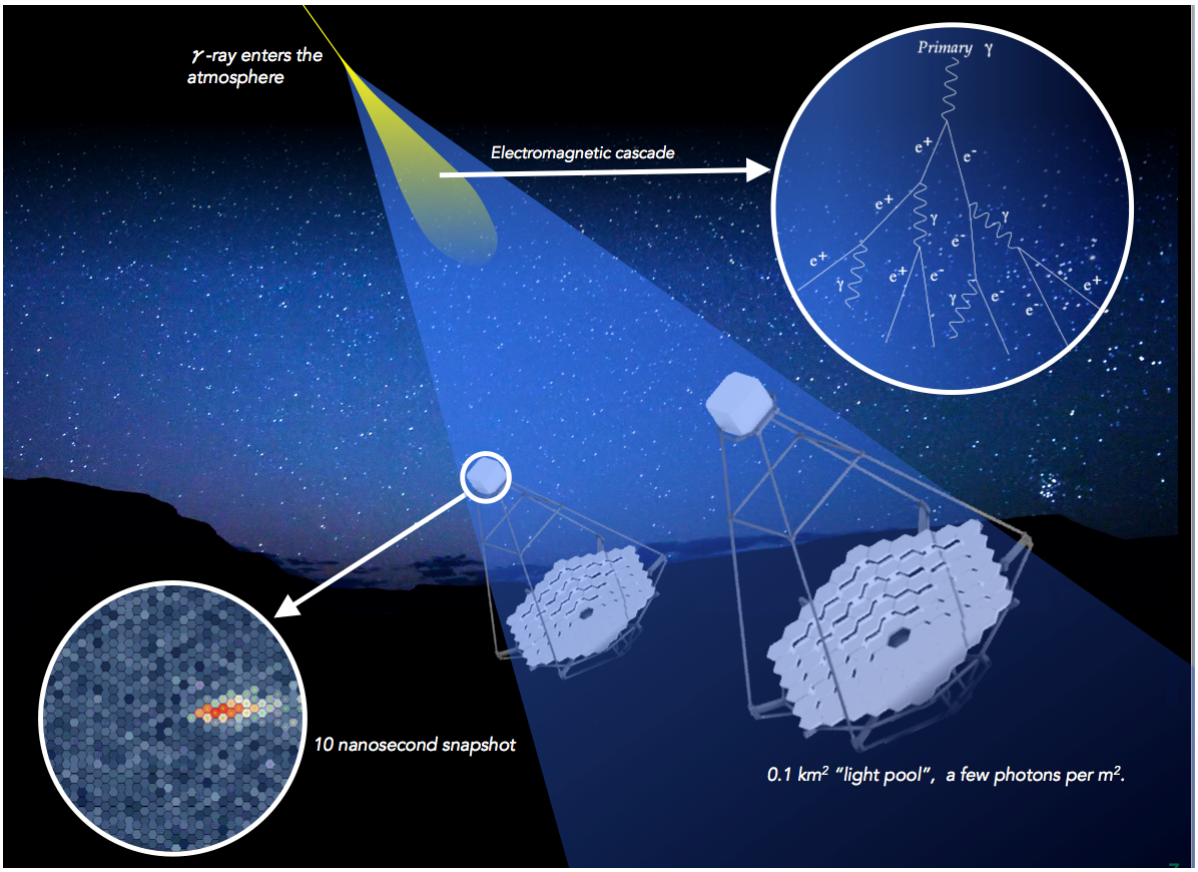

Figure 2.21: Graphical view of the IACT technique. On the left lower corner, an image of a gamma-ray shower recorded by the camera is shown. On the right upper corner, a scheme of an electromagnetic shower. Credit: CTA.

Imaging Atmospheric Cherenkov Telescopes (IACTs) also detect Cherenkov light, in this case produced by the charged particles of an EAS, as they cross the atmosphere. IACTs collect these Cherenkov photons using a large mirror surface, that projects them onto the telescope camera, as shown in Figure 2.21. Up to date, IACT is the most effective technique to detect gamma rays above 100 GeV.

The camera is composed by pixels that allow to measure not only the amount of Cherenkov photons − that is proportional to the energy of the initial γ ray since the atmosphere acts as a calorimeter for this technique − by also to have a pixelated image of the air shower. The Cherenkov photons from the different stages of the EAS development illuminate pixels in different regions of the camera, depending on the angle between the incoming photon and the telescopes axis. By means of analysis of the image (analysis detailed in Chapter 4), it is possible to extract the nature, the energy and the incoming direction of the particle that triggered the EAS.

In general, IACTs are characterized by a small FoV of few degrees, that forces the instrument to work in pointed mode, a small duty cycle − restricted to night time with good weather conditions − and sophisticated data analysis methods for background rejection. Moreover, IACTs deal with signals of very low intensity and very short duration that force them to use fast and sensitive data acquisition systems.

Some important parameters to define an IACT [8] are: its sensitivity, that indicates the minimum detectable gamma-ray flux in a specific observation time, its energy threshold, that indicates the minimum

[8] These parameter are also used to define the performance of the rest of gamma-ray instruments.

energy of a γ ray that the telescope can detect, the angular resolution or accuracy in the reconstructed incoming direction and the energy resolution or accuracy in the reconstructed energy of the gamma rays .

The main challenge faced by IACTs is the huge amount of background that has two main contributions: the Night Sky Background (NSB), that comprises the contribution of artificial lights, star light, polar and zodiacal lights and airglow [9]; and the CRs, that also produce EAS.

The currently active IACT experiments, briefly exposed at the end of this section, have several concepts in common:

- Large mirrors to collect light even from low-energy showers. The energy threshold decreases as the mirror area increases. For this reason, IACTs count with large mirror surfaces, fragmented in relatively small pieces. Depending on the mirror size, several techniques are followed to avoid optical aberrations or in order decrease the instrument impact on the signal arrival time. For example, larger telescopes use parabolic mirror shapes, so that the arrival time of the photons is isochronous at the focal plane.
- Instruments composed by more than one telescope, allowing stereoscopic observations. Stereo observations result in a much better gamma-hadron separation and an improved energy and angular resolution.
- Fine-grained cameras with relatively small-sized pixels ($\sim 0.1^\circ$ FoV) in order to have well defined shower images, improve the energy and angular resolution and decrease the NSB contribution. The random light fluctuations due to the NSB, are diluted for small pixels.
- Fast integrated electronics (sampling rates higher than 500 MSamples/s) to detect the very fast shower signal and decrease the contribution of the NSB.
- Fast trigger systems, that take the decisions on whether an event should be recorded, usually divided in three levels:
  - Pixel-level: A minimal signal is required on a single pixel, usually using a discriminator.
  - Pattern-level: Requires a group of neighbouring pixels, or pixels inside a given area, to have passed the pixel-level trigger condition within a short time window.
  - Array-level: Requires trigger coincidence between two or more telescopes of the array inside a specific time window.

Currently, there are three active IACT Collaborations − H.E.S.S., MAGIC and VERITAS − and the new IACT observatory CTA is under construction. All of them are briefly described below. A summary about the characteristics of the different active IACT is found in Table 2.2.

MAGIC

The Major Atmospheric Gamma-ray Imaging Cherenkov (MAGIC) Collaboration counts with two IACTs located at La Palma, one of the Canary Islands. The first telescope, with 17 m of diameter, was inaugurated in 2003. The second one was constructed in 2008 and during the period 2011-2012, both underwent an upgrade to obtain finer-grained cameras, larger trigger area and better readout systems. Chapter 4 is entirely dedicated to these telescopes.

[9] Light due to processes in the upper layers of the atmosphere.

Figure 2.22: The MAGIC telescopes.

H.E.S.S.

The High Energy Stereoscopic System (H.E.S.S.) experiment started as an array of 4 IACTs of 12 m diameter located in Namibia, at an altitude of 1800 m. The array went into operation between 2002 and 2003. Years later, the H.E.S.S. collaboration built a much bigger fifth telescope (Figure 2.23) of 28 m diameter located in the middle of the original array, that is operational since 2012. This last telescope allows the array to have larger coverage at low energies. During 2015-2016, the cameras of the original array were refurbished using new readout electronics and were re-inaugurated in September 2016.

The energy coverage of H.E.S.S. extends from tens of GeV to tens of TeV. The H.E.S.S. collaboration is comprised of 240 scientists from more than 40 institutions, located in 13 different countries.

Due to its location in the Southern hemisphere (the only currently active IACT located there), H.E.S.S. can look very precisely to the galactic plane and has detected many galactic sources [191].

The hardware characteristics of the original array and the new telescope present some differences, indicated in Table 2.2, being the later focused on extending the energy coverage towards lower energies and improving further the sensitivity.

VERITAS

The Very Energetic Radiation Imaging Telescope Array System (VERITAS) collaboration works with an array of four telescopes of 12 m diameter located in Arizona, U.S.A., at an altitude of 1250 m. One of the original telescopes was moved to a new location to optimize sensitivity in 2009. The PMTs of the four cameras were changed for more sensitive ones in 2012, to lower the energy threshold and improve sensitivity. The VERITAS array covers an energy range from 50 GeV to 50 TeV.

The VERITAS telescopes, as Major Atmospheric Gamma-ray Imaging Cherenkov (MAGIC), are located in the Northern hemisphere so most of its observation time is dedicated to the study of extragalactic

Figure 2.23: The H.E.S.S. telescopes.

sources as blazars and, since the initial operation, more than 138 Active Galactic Nuclei (AGNs) have been observed and identified.

The VERITAS collaboration is composed of 110 scientists, most of them from the American continent. It also collaborates with other institutions via associate membership or multi-wavelengths campaigns with instruments in other energy bands.

Figure 2.24: The VERITAS telescopes.

CTA

The CTA project is composed of 800 scientists and engineers around the world that join efforts to build a new gamma-ray observatory. CTA will cover the complete night sky by counting with two installations, one located in the Northern hemisphere and the other in the Southern hemisphere.

Each observatory will be composed of an array of telescopes of different characteristics. At the center

	H.E.S.S. / H.E.S.S.II	MAGIC	VERITAS
Number of telescopes	4 / 1	2	4
Disk diameter (m)	12 / 28	17	12
Site	Namibia	La Palma	Arizona
Altitude (a.s.l)	1800	2200	1250
Pixels per camera	960 / 2048	1039	499
Field of view(°)	5 / 3	3.5	3.5
Readout speed	1GHz ARS / SAM analog memory	2 GHz DRS4	500 MHz FADC

Table 2.2: Current IACT instruments characteristics.

of the array, the Large-Sized Telescopes (LSTs) will be built, with 23 m diameter. The Medium-Size Telescopes (MSTs), of 12 m diameter, will surround the central ones. Apart form these two telescope sizes, the Southern array will count with telescopes of smaller size, the Small-Sized Telescopes (SSTs), surrounding the central cluster.

With the presence of telescopes of different sizes, CTA will be able to detect gamma-ray radiation in a wider energy range, from 20 GeV up to hundreds of TeV.

Figure 2.25: Graphical simulation of the future CTA telescopes.

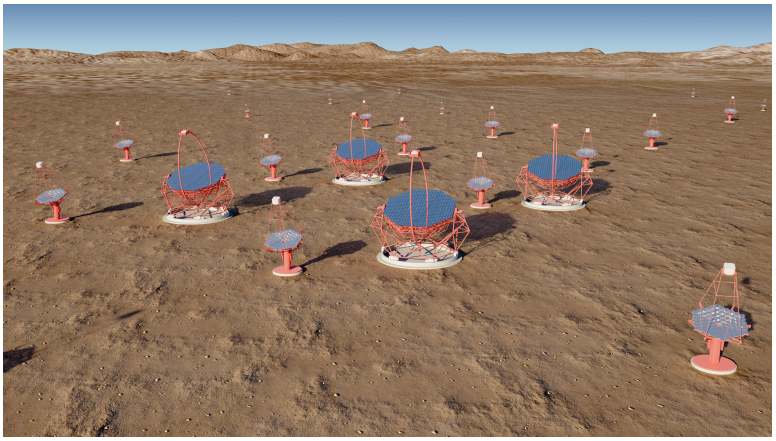

2.3 VHE gamma-ray sources

With the different detection strategies − from space and from ground − which complement each other, and taking as reference the sources detected in other wavelengths, the gamma-ray known sky has been increasing during the last 25 years.

The first robust detection of TeV gamma rays took place in 1989 [169], from the Crab Nebula, detected by the Whipple telescope, a 10-m diameter IACT located at the Whipple Observatory, in Arizona. Since then, more than 200 sources has been discovered in the TeV regime. All of them are collected in TeVCat [191], a daily updated database that collects the detected sources, together with the source description, associated papers and other useful information, as the instruments the source was observed by. Figure 2.26 shows the status of the TeV sky at the moment of the writing of this thesis.

Even though, compared with other energy bands, the TeV sky has a modest number of sources, they present a large variety. Many of these sources gather along the galactic plane together with a collection of extragalactic sources at higher latitudes, as shown in Figure 2.26.

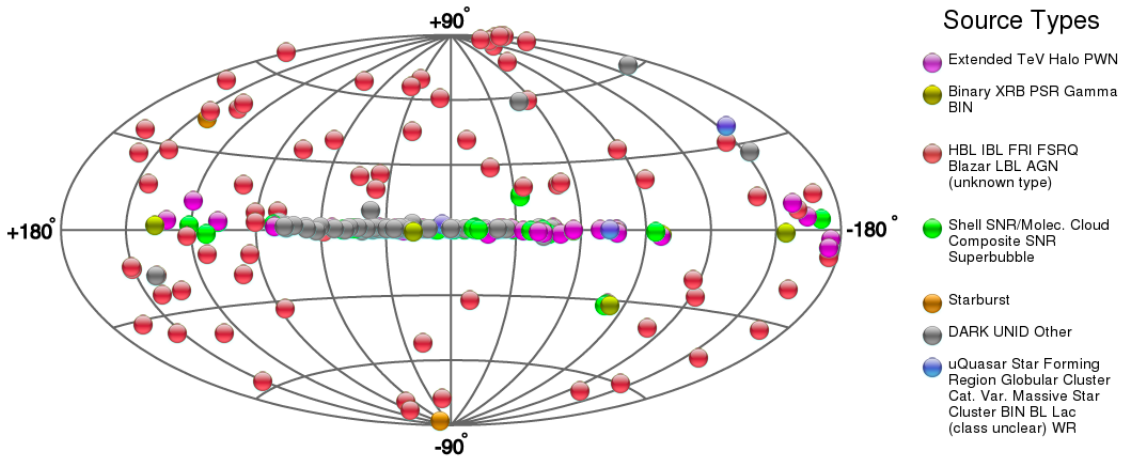

Figure 2.26: Map in galactic coordinates with all detected TeV gamma-ray sources. Courtesy of TeVCat [191], with a description for the different source types.

In this section, a description of the different gamma-ray sources and their properties is presented, divided in two categories: galactic and extragalactic sources. The diffuse TeV emission will no be treated in this chapter since, in contrast to the GeV energy band, the sources dominate over this emission in the TeV case. A review can be found in [192].

2.3.1 Galactic Sources

These sources are located inside our galaxy and are numerically dominant in the TeV regime. Due to their proximity, their morphology can be resolved and studied, allowing to study spectral variations. On the other hand, some of them are harder to detect and classify due to the large density of sources in the galaxy plane and the presence of diffuse emission.

Many of these sources have a "*parental*" relation to each other. In this section, the galactic sources will be explained following such temporal evolution.

Supernova remnants

Supernovas (SNs) are highly energetic stellar explosions that occur when massive stars[10] reach the end of their natural lifetime. The explosion causes a large part of the stellar material to be expelled at thousands of kilometres per second into the surrounding environment, creating a shock wave that travels though the interstellar (IS) medium, while simultaneously the nucleus of the star collapses, losing gravitational potential. SNs can also be triggered when a star accretes enough material from a companion star in a binary system until a runaway nuclear reaction ignites. A SN explosion will create a Supernova Remnant (SNR), classified as type I or II, due to the expel of material, and a compact central object due to the collapsing nucleus.

The resulting central objected from a SN explosion depend on the mass of the initial star; for less massive stars (8-15 $M_{\odot}$), a Neutron Star (NS) will be produced, and in case of more massive stars (20-30 $M_{\odot}$), a Black Hole (BH) will we formed instead. During this process, the external layers of the star are ejected at very high speeds, then slowed down by the interstellar surrounding medium, generating the SNR.

[10] A star is considered massive when its mass exceeds more than 8 times the solar mass $M_{\odot}$

SNRs are shells of gas and dust, that consist on the remains of the material in the outer layers of the star after the explosion. SNRs are bounded by the shock wave that expands and the IS medium that interacts with it along the way. Supernovas are classified into:

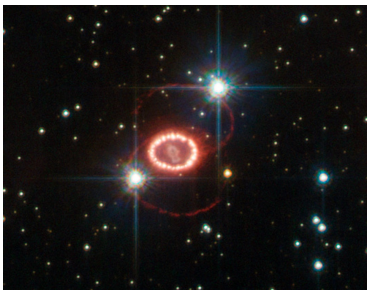

Figure 2.27: Image of SN1978, one of the closest Supernovas, observed from Earth on February, 1987. It was the first chance for modern astronomers to see one by naked eye.

- Pulsar Wind Nebulae (PWNe), characterized by the presence of a central pulsar that emits a continuous flux of ultra-relativistic charged particles. These objects are the subjects of Sections 2.3.1 and 2.3.1.

- Shell-like SNRs, characterized by the shock wave of the SN that, by interacting with the IS medium, creates a big shell of hot material where charged particles are accelerated due to Fermi mechanisms [11]. These diffusive shocks are thought to be the major responsible of the galactic CR flux. This hypothesis is supported if we considered that only 10% of the energy produced in the SN explosion, taking into account the energy output and the SN rate, needs to be used to accelerate CRs [194]. With these assumptions, SNRs allow to reproduce the power-law spectrum of CRs. The inelastic collisions of these CRs with the the shell material would produce big amounts of neutrinos and gamma rays , the later due to hadron collisions and further π^0 decay [195].

The first object detected in the VHE band belongs to this family, the Crab PWN, known as Crab Nebula, back in 1989 [169]. Since then, in the HE band, Fermi-LAT has detected several galactic objects associated to SNRs. Moreover, Fermi has found evidence of galactic CR production in SNRs [196], and evidence of the pion-decay signature in two PWNe [197]. On the VHE band, by the moment of the writing of this thesis, there are 53 sources associated with SNRs, 37 of then to PWNe, 16 with shell-type SNR [191].

Pulsars

Pulsars are rotating NSs with a mass of $\sim 1.4 M_{\odot}$, extremely strong magnetic fields ($\sim 10^{15}$ G) and whose magnetic axis is not aligned with the rotation one. As mentioned in Section 2.3.1, these sources are produced by SN explosions. When the pulsar is created, it preserves the angular momentum of the parent star but with a much smaller radius ($\sim$ 10 km), resulting in a high rotation speed.

Pulsars receive their name due to their "pulsed" emission with short ($\sim 1.4 - 8.5$ s) and regular periods. The most generally accepted model to explain this pulsation is called "The lighthouse model"[198]. This model states that, as the NS rotates, charged particles on the surface of the star are accelerated along the magnetic field lines (curved black lines in Figure 2.28), and emit electromagnetic radiation creating a beam of photons in the direction of the magnetic field axis. As the star rotates, pulsars signal their presence only when the direction of the light is in the line of sight of the observer, so that the emission appears as pulses.

[11] Also known as diffusive shock acceleration, happens when charged particles are repeatedly deflected by magnetic mirrors [193].

Pulsars produce highly magnetized magnetospheres, a region filled with charged particles, as electrons and positrons, extracted from the NS surface by the induced electric fields. The magnetosphere is confined in the light cylinder − see Figure2.28 − a zone centered on the rotation axis of the pulsar with a radius, that is equivalent to the distance at which the star's co-rotating plasma reaches the speed of light.

The magnetic field lines cannot remain closed beyond the light cylinder, since that would mean that the co-rotating plasma should travel faster than light. Those particles, that follow open field lines, can escape the magnetosphere carrying away most of its magnetic flux and generating the so-called pulsar wind [199], that streams into the IS medium and generates a standing shock wave before slowing down to non-relativistic speeds.

Due to the loss of electromagnetic energy, the rotation NS model predicts a spin down of the pulsar, expressible as the temporal evolution of the rotation energy $E(t)$ [200], related to the initial period of the pulsar $P_{0,ms}$ and its characteristic spin down time τ as

$$\dot{E_(}t) = \dot{E}_0/(1 + t/\tau)^p, \tag{2.15}$$

where $p = (n+1)(n-1)$ and n depends on the radiation type, and $\tau \sim P^2_{0,ms}/B$, being B the surface magnetic field.

Pulsar signals are found from radio up to the highest photon energies. The gamma-ray emission is attributed to three different emission regions: The pulsar magnetosphere, the relativistic wind, and the synchrotron nebula (Section 2.3.1). The first region produces gamma rays due to synchrotron and curvature radiation of the particles accelerated by the pulsar, while the other two regions are dominated by IC scattering.

The theoretical models of the pulsar radiation are very sophisticated and involve several productions mechanisms related to the different environment conditions. The HE gamma-ray emission (1-10 GeV) is well explained by the so-called "polar cap" emission model [201], where photons are produced in the pulsar inner part of the magnetosphere via synchrotron. The first VHE pulsed signal was detected by MAGIC for energies below 60 GeV [202], then both VERITAS and MAGIC extended the energy spectrum up to 400 GeV [203, 204]. This data ruled out the super-exponential cut-off spectral behaviour suggested by Fermi-LAT and required emission models for VHE photon production. Among them, the slot gap and the outer gap models [205, 206, 207, 208] that predict the production of the emission in the outer magnetosphere of the pulsar, close to the light cylinder. These models can explain radiation production up to few hundreds of GeV.

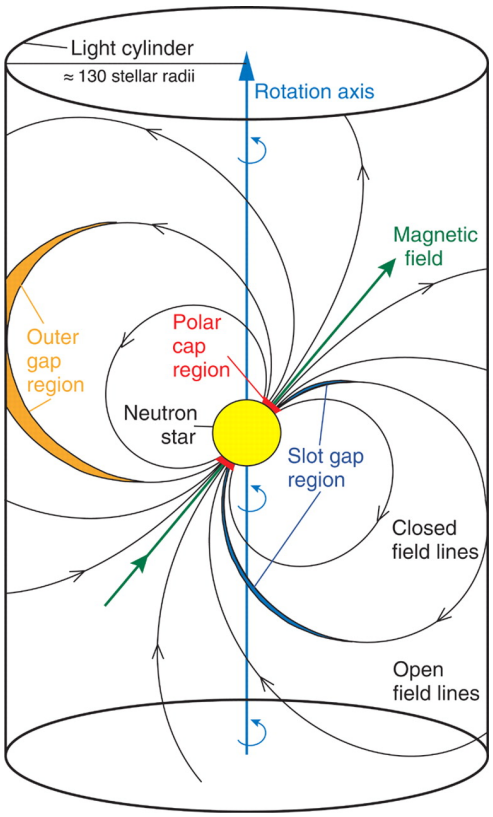

Figure 2.28: Schematic view of the rotating neutron star model with the different emission regions.

Until now, only two pulsar have shown pulsating emission in the TeV range, the Crab Pulsar, detected by MAGIC, showing energies up to 2 TeV [209] (See Figure 2.29), and the Vela Pulsar, detected by H.E.S.S. for energies up to 7 TeV [12]. In order to explain emission inside the TeV range new models

[12]Paper ongoing. Preliminary results presented at TeVPa2017: `https://fskbhe1.puk.ac.za/people/mboett/`

outside the magnetosphere were developed, where the emission is produced in the the pulsar wind, as the "current sheet" model [210].

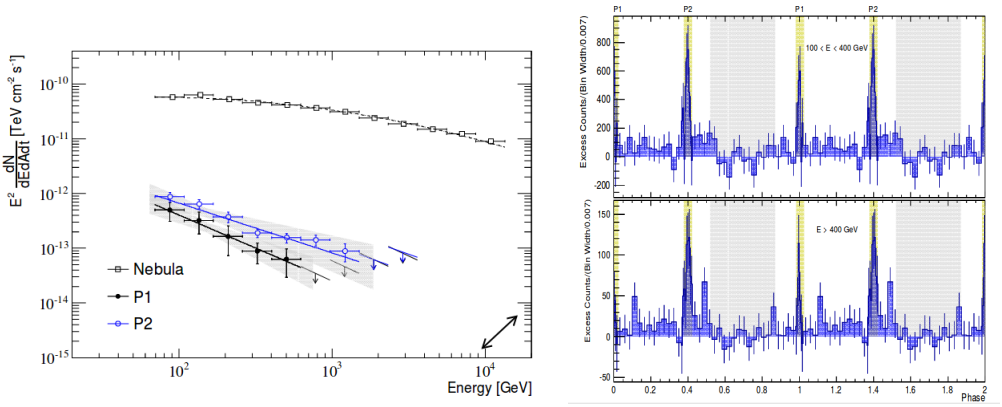

Figure 2.29: On the left: Phase-folded SED of Crab Pulsar peaks (P1 in black, P2 in blue) between 70 GeV and 1.5 TeV with systematic uncertainties. The Crab Nebula spectrum is also shown for comparison. On the right: Pulse profile of the Crab pulsar between 100 and 400 GeV (upper panel) and above 400 GeV (bottom panel). The pulse profile is background subtracted. Credit: MAGIC Collaboration [209]

Pulsar Wind Nebulae

PWNe are nebulas powered by a pulsar's wind. In young SNs, they are usually found inside the shells of the SNR, however, they have also been found around old pulsars whose SNR no longer exists.

PWNe are characterized by the presence of a central pulsar that emits a continuous flux of ultra-relativistic particles, the so-called pulsar wind.

When the pulsar wind balances the total pressure of the surrounding environment, it creates a stable shock front, generating the PWN. In such shock, the charged particles loose energy via synchrotron − dominating the MeV range − and via IC of those synchrotron photons and other lower energy photons of the ambient gas, dominating the GeV rage. The reverse shock of the SNR might collide with the expanding PWN, halting the expansion. A description of PWNe evolution can be found in [211].

The formation process of the nebula itself is still not completely understood, although it is believed to come from the interaction of the ejected material from the SN explosion with the IS medium. This view is well accepted since it describes well the main features of the Crab Nebula, the most studied PWN [212].

At the moment, there are 37 PWNe detected in the TeV regime. Among them, the Crab Nebula is the most steady and strong VHE emitter, used as a standard candle in the GeV - TeV range, showing VHE emission coming from the nebula and the pulsar.

gamma-ray binaries

A binary system is a system of two close astronomical objects that orbit each other by gravitational attraction. There are several types of binary systems, the ones producing gamma-ray radiation are composed of a star of several solar masses and a compact object of a few solar masses, that accretes mass from the star. The compact object can be a NS or a BH. In the BH case, the system receives the name of microquasar, since its properties recall the quasar ones, a sub-type of AGN galaxies (Section 2.3.2). If the compact object is a NS, they are called binary pulsars.

Texas2017/Djannati.pdf

For microquasars, the BH accretes material from the companion star, generating an accretion disk. The rotation of the accretion disk due to shear forces and viscosity, makes the surrounding gas reach very high temperatures that lead to radiation in the HE and VHE regimes. The jets of the BH produce another component of the radiation, by accelerating particles up to relativistic energies.

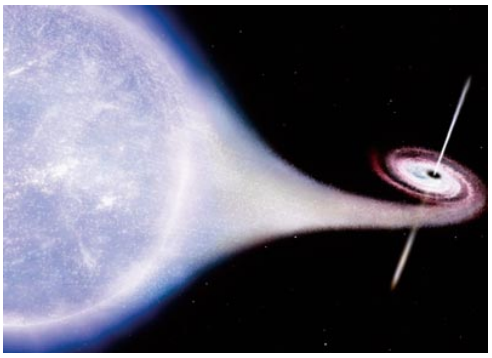

Figure 2.30: Artist's view of a gamma-ray binary.

In the binary pulsar scenario, the emission production is believed to happen when the pulsar wind interacts with the companion star wind, developing a front shock, where particles are accelerated. Binary pulsars accrete material from the companion star, receiving the name of accretion-powered pulsars. The accretion compensates their loss of rotation energy (see Section 2.3.1) and make them spin up, increasing the rotational periods to the order of milliseconds [213].

Only 9 TeV emitters associated to binary systems have been detected in the TeV regime. The H.E.S.S. telescopes detected most of them like HESS J0632+057 [214], HESS J1018-589 [215] or HESS J1832-093 [216]. Additionally, the VERITAS telescopes detected PSR J2032+4127 [217] and the MAGIC telescopes discovered LS I +61 303 [217].

Unidentified VHE gamma-ray sources

Around one-third of the galactic TeV sources have no identified counterpart at other wavelengths, so they are detected in VHE regime but present no emission at lower energies. This situation makes difficult to identify which source type they belong to and, sometimes, they are referred as *"dark accelerators"*.

It is not clear whether they represent a new class of sources or if they are members of already known classes, since their size and spectra do not differ much from other source families.

Their emission is thought to have hadronic origin since with leptonic origin, we would expect some synchrotron counterpart. Most of these unidentified sources are located in the galactic plane, shown as grey spots in Figure 2.26, since the large density of sources complicates the source identification.

Follow-up observations of unidentified sources often take to the discovery of new sources that, in some cases, became very probable counterparts of the unidentified ones, as happens with the source HESS J1303-631[218]. At the present moment, there are more than 60 unidentified sources in the TeV sky.

2.3.2 Extragalactic sources

This second section shows the gamma-ray sources located outside our galaxy. The observation of extragalactic gamma-ray sources is limited by the EBL absorption of gamma rays on their path to Earth. As stated in Section 2.1.1, the energy range of EBL allows electron-positron pair creation with radiation of the VHE band. Therefore VHE photons from distant sources are mostly lost during their propagation to Earth and the absorption feature should be taken into account in the analysis and interpretation of extragalactic observations.

Active Galactic Nuclei

AGNs are distant galaxies that harbor an active galactic nucleus, where a Supermassive Black Hole (SMBH) – from millions to billion of $M_\odot$ – accretes matter and powers jets, that show relativistic flows and are highly collimated. A galaxy is designated as AGN, thus it is considered to host a SMBH, when its central region brightness is larger than the brightness of the combination of all of its stars. AGNs are bright objects in many different wavelengths, from radio to VHE gamma rays (Figure 2.32).

AGNs are classified in two groups according to their emission in radio wavelengths: radio-loud and radio-quiet AGNs. These groups are composed of different members depending on their emission energy range. Among radio-quiet AGNs we find Seyfert or radio quiet QSO AGNs, while for radio-loud, there are BL Lac, blazars or radio loud QSO, among others. The later group is much brighter in the gamma-ray band. Accordingly to the unified AGN model, these AGN sub-types are really a single object, but observed at different viewing angles, as indicated in Figure 2.31. The orientation would allow the observer from Earth to "see" different emission regions.

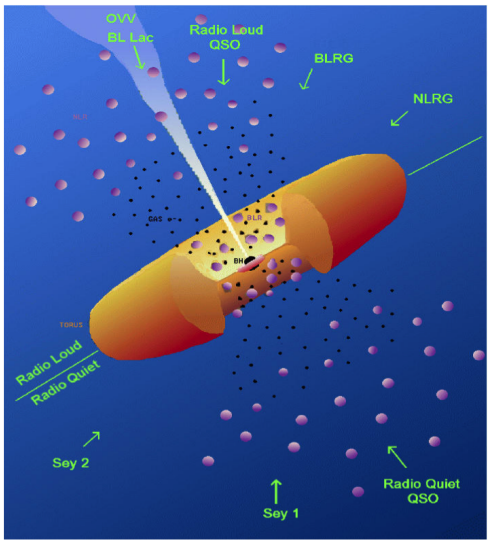

Figure 2.31: AGN structure and classification according with the viewing angle.

The structure of AGNs is formed by some principal elements. The SMBH, with mass between 10^3 and 10^{10} $M_\odot$, that attracts the surrounding matter and powers the emission engine of the whole system. The accretion disk, formed around the SMBH by in-falling galaxy matter – IS medium, star members, etc. – due to gravitational attraction. The acceleration and friction of matter in the accretion disk produces its heating, becoming a plasma of relativistic particles, that emit EM radiation. Radio-loud AGNs also show two giant jet-like structures, originated at the center of the accretion disk and growing perpendicularly to it. Inside the jets, accelerated particles up to ultra-relativistic energies flow into the IS medium, forming blobs by turbulence at their extremes. The jets are powerful emitters over the entire EM spectrum, including gamma rays , however, their formation and emission mechanisms are still poorly understood. Their emission is believed to be due to Synchrotron Self Compton (SSC). One last structure element confirmed by observations is a toroidal structure situated around the accretion disk and composed by dust. Its formation, still not understood, is believed to be a consequence of the merging of interstellar clouds or an effect of the local magnetic field, among others proposals.

AGNs are unstable gamma-ray sources, that suffer flaring state periods where the flux is much higher than its usual level at quiescent state. The flares variability that can go from few days to few minutes. Distant AGNs showing order-of-minute variability flares are good targets for LIV studies (Chapter 1), since they allow to check for time delays between photons of different energies [219]. AGNs observation are also used to constrain EBL models looking at the effect of the absorption at the high end of the energy spectrum. EBL models describe the absorption of photons as a function of their energy and their source distance, and they are used to reconstruct the real spectrum of extragalactic sources, taking as reference the observed one. Among the different existing models, the most common for gamma-ray observations

are Dominguez [220] and Francescini [221] models. More details about these models can be found in Chapter 3.

Detected VHE AGNs usually present counterparts in radio and X-ray bands. In particular, AGNs present two peaks in their emission, one at the low frequency region − optical and X rays − and one at higher frequencies, in the GeV to TeV region. Usually both emissions are correlated suggesting that the emission is produced by the same electron population that emits photons via synchrotron (low frequency), that later become targets and are scattered-up via IC (high frequency), as seen in Figure 2.32.

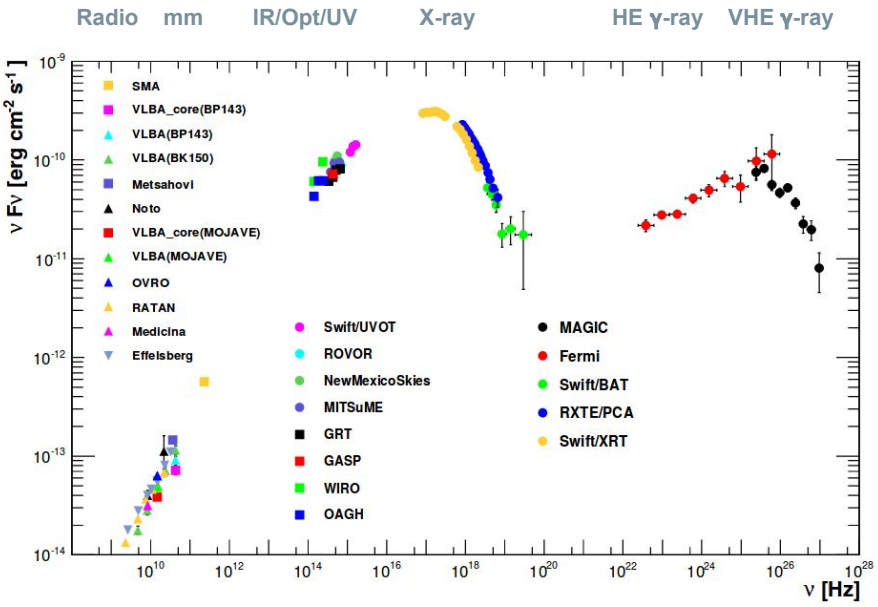

Figure 2.32: Averaged spectral energy distribution of Mrk 421 during the MW campaign between January and June 2009. The legend reports the correspondence between the instruments and the measured fluxes. The host galaxy emission has been subtracted and corrections have been applied for Galactic extinction and EBL absorption. Credit: Modified from [222].

However, there are many open fundamental questions about AGNs, as how particles are accelerated in the blob, how jets are created and what is their composition, or the particle population responsible for the emission, that is also not completely clear. Further observations in the VHE band are expected to clarify some aspects about the jet properties and the environment around the SMBH.

The second VHE detected source was the AGN Mrk421 [223]. It belongs to the radio-loud blazar category. Blazars are radio-loud AGNs is which the jet direction is parallel to the line-of-sight. Blazars are the most frequent gamma-ray source. In the HE band, the last Fermi-LAT catalog shows that out of their 1231 extragalactic sources, 750 are blazars [224]. Similarly happens in the VHE regime, but scaled down to the number of detected AGNs. At the writing of this thesis, are are more than 45 blazars detected in the TeV range. All the detected AGNs in the TeV ranges are represented as red points in Figure 2.26.

In the gamma-ray regime, the observation of AGNs allows to study not only emission mechanisms, but also open question about fundamental physics. Moreover, the broadband emission of these sources has led to the collaboration of different instruments in all energy ranges to develop simultaneous extensive Multi Wavelength (MW) campaigns. It is worth mentioning the case of the bright nearby blazars Mrk 421 and Mrk 501 ($z \sim 0.03$), that have triggered MW campaigns from 2009 [225] up to the present time [226]. These collaborations, that include instruments from radio to gamma-ray frequencies, aim to considering

these sources as *"high energy physics laboratories"*, in the same sense of LHC on Earth, to study the AGNs emission mechanisms and produce plots as the one in Figure 2.32, that allow to study the entire evolution of the SED over many decades of energy. These collaborations will potentially solve some of the open questions about AGNs.

Gamma-ray Bursts

GRBs are the most powerful short-lived phenomena in the universe. These "explosions" − that consist on an outburst of radiation at all energies − are isotropically distributed in the sky and neither their location nor their duration can be predicted. GRBs are considered extragalactic sources since they have been detected in a redshift range between 0.09 up to 7.

GRBs are classified in two groups according to their duration; short GRBs, that last from few milliseconds up to few seconds, and long GRBs, that can last up to hundreds of seconds. Even though the origin of GRBs was unknown, very recently, the near-simultaneous temporal and spatial detection of a gravitational wave produced by the merge of two NS and its EM counterpart [227], as a short GRB, has proved the prediction that short GRBs are a consequence of binary mergers. The origin of long GRBs is still unknown but they might be related to supernova or hypernova[13] explosions.

The GRBs light curves are characterized by a prompt emission in the gamma-ray regime, followed by an afterglow later emission that covers a wide range of the EM spectrum, from radio to X-rays. The afterglow emission can extend up to weeks after the initial gamma-ray outburst. Figure 2.33 shows the comparison of the light curve of the events GRB080916C at different energy bands, where the initial emission and the afterglow are visible.

The usual model to describe GRBs emission is called *"Fireball model"*. The Fireball model tries to explain why GRBs emission reaches such high energy levels. It also attempts to explain the time scales that govern GRBs and why they generate an afterglow. This model states the existence of a "inner engine", whose nature is still unknown but must be a very compact object, that produces a ultra-relativistic energy flow by pushing material out at speeds close to the speed of light [230].

Two different shock wave models are stated to explain both the initial burst of gamma rays and the extended afterglow that is detected after the GRB. The generation of gamma rays occur either within an internal process, as shocks or collisions inside the flow after the initial explosion [231], or in an external medium, when the shocks, at a later stage and already cooled down, interact with the IS medium [232] (Figure 2.34). The first case would explain the VHE emission right after the GRB event, while the second one, would explain the afterglow, mainly composed by thermal emission. A detailed description of the fireball model can be found in [233] and references therein.

GRBs were first detected in the gamma-ray band by the Vela satellite in 1967 [234] but was not until 1997 that the afterglow was detected in X-rays by the Beppo-SAX satellite [235]. The first detection in the HE band was made by he CGRO instrument on board of the EGRET satellite [236]. Since then, with the help of the GMB monitor on board the Fermi-LAT telescope, the number of detected GRBs has increased in a relevant way, with the detection of 72 GRBs during the first 6 years of operation of the instrument [237].

Up to now, there has been no significant detection of GRBs in the VHE range. With the current instrumental sensitivity, GRBs would be expected with an incidence of more than one per day, but the EBL

[13] Hypernovas are stellar explosions more than 10 times brighter than a normal SN [228]

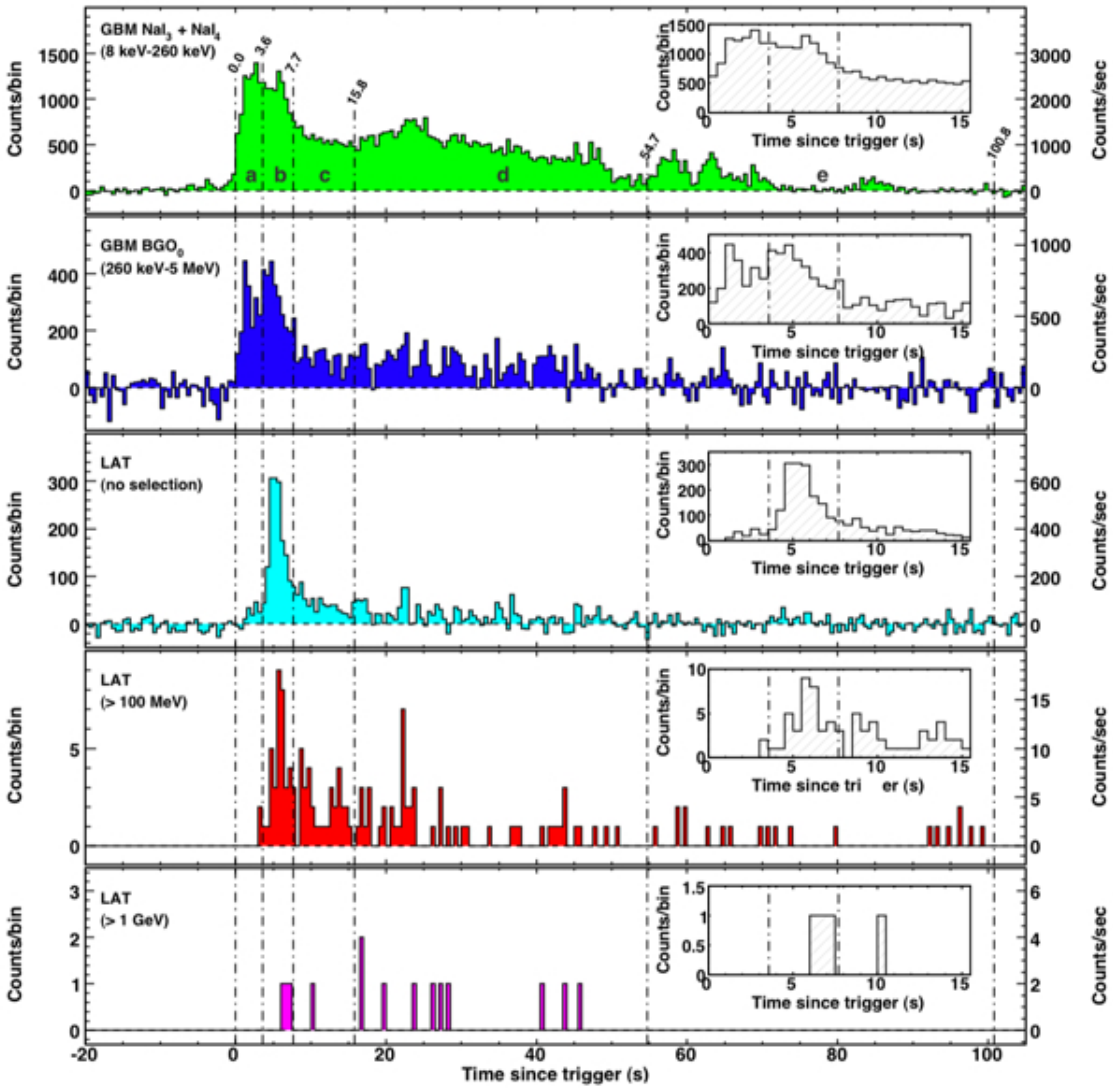

Figure 2.33: Comparison of the GBM and LAT light curves of GRB 080916C showing that the HE GeV emission peaks later than the MeV emission typically associated with GRB. Credit: Fermi LAT and Fermi GMB Collaborations [229]

absorption would restrict our detection to seldom nearby events, taking into account the redsfhit range of these events. Moreover, the short duration of the emission and the small field of view of ground-based VHE gamma-ray instruments, also decreases the probability of catching a GRBs by chance. Among the current generation of Cherenkov telescopes, only MAGIC was specifically designed with a fast slewing system (see Chapter 4) that allows re-positioning of the telescopes as fast as 40s after receiving a GRB alert. Even though the promptly reaction, MAGIC has only reported upper limits on GRBs [238].

Other extragalactic sources

- **Starburst galaxies**: These are galaxies in which the star formation rate is large due to a high concentration of gas. For this reason, starburst galaxies are characterized by an enhanced SN rates, where the SN explosions occur in regions of high density of protons and gas, generating large amounts of CRs and seed photons, that later produce gamma rays via IC and pion decay. Only two sources of this kind has been detected in the TeV regime, NGC 253 discovered by H.E.S.S.

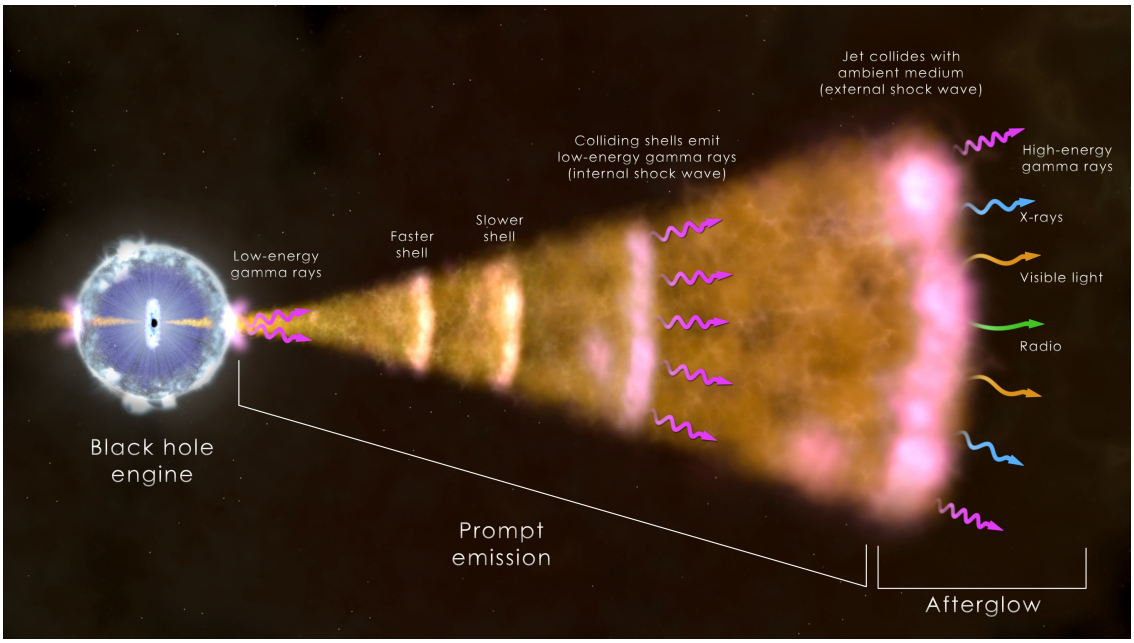

Figure 2.34: Fireball emission GRB model with the emission regions and corresponding emission products.

[239] and M82 discovered by VERITAS [240]. In the HE band, Fermi-LAT has also confirmed the gamma-ray emission from these sources [241].

- **Galaxy clusters**: They consist on large groups of galaxies gravitationally bounded. Galaxy clusters are expected to contain a relevant non-thermal particle population due to particle acceleration in accretion shocks during the formation of the cluster, to the SN activity inside the cluster and to the acceleration in the different galaxies [242]. A fraction of these particles would be CRs, confined inside the structure, colliding and producing gamma rays via pion decay. Among these particles there would be also relativistic electrons that would produce gamma rays via IC, by up-scattering photons from the star formation process or from the gas. So far, no gamma-ray emission has been detected from galaxy clusters. However, Fermi-LAT has place strong limits in the HE emission using a population of galaxy clusters [243] and MAGIC has set competitive limits to the gamma-ray emission produced by CRs in the Perseus cluster [244].

Chapter 3

Lorentz Invariance Violation Tests with IACTs

The non-renormalizable operators added to the SM Lagrangian are naturally suppressed by the Planck energy, so that in order to constrain them, we have to use experiments dealing with very high energies. Astrophysics is well suited for this purpose, since it can access energies much above the ones reachable in Earth-based experiments.

As mentioned in Chapter 1, the existence of higher dimension LIV operators would generically generate lower dimension ones in a EFT framework through radiation corrections and, at the current sensitivity of astrophysical tests, the size of the corresponding lower dimension operators should have given rise to a signal in terrestrial experiments. For this reason, if a LIV signal is seen in astrophysics, it should be explained why LI passes all the low energy tests. The only known mechanism to completely protect these lower dimension operators is SUSY.

Within the study of LIV in astrophysics, IACTs play an important role due their sensitivity to VHE photons and their precision for time measurements, that make them perfect tools for Time-of-Flight (ToF) studies. This chapter focuses on the Time-of-Flight (ToF) tests carried out with IACTs, explaining the theory, sources and analysis techniques, with a brief mention of other LIV tests that have been developed within the IACT community.

3.1 High-Energy Lorentz Invariance Violation in EFT

When describing HE LIV tests within an EFT approach, we assume some mechanism to protect the lower mass dimension operators and focus on the higher mass dimension ones in the Lagrangian. Additionally, we focus on the photon sector, considering modified dispersion relations resulting after adding terms of mass dimension 5 and 6 in the SM Lagrangian, due to the limit in sensitivity of the current generation of IACTs. These assumptions lead to a photon modified dispersion relation of type:

$$E^2 = p^2 \pm \frac{f_\gamma^{(3)}}{E_{Pl}} p^3 + \frac{f_\gamma^{(4)}}{E_{Pl}^2} p^4. \tag{3.1}$$

Equation 3.1 is mostly used in particle physics to compare results of different LIV tests for low and high energies [110]. However, in astrophysics, an alternative notation has been used by considering the coefficients to be of the order $O(1)$, and to be suppressed by an effective QG energy scale [14]. Moreover,

the expansion is expressed in terms of energy, equivalent to momentum for photons. It can be written in a compact version as

$$E^2 \simeq p^2 \times \left[1 - \sum_{n=1}^{\infty} \pm \left(\frac{E}{E_{QGn}}\right)^n\right]. \tag{3.2}$$

Astrophysical experiments try to set constrains on E_{QGn} for $n = 1, 2$, commonly called *linear* and *quadratic* terms even though they correspond to the third and fourth terms in the original power expansion. This nomenclature is adopted during the rest of the thesis. The subluminal (+) and superluminal (-) cases are considered (See Section 3.2).

3.2 Time-of-Flight studies

The simplest astrophysical description from a modified dispersion relation that provides interesting constraints for LIV at the Planck scale are Time-of-Flight (ToF) measurements of photons from distant sources [245, 246, 247]. From the dispersion relation in Equation 3.2 and the assumption $v = \partial E/\partial p$,[1] the speed of a photon in vacuum is given by

$$v_\gamma \cong \left[1 - \sum_{n=1}^{\infty} \pm \frac{n+1}{2} \left(\frac{E}{E_{QGn}}\right)^n\right], \tag{3.3}$$

which shows an energy-dependent speed, hence, for photons of different energies emitted simultaneously, the arrival times at the detector will be different. This can be a subluminal effect (+), so that the photons with higher energies arrive later, or superluminal (-), if their arrival time is earlier.

Considering two photons with energies E_1 and E_2, the difference in their arrival time Δt after travelling a given time t ($t \gg \Delta t$) is given by

$$\Delta t \cong \Delta v \cdot t \cong \frac{(n+1)(E_1^n - E_2^n)}{2E_{QGn}^n} \cdot t. \tag{3.4}$$

The travelling time t plays the role of an amplifier of the process, compensating for the small ratio E/E_{QG}. The travelling time is proportional to the co-moving distance to the source $\kappa(z)$. If the source is galactic, this distance is directly the distance between the source and the Earth. For close-by extragalactic sources ($z \ll 1$), the co-moving distance is given by the Hubble law as

$$l(z) = \frac{z}{H_0}, \tag{3.5}$$

where $H_0 \simeq 70$ km/s/Mpc is the local Hubble constant [248]. For more distant sources, the expansion rate of the universe has to be taken into account, and the co-moving distance is given by

$$l(z) = \frac{1}{H_0} \int_0^z \frac{(1+z')}{\sqrt{\Omega_\Lambda + \Omega_m (1+z')^3}}\, dz', \tag{3.6}$$

where $\Omega_\Lambda \cong 0.7$ and $\Omega_m \cong 0.3$ are the standard cosmological parameters of the ΛCDM model [249].

With these ingredients, the expressions for the delay between two photons in the linear and quadratic case are given by

$$\Delta t_{linear} = \frac{\Delta E}{E_{QG}}\, l(z), \tag{3.7}$$

[1] This relation holds in field theory approaches to LIV, but might be modified in DSR models.

$$\Delta t_{quadratic} = \frac{3}{2}\frac{\Delta E^2}{E_{QG}^2}\, l(z), \tag{3.8}$$

where commonly ΔE is $O(E)$ and ΔE^2 is $O(E^2)$, when the difference in energy between the two photons is very large, since the scale of the subtraction is determined by the energy scale of the most energetic photon.

If we find no ToF delay between photons, we can set a limit on $\Delta t_{linear}/\Delta E$ or $\Delta t_{quadratic}/\Delta E^2$. Thus

$$\Delta t_{linear} < \Delta t_{lim} \quad \longrightarrow \quad E_{QG1} > \frac{\Delta E}{\Delta t_{lim}}\, l(z), \tag{3.9}$$

$$\Delta t_{quadratic} < \Delta t_{lim} \quad \longrightarrow \quad E_{QG2} > \sqrt{\frac{3}{2}\frac{\Delta E^2}{\Delta t_{lim}}\, l(z)}, \tag{3.10}$$

where t_{lim} is our sensitivity to observe energy-dependent time delays with a certain significance.

A possible problem with this technique is that it cannot be assured that photons of different energies are produced simultaneously at the source and, if different energies are emitted at different times, a possible LIV signal might be masked. However, a study of its redshift dependence would allow to disentangle LIV from intrinsic source effects (see Chapter 6).

DSR models also predict a ToF signal[2] with energy-dependent group velocity for $n = 1$, that would not yield birefringence as in the EFT case.

3.3 Other techniques with IACTs

The IACT community is also involved in other astrophysical LIV tests related to threshold reactions. It has been argued that threshold constraints cannot be applicable to kinematic models without the knowledge of their dynamics. However, for rapid reactions − as photon decay − even an enormous change in the dynamics is irrelevant for deriving a kinematic constraint [97]. Under the assumption that the dynamics are not drastically different from the LI case, one can effectively apply particle reaction constraints to kinematic theories for short decay times.

Within the EFT framework, there are a number of changes that can occur to threshold reactions (see Section 1.5). By demanding that the energy of these reaction thresholds lies inside or outside a certain range, in order to be compatible with observations, it is possible to set stringent constraints on LIV.

- **Gamma-ray opacity through pair production interaction with EBL photons**. The intrinsic flux of gamma rays emitted by distant sources is reduced due to the interaction between gamma rays and EBL photons, creating electron-positron pairs (see Section 2.1.1). The relation between the intrinsic flux $\phi_{int}(E_\gamma)$ and the observed flux $\phi_{obs}(E_\gamma)$ for a given gamma-ray energy (E_γ) and a given source located at redshift (z_s) is:

$$\phi_{obs}(E_\gamma) = \phi_{int}(E_\gamma) e^{-\tau(E_\gamma, z_s)} \tag{3.11}$$

[2]There is some disagreement about this. At the beginning, DSR was believed to always lead to modified dispersion relations [250], it has been proven, however, that it is not a necessary condition [251].

and it is related through the opacity $e^{-\tau(E_\gamma,z)}$, where $\tau(E_\gamma, z)$ is the optical depth that indicates the absorption probability in the interaction between the γ ray and a background photon of energy ϵ [252]

$$\tau(E_\gamma, z) = \frac{m^4c^9}{E_\gamma^2}\int_0^{z_s} dz \frac{dt}{dz}\frac{1}{(z+1)^2}\int_{\epsilon_{thres}}^{\infty} d\epsilon \frac{dn(\epsilon, z)}{\epsilon^2 d\epsilon}\int_1^{s_{max}} ds \frac{s}{2}\sigma_{\gamma\gamma}(s, z), \tag{3.12}$$

where $\sigma_{\gamma\gamma}(s, z)$ is the pair production cross section, ϵ_{thres} is the threshold energy for pair creation (see Equation 2.4), $dn(\epsilon, z)$ is the background light density and $s = (E^2/mc^2)^2$, so that pair production is allowed for $s > 1$ in the LI case. The modified dispersion relation for photons in Equation 3.2 leads to a modification of the pair-production energy threshold and correspondingly a new formula for the optical depth [253, 254]:

$$\epsilon_{thres}(LIV) = \frac{2m_e^2c^4}{E_\gamma(z+1)} + \frac{1}{4}\frac{(E_\gamma(z+1))^{n+1}}{E_{QG}^n}, \tag{3.13}$$

$$\tau(E_\gamma, z) = \frac{m^4c^9}{E_\gamma^2}\int_0^{z_s} dz \frac{dt}{dz}\frac{1}{(z+1)^2}\int_{\epsilon_{thres}(LIV)}^{\infty} d\epsilon \frac{dn(\epsilon, z)}{\epsilon^2 d\epsilon}\int_1^{s_{max}(LIV)} ds \frac{s - \frac{((z+1)E_\gamma)^{n+2}}{E_{QG}^n}}{2}\sigma_{\gamma\gamma}(s, z), \tag{3.14}$$

that would be reflected in the relation between the intrinsic and observed fluxes, given by Equation 3.11.

In summary, with an intrinsic flux distribution, assuming a spectral energy distribution for background photons and introducing the LIV modification, we can derive an expected observed flux distribution that, by comparison with the real observed flux, allows to set constraints on the linear and quadratic terms for LIV dispersion, as graphically shown in Figure 3.2.

The most common models to estimate the EBL density are those of Franceschini [221] and Dominguez [220], shown in Figure 3.1. The most stringent constraints cast using this technique can be found in Table 3.1.

Intrument	**Source**	**Date**	E_{QG1} **(GeV)**	E_{QG2} **(GeV)**
H.E.S.S.[256]	Mrk501	2014	$2.8 \cdot 10^{19}$	$7.5 \cdot 10^{11}$
TeV Intruments[257]	38 TeV Sources	up to 2014	$7.32 \cdot 10^{18}$	-

Table 3.1: Best LIV limits obtained with the gamma-ray opacity technique.

This technique, still under development, suffers from several complexities, due to the fact that the TeV photon are potential targets for the IR background photons for electron-positron pair production. For this reason, when estimating the sensitivity in this kind of analysis we have to take into account, apart form the threshold condition, that also the infrared diffuse extragalactic background plays an important role in the photon absorption [258, 259]. The analysis of the LIV effect will become more effective as our quantitative characterization of the IR absorption improves.

- **Photon decay**. The modification in the energy threshold for pair production (Equation 3.13) would kinematically allow the forbidden reaction, in the LI case, of vacuum photon decay:

$$\gamma \longrightarrow e^- + e^+. \tag{3.15}$$

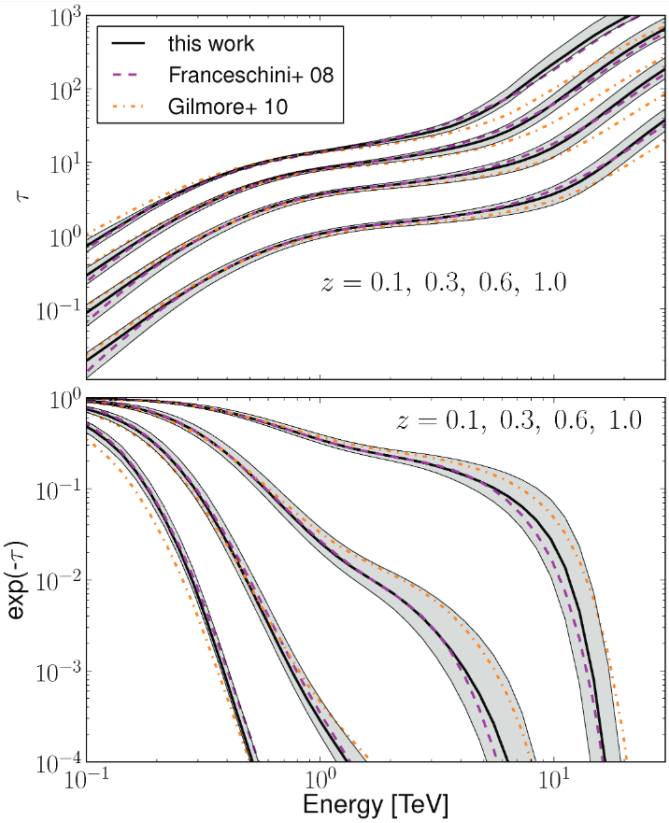

Figure 3.1: Upper panel: optical depth versus observed energy of gamma-ray photons for sources at different redshifts (from bottom to top z= 0.1, 0.3, 0.6 and 1), due to the EBL computed for the Dominguez model[220] with a solid black line ("this work" label), for Franceschini model[221] with a dashed magenta line and for Gilmore model[255] with a dot–dashed orange line. Lower panel: opacity versus observed energy of gamma-ray photons for the same redshift and models. The EBL uncertainties are shown here with a shadowed area in both panels. Credit: A.Dominguez [220].

If LI is conserved, a single photon cannot decay into an electron-positron pair since the energy and momentum would not be conserved at the same time. However, if we break LI and consider that the photon obeys a dispersion relation of the form (cubic term in Equation 1.6):

$$E^2 = p^2 + f_\gamma^{(3)} \frac{p^3}{E_{Pl}}, \tag{3.16}$$

while the electrons/positrons maintain their usual LI dispersion law, we can satisfy the conservation equation if $f_\gamma^{(3)} > 0$. Therefore, with LIV, photons can decay to an electron-positron pairs. This threshold reaction can happen above an energy threshold $E_{th} \sim (m_e^2 E_{Pl}/f_\gamma^{(3)})$, where m_e is the electron mass. By not observing the decay above E_{th}, the threshold energy constraint is translated into a constraint on $f_\gamma^{(3)}$.

The possibility of single decaying photons would have an effect on the amount of HE photons reaching the Earth, reflected as an abrupt decrease in the photon rate versus the predicted fluxes, making this technique of special interest for gamma-ray astronomy, by using the highest photon energy from astrophysical measurements. The computed photon decay rate for the modified reaction [260], shows to be very fast and effective once the process is allowed and, above a certain energy, the photon decay rate is so efficient that it leads to a cut-off in the photon spectrum so that no HE photon reaches the Earth. One of the pioneering results based on this idea was obtained by observing

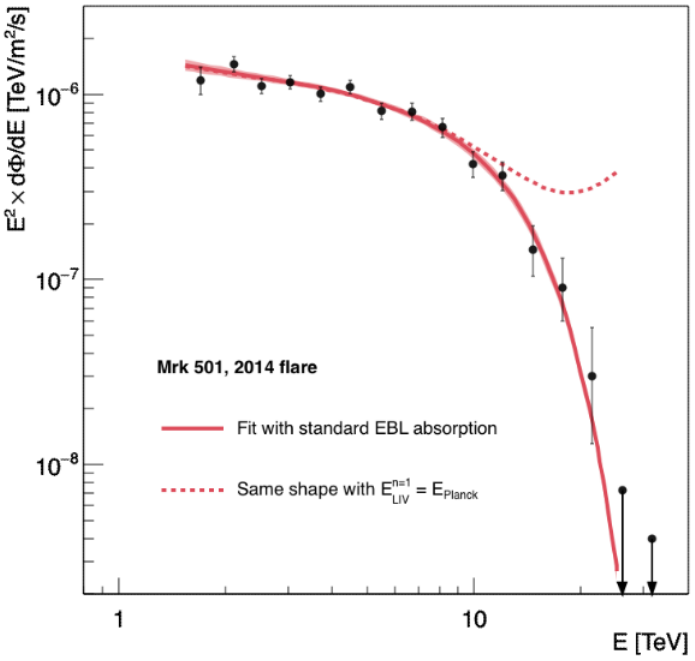

Figure 3.2: Energy spectrum of Mrk 501 obtained from the H.E.S.S. phase-I analysis of the 2014 flare data. The fitted EBL-absorbed power law (Francescini model) for the standard case is showed by the solid red line, as well as the corresponding 1σ confidence band. For comparison the same intrinsic power law with modified EBL absorption due to linear Planck scale perturbations is represented by the dashed line. Credit: H.E.S.S. Collaboration [256].

50 TeV gamma rays from the Crab Nebula [261] that cast a constraint of $E_{QG1} > 1.5 \cdot 10^{20}$ GeV and $E_{QG2} > 2.8 \cdot 10^{12}$ GeV for n=1 and 2, respectively. Other results using photon decay by different experiments [262], together with predictions for the HAWC experiment [263], for the linear and quadratic cases, are shown in Figure 3.3.

In conclusion, photon decay restricts the photon propagation to very short distances from the sources and permits a direct and simple way to bound the LIV energy scale. For recent results and further detail in the technique see [262].

- **Vacuum Cherenkov effect.** In the LI case, the emission of Cherenkov light is produced when a charged particle travels faster than the speed of light in a medium. However, in the presence of LIV the process of vacuum Cherenkov radiation,

$$e^{\pm} \longrightarrow e^{\pm}\gamma, \tag{3.17}$$

can occur, where the LIV-vacuum acts as an optical medium with a non-trivial refractive index, where particles with energies above a certain threshold are allowed to spontaneously radiate. This threshold reaction is allowed, that is, it preserves the energy-momentum, if the charged particle has a modified dispersion relation due to LIV of the shape:

$$E^2 = p^2 + m^2 + f_e^{(n)} \frac{p^n}{E_{Pl}^{n-2}}, \tag{3.18}$$

with $f_e^{(n)} > 0$. For simplicity, we shall consider that the photon dispersion is not changed, that

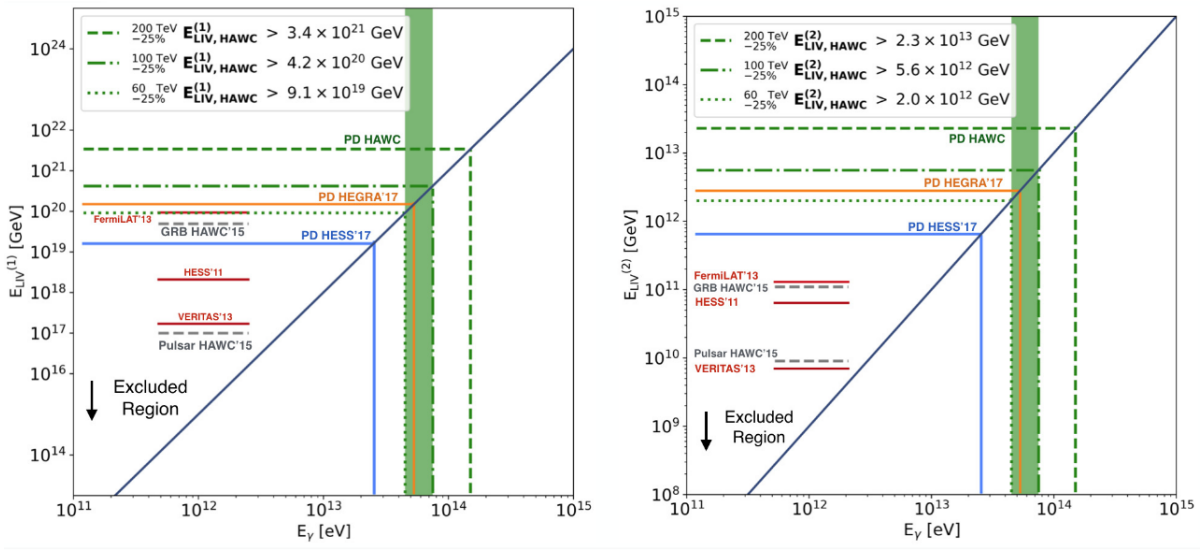

Figure 3.3: E_{LIV} excluded regions and limits from LIV photon decay into electron-positron pairs. On the left, potential limits from HAWC for n=1 and assuming 25% energy resolution uncertainty. On the right, for n=2 and assuming same uncertainties.For comparison, current limits from other telescopes and different approaches are also shown. Credit: HAWC Collaboration [263].

leads to a energy threshold

$$E_{th\,VC} = \left(\frac{m_e^2 E_{Pl}^{n-2}}{(n-1) f_e^{(n)}} \right)^{1/n} . \tag{3.19}$$

For this reason, the energy threshold can actually be far below the Planck energy, since it is also controlled by the mass of the particle. In this simplified scenario (photons are LI) for $n = 3$ and considering $f_e^{(n)}$ of $O(1)$, electrons will become unstable at 10 TeV, within the energy range of current astrophysical instruments. In this scenario, the estimated energy thresholds for different kinds of particles can be found in [97].

In a more general scheme and in the framework of the SME, this process can produce helicity-changing vacuum Cherenkov radiation ($e^- \longrightarrow e^+\gamma$), but the expected rate is extremely small at low energies [97, 90], or preserve helicity ($e^- \longrightarrow e^-\gamma$), where the rates are substantially larger and would allow to set constraints with the 50 TeV gamma rays observed from the Crab Nebula. However, assuming that these gamma rays are mainly produced via IC, it can be derived [97, 90, 264] that for electrons of energies up to 50 TeV, vacuum Cherenkov emission is still ineffective.

3.4 Sources

From this section on, we focus on the conditions for an observation to be suitable for LIV ToF studies, the current constraints in the field and the data analysis methods.

In order to be an ideal probe for testing LIV with the ToF technique, there are three criteria that a source should meet:

- Emit very high energy photons.

- Be located at a very large distance.
- Show rapid variability.
- Emit photons through a well-understood emission process.

Unfortunately, some of these conditions are mutually exclusive, for example, VHE photons from distant sources will be attenuated via pair production due to EBL absorption, thereby limiting the distance at which these sources show a detectable signal.

The different algorithms to look for LIV use different assumptions − simultaneous emission of photon of all energies, a given time distribution, a redshift dependence − that are not as accurate as one would like them to be, due to the lack of knowledge about the acceleration sites. For this reason, it is best to search for LIV signatures in a collection of sources at varying redshifts, since the intrinsic effects unlikely scale with distance, although it might be possible [265].

The main sources fulfilling the criteria mentioned above are GRBs, AGNs and Pulsars. Each of them has different strong and weak points for the ToF study.

3.4.1 Gamma-ray Bursts

GRBs show the fastest variability with durations of less than 2s for short GRBs[266]. Moreover, they have been observed up to the farthest distances of known sources. These properties make GRBs very suitable sources for ToF studies, and the most constraining limits have been derived using such sources, like GRB090510 observed by Fermi LAT [267]. That observation provided a limit above the Planck scale for the linear case. However, GRBs present some disadvantages. First, they are impossible to predict because they occur randomly in space and time. Secondly, their duration is so short that the ground based Cherenkov telescopes, due to their small FoV and their required reposition time, have still not detected any GRB after more than 10 years of trial. Finally, their unpredictability and short duration makes it difficult to built up statistics which complicates the task of differentiating intrinsic source effects from the LIV induced ones.

3.4.2 Active Galactic Nuclei

Jets found in AGNs emit flares and create repeatable sources of photons observable to higher energies than GRBs. This comes at the expense of longer variability of time scales up to minutes. AGN observations have led to LIV limits just below the Planck scale with the current generation of instruments [268, 269, 270], but the next generation of IACTs, CTA, is predicted to have sufficient sensitivity to go beyond the current GRB limits [271]. Even though the time variability is smaller, the higher energy of the photons will allow to set strong constraints on the quadratic scenario. In addition, the accumulation of long term monitoring data will allow to determinate time delays at higher confidence, by using cross-power spectral analysis methods [272]. AGN analysis will exploit extreme fluxes during flaring periods, even though intrinsic emission delays could mask the LIV signatures.

3.4.3 Pulsars

Pulsars are fastly varying, better understood sources with very different intrinsic emission processes to GRBs and AGNs. In the past, the limits from pulsars were inferior to those from AGNs and GRB

but, after the detection of pulsed emission up to 2 TeV from the Crab Pulsar by the MAGIC telescopes [209], the limits have reached the order of magnitude of the other two source types, especially in the quadratic case [273]. Millisecond pulsars reaching TeV energies will be observable by CTA allowing to improve the constraints even further. Though there are not many pulsars detected at TeV energies, their very well measured light curve profiles make them interesting objects to study any possible light curve broadening from a polarization dependent correction [53, 141]. The strongest point about pulsars is that their steady emission allows to built up much statistics and improve LIV delay sensitivity just by increasing the observation time on the source. On the other hand, we have to deal with a large background from the SNR which cannot be spatially resolved from the pulsed emission so far.

Looking at the properties of the above exposed sources, it is possible to make theoretical predictions about their potential to cast limits on the LIV energy scales by using Equations 3.9 and 3.10 , as shown in Table 3.2.

Source	**Distance (pc)**	**Energy (GeV)**	**Variability (s)**	E_{QG1} **(GeV)**	E_{QG2} **(GeV)**
GRB	10^{10}	10^{1}	10^{0} - 10^{2}	10^{17}-10^{19}	10^{9}-10^{10}
AGN	10^{8}	10^{4}	10^{2} - 10^{5}	10^{15}-10^{18}	10^{9}-10^{11}
Pulsar	10^{3}	10^{4}	10^{-4} - 10^{-2}	10^{17}-10^{19}	10^{10}-10^{11}

Table 3.2: Order of magnitude of the main properties of astrophysical candidates to test LIV and expected limit in case of no energy-dependent delay found, for the linear and quadratic cases.

3.5 Current limits obtained by astrophysical ToF tests

Among the different techniques to test LIV with IACTs, ToF tests have been pursued very actively with all available types of sources mentioned in Section 3.4. IACTs have $\sim$ nanoseconds time precision and energy coverage up to tens of TeV, making them powerful tools to look for the tiny expected delays due to LIV. Up to now, no significant energy-dependent delay has been detected, albeit new analysis techniques have been developed which allow to boost sensitivity.

This section summarizes the current situation of ToF studies and the lower limits on the QG energy scale achieved so far.

3.5.1 Challenges for IACTs

- **Source selection:** Among the sources exposed in Section 2.3, GRBs have not yet been detected by IACTs. Space-based instrument have detected several thounsands, but not all of them have a redshift associated and reach high energies. Among the few pulsars detected in the gamma-ray regime, only two have shown emission at TeV energies, namely the Crab and Vela pulsars. On the other hand, there are many AGNs detected at TeV energies, but, in order to show suitable variability for LIV studies, we need to catch them in flaring state.

- **Lack of statistics:** Especially short duration emission like GRBs and AGN flares show low statistics. The sensitivity provided by the analysis methods is usually directly linked to the number of available events.

- **Assumptions:** In all analysis methods, several assumptions have to be made, like the simultaneous emission of the events at all energies, the shape of the real time and energy distributions of the events or the effects of the instrument on the observed data. The retrieved LIV effect depends on these assumptions.

- **Background:** All observations contain some hadronic background, apart from the gamma-ray events. The effect of LIV on these other species, if there is indeed an effect, is not expected to affect the LIV analysis. However, if the ratio between background and signal is big, the sensitivity degrades.

- **Intrinsic effects:** One of the most problematic issues in the LIV analysis is the lack of detailed understanding of the sources themselves that produce gamma-ray emission. The detection of an energy-dependent delay may not be due to LIV, unless we can discard any other possibility and, for that, we need to understand well the sources, which is seldom the case. Intrinsic effects could be expected to scale with energy [274], but not with distance, thus a possible solution to disentangle these effects would be a LIV analysis combining different sources, even sources of different types, located at different distances (see Chapter 6).

Different experiments have set stringent limits, so far currently above the Planck energy scale [267, 275] for the linear case. The goal of improving such limit has driven the different collaborations to improve data selection, observation techniques, analysis methods and to combine different observations in order to increase statistics and avoid intrinsic effects [275, 276]. At present, all currently active IACT collaborations have agreed to share data in order to increase the number of available sources for ToF studies. This collaboration has released its first results, that show a potential improvement compared to the individual ones [277]. This initiative is the subject of Chapter 6.

3.5.2 Current limits

The first attempts to cast limits on LIV by analyzing energy-dependent features in the light curves of GRBs used photons up to 80 MeV energies [278]. These however used an approximation for the co-moving distance travelled by the gamma rays (Equation 3.6) that neglected the cosmological expansion. Later, a systematic study combining GRBs with redshifts up to z=6 [247, 279], and taking into account the cosmological expansion, set a lower bound in the linear case of $E_{QG} \geq 10^{-3} E_{Pl}$. This correction was employed by different groups to perform additional ToF studies on GRBs [280, 281, 282, 283, 284]. Later on, it was found that a small mistake in the delay expression had been made [249] that changed by a factor (1+z) the LIV limits derived previously.

Since 2008, all the ToF limits take into account the (1+z) correction. At that moment, the current generation of Cherenkov telescopes − MAGIC, H.E.S.S. and VERITAS − were already active, together with the current generation of space-borne gamma-ray instruments, like Fermi-LAT. With a larger energy coverage and better time and energy resolution, the limits set by these instruments improved the earlier ones and reached two orders of magnitude below the Planck scale. Also the introduction of new analysis methods, as the Likelihood analysis in 2009 [285], resulted in better performance.

The most recent limits set by the current generation of instruments are shown in Table 3.3 and Figure 3.4, together with the respective analysis methods applied (see Section 3.6). For more information about

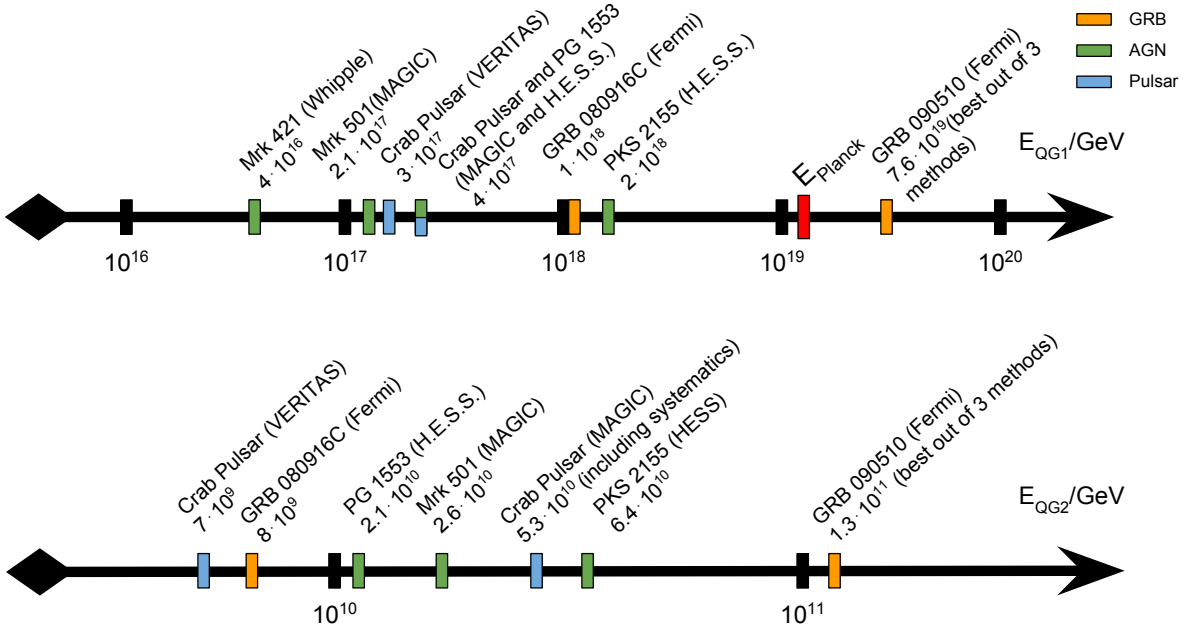

Figure 3.4: Limits on the photon LIV energy scale for the linear (upper part) and the quadratic (lower part) case.

limits before 2008, see Table 1.1 in [286], and for the correction of these limits after applying the (1+z) factor, see [269].

The individual source limits have already surpassed the Planck energy scale. The most stringent limit set with the ToF technique at the moment of writing of this thesis is $E_{QG} \geq 7.6 \cdot 10^{19}$, achieved with the observation of GRB 090510 (z=0.903) and PairView analysis. However, this limit needs to be corrected by a trial factor, since it was chosen for being the best out of three statistically equivalent methods on the same data set. Until now, there has been no attempt of combining several sources. Due to the unknown intrinsic effects and the low statistics for some sources – GRB 090510 has only 125 events used in the analysis [275], in case of detection of a significant delay, it would be difficult to justify that such detected delay is due to a LIV effect. This encourages the combination of different sources.

However, the individual experiments do not count with many sources suitable for LIV studies – Fermi-LAT made a selection of its bright GRBs with known redshift and was left with only 4 GRBs [275] – and it gets harder if we desire different types of sources. Therefore, the best solution is to associate between different collaborations in order to increase the available number of sources to a maximum (see Chapter 6).

3.6 ToF Analysis methods

Different analysis methods that produce constraints on the LIV parameter have evolved along the years. Albeit following different approaches, all of them share some common points:

- A time and energy distribution of the events must be provided. Some analysis act on the individual data events while others work with binned time and energy distributions.

Experiment	Source	Year	Analysis method	E_{QG1} (GeV)	E_{QG2} (GeV)
MAGIC[270]	Mrk 501	2008	ECF	$2.1 \cdot 10^{17}$	$2.6 \cdot 10^{10}$
H.E.S.S.[268]	PKS 2155-304	2008	MECF	$7.2 \cdot 10^{17}$	$2.6 \cdot 10^{10}$
H.E.S.S.[268]	PKS 2155-304	2008	CWT	$5.2 \cdot 10^{17}$	-
MAGIC[270]	Mrk 501	2008	Likelihood	$3.0 \cdot 10^{17}$	$5.7 \cdot 10^{10}$
Fermi-LAT[287]	GRB 080916C	2009	Comparison to trigger time	$1.3 \cdot 10^{18}$	-
Fermi-LAT[267]	GRB 090510	2009	Comparison to trigger time	$1.19 \cdot 10^{19}$	-
H.E.S.S.[269]	PKS 2155-304	2011	Likelihood	$2.1 \cdot 10^{18}$	$6.4 \cdot 10^{10}$
VERITAS[288]	Crab Pulsar	2011	Peak Comparison	$3.0 \cdot 10^{17}$	$7.0 \cdot 10^{9}$
Fermi-LAT[275]	GRB 090510	2011	PairView	$7.6 \cdot 10^{19}$	$6.7 \cdot 10^{10}$
Fermi-LAT[275]	GRB 090510	2011	SMM	$5.9 \cdot 10^{19}$	$1.3 \cdot 10^{11}$
Fermi-LAT[275]	GRB 090510	2011	Likelihood	$5.2 \cdot 10^{19}$	$8.6 \cdot 10^{10}$
H.E.S.S.[289]	PG 1553+113	2015	Likelihood	$4.1 \cdot 10^{17}$	$2.1 \cdot 10^{10}$
MAGIC[273]	Crab Pulsar	2016	Peak Comparison	$6.7 \cdot 10^{17}$	$2.9 \cdot 10^{10}$
MAGIC[273]	Crab Pulsar	2016	Likelihood	$4.5 \cdot 10^{17}$	$5.3 \cdot 10^{10}$

Table 3.3: List of recent LIV studies and their lower limits on the QG energy scale for the linear and quadratic cases, using the ToF technique. Some cases present limits on the same observed data set, but using alternative analysis methods. A trial factor has not been applied for this.

- An estimator associated to the parameter of interest E_{QGn}: Since the expected energy scale has a very large value ($\sim 10^{19}$ GeV) and tends to infinity in case of no LIV effect, usually the analysis methods use alternative parameters, whose values lie in a more reasonable range.

In this section, the analysis methods used to extract the results of this thesis are explained in more detail, however, a brief overview and references are given for additional analysis methods.

3.6.1 PairView analysis

The PairView (PV) is an event-wise method that calculates spectral lags $l_{i,j(n)}$ between all possible pairs of photons in a data set. The resulting $l_{i,j(n)}$ for a given data set are collected and their distribution is used to estimate the LIV effect. For a data set of N photons with arrival times $t_{1...N}$ and energies $E_{1...N}$, the method computes the $N \times (N-1)/2$ photon-pair spectral lags for each $i > j$, defined as

$$l_{i>j(n)} = \frac{t_i - t_j}{E_i^n - E_j^n}, \tag{3.20}$$

where $n = 1, 2$ is the linear or quadratic order for LIV.

If all the events were emitted by the source exactly at the same time $-$ δ-function light curve at emission $-$ and there was no effect due to LIV, the $l_{i,j(n)}$ distribution would be a δ-function centered at 0. If there was a dispersion effect (a given relation between time and energy of the events) due tu LIV, τ_n, the δ-function will peak at that value. Since in real observations, the light curves at emission are more complex structures consisting of one or more superimposed peaks, the resulting distribution of $l_{i,j(n)}$, in case of LIV dispersion , will present a peak at $\sim \tau_n$ produced by pair-events emitted close in time but distant in energy, convoluted with a smoother underlying wide background, produced by the $l_{i,j(n)}$ of the rest of the pair-events.

The PV method considers that the estimator $\hat{\tau}_n$ of the LIV effect is the location of the most prominent peak in the $l_{i,j(n)}$ distribution. By comparison with Equations 3.7 and 3.8, we can extract the relation

between the LIV estimator (τ) and the LIV energy scale:

$$\hat{\tau_1} = \frac{1}{E_{QG}}\, l(z) \qquad \hat{\tau_2} = \frac{3}{2E_{QG}^2}\, l(z). \tag{3.21}$$

In the search for the estimator value, the binned $l_{i,j(n)}$ distribution can be used or a more sophisticated method called Kernel Density Estimation (KDE) [290]. The details of the KDE method and its application to data are exposed in Chapter 5.

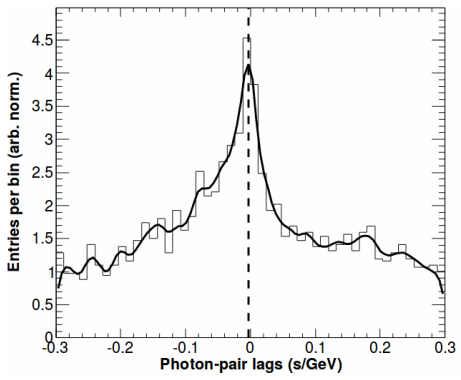

Figure 3.5: Plot demonstrating the application of PV. The histogram shows the distribution of photon-pair spectral lags, the thick curve represents the PDF of the distribution computed with the KDE method, and the vertical dashed line, the location of the PDF's maximum used as the estimator for the spectral lag τ.

The confidence intervals on the estimator value are computed by means of a randomization analysis. Using the detected data set, we shuffle the association between energy and time of the events to remove any potential dispersion. This process is repeated several hundreds of times, in order to have a big sample of randomized data sets with equal statistical power as the original data sample. The PV analysis is applied to every set and the results are used to create a normalized distribution f_r. We define the measurement error for any τ_n as $\varepsilon = \hat{\tau}_n - \tau_n$, where $\hat{\tau}$ is the PV result in that case, and its Probability Density Function (PDF) as $P_\varepsilon(\epsilon)$, where ϵ is a random realization of ε. We assume that P_ε has a negligible dependence on τ_n, at least of the range of τ_n values expected in the data, and consider:

$$P_\varepsilon(\epsilon) = P_\varepsilon(\epsilon|\tau_n = 0). \tag{3.22}$$

The PDF for the case of zero τ_n can be identified with the normalized distribution f_r

$$P_\varepsilon(\epsilon) \simeq f_r(\epsilon). \tag{3.23}$$

Since ε has a known PDF and depends on the unknown τ_n, it can be used as a pivotal quantity to construct a two-sided Confidence Interval (CI) of Confidence Level (CL) for τ_n as:

$$\begin{aligned} CL &= Pr\left(q(1-CL)/2 < \varepsilon < q(1+CL)/2\right) \\ &= Pr\left(q(1-CL)/2 < \hat{\tau}_n - \tau_n < q(1+CL)/2\right) \\ &= Pr\left(\hat{\tau}_n - q(1+CL)/2) < \tau_n < \hat{\tau}_n - q(1-CL)/2\right) \\ &= Pr\left(LL < \tau_n < UL\right), \end{aligned} \tag{3.24}$$

where $LL = \hat{\tau}_n - q(1+CL)/2$ and $UL = \hat{\tau}_n - q(1-CL)/2$ are the lower and upper limits defining the CI and $q(1 \pm CL)/2$ are the quantiles of f_r. Therefore, to produce a lower limit on E_{QG}, we need to use Equation 3.21, substituting τ_n with its upper or lower limits.

The PV analysis was used for the first time to estimate the LIV effect in a ToF study using four GRBs detected by Fermi-LAT [275]. A worth to mention characteristic of this first application of the PV approach it that is makes use of the observed energy of the events, while the LIV effect is related to the real o "true" energy of the events, that is unknown due to the limited energy resolution of the detector. In the case of GRBs, detected by space-based instruments, this may not have a big impact since the

energy resolution[3] is small (<10%). However, for observations of ground-based telescopes, with energy resolutions above 15%, there might be an effect on the value of the estimator that should be taken into account. An example of a PV analysis, taking into account the energy resolution can be found in [291]. The advantages of the PV method are its easy implementation and its unbinned character. However, it does not include detector effects and associates the LIV effect with the reconstructed energy of the events, points that can be corrected in other more refined methods as the Maximum Likelihood (ML) analysis.

3.6.2 Sharpness-Maximization analysis

The Sharpness-Maximization Method (SMM) [292], together with similar approaches like "Dispersion Cancellation (DC)" [293], "Minimal Dispersion (MD)" [294] or "Energy Cost Function (ECF)"[270], are based on the idea that the application of any spectral dispersion, like the one due to LIV, to a set of data, will smear the light curve, decreasing its sharpness. These methods try to identify the degree of dispersion and removed it from the data $-$ by applying an opposite dispersion $-$ in order to recover the original sharp light curve. To achieve this goal, the methods test several values of opposite dispersion, and choose the one that gives the most "peaky" or sharp resulting light curve. The most important difference between these approaches is the way the sharpness of the light curve is measured.

We show here the SMM because it is particularly straightforward to use and performs well for modest energy resolution ($\sim$20%), typical of IACT observations. If the expected energy-dispersion due to LIV is small, we treat it perturbatively and express it as the first terms of a Taylor expansion of Equation 3.2. When doing so (Equation 3.3), the arrival time shift of a specific photon, in case of LIV $t_{i,LIV}$, is related to the arrival time for the case of no LIV $t_{i,LI}$, by:

$$t_{i,LIV} = t_{i,LI} + f(E_i^n), \tag{3.25}$$

where E_i is the energy of the photon and $n = 1, 2$ for the linear and quadratic case. We indicate the LIV time effect with a parameter $f(E_i^n) = \tau E_i^n$, where τ would be 0 in case of no LIV effect.

All the dispersion cancellation algorithms work directly on the time-and-energy-tagged events to search for a non-zero parameter τ, that cancels any spectral dispersion in the light curve. The LIV lag-correction δt_i (the opposite dispersion effect) for a photon of energy E_i would be given by

$$\delta t_i = -\tau E_i^n. \tag{3.26}$$

The dispersion cancellation algorithms cycle through a range of possible values for τ and apply them to data, looking for the estimator $\hat{\tau}$, that maximizes the sharpness of the light curve, with the only assumption that the emission was simultaneous. In SMM, the "sharpness" of a burst is considered proportional to the gradient of the photon density at the time of the maximum in emission. The principle behind this choice is the idea that, whilst the emission of high and low energy photons at the source is simultaneous (top left panel of Figure 3.6), an energy-dependent dispersion introduced during the photon propagation, as the one produced by LIV, will always skew the overall light curve (lower left panel in Figure 3.6). In the example in Figure 3.6, the delayed arrival of the high energy photons skews and broadens the resulting burst profile. In order to retrieve the maximally sharp burst, the temporal sequence of events must again be randomized in energy, after applying the exact cancellation of the dispersion. This approach will give a

[3]The energy resolution is defined as $\Delta E/E$ where ΔE is the difference between the true energy and the analysis-reconstructed energy of an event. A detailed explanation of the energy resolution for IACTs can be found in Chapter 5.

unique solution $\hat{\tau}$ for each given dispersion model, since with an under- or over- correction, the burst will remain broadened with respect to its original width.

The SMM approach proposes a test metric, to compute the value of $\hat{\tau}$, based on the Kolmogorov distance between two probability distributions, exploiting the fact that, whilst the energy resolution of an individual photon is far from ideal, the overall energy bias of a sample of them is actually $\sum_i \Delta E_i \simeq 0$.

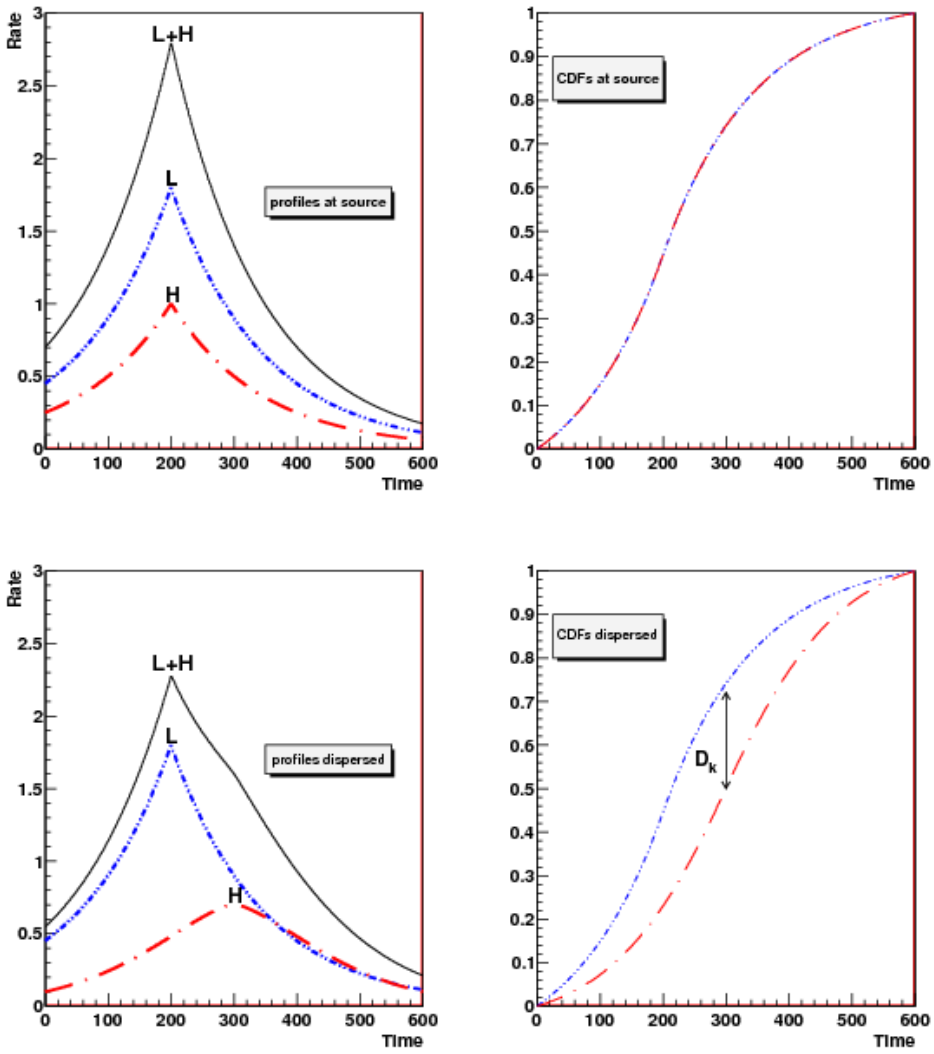

Figure 3.6: Graphical description of the SMM method.

The Kolmogorov distance D_k is the maximum vertical distance between the two Cumulative Distribution Functions (CDFs) of two random variables X and Y in $\mathbb{R}$

$$D_k \equiv \sup_{x \in \mathbb{R}} |F_X(x) - F_Y(x)|, \tag{3.27}$$

where $F_X(x) = \text{prob}(\text{X} \leq \text{x})$ and $F_Y(x) = \text{prob}(\text{Y} \leq \text{x})$.

For a data sets with enough number of photons $-$ around a few tens $-$ the photon list can be separated in low- (L) and high-energy (H) bands to create two independent data sets. In the absence of any spectral dispersion, the temporal profiles of the two sets are expected to superpose (top left panel of Figure 3.6). However, a systematic spectral dispersion, will skew the light curves with respect to each other (bottom

left panel of Figure 3.6). The right panels in Figure 3.6, illustrate the increase in the Kolmogorov distance between the Cumulative Distribution Functions (CDFs) of the high- and low-energy distributions due to the introduction of an energy-dependent dispersion, assuming that the events are generated simultaneously and co-spatially at the source. Therefore, the τ value required to cancel any present dispersion would be the one that minimizes the Kolmogorov distance. Moreover, by the properties of the Kolmogorov-Smirnov test, this distance is insensitive to the tails of the distributions and tend to fall around the central region of the CDF, near to the peak of the profiles, naturally attributing a greater weight to the transient part of the light curve.

Summarizing, to apply the SMM, the data needs to be split in high-energy and low-energy data sets, having the largest possible number of events per set and asking for the difference between the average energy of the sets to be maximum. After that, the CDFs of both sets must be build and a dispersion model chosen. Later, using Equation 3.26, we apply the dispersion correction for different values of τ and compute the Kolmogorov distance for every value, until finding the estimator $\tau*$, that minimizes D_k.

The CI on the values of the estimator are computed in an equivalent way as in the PV case, by applying the SMM analysis over a large sample of randomized data sets and defining the CL from the normalized distribution of the resulting values, as shown in Equation 3.24. To cast limits on E_{QG}, we substitute the CL values in Equation 3.21.

The SMM method's sensitivity to detect energy-dependent dispersion is affected by four main factors [292]: Burst width, energy resolution, burst intensity and burst asymmetry. In order to test the magnitude of the impact of these effects on the reconstructed dispersion, a statistical test using Gaussian flares with a power-law spectra was developed.

From this test, it was concluded that:

- The uncertainty in the dispersion scales inversely with the hardness of the spectrum, that leads to the counter-intuitive consequence that nearer AGNs could give better limits than more distant objects for similar variability timescales, due the EBL absorption.

- The narrower the burst width with respect to the introduced delay, the better the delay can be determined. The test demonstrated that the SMM method can reconstruct correctly the injected lag level if the magnitude of the dispersion is smaller than 20% the width of the burst.

- There is a small systematic trend for the reconstructed lag to be under-estimated as the energy resolution of the instrument gets poorer but it is small compared to the overall error in that reconstructed lag.

- An increase in the number of events, decrease the RMS of the reconstructed dispersion parameter, that tends towards a plateau. The plateau is reached earlier if the burst is sharper. The method is not affected by any intrinsic burst asymmetry, but only by its overall width.

Such conclusions are not changed when applying the method to the complex lightcurve of the gamma-ray flare of PKS2155-304 detected by H.E.S.S. in 2006, as proven in [292].

3.6.3 Maximum Likelihood analysis

The ML analysis to develop ToF studies was introduced in 2009 [285], to measure the time dispersion parameter in the data of flaring astrophysical sources. This method is particularly well suited for gamma-

ray astrophysics, since it is unbiased even in the case of low statistics and allows any complex time structure (overlapping flares, non-contained flares, etc.). Moreover, the ML method is the most efficient, i.e. it makes the best use of the available information. Furthermore, any extra information about the detector effects, environmental effects or the background data, can be included in the analysis, with as many details as known. On the other hand, these features make the algorithm more complex and CPU consuming. The ML analysis method makes use of an optimal estimator that, properly applied, uses all the information contained in the data and provide the most accurate estimate of the correlation between energy and arrival time of the photons. This estimator is the *Likelihood function* ($\mathcal{L}$), built from the combined PDFs of all the events in the data set. The PDF of an event with measured energy E_i and arrival time t_i, describes its probability of being detected, taking into account a physical description of the assumed processes involved at the emission, propagation and detection of such an event. The Likelihood function is defined as

$$\mathcal{L} = \prod_{1}^{N_\gamma} \frac{dP}{dE_i dt_i}, \tag{3.28}$$

where $\frac{dP}{dE_i dt_i}$ is the PDF of every event.

The ML estimate requires a model of all statistical processes involved. A general expression of the PDF of an event in gamma-ray astrophysics is

$$\frac{dP}{dE_i dt_i} = N \int_0^\infty \Gamma(E_s) C(E_s, t) G(E - E_s, \sigma_E(E_s)) F(t - D(E_s, E_{QGn}, z)) dE_s, \tag{3.29}$$

where E_s is the $-$ unknown $-$ true energy of the event and E, its reconstructed energy when detected. We consider that the time resolution of the detector is very good so that the true time of the events (t_s) and their reconstructed time (t) can be assumed equal if there is no LIV effect. The different functions composing the PDF are:

- $\Gamma(E_s)$ is the intrinsic energy spectrum of the photons at the source, assumed to be stable in time and without EBL absorption effect.
- $C(E_s, t)$ describes the effective area of the detector which may change during the observation.
- $G(E - E_s, \sigma_E(E_s))$ accounts for the energy smearing produced by the detector, obtained from simulations of the energy response of the detector.
- $D(E_s, E_{QGn}, z)$ is the LIV propagation delay as a function of the energy of the photon and the QG energy scale E_{QGn}. Its mathematical expression for the linear and quadratic case are given by Equations 3.7 and 3.8.
- $F(t - D(E_s, E_{QGn}, z))$, equivalent to $F(t_s)$, is the emission time distribution of the events, that can be extracted from the measured time distribution of the low energy events, assumed to be free of any corresponding LIV delay effect.
- N is the PDF normalization ensuring that the integral of the PDF over energy and time is always equal to 1, independently of the values of the parameters in the PDF.

The PDF can contain several nuisance parameters ($\vec{v}$) plus one related to the LIV effect, included in the dispersion delay $D(E_s, E_{QGn}, z)$ and directly related to the energy scale. Different experiments parametrize the LIV effect differently, in the case of MAGIC when working with AGNs, a parameter called α is defined as the ratio between the Planck and the LIV energy scale (see Section 5.6),

$$\alpha = \frac{M_p}{M_{QG}}, \tag{3.30}$$

so that the delay can be expressed as $D(E_s, \alpha, z)$ and α equals to 0 for the LI case. The nuisance parameter values are not interesting for the analysis but may show some correlation with the LIV estimator α and there is not enough information available to fix them. For that reason, their values are fitted, together with the estimator, using the detected data. This does not make the Likelihood a multi-dimensional function, since it can be constructed as one-dimensional using the profile Likelihood technique.

The data set included in the likelihood can contain background events whose information can be as well included in the PDF of the event, that becomes a normalized combination of the PDFs of the gamma-ray events and the PDFs of the background events.

$$\frac{N_b \cdot (dP/(dE_i dt_i))_b + N_\gamma \cdot (dP/(dE_i dt_i))_\gamma}{N_b + N_\gamma}, \tag{3.31}$$

where N_b and N_γ are the normalizations of the background and gamma-ray events, and $(dP/(dE_i dt_i))_b$ and $(dP/(dE_i dt_i))_\gamma$ their PDFs, respectively. The PDF of the background events is also described by Equation 3.29, but usually the background is not considered to be affected by LIV, so that $D_b(E_s, \alpha, z) = 0$.

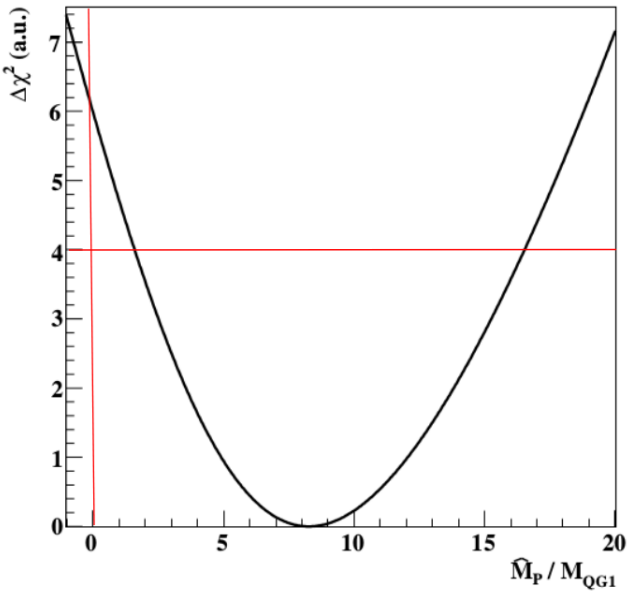

Figure 3.7: Behaviour of the function $-2\ln\mathcal{L}$ for the Mrk 501 data set with respect to the parameter M_P/M_{QG1} around the minimum. The shape is rather parabolic and allows excluding the value $M_P/M_{QG1} = 0$ at more than 2-sigma significance ($\Delta(-2\ln\mathcal{L}) > 4$)

The ML analysis consists of fitting the function $-2\ln\mathcal{L}$ to the data using a numerical procedure to find the set of free parameters that minimizes the function. In the large sample size limit, the function

$-2\ln\mathcal{L}$ follows a χ^2-distribution that allows a straightforward-way of defining the CL of the obtained result. The minimum is then located at $\hat{\alpha}, \hat{\vec{v}}$.

Afterwards, we can study the evolution of the system by changing the α parameter in small steps while refitting the rest of nuisance parameters to find a minimum of $-2\ln\mathcal{L}$ at each tested value of α, and construct such the profile likelihood. If the fits are well behaved, this profiling curve will have a parabolic behaviour around $\hat{\alpha}$, a typical example obtained with the data of the Mrk 501 flare detected by MAGIC in 2005 can be found in Figure 3.7.

We can define the CI with a desired CL, on the data sample from a given cut on the profile likelihood curve. For example, an increase of the value of the function $\Delta(-2\ln\mathcal{L}) = \Delta(\chi^2) = 1$ will take place at those values of α which include its true value within at a 68% CL [295]. However, in case the profile likelihood has not such a well-behaved parabolic shape, the cut might not provide the desired coverage. In this case, by using Monte Carlo (MC) simulations with the same number of events as the data, we can find the correct the cut of the profile likelihood which yields the desired coverage. The results and coverage corrections shown in Chapter 5 yield a 95% 2-sided CL.

3.6.4 Other analysis techniques

Continuous Wavelet Transform (CWT)

The CWT is a mathematical approach, binned in energy, that allows to define with high precision the peaks of light curves, in HE and LE energy bands, and extract a limit by comparison. This methods was used by H.E.S.S. to set a limit in the source PKS 2155-304 [268].

Peak comparison

This method compares peaks of the light curves of distinct energy bands. This method was traditionally used to produce the first limits on LIV [288, 296]. Nowadays is sometimes used to compared limits among different approaches [273].

Chapter 4

The MAGIC telescopes

The Major Atmospheric Gamma-ray Imaging Cherenkov (MAGIC) telescopes are a stereoscopic system of two IACTs located in the Canary Island of La Palma. The system is designed to measure Cherenkov light flashes from EAS above few tens of GeV. Both telescopes undertook a major upgrade in 2011-2012 in order to make the stereoscopic system more uniform (both telescopes having the same characteristics), to improve the overall performance and to make the maintenance easier.

The data analyzed in this thesis correspond to the post-upgrade period and was taken with both telescopes simultaneously, so that only this observation mode analysis chain will be described. For description of other operation modes, detailed information can be found in [297] for stand-alone mode for MAGIC I and for MAGIC II in [298].

The first sections of this chapter describe the current status of the MAGIC telescopes after the upgrade, the hardware components and the telescopes operation procedure. The last section exposes the details of MAGIC data treatment, for stereo observations.

4.1 Telescopes description

The MAGIC telescopes are located at 2200 m (a.s.l.) at the observatory Roque de los Muchachos, situated on the edge of the *"Caldera de Taburiente"* National Park, 2.396 m (a.s.l), the highest part of the Canary Island of La Palma, in Spain. MAGIC is, together with H.E.S.S. and VERITAS, the most sensitive instrument for VHE gamma-ray astrophysics from tens of GeV to tens of TeV.

MAGIC observes very dim ($\sim$ 400 photons / m^2 / TeV) and very short ($\sim$ ns) flashes of Cherenkov light produced by EAS in the UV and optical wavelengths. From the amount of light and its spatial and angular distribution, MAGIC reconstructs the energy and incoming direction of the primary particle $-$ CR or γ ray $-$. This goal is achieved by analyzing the image formed on the focal plane of the IACT and projected onto its camera. The characteristics of this image and the treatment to extract the final information from it are detailed in Section 4.5.

The MAGIC telescopes are self-triggered by requiring several neighbouring pixels to have a signal above a specific threshold. A coincidence or stereo trigger among individual telescopes allows later to minimize the spuriously triggered events. Stereo observations produce multiple images of the EAS leading to a more precise reconstruction of the energy and incoming direction of the initial γ ray.

Figure 4.1: Picture of the MAGIC telescopes, MAGIC I on the left and MAGIC II on the right. On the lower right corner, the Counting House (CH) building is seen, from where the telescopes are operated. Above the MAGIC telescopes appear, the 3.5 m Galileo telescope (left side) and the 10 m GTC telescope (right side), currently the biggest optical telescope worldwide. Credit: Dr P.Peñil.

4.2 Telescopes evolution

Between the construction of the two IACTs that now compose MAGIC, five years passed. While MAGIC I was inaugurated in 2004, MAGIC II, inaugurated in 2009, was born as an "improved clone" of the former. The differences were mainly in the funding constraints and the technological progress between both design periods. The array had two main goals,

- An energy threshold as low as possible, achieved by fine pixelated cameras, fast sampling electronics and a large mirror area.
- A fast repositioning speed, in order to catch rapid transient events as GRBs or AGN flares, achieved by a light carbon fiber structure and an Active Mirror Control (AMC) to maintain the telescope focused after fast movements.

Even with the same goals in common, there were important design differences between MAGIC I and MAGIC II before the upgrade. Due to funding constraints, MAGIC I camera mixed 1 and 2 inch pixel configuration, while MAGIC II was equipped fully with homogeneous 1 inch pixels. MAGIC I active trigger region was restricted to the central region of the FoV ($\sim$0.9 deg) and was enlarged $-$ during the upgrade $-$ to the MAGIC II trigger area of $\sim$1.2 deg, still with the same trigger electronics. To unify these differences, the MAGIC I camera was replaced by a new one. The readout of MAGIC I was based on an multiplexer and off-the-self Flash Analog to Digital Converter (FACDs)[299], robust with good performance but expensive and bulky. On the other hand, MAGIC II counted with a DRS2 chip [1], compact and inexpensive but noisy and non-linear. Both readouts were changed to the DRS4 chip during the

[1] https://www.psi.ch/drs/

Figure 4.2: Picture of the profile view of the MAGIC II telescope in parking position. On the left, the mirror structure and reflecting surface, on the right, the camera resting on the access tower. Credit: Dr P.Peñil.

upgrade. Finally, the receiver boards of MAGIC I , that convert the optical signals from the camera and produce the pixel trigger signal where changed due to their lack of programmability and their failure rate. The hardware specifications of both telescopes before and after the upgrade can be found in Table 4.1.

The main motivations for the upgrade, apart from the improvement of the stereoscopic performance, were the access to the lowest possible energies, that was limited by the noise of the DRS2 chip system. The increase of the trigger region aimed for a better flux sensitivity to extended sources, that now allows to measure sources with an extension up to $\sim 0.5^{\circ}$ and with a better control of the background region. The change of the DRS2 readout reduced the dead time per event by a factor ~ 10, which translates into an increase of $\sim 10\%$ in MAGIC observation time. Finally, the homogeneous small pixel cameras improved the angular resolution and the image parametrization that lead to a better reconstruction of the primary γ ray characteristics.

Additionally, another motivation was the reduction of downtime due to technical problems, that was achieved by upgrading the most failing subsystems and implementing diagnostic and online monitoring tools, also the production and storing of hardware spare pieces at the telescopes site. Finally, the smaller diversification between the telescopes allows to reduce manpower and expertise needed to run the MAGIC system and make troubleshooting easier.

4.3 MAGIC hardware components

This section comprises the main hardware components of the MAGIC telescopes, primarily the most relevant for data taking.

	Before Upgrade		After upgrade
Parameter	**MAGIC I**	**MAGIC II**	**MAGIC I / MAGIC II**
Digitizer type	FACD	DRS2	DRS4
ADC res (bits)	10	12	14
Sampling (GS/s)	2.00	2.05	2.05
Dead time (μs)	25	500	27
Camera shape	hexagonal	round	round
Total pixels	577(180*)	1039	1039
N trigger pixels	325	547	547
Trigger area (deg^2)	2.55	4.30	4.30
Field of view(°)	3.5	3.5	3.5

Table 4.1: Hardware specifications of the MAGIC system before and after the upgrade. *: Number of outer large 2 inch pixels.

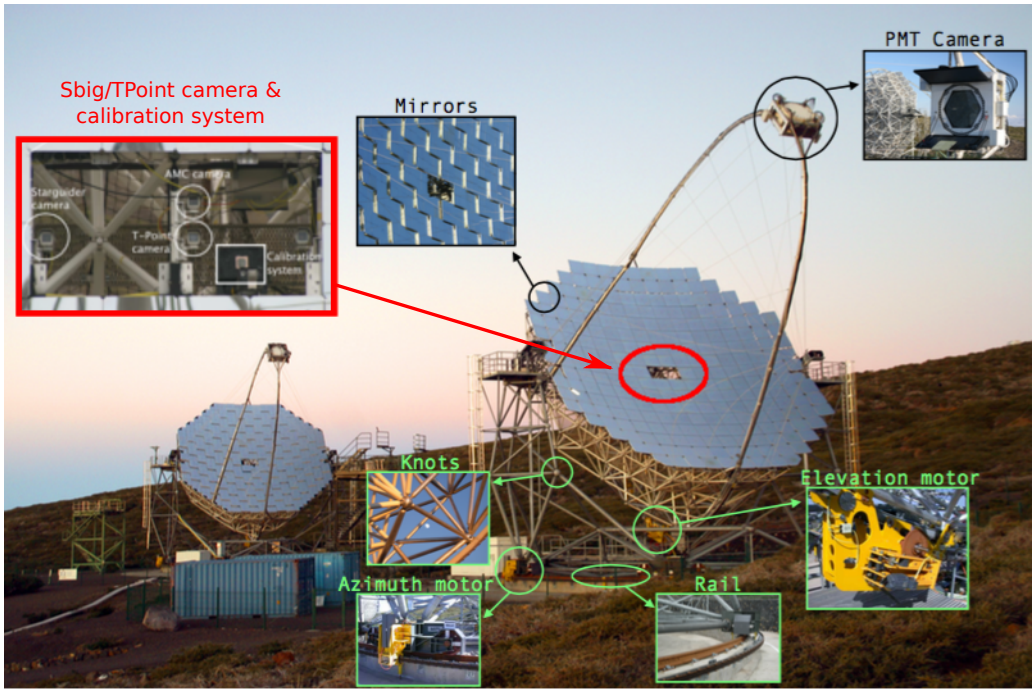

Figure 4.3: Picture of the MAGIC telescopes −MAGIC I of the left, MAGIC II on the right − with some of their hardware subsystems highlighted. Credit: Image taken from https://magic.mpp.mpg.de/, modified by [297, 300].

4.3.1 Structure and drive system

The MAGIC telescopes have an alt-azimuthal mount, that runs on six bogies on a circular rail. The two rotation axes determine the pointing position, the vertical (zenith) and the horizontal (azimuth). The allowed azimuth range covers from -90° to 318° while the zenith range expands from -70° to 105°. The rail and bogies are made of steel, located on a circle that spans 17 m in diameter. The structure to support the mirrors, identical in both telescopes, is mounted over them. The mirror dish is held by a octagonal frame made of carbon fiber reinforced plastic tubes and based on a rod-and-knot system (See Figure 4.3). The camera is mounted on a single aluminum tubular arc, secured against transverse movements by pre-stressed steel cables. The deformation of the structure, for any given orientation, is less than 3.5 mm [301]. Moreover, before data taking, the Active Mirror Control (AMC) corrects the small bending of the structure due to the telescopes movement. The bending in different positions is parametrized by a bending

model, constructed by taking images of bright stars − during the so-called TPoint procedure − in the complete allowed range in azimuth and zenith.

The chosen materials allow the frame to be rigid but light-weight, with a moving weight of 64 tons in azimuth direction and 20 tons in altitude. The movement in both axes is achieved by two electric driving motors, with a maximum output of 11 kW. Re-orientation of the telescope to any position in the observable sky is possible in about 40 seconds with average speed. A maximum speed of about 7 degrees per second can be achieved, making a re-positioning in less than 25 seconds possible, in case of a GRB alert. The pointing direction of the telescopes is cross-checked by a starguider camera mounted on the center of the mirror dish, that makes use of the starts in the FoV and the bending model. The final pointing precision after correction is 0.01 °.

4.3.2 Mirrors

The reflecting surface composed by the mirrors in both MAGIC telescopes covers 234 m^2 and has a parabolic and, therefore, isochronous shape. This allows a timing difference in the reflected signal of less than 1 ns and reduces the NSB contamination.

Originally, MAGIC I consisted of 974 square mirrors of dimensions 49.5x49.5 cm, made of diamond-milled aluminum with quartz coating. In groups of 4 mirrors (see Figure 4.4, left side), were mounted on 1x1 m panels with heating systems to prevent dew and ice deposition on the mirror surface. Over the years some of them, especially in 2014, were exchanged by 99x99 cm mirror, most of them made of glass. The change reduced the mirror dish weight in 1 ton.

The MAGIC II telescope has 249 mirrors of dimension 99x99 cm. The outer part, composed of 104, is made of glass while the inner part, is made of aluminum. The focal length and diameter of the parabolas are both 17 meters, so the focal length to diameter ration is f/D = 1.03.

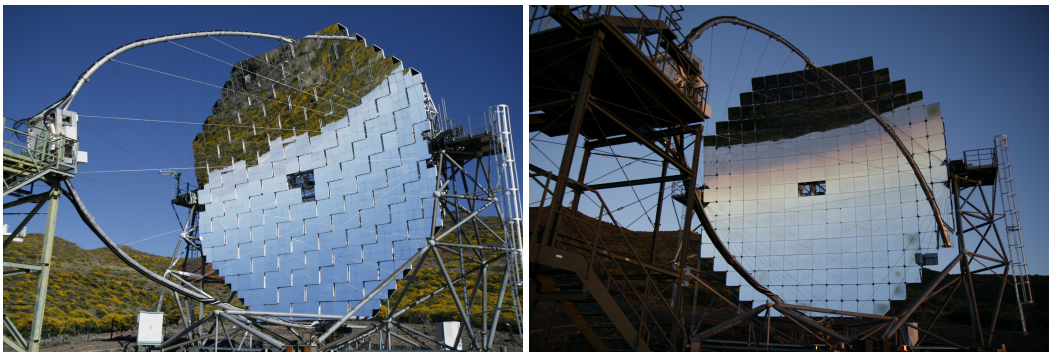

Figure 4.4: Reflecting surface of the MAGIC system. MAGIC I on the left and MAGIC II on the right. Credit: Dr. P.Peñil.

The average reflectivity of the mirrors, in the wavelength regime between 290-650 nm, is 80% and the individual deviation from an ideal parabola is less than few μm.

Each mirror panel is mounted on three points, one fix point and two computer-controlled actuators that can move the panel in any direction. Automatic adjustment of the mirror panel orientation by an AMC system ensures optimum focusing for each telescope pointing. The AMC corrects the position of the mirrors depending on the zenith value with a precision of less than 20 μm, using LUTs binned in zenith and azimuth.

4.3.3 Camera

The cameras of both MAGIC telescopes after the upgrade are identical, composed by 1039 PMTs, arranged in a circle of 1 m diameter that covers a FoV of 3.5° in the sky.

The PMTs are cylindrical with a diameter of 25.4 mm from the Japanese manufacturer Hamamatsu [302]. The PMTs are composed of a hemispherical photocathode and six dynodes. Each PMT has a hexagonal Winston cone mounted on top, in order to increase the amount of collected light and to avoid gaps between the circular pixels. Each pixel module has a power unit to provide the bias voltage. The power unit can provide up to 1250 V peak voltage. In each pixel, the electrical signals are amplified and transmitted via independent optical fibers (see Figure 4.5). The average pulse width is measured to be 2.5 ns (FWHM) [302]. The fibers transfer the analog signals from the PMTs to the readout and trigger electronics (see Section 4.3.5) located in a small building close to the telescopes, called the Counting House (CH). The fibers connecting the telescopes and the CH are about 162 meters long and are protected by UV resistant PVC covers.

In order to increase the telescopes duty cycle by working under moderate moonlight conditions, PMTs operate at low gain. The gain differences for different pixels are compensated by adjusting their High Voltage (HV), that can be set individually with the so-called flatfielding [2] procedure.

The pixels are grouped in clusters − composed by 7 pixels − to create a modular unit that facilitates the installation and maintenance. Every cluster weighs around 1 kg, with 50 cm of length and 9 cm of width. Between the pixel centers, there is a distance of 3 cm.

The Test Pulse (TP) is an electrical signal that can be injected into every PMT in order to develop daily tests of the whole electrical chain that goes from the PMT to the readout and trigger systems without the necessity of applying HV. This signal is similar to the Cherenkov light pulses (2.6 ns FWHM) to obtain a realistic response from the system. Moreover, the calibration of the camera is performed through a calibration box, located at the center of the mirror dish (see Figure 4.3), 17 m away from the camera plane. This system provides uniform illumination over the PMTs via well-characterized light pulses of different intensities.

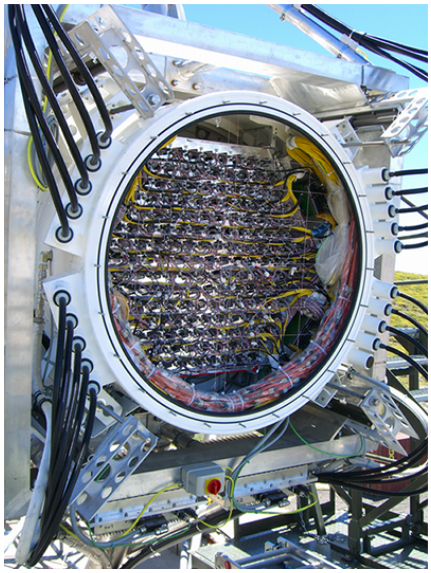

Figure 4.5: View of the MAGICII camera from the back side with the modular design of 169 clusters with 7 pixels each. Credit: D. Borla [303]

4.3.4 Readout electronics

The signal generated in a PMT is duplicated and split into two paths, one goes to the trigger system (see Section 4.3.5) and the other one goes to the readout system.

The readout system is in charge of recording the signal if the trigger system determines that such signal is indeed produced by a γ ray and should be recorded by the Data Acquisition System (DAQ). For

[2] Flatfielding is a correction technique that consist on taking a camera image with uniform illumination and divide the original images by this flat-fielded image. Flatfielding corrects variations in the pixel-to-pixel sensitivity by compensating for different gains and dark currents in order to achieve a uniform output in the detector.

this reason, the signal going to the readout system is delayed few ns to wait for the trigger response.

The DRS4 analog memory readout system is now installed in both MAGIC telescopes. It consists of two main parts, the receiver boards and the digitization electronics, controlled by the same communication network. The receiver boards transform the optical signals from the PMTs of the camera back into analog ones to generate the L0 trigger (see Section 4.3.5) and split the analog signal to send a signal copy to the Sum trigger [304]. On the other hand, the digitization electronics is an ultra-fast analog memory composed of a ring buffer of capacitors, that is read by a analog-to-digital converter (see Figure 4.6).

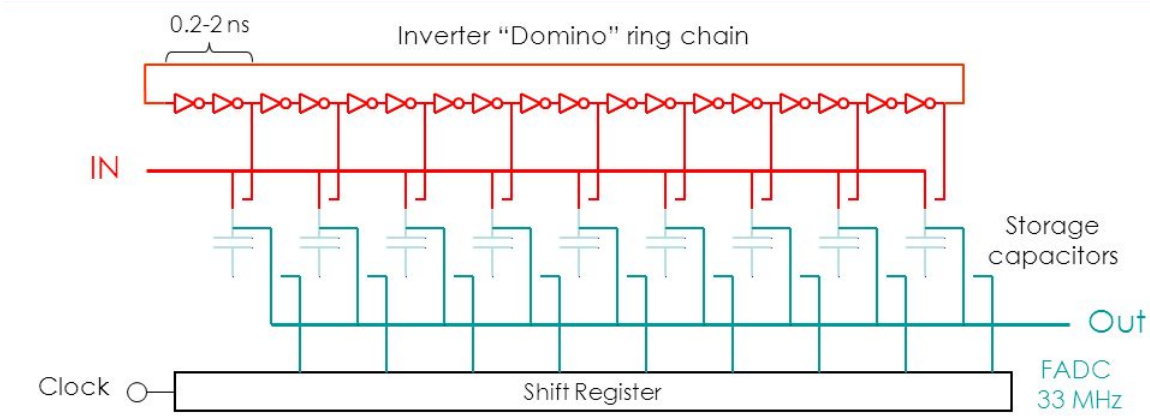

Figure 4.6: Scheme of the DRS4 chip Domino ring chain readout.

The readout process is, briefly explained, as follows: the signal coming from the receiver boards enters the capacitor array. The signal charges one capacitor and goes to the next one, where the change from one capacitor to another is controlled by an external clock so that the charge in the capacitors is proportional to the time period of the clock. When all capacitors in the ring are charged, the chip starts overwriting them. If the trigger system accepts one event, the process is stopped and the signal of some capacitors (the ones inside the Region of Interest (RoI)) is digitized and saved during the so-called dead time. The RoI number of capacitors should be a compromise of not too many in order to avoid electronic noise and not too few in order to measure EAS with long time development.

The last upgraded MAGIC reading sampling speed is 1.7Gsample per second. This assures the detection of ns Cherenkov signals, increasing the signal-to-background ratio and getting the best out of the arrival time information. The readout system has a linear behaviour over a large dynamic range (from 1 to 600 photoelectrons), less than 1% dead time, low noise and negligible channel cross-talk [305]. The DRS4 readout system maintains the performance of the old FACD system of MAGIC I with better charge resolution, less cost and less space, that allowed to install all the required electronics inside the CH.

4.3.5 Trigger System

The second path followed by the signals of the PMTs − only those pixels inside the trigger region (see Figure 4.7) − goes to the trigger system that takes the decision on whether a signal was produced by a γ-ray and must be recorded or not. The trigger region in the MAGIC cameras is composed by 547 inner pixels and has three levels.

The first level, called L0 level, is an amplitude discriminator applied to every pixel signal individually. This trigger provides a squared signal when the analog signal of a PMT surpasses a given amplitude

threshold, called Discriminator Threshold (DT) (See Figure A.5). The DT value depends on the observation conditions (dark, moon, etc.) and can be different for every pixel. During the data taking, the DT values are slightly modified to maintain the Individual Pixel Rate (IPR) stable. The 547 digital L0 trigger signals are produced in the receiver boards (See Section 4.3.4) and sent to the second trigger level, the L1 level.

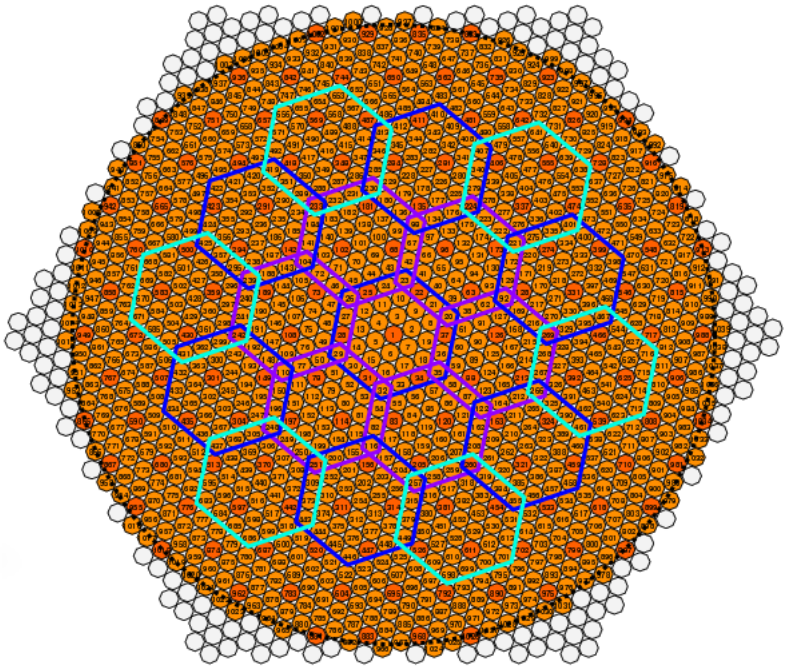

Figure 4.7: Scheme of the MAGICII camera pixel distribution. The hexagonal shapes indicate the trigger regions or so-called macrocells. Credit: J. Cortina [306].

The L1 trigger level is a signal filter arranged in 19 overlapping hexagonal macrocells (see Figure 4.7), each of them comprising 36 PMTs. The task of the L1 trigger is to find spatial and timing coincidence between neighbouring pixels. Several logic patterns, all compact, can be selected in order to decide if there is a trigger at L1 level. The options are 2 Next-neighbour logic (2NN), 3NN, 4NN and 5 NN. Inside these patterns, the L1 level produces a trigger if nNN neighbouring pixels give a L0 trigger. A single pattern can be selected at a time, at the beginning of the observation. For stereo observations, the 3NN patern applies. When one of the macrocells reports a coincidence trigger, inside the programmed logic pattern, a L1 trigger signal is produced at the telescope level.

The L1 trigger signals, one per telescope, are sent to the third trigger level, the L3 or stereo trigger level. These signals are artificially stretched to 100 ns width and delayed according to the zenith and azimuth orientation of the MAGIC telescopes to compensate the differences of the arrival time of the Cherenkov photons from air showers to the telescopes focal planes. At L3 level, a logical AND operation is made between both signals that are sent back to the individual redout systems afterwards. The maximum delay between two L1 signal capable of producing a L3 trigger is $\sim$200 ns. When there is a L3 trigger, the trigger system orders the readout system to record the corresponding signals. The L3 trigger assures a simultaneous detection of the signal by the two telescopes.

4.4 Telescopes operation

The operation of the MAGIC telescopes is uninterrupted during the year, with the exception of full-moon periods − 3 days per moon cycle − due to the large amount of background light. If the weather conditions exceed the security limits − strong wind guts, very high humidity, ice on the telescope, rain , etc. − the telescopes are stopped until the weather conditions improve.

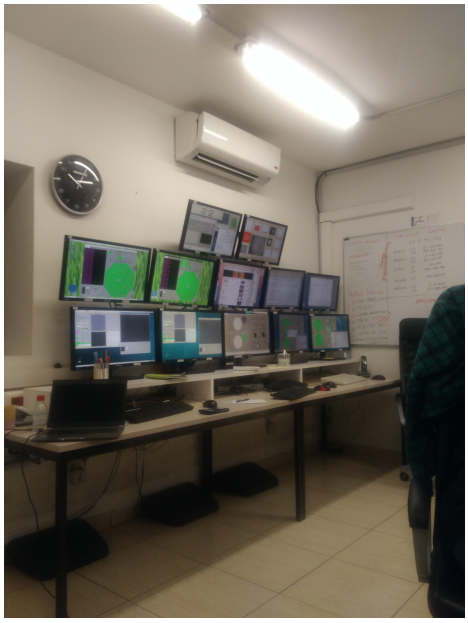

Figure 4.8: Inside photo of the MAGIC Counting House. The screens show the different telescope subsystems controlled by SA. Credit: M.Çolak

During normal operation, the telescopes are operated by a shift crew, composed of 3 or 4 members belonging to the different institutes of the MAGIC collaboration. The crew has different roles that depend on their level of expertise, from operator (O), through deputy shift leader (DSL), to shift leader (SL) for the highest expertise. The new crew members start as operators, with a shift that lasts 4 weeks, and have no responsibility apart from learning the basic working routines and the reaction to emergency situations. The next shift, the shifters are promoted to DSLs and should help with the operation of the telescopes and the operators instruction, but are not responsible for the safety. When promoted to SLs, the members have the responsibility of any decision related to the operation of the telescopes and safety of the crew. During the shift period, the shift members work for three days in a row and rest the forth one, in turns. The operation of the telescopes is done using the Central Control software, called SuperArehucas (SA), located in the CH (see Figure 4.8), a small building between the MAGIC telescopes, connected to both telescopes via optical fibers.

The MAGIC telescopes take around 1800 h of data in dark conditions and 600 h in moderate moonlight conditions. The decision about the sources to observe is taken by the Time Allocation Committee (TAC), that evaluates observation proposals submitted by the members of the MAGIC collaboration. The TAC allocates the available time between the selected proposals with the goal of obtaining the maximum scientific output. From the TAC decision, a calendar for a whole data taking cycle − around 1 year long − is produced. Every cycle ends with more than 250 TB of recorded raw data, that is reduced daily on site and sent to the computing infrastructure PIC ("Port d'Informació Científica"), located in Barcelona (Spain). At PIC, the data is analyzed up to high level and released to all the MAGIC members.

4.4.1 Observation modes

This section explains the two possible stereoscopic observation modes for the MAGIC telescopes, with special focus on the wobble mode, since all the data used in this thesis was taken with it.

- **ON/OFF mode:** This observation mode consists of pointing the telescopes directly to the source candidate and the pointing position is called ON region. In order to estimate the corresponding background, the telescopes point later to a close-by region in the sky with no known gamma-ray

source, that is called the OFF region. As the two regions are close, the background is considered identical for both of them and the signal is estimated as the difference between the ON and OFF regions.

- **Wobble mode:** The wobble observation mode [307] has been conceived to decrease the amount of observation time needed for background estimation. In this observation mode, the telescopes do not point directly to the source, but to a region with a slight offset (0.4° usually in MAGIC) away from it, called wobble 1 (W1, Figure 4.9). Then, to compensate asymmetries in the background and in the camera, the telescopes point to a new region, opposite to W1 with respect to the source, called wobble 2 (W2). Usually, there are also the wobble positions W3 and W4, in the perpendicular line to the W1-W2 pair. The telescopes point the same amount of time to the different wobble positions in order and start over again. The wobble mode observation procedure permits the observation of the source and the background at the same time. For the background determination, there are two different techniques, detailed in Appendix B. This observation mode preserves the maximum degree of symmetry in the camera, allowing an evaluation of the background in the same azimuth and zenith range of the signal and taking into account inhomogeneities in the background. Its main disadvantage is a loss of gamma-ray efficiency since the source is not at the center of the camera − where the detection efficiency is maximum − and a systematic uncertainty in the background determination due to the fact that the camera is not completely homogeneous (dead pixels, non-flat trigger efficiency, etc.). When operating in wobble mode, MAGIC observes each wobble position during one data run (20 minutes), subdivided in sub-runs lasting 2-3 minutes. The observation tries to maximize the variety in the wobble positions in which a given source is observed, in order to have a better estimation of the background. In this observation mode, signal is also estimated as the difference between the ON and OFF regions. Such regions are defined taking a radius called θ^2 around the central point of the region. For the ON region, such central point is the source position. The events inside the radius for the ON and the OFF regions are used to estimated the amount of signal. When using more than one OFF region, the number of detected events in all of them in re-scaled before comparing it with the ON region events in order to extract the signal.

4.4.2 Monte Carlo simulations

Since there is no gamma-ray calibration beam available, IACT analysis requires simulations that "teach" the analysis chain to reconstruct the energy and the incoming direction of the gamma-ray events. The MC simulated gamma-ray events resemble the real data and take into account variations in the telescopes as the Point Spread Function (PSF)[3], the decrease of the mirrors reflectivity, etc. The production of MC simulations is a separate part of the MAGIC analysis chain (see Section 4.5) and consists of three steps [309].

The first part is the atmospheric simulation, where the air showers and the hadronic and leptonic interaction of the particles of the cascade in the atmosphere are simulated. The second part simulates the mirror response to Cherenkov light, that comprises the absorption of the Cherenkov photons in the atmosphere and their reflection at the telescopes dish. Finally, the response of the PMTs and readout

[3]The PSF describes the response of an imaging system to a point source. It is obtained by studying the blur out in the image of a point-like object. The PSF indicates the resolution of the instrument.

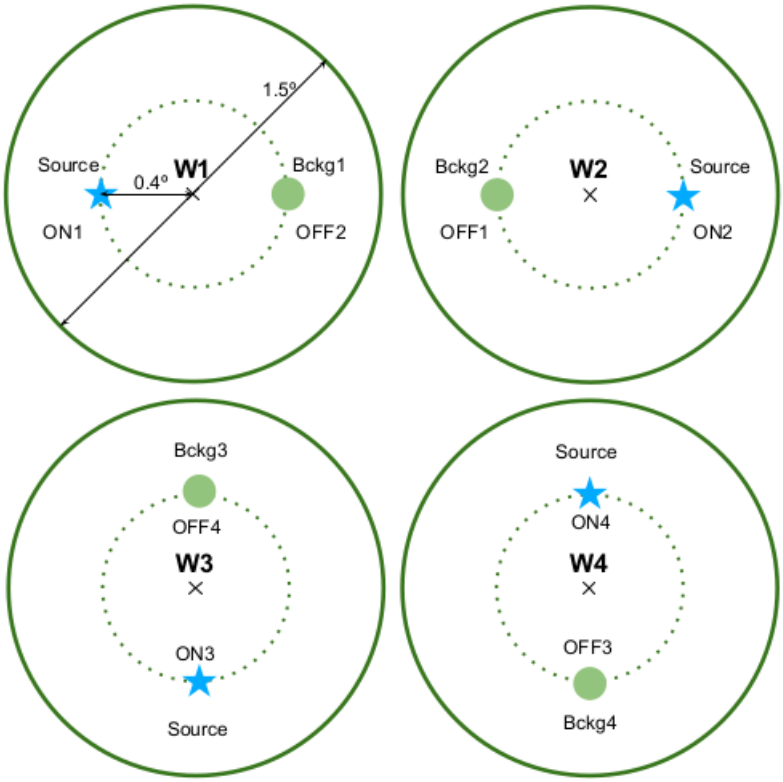

Figure 4.9: Scheme of the different wobble positions. The background region of in W2 (W4) position is used to estimate the background (OFF region) for the W1 (W3) position in order to avoid camera asymmetries. Credit: Dr. D. Garrido [308]

electronics is simulated, taking into account the trigger response, the readout noise and even the effect of the mirrors alignment.

Usually gamma rays are simulated inside a ring of 0.4° radius centered at the camera center, except for extended sources where the gamma rays are simulated inside a circle of radius 1.5°, around the center of the camera. MAGIC counts with many different MC productions along the years. Every time there is a substantial change in the telescope hardware, for example an exchange of mirrors or an upgrade of a subsystem, a new MC production is created. The analyzers choose the MC production required for the data analysis depending of the observation date of that data.

The final product of the MC simulations are events with the same format as the raw data recorded by the telescopes so that they can be analyzed with the same analysis software used for the real data.

4.5 MAGIC data analysis

The standard software to analyze MAGIC data is called MAGIC Analysis and Reconstruction Software (MARS). MARS is a collection of programming codes written in C++ that operates in a ROOT framework, a series of libraries, also in C++, developed at CERN.

The data analysis aim is to extract from the raw data the direction and energy of the gamma-ray candidates. In the following, a brief review of the stages of the standard analysis performed by MARS from the Analog-to-Digital Converter (ADC) counts recorded by the readout system to the high-level products is described.

4.5.1 Calibration

The first stage consists on transforming the recording raw data of the telescopes to number of photo-electrons (phe). An event is composed by the waveforms observed in each of the pixels, that span 30 ns and are sampled at a frequency of 1.7 Gsamples per second. In normal stereo operation, the telescopes stereo trigger have a rate of 250-300 Hz. The signal of the pixels are reduced to two numbers: arrival time and charge. For every pixel, 60 time slices are stored that correspond to 60 capacitors of the domino ring. A sliding window algorithm extracts the signal by going through the 60 slices and selecting those 6 consecutive slides that give the maximum integrated signal, that corresponds to the signal charge. The signal arrival time is the average position of the selected 6 slices weighed with the ADC counts contained in each of them. The charge − in counts − is then translated to phe using the F-Factor method [310]. On average, one phe generates a signal of $\sim$100 readout counts. Some corrections, as the inhomogeneity of the ring domino (due to the difference in the number of times a capacitor has been read or the difference response between capacitors) or the effect of malfunctioning channels, are applied at this stage [311].

4.5.2 Image cleaning and parametrization

This stage makes the transformation from pixel level information to shower image information. A typical air shower event illuminates around 10 pixels of the whole camera. Nevertheless, many other pixels have induced signals due to NSB or electronic noise. The so-called sum image cleaning [312] is performed to remove the pixels containing only noise, in order to extract the shower image. The first step is to find compact groups of 2,3,4 − 2NN, 3NN, 4NN − neighbouring pixels whose summed signals are above a given threshold and inside a given time window. These pixels constitute the core pixels. The threshold value is chosen so that noise events have a survival probability of less than 6%. The second step consists of looking for boundary pixels, that are pixels with a neighbouring core pixel, that are included in the image if their signal is above 3.5 phe and their arrival time is within 1.5 ns with respect to the core pixel. The Figure 4.10 shows an example of the core and boundary pixels surviving the cleaning procedure.

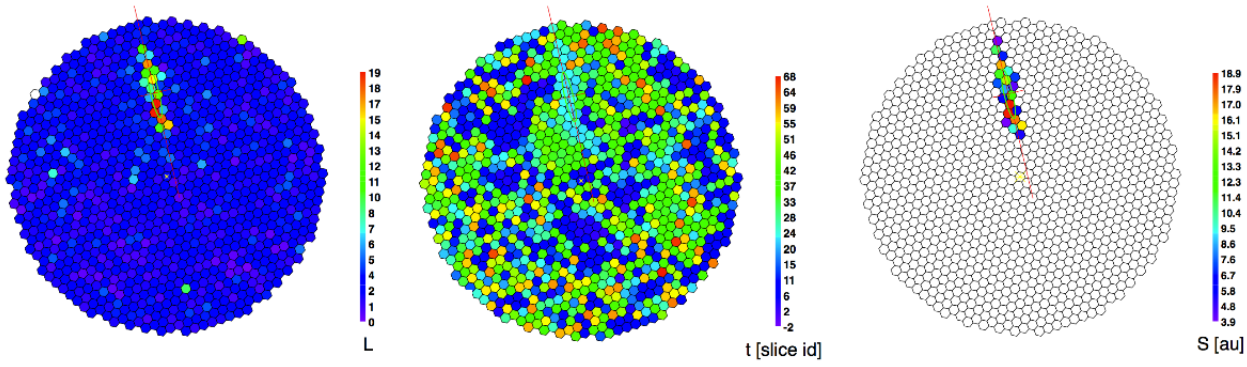

Figure 4.10: Charge distribution − on the left − and time distribution − in the center − along the camera. On the right, the final cleaned image formed by the core and boundary pixels. Credit: Dr. R. López [298]

.

The core and boundary pixels are parametrized using the *Hillas* parameters [168] (see Figure 4.11):

- **Size:** Total charge in phe of the image. The size is related to the primary γ ray energy.

- **Width:** Root Mean Square (RMS) spread along the minor axis of the ellipse. The width is related to the lateral development of the EAS.
- **Length:** RMS spread along the major axis of the ellipse. The length is related to the longitudinal development of the shower.
- **Center of Gravity (CoG):** Center of gravity of the image. The CoG consists of a pair of coordinates (x,y) that determine the position in the camera of the weighted mean signal along the x and y axis respectively.
- **Conc(N):** Fraction of the image concentrated in the N brightest pixels. This parameter is related to the compactness of the shower.

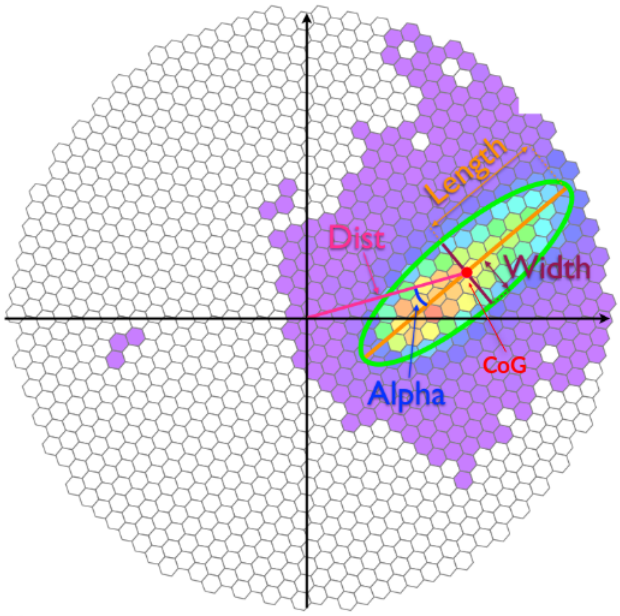

Figure 4.11: Cleaned and parametrized event image with some of the Hillas parameters indicated. Credit: Modified from [297].

At this stage, the data affected by technical problems, bad weather or different light conditions is separated from the good-quality data. Some of the indicators used in this selection are the cloudiness, the event rate, or the atmospheric conditions.

4.5.3 Stereo reconstruction

The stereo stage goes from telescope events to array events, from where the first information about the shower properties can be extracted. The survival parametrized and good-quality events of the cleaning procedure, around 80% of the total number of triggered events, are saved for later analysis. The events from both telescopes are paired and new extra parameters, useful for direction and energy reconstruction are calculated:

- **Impact point:** The impact point of the shower on the ground is calculated by the crossing of the two major axes of the parametrized ellipses from both telescopes (see Figure 4.12).

- **Shower axis:** The air shower axis is pointing towards the direction of the primary gamma ray source. Also the projected image of the shower, as seen by one telescope, points in that direction. For these reasons, superimposing the ellipses on the camera plane, the crossing point of the major axes indicates the shower axis. This parameter is used to perform a basic determination of the shower direction with the *crossing point* method [313]. This technique works well as long as the angle between the two image axes is large enough.

- **Impact parameters:** The impact parameter corresponds to the distance between the shower axis and the telescope position, projected in a plane perpendicular to the shower direction. The impact parameter is calculated for both telescopes (see top picture in Figure 4.12).

- **Height of the shower maximum:** By definition, the shower maximum is the position where the shower is the brightest. Seen from the telescope, this position corresponds to the image CoG. Once the shower direction is known, the height of the shower maximum (H_{max}) is obtained using the angle at which the image CoG is viewed from each telescope. H_{max} depends on the primary particle energy: higher energy particle showers penetrate deeper into the atmosphere, hence their H_{max} are closer to ground (smaller values). This parameter has a high discriminating power mainly at low energies.

4.5.4 γ/hadron separation

This stage of the analysis provides the events with a parameter that allows to discriminate gamma rays from the hadronic background. Most of the recorded events by the MAGIC telescopes are of hadronic origin. Usually, the fraction of gamma-ray events is or the order of 10^{-3} or smaller. For the background rejection procedure, the information of the image shape and the shower reconstructed direction is used. The γ/hadron separation is done through the Random Forest (RF) algorithm [314]. The RF method combines the image shape parameters, the timing of the shower and the stereo parameters into a single classification parameter, called *Hadronness*, whose value ranges from 0 to 1. The RF is first trained with events of known nature, i.e. MC simulated gamma-ray events and hadron events from the OFF regions before applied to the ON region events. Data events with an assigned small hadronness value are very likely to be gamma-ray events while hadronic events present hadronness values preferable close to 1. A event classification based on a cut according to the value of hadronness, achieves a background rejection with an efficiency better than 90% and a small loss of gamma-ray events. The method performs better at higher energies since the images are better defined. The gamma-ray efficiency is defined as

$$\epsilon = \frac{N_{\gamma}^{MC}(after\ cuts)}{N_{\gamma}^{MC}(simulated)}. \tag{4.1}$$

The selected value of hadronness to cut the ON data in order to reject background events should not be too strong. For hadronness values below 0.1, a non-negligible mismatch between the MC simulations efficiency with respect to the one achieved from the data has been observed, leading to an underestimation in the flux and spectra (described in Section 4.5.7) of sources [311]. The direction reconstruction method (see Section 4.5.5) also provides an additional background suppression tool.

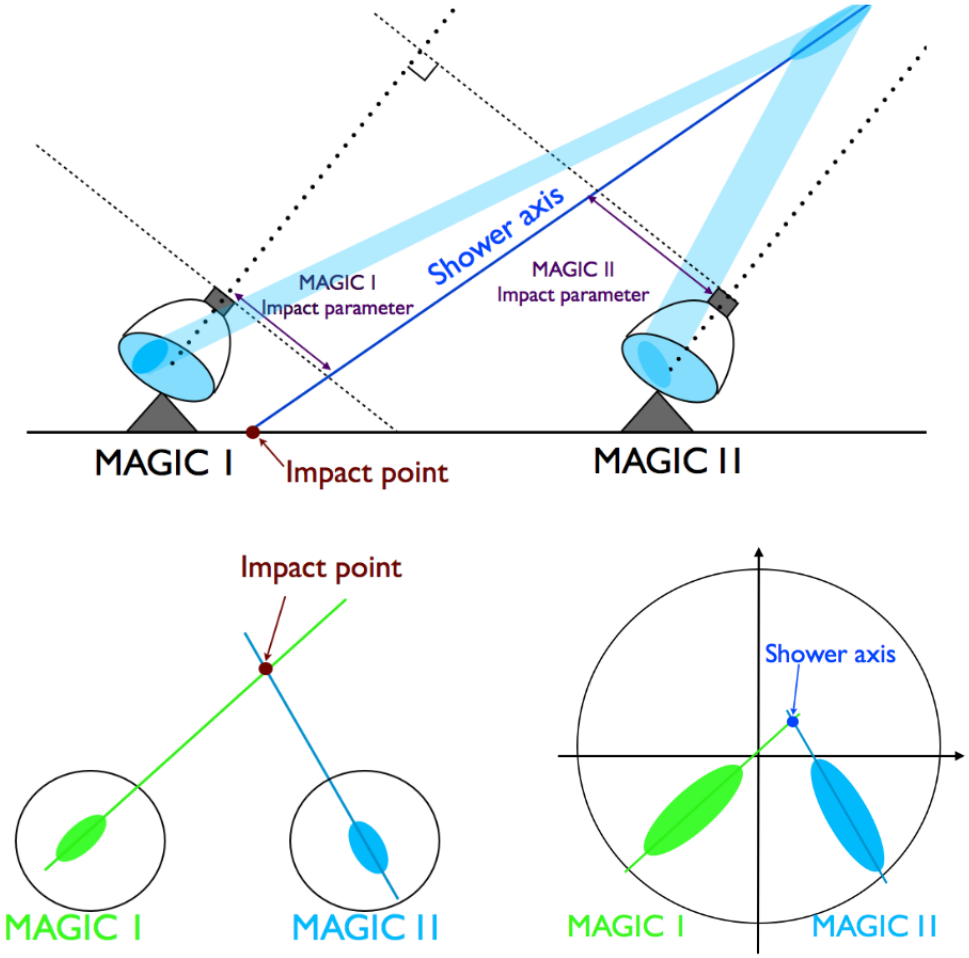

Figure 4.12: On top: Picture of the geometry of a stereo event. Below: Reconstruction of the impact point on the ground − on the left − and the shower axis − on the right − on the camera plane. Credit: Dr. R. López [298]

4.5.5 Arrival direction reconstruction

Classically, the arrival direction was computed with the *crossing point* method [313], indicated in Section 4.5.3. The current standard MAGIC analysis chain includes an event-wise direction reconstruction performed by the DISP RF method. This method takes into account the image shape and the time gradient along the major axis of the ellipse [315]. The DISP RF method consists of computing, for each telescope, an estimated distance called DISP. DISP is the distance between the shower image CoG and the source position. As the source position is located along the line containing the ellipse major axis, there are two possibilities or source reconstructed positions, one at each side of the CoG (indicated by the black dots in Figure 4.13, left picture).

The ambiguity about which of these two possible source positions is the real one can be solved by using the asymmetry along the ellipse major axis or using the crossing point of the two superimposed telescope images (As in Section 4.5.3). However, these solutions sometimes fail for the lowest energies where the image is composed by a few pixels or if both images are very parallel. For this reason, a more robust method as the DISP RF method is required to solve the ambiguity. The four distances (black dotted lines in Figure 4.13, right side) between the possible source reconstructed positions from M1 and M2 ellipses (black points in Figure 4.13, right picture), are computed and the pair of positions giving the

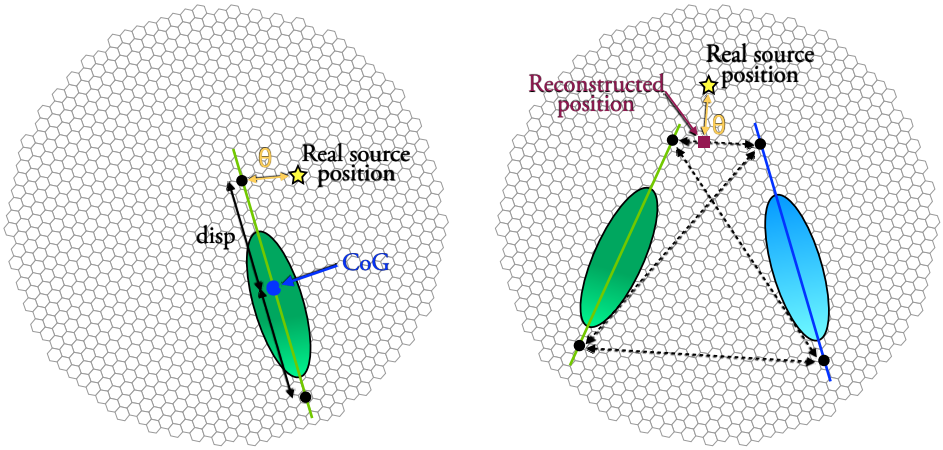

Figure 4.13: DISP method for one telescope (right) and for both telescopes (left). The possible source positions are indicated with black dots. The dotted lines indicated the distances between these possible positions. Credit: Dr. A. Fernández [297]

smallest distance are selected. After that, the reconstructed source position (purple dot in Figure 4.13, right side) is computed as the average of the selected positions from both telescopes weighed with the number of pixels in each image. The angular distance from this point to the assumed source position is called θ.

The estimation of the DISP parameter is trained with simulated gamma rays so that it usually gives inconsistent results for hadronic showers. Therefore, the DISP RF method is also used as an extra γ/hadron separation criterion and, if the none of the four pairs gives a similar arrival direction in both telescopes, the event is discarded.

4.5.6 Energy estimation

Until very recently, the energy estimation in MAGIC was a event-wise process developed in every telescope using Look-Up Tables (LUTs). The LUTs are information tables constructed using simulated gamma rays .

These tables are based in a simple model for the Cherenkov light distribution of a shower based on the $Size$ and $Impact$ parameters of each telescope and on the stereo parameter H_{max} (Section 4.5.3), together with the zenith angle of the observation. Assuming that most of the light produced by a γ ray in the atmosphere is contained in a light pool of radius r_c, the mean photon density in the light pool from a single charged particle of the gamma-ray shower can be calculated from the total power of emitted light by such a particle at a given height in the atmosphere. In such simple atmospheric model, by taking the gamma-ray energy, the H_{max} and the zenith angle of a gamma-ray event, we can compute the amount of light produced, the light pool radius r_c and the mean photon density in the pool from a single particle (ρ_c). With this information, the LUTs are filled with the information of $E_{true} \times \rho_c / Size$ as a function of $Impact/r_c$ and $Size$ for each telescope.

This parametrization takes advantage of the fact that E_{true} is roughly proportional to the number of secondary particles in the shower maximum, which scales as $Size/\rho_c$, and that the zenith angle dependence is automatically included. Using the MC tables generated in the previous step, the energy is calculated for each telescope based on the values of $Impact$, r_c, ρ_c and $Size$, computed for each

event. The final estimated energy E_{rec} is the average of the energies reconstructed individually for each telescope, weighted by the inverse of their uncertainties.

There is a new recent energy estimation technique, based in the RF algorithm motioned before [314], that can also be used for the estimation of a continuous variable. In an analogous way as for the hadronness case, the RF is trained with MC gamma rays , of known energy. Then, the built decision trees are applied to real data to estimate the energy of the primary gamma rays . The collection of image parameters used to train the RF are: size, width, length, dist, ConN, Leakage and zenith angle.

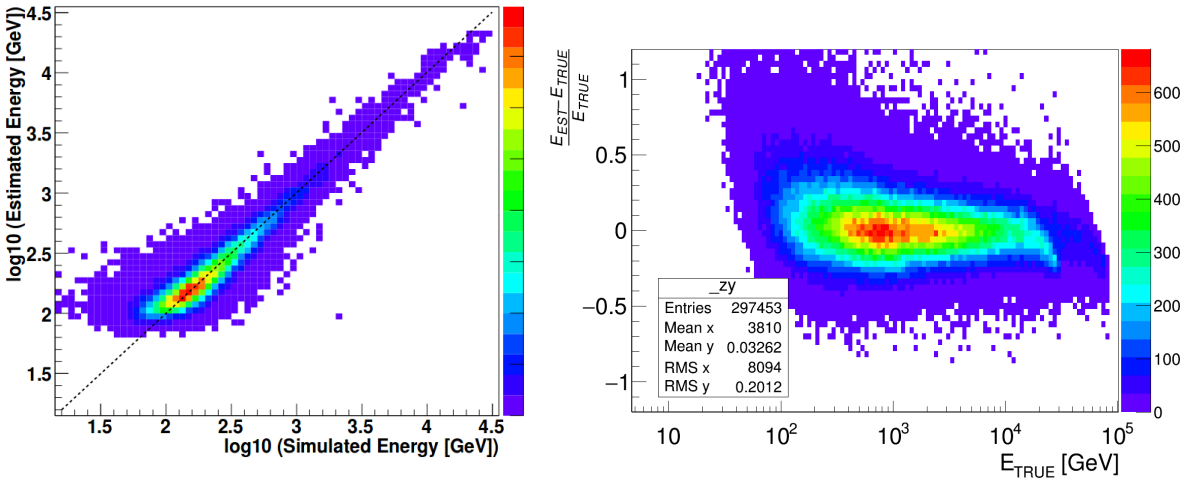

Figure 4.14: On the left, the migration matrix relating the true and reconstructed energy of the simulated event. On the right, the resolution of the energy reconstruction as a function of the simulated energy.

Figure 4.14 shows, on the righ side, the Migration matrix, that indicates the relation between the estimated and the simulated energy of the MC events. On the left side, the energy resolution is shown, that indicates the probability of an event with true energy (E_{true}), to be reconstructed with a estimated energy (E_{est}).

Once the arrival time, the energy and the incoming direction of the events have been estimated, some high-level analysis products that can be computed. Among them, the ones necessary for the development of a LIV analysis using MAGIC data, detailed in the next sections.

4.5.7 Spectrum and Lightcurve

The differential gamma-ray spectrum $\frac{d\phi}{dE}$ of a source is defined as the number of photons per unit of energy, unit of time and unit of area. Mathematically, it is expressed as

$$\frac{d\phi}{dE} = \frac{dN_\gamma(E)}{dE\ dA(E)\ dt}, \tag{4.2}$$

where

- $dN_\gamma(E)$ is the number of excess gamma-ray events in a given energy range E. As mention in Section 4.4.1, the excess events estimated as the difference of the events in othe ON region and in the OFF region, for that given energy range.
- t indicates the effective time of the observation of the source. This time is not coincident with the elapsed time between the beginning and the end of the observation, due to the gaps between runs during the datataking of the dead time during the events recording.

- A(E) is the collection area, defined as the geometrical area around the instrument where the gamma rays are detected. For a given energy range E, the collection area $A_{eff}(E)$ is computed using MC events as

$$A_{eff}(E) = A_{sim}\frac{N_{sel}(E)}{N_{sim}(E)}, \tag{4.3}$$

where A_{sim} is the simulated area, N_{sim} is the total number of simulated events and N_{sel} is the number of events surviving the analysis cuts in the energy range E. The simulated area for MAGIC is a circle whose radius depends on the simulated zenith. The effective area depends on the zenith of the observation, being larger with larger zeniths since the the shower is produced further away in the atmosphere and the lightpool on the ground is larger (see picture 4.15). An example of the evolution of the MAGIC collection area can be found in Figure 4.16. The collection area, together with other functions indicating the instrumental behaviour as the migration matrix or the angular resolution, are called Instrument Response Functions (IRFs).

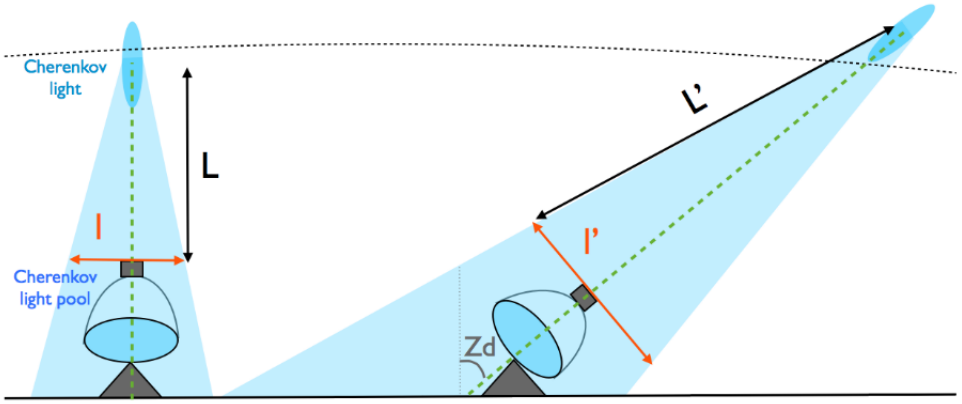

Figure 4.15: Development of the EAS for high zenith angle, on the right, and low zenith angle, on the left. The distance from the telescope camera to the source (L) and the diameter on the of the light pool (l) is a perpendicular plane to the telescope pointing position increase with the zenith angle. Credit: Dr. R. López [298].

The lightcurve shows the integral flux of events inside a given energy range as a function of the observation epoch. The integral flux is the total total number of events detected in that time interval whose energy is contained inside the considered energy interval. The time bins used to graphically show the lightcurve depend on the observation properties. As Cherenkov telescopes observations are not evenly performed, we might have some observations of the same source lasting few hours along an observation cycle. In the analysis chain, the choice of a time-binning is a trade-off between having the maximum number of points and having reasonable small error bars in those flux points. For stronger sources, the number of bins can be increased. An example of a lightcurve obtained with MAGIC with two different time binnings is shown in Figure 4.17.

4.5.8 Unfolding

The unfolding is a procedure applied to the energy spectrum computed with the estimated energy of the events in order to correct the known biases in the energy reconstruction. This process allows to obtain the true spectrum of the source, after removing the telescope and propagation effects.

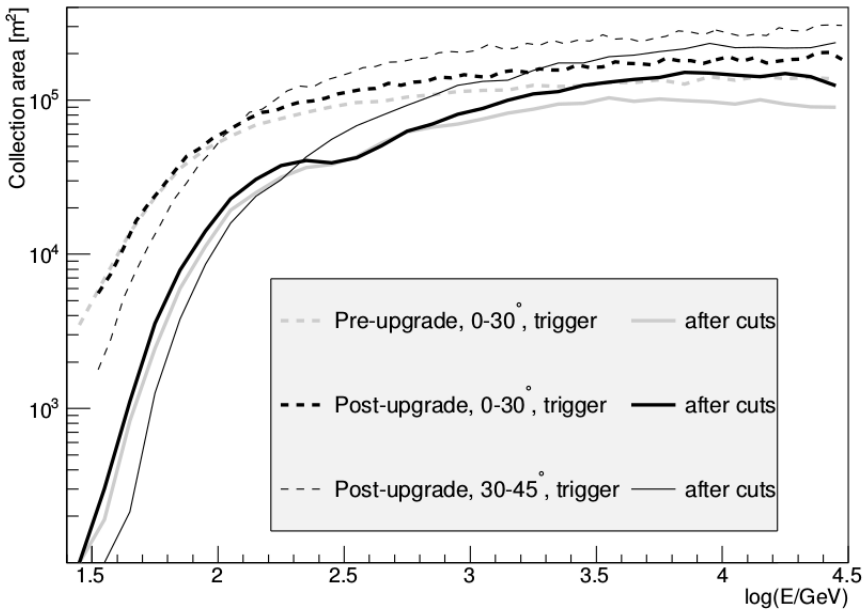

Figure 4.16: Collection area of the MAGIC telescopes after the upgrade at the trigger level (dashed lines) and after the analysis cuts (solid lines). Thick lines show the collection area for low zenith angle observations, while thin lines correspond to medium zenith angle. For comparison, the corresponding pre-upgrade collection areas are shown with gray line. Credit: MAGIC Collaboration [311].

In order to achieve this, MAGIC makes use of the Migration Matrix (Figure 4.14), that shows the correspondence between true and reconstructed energy. The correction cannot be done by simple inverting the matrix, due to the correlation between adjacent bins and the fact that sometimes the matrix is not invertible.

The unfolding procedure requires one assumption, a parametrization of the true energy spectrum ($\Gamma'(E_{true})$). With it, the distorsion due to the energy reconstruction can be mathematically expressed as

$$\Gamma'(E_{true}) = \int M(E_{true}, E_{rec})\Gamma(E_{rec})dE_{rec}, \tag{4.4}$$

where $M(E_{true}, E_{rec})$ is the migration matrix and $\Gamma(E_{rec})$ is the observed spectrum obtained from the analysis.

Inside the MAGIC analysis chain, there are several unfolding methods to operate the unfolding procedure, that differ on the algorithm that calculates the spectrum true distribution.

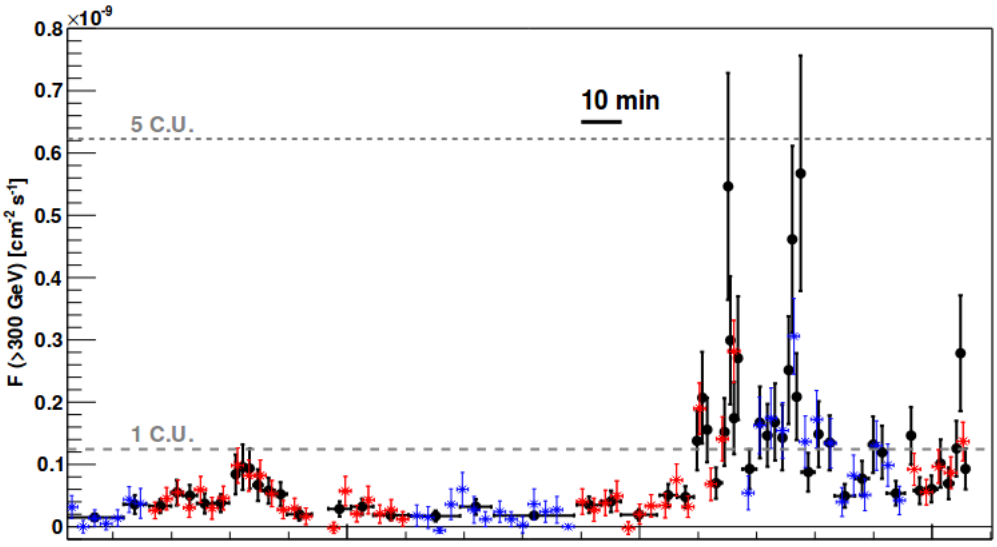

Figure 4.17: Light curve of IC 310 as measured in the night of November 13, 2012 above 300 GeV. The black points show the results obtained from a binning with fixed number of ON events (here: 9 events). The colored light curve presents the result from a fixed time binning (here: 3 minutes), red from the data of the wobble pointing with 0.4°, and blue with 0.94° offset, respectively. The two gray lines correspond to 1 and 5 times the flux of the Crab Nebula (C.U.). Credit: MAGIC Collaboration [316].

Chapter 5

LIV with the MAGIC data

The MAGIC telescopes, able to reach energies up to tens of TeV and with a $\sim$ ns time resolution, are a perfect tool for QG studies and this makes LIV a must in their science program.

This chapter shows the details of the process to select (Section 5.2), extract and analyze the MAGIC data (Section 5.4) to study a potential LIV effect (Section 5.5), using the different analysis methods exposed in Chapter 3.

5.1 LIV with AGN flares

The first step consists on selecting appropiate source candidates for the study. As mentioned in Section 3.4, individual VHE experiments do not count with that many sources well-suited for LIV studies.

In the case of MAGIC that have recently celebrated its 15 years anniversary, no GRBs have been detected so far. At the starting moment of the analysis contained in this thesis, among all pulsars, only the Crab Pulsar was detected and a LIV analysis using its data was ongoing, so that the focus was put on the potential of AGN flares. MAGIC has detected several tens of AGN flares along the years but there was not a straightforward and automatic way to access such flares information, contained in the analysis, in order to classify them and, more importantly, in order to compare them to choose the best suited candidates for the LIV study.

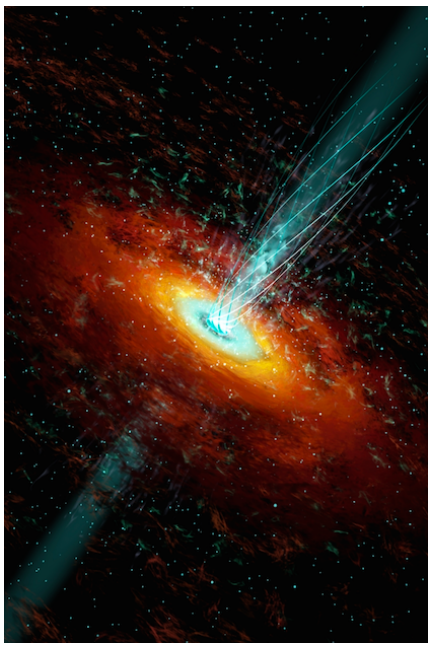

Figure 5.1: Artist's view of an AGN flare.

AGN flares are very interesting phenomena that can be used, apart from LIV studies, to study other topics like source periodicity, the EBL absorption effect, acceleration and production mechanisms at the source, etc. For this reason, creating a systematic way to provide information on the AGN flares detected by MAGIC could help to speed up the work of many analyses and to produce scientific results in a more efficient way. Therefore, we decided that the best way to show and distribute such information about the detected AGN flares was a database.

5.2 Source selection: Flares DataBase

Figure 5.2: Graphical interface of the query for the AGN flare database.

5.2.1 Goals of the DB

The AGN Flare DataBase (DB) is a new MAGIC tool designed to help the user find the best suitable sources for a given kind of study. The data included in the DB is a collection of selected results from AGN flare analyses provided through MAGIC internal documents by the analyzers. Neither all these analyses are final nor are they published, such that this section will focus on the DB itself and the criteria followed to choose suitable LIV sources, but will not go deeper into the specific data contained in the DB.

The selection of the data displayed in the database responds to the necessities of:

- Finding selected features about the different sources.
- Selecting useful information for source comparison and selection.
- Displaying easy access information (obtained in any standard MAGIC analysis).

The goals of the database are:

- Easy and quick access and visualization of all AGN flares detected by MAGIC so far.
- Allow selection of sources in relation to common properties such that comparison is straightforward.
- Direct selection of targets for specific studies (EBL, LIV, periodicity, source modeling, etc.).
- Provide information for statistical studies

- Frequency of flaring periods for a given source.
- Temporal distribution of VHE flares.
- Distribution of flare alerts by other experiments.

An important feature of the DB is that it connects directly the detection parameters of the source with the performed analysis and published data, in case there is a published paper. It permits a much better organization of the MAGIC flares and a quick overview of the current situation for new members.

The DB is a tool in continuous evolution that suffers changes and modifications as new flares are detected, the analyses achieve improvements or reach their final stage, or new papers are published.

5.2.2 Views and entries of the DB

Due to the fact that some flares last more than one night, the DB counts with two view options: the "Flare summary view", that shows a summary of the complete flare, taking into account all the nights in which it occurred; and the "Nightly view", that can be expanded from the first view and provides information of the flare on a daily-basis (Figure 5.3).

In the case of the "Flare summary view", due to the large number of entries, only some information is displayed for a specific search, the rest is only displayed if the user requires so at the query box (see Figure 5.2). The entries of every view with a brief description can be found in Table 5.1.

Most of the entries show values obtained directly from the analyses. However, every analysis is different and often adapted to its specific flare, making use of different cuts on the data in order to obtain the flux or the energy spectrum.

These source-dependent analyses make it sometimes hard to see if a source is stronger or more energetic than others. For this reason, the DB includes extra entries, common for all the flares, that are calculated using some of the original analysis values, described below, and allow the comparison between different flares because they have a common energy reference value. These calculated entries are:

- **Integral flux above 200 GeV**: In the analysis of every flare, the cut in reconstructed energy used to obtain the integral flux is different, indicated in the energy threshold entry. To permit a comparison between the source fluxes, we have chosen a common energy threshold, $E_{ref} = 200$ GeV, since it adapts well for weak and strong flares. Thus, all the integral fluxes has been re-calculated with respect to the new energy threshold. For the calculation, we assumed power-law spectrum whose parameters are also obtained from the analyses. The integral flux (provided by the individual analysis) for a power-law spectrum between the energy threshold E_1 and an upper limit E_2 is given by:

$$F(E_1 < E < E_2) = \int_{E_1}^{E_2} C_1 \, E^{-\Gamma} dE = \frac{C_1}{\Gamma - 1} \, (E_1^{-\Gamma+1} - E_2^{-\Gamma+1}). \tag{5.1}$$

  In the same way, the integral flux above our new energy threshold is

$$F(E > E_{ref}) = \int_{E_{ref}}^{\inf} C_2 \, E^{-\Gamma} dE = \frac{C_2}{\Gamma - 1} \, E_{ref}^{-\Gamma+1}. \tag{5.2}$$

  Assuming that the spectrum shape is preserved during the night, we have $C_1 = C_2$ and both cases are related

$$F(E > E_{ref}) = \frac{E_{ref}^{-\Gamma+1}}{E_1^{-\Gamma+1} - E_2^{-\Gamma+1}} \, F(E_1 < E < E_2), \tag{5.3}$$

DB entries in the Flare summary view	
Source	Name of the source.
Redshift	Distance of the source.
Year/Month	Year and month in which the flare was detected by MAGIC.
Initial day	First day in which the flare was detected by MAGIC.
Total observation time (h)	Elapsed time of observation of the source. It is the sum of the elapsed time of every day that the flare was detected.
Energy threshold (GeV)	Low energy limit for the integral flux calculation. It varies from one analysis to another.
Av. flux (cm^{-2} s^{-1})	Average integral flux above the energy threshold of the complete observation.
Max flux (cm^{-2} s^{-1})	Maximum value of the nightly integral flux above the energy threshold.
Av. Flux (>200 GeV, CU)	Averaged integral flux above an energy threshold of 200 GeV for the whole observation. Expressed in units of the Crab Nebula flux (CU) for the same energy threshold.
Av. Flux (>200 GeV, cm^{-2} s^{-1})	Averaged integral flux above an energy threshold of 200 GeV for the whole observation.
Total Sig. (FR/LE)	Significance for the whole flare in the Full Range (FR) and Low Energy (LE) ranges.
Av. Spec Index	Averaged assumed spectral index for the source spectrum before the atmosphere, after EBL absorption and before instrumental effects.
Analyzers	Names of the analyzers. DB information is taken from the first analysis unless some information is missing.
Analysis link	Link to the internal web page where the analysis is reported.
Paper link	Link to the published paper.
Alerts	Instruments that gave the alarm about the detected flare.
DB entries in the Nightly view	
Observation date	Indicates the night of observation.
Night obs. time	Elapsed time of observation in that night.
Energy threshold (GeV)	Low energy limit in the integral flux calculation.
Night Av. Flux(cm^{-2} s^{-1})	Integral flux above energy threshold during that night.
Night Av. Flux (>200 GeV, CU)	Nightly integral flux above an energy threshold of 200 GeV. Expressed in units of the Crab Nebula flux (CU) for the same energy threshold.
Night Av. Flux (>200 GeV, cm^{-2} s^{-1})	Nightly integral flux above an energy threshold of 200 GeV.
Sig.(FR)	Nightly observation significance in FE range.
Sig.(LE)	Nightly observation significance in LE range.
Spectral Index	Assumed spectral index for the source spectrum after EBL and before the atmosphere.

Table 5.1: Description of the DB entries for the two view options.

so that the common flux $F(E > E_{ref})$ can be calculated for every source. In the usual case that $E_2 = \infty$, Equation 5.3 is simplified to

$$F(E > E_{ref}) = \frac{E_{ref}^{-\Gamma+1}}{E_1^{-\Gamma+1}} F(E > E_1). \tag{5.4}$$

- **Mean integral flux**: This calculus uses the integral flux of every night of the flare and the elapsed time of observation of that night to produce an average integral flux for the complete flare with the formula:

$$F(E > E_f)_{mean} = \sum^{nights} \frac{F(E > E_f)_i \, t_i}{t_{total}}, \tag{5.5}$$

  where $F(E > E_f)_i$ is the integral flux above E_{ref} for the ith observation night and t_i is the elapsed time of that night. The energy threshold of the individual nightly fluxes as well as the the calculated average one is E_{ref}, such that these variables can also be used for comparison purposes. In some cases, the integral flux for the complete flare is provided directly by the analyzers and the database only requires to express it with respect to E_{ref} using Equation 5.3.

- **Mean Significance**: This calculation is needed when the analyzers did not compute the significance of the complete set of nights composing the flare. Most of the time it is provided, but if this is not the case, it is determined with the simplified formula:

$$S_{mean} = \frac{\sum^{nights} N_{ex}}{\sqrt{\sum^{nights} N_{OFF}}}, \tag{5.6}$$

  where N_{OFF} is the number of detected events in the OFF region for each night and N_{ex} is the number of excess event that night, calculated as $N_{ON} - N_{OFF}$.

5.2.3 DB functionalities

Apart from displaying information about the flares, the DB counts with other functionalities to ease the search and collection of the flare information by the user and to facilitate maintenance and addition of the newly detected flares by non-experts.

- **Saving:** The DB allows to save the table with the obtained results from a search in several formats as PDF, excel or CVS.
- **Ordering:** Every entry, represented as a column, can be ordered in increasing or decreasing order.
- **Searching:** A motor search allows to look for specific information among the displayed results.
- **References:** Every flare has a link to the analysis where the information has been extracted from and to the published paper, if available.
- **Addition and edition:** The database counts with a tool to edit the flares (in case of updates in the analyses) and to add new flares, that requires no knowledge about the DB technical internal details. These functionalities are limited for the administration and management of the DB contents. The access is restricted by a user and a password, integrated in the user management of the MAGIC data center and it is only accessible by a few users in the collaboration.

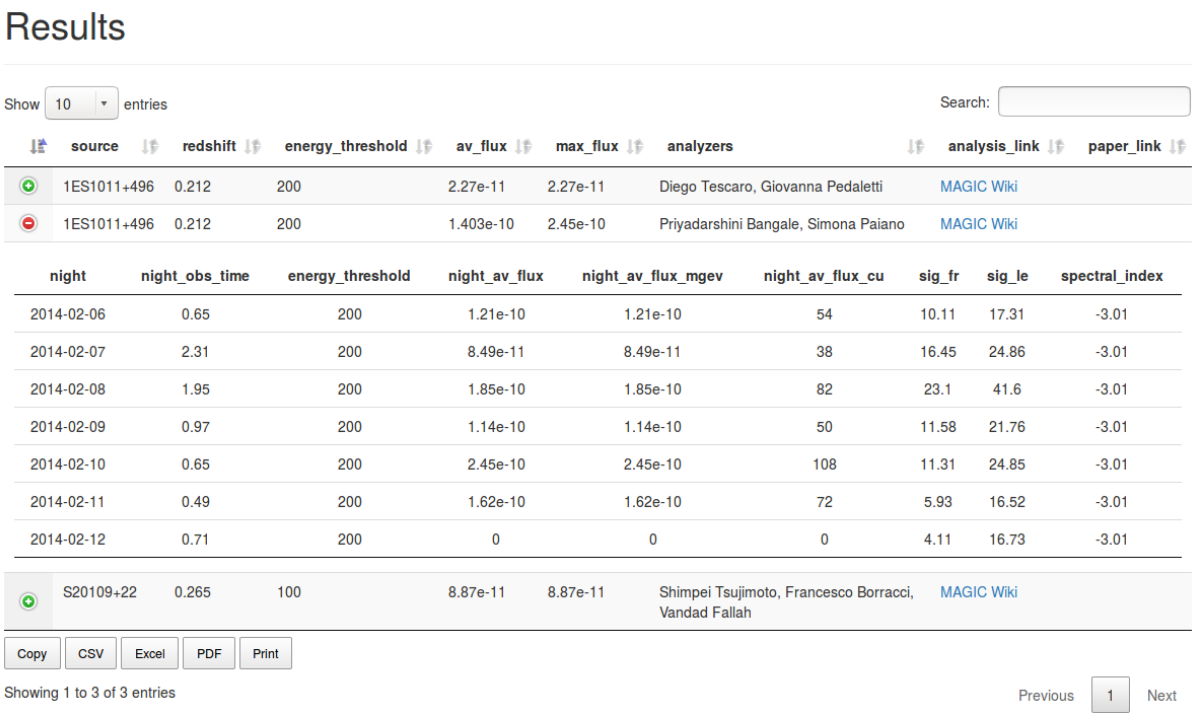

Figure 5.3: Graphical interface of the views offered by the DB.

5.2.4 DB Technical details

The author of this thesis provided the original idea of the DB, designed the different DB views and its corresponding entries, collected all the available information of the flares detected by MAGIC since 2005 and calculated the required DB entries using the analyses information.

On the other hand, all the technical implementation of the DB and the development of the functionalities was made by Jordi Delgado, the responsible of operation of the data center of the MAGIC telescopes, who agreed to collaborate with this project, motivated by the chance of introducing new components in the MAGIC data center services, generate new tools to manage data easily, make MAGIC data reusable and introduce new technical frameworks.

The DB is programmed following the Model-View-Controller (MVC) scheme (Figure 5.4). This modular design divides an application into three interconnected parts, to separate internal representations of information from the way that information is presented to the user. The three parts are:

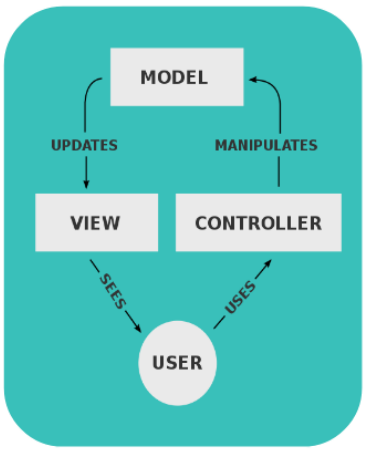

Figure 5.4: Scheme of the Model-View-Controller (MVC) design. Credit: Wikipedia.

1. **View:** It is the graphical interface that allows the visualization of the Model, that is, the information tables composing the DB, in an adequate format, such that the user can interact with it. When the user executes an action or a command, its consequences are shown by this interface.

2. **Model:** The Model is the representation of the DB information and controls the access to that information. It sends all the information that the user requires (through the Controller) to the View, in order to be displayed.

3. **Controller:** The Controller is a web engine that executes all the user commands like the selection of a flare based on a parameter cut, the edition of a flare or the addition of a new flare. The Controller manipulates the Model in order to apply the user requirements. Its changes are then visualized through the View.

For the development of the different components, there are several implementation levels that count with different frameworks for the parts mentioned above. The frameworks for each part are exposed in Figure 5.5.

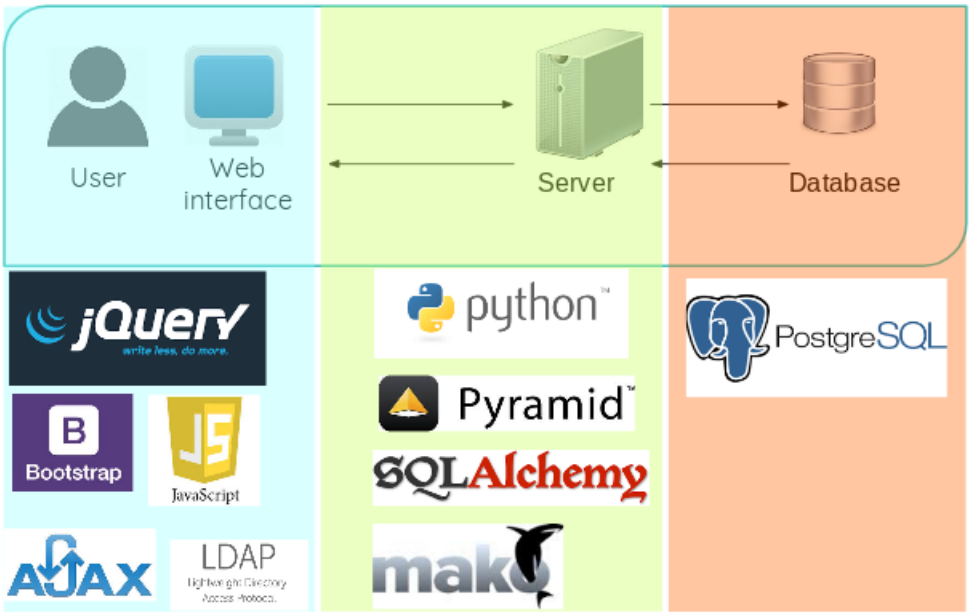

Figure 5.5: Schematic view of the different frameworks used the development the web interface, the server and the database. Credit: J.Delgado.

The AGN flare DB implementation follows the policies and rules of the rest of the MAGIC data center tools, in the sense that the management of the DB itself, the web portal and the backup organization follows the rest of the MAGIC DBs.

As a further improvement, the AGN Flares DB plans to be improved in the close future by including a direct link to the recommended version of the flare data, such that the users have direct access to the data in case they want to repeat the analysis.

5.2.5 LIV source selection

In order to select the best candidates to detect potential LIV effect, we use all the data collected in the data base and impose selection cuts over the values of some of the entries.

Firstly, in order to have enough number of events, we require an integral flux above 200 GeV greater than 1 CU. Twelve candidates fulfill this condition. Since this cut already entails the signal to have high significance and we are, in general, dealing with powerful flares, we do not apply any cut in significance.

Criteria for DB LIV source selection	
Conditions	**SB flares**
Int.Flux(>200 GeV) > 1CU	12
Int.Flux(>200 GeV) > 1CU, Spec.Index > -3	11
Int.Flux(>200 GeV) > 1CU, Spec.Index > -3 and date > 2009	9
Int.Flux(>200 GeV) > 2CU, Spec.Index > -3, date > 2009	3
Int.Flux(>200 GeV) > 2CU, Spec.Index > -3, date > 2009, Night Flux(>200 GeV) > 1CU	1

Table 5.2: Steps followed in the selection of DB flares to study LIV.

Apart from statistics, the flare must reach energies as high as possible, hence we are interested in spectra which are not too soft. For this reason, we ask the spectra to have a spectral index greater than -3. This new condition excludes only one candidate and we are left with 11.

Moreover, we are interested in stereo data since the energy resolution also has an impact on the sensitivity of LIV studies. Choosing flares detected before 2009, we discard two more candidates.

Since we still have a rather large amount of candidates, and the spectra cannot be used to discriminate further, we impose a stronger cut on the integral flux, requiring more than 2 CU. This removes most of the flare candidates, and we are left with three. One of them shows an integral flux slightly above 2 CU, while the remaining two show fluxes larger than 7 CU, being, by far, the strongest flares ever detected by MAGIC.

Since the flares last more than one night, as a last criterion, we impose a nightly flux large than 1 CU. Only one candidate survives this last cut: The flare of Mrk421 detected on April 2014. The characteristics of the source and the flare are introduced in the next two sections. Table 5.2 shows an overview of the source selection procedure.

5.3 Mrk 421

The blazar Mrk 421 is one of the most intense and therefore most studied sources in the TeV energy range. It was the first extragalactic object detected in the VHE band by the Whipple telescope [223], and the second source after the Crab Nebula. Mrk 421 is located in the northern hemisphere, at a redshift of 0.031($\approx$ 400 million light-years) and hosted inside the galaxy UGC 6132 (R.A. = 116.11 h, DEC. = 38.21 $^{\circ}$).

Mrk421 has been detected at all wavelengths across the electromagnetic spectrum $-$ from radio to VHE gamma rays $-$ and, together with Mrk501, is among the brightest TeV blazars known to date. In addition, it presents a relatively high flux even in quiescent state, fact that has triggered many multiwavelength campaigns to study correlations between the fluxes in different energy bands, variability studies and studies of the physics of the source. MAGIC has collaborated in MWL campaigns of Mrk 421 since 2009 up to today, with planned observations of the source every 2-3 days.

Mrk 421 is known as one of the fastest gamma-ray sources [258], showing significant flux variation on time scales of minutes, making it a natural candidate for LIV studies.

The mass of the black hole in the center of Mrk 421 has been estimated to be $(1.9\pm0.5)\times10^8$ $M_\odot$ by velocity dispersion measurements [317]. Due to the elliptical shape of its host galaxy, it has been claimed that it could be the result of the merging of two galaxies such that Mrk 421 could be powered by two black holes [318]. Analyzing historical data in the B and V bands, a periodicity of 1.36 years has been extracted,

that would correspond to a binary system of two black holes of masses 1.7×10^8 $M_\odot$ and $(0.49\text{-}2.9)\times10^7$ $M_\odot$ [319]. Such a periodicity has not been claimed in any other wavelength so far.

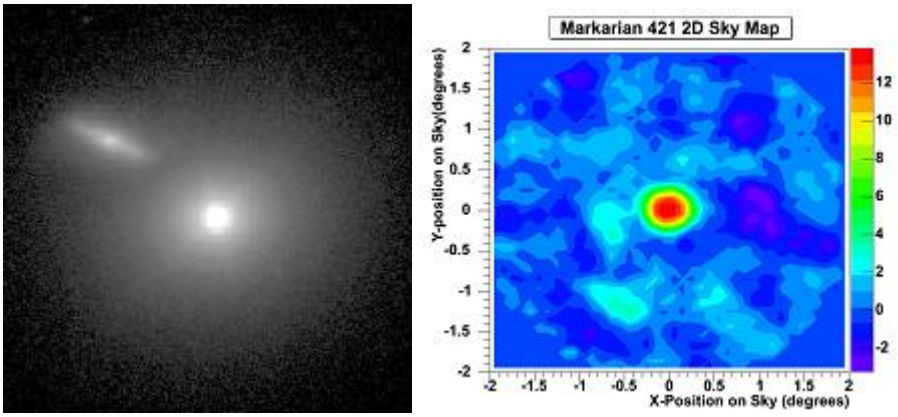

Figure 5.6: Image of Mrk 421 in different energy bands. Left plot: Mrk 421 in optical. Its companion galaxy Mrk 421-5 can also be seen. Right plot: Skymap of Mrk 421 obtained by the Whipple telescope [223].

5.4 The 2014 flare

The selected flare from the database was detected by MAGIC during a scheduled multiwavelength observation of Mrk421, that was extended due to the extreme flux obtained by the online analysis MOLA that reported a persistent flux of about 7 CU during more than half an hour. The next sections give details about the observation night of the flare, and the different data analyses.

Note that the dates stated in the analysis follow the "date of the morning after" convention of all MAGIC dates. Thus, the specified day is that of the morning after the observation. In addition, the hours and minutes specified are in UTC, that differs in 2h with respect the European time, during summer time.

5.4.1 Observations

The observation of Mrk421 during the night from 24 to 25 of April 2014 was scheduled from 22h25 to 22h55. At the end of the time slot, the online analysis showed a flux in the LE and HE ranges of about 6 CU, according to the log entries of the observers, such that the observation was extended. Half an hour later the flare reached its maximum intensity presenting a flux of 7 CU in the HE band. From that moment on, the flux decreased down to the 2 CU flux level until the end of the observation. The complete observation lasted around 3 hours and a half and was divided in 13 wobbles. Table 5.3 describes the development of the observation with several notes about the preliminary results from the MAGIC online analysis and annotations from the observers.

The complete flare observation took place during dark time, was performed in wobble mode and the zenith angle ranged from $10°$ to $50°$ (Figure 5.7). The trigger rates were inside their expected values, and the weather conditions were optimal, with no presence of clouds reported. Table 5.4 shows details of the observation conditions.

Mrk 421 Flare on 24 April 2014		
UTC time	**Observation**	**Notes**
22:25	Start	MW fixed-time observation
22:55	Extension due to high flux	HE flux above 6 CU
23:25	Maximum flux	HE flux around 7 CU. Alert to other IACTs sent out
00:49	Decrease of flux, 2h extension	HE flux around 2 CU
2:09	End	HE flux below 4 CU for 2h

Table 5.3: Development of the night observation during the flaring episode.

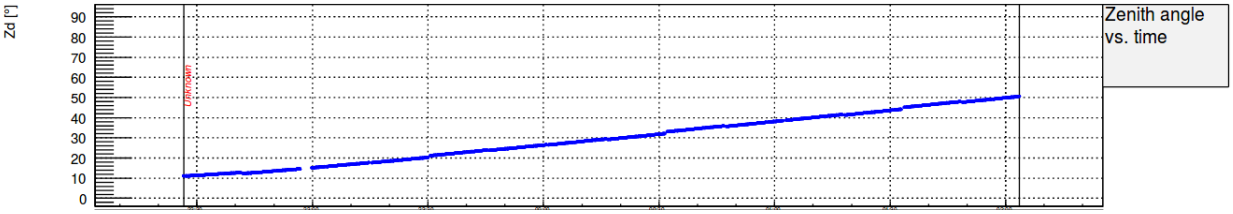

Figure 5.7: Zenith variation during the Mrk421 flare observation.

Trigger and weather conditions	
L1 trigger rate	15 kHz
L3 trigger rate	280 Hz
Zenith range	10-50
Temperature	11C°
Wind	13 km/h
Humidity	12%

Table 5.4: Weather conditions during the flare observation.

5.4.2 Data analysis

The flare data were analyzed using MARS, the MAGIC standard analysis package (see Chapter 4 for a general description of the analysis procedure and the analysis final products).

The original analysis was performed by Mireia Nievas, who provided the author with the high level analysis products, from where the relevant inputs for the study of LIV can be extracted. Since the low-level data reduction has not been part of this thesis, therefore, we will not go further into details, however, its detailed description can be found in [320], together with all the tests to validate that the analysis is correct, where the data of the flare is used to implement an study about the EBL absorption.

In this section and the next ones, we will skip the analysis products not relevant for the LIV analysis discussion, mentioning only the important results when opportune.

Original Analysis

During the entire flaring period the weather conditions were optimal, such that the analysis followed the standard MAGIC analysis pipeline, based on the stereo reconstruction and the gamma-hadron separation using the Random Forest (RF) algorithm [314]. The RF itself is trained with a sample of OFF data − taken close to the date of the flare data and in the same zenith range − and a set of MC simulated gamma-ray data, optimized for the telescope conditions at the moment the data taking of data to be analyzed.

In order to reconstruct the energy of the events, a LUT has been used, leading to an averaged energy

	Original analysis	RF analysis
ON events (E > 120 GeV)	11474	12520
OFF events (E > 120 GeV)	1109	4422
ON VHE events (E > 4 TeV)	122	47
Energy range (TeV)	0.12 - 50	0.12 - 30
Energy resolution at 1 TeV (%)	18	12

Table 5.5: Differences in number of events and energy ranges between the original and the RF analysis.

Event	Wobble (W)	ID inside W	Arrival time (s)	$E_{\rm rec}$ (GeV, LUT)	$E_{\rm rec}$ (GeV, RF)
1	14	148115	12927.28	51086.44	36783.72
2	14	125955	12808.95	40371.41	33589.35
3	13	99581	11742.52	37268.37	26384.10
4	14	75241	3302.79	31442.94	2182.11

Table 5.6: Difference in the reconstructed energy for four very energetic events of the flare data set.

resolution − obtained by Gaussian fits to the energy Migration Matrix − of ∼20 %.

Due the fact that a good energy resolution is crucial for LIV analysis, since the expected time-lag is proportional to the real energy of the events, and to make profit of the recently optimazed MAGIC RF tool for energy reconstruction, that has been proven to improve the energy resolution up to ∼10% for energies close to 1 TeV, a second data analysis has been developed to study the impact of the energy on this LIV study.

Analysis with Random Forest for energy reconstruction

The second data analysis developed for the thesis by the author does not differ from the original analysis, in the sense that it uses the same criteria and analysis cuts as the original analysis, but makes use of a RF instead of LUTs for the estimation of the energy of the events. One more difference is that the second analysis uses 3 OFF regions instead of 1 OFF region to estimate the background contribution. This change allows to enlarge the background statistics such that the background time and energy distributions can be reproduced more precisely.

The resulting energy resolution improves in this second analysis but reduces the reconstructed energy range of the data. Table 5.5 exposes these differences between the two analyses, focusing on the more important aspects for LIV, and Table 5.6 shows the difference in the estimated energy of four of the most energetic events in the data set. The plots in Figure 5.8 exhibit the time (Plot 5.8g for LUT and 5.8h for RF) and energy distributions (Plot 5.8e for LUT and 5.8f for RF) of the events, as well as the Instrument Response Functions (IRFs) (Plots 5.8a, 5.8c, 5.8b and 5.8d) obtained for both analyses.

An explanation for the low-energy cut for the events at 120 GeV is given in Section 5.5, the parametrization of the energy resolution for the ML analysis can be found in 5.6.3 while its impact on the sensitivity for such analysis is discussed in Section 5.7.2.

5.5 LIV analysis

To perform an analysis to extract any possible energy-dependent time-lag in data due to LIV, independently of the analysis method, it is necessary to extract from the data a photon list, which consists of the

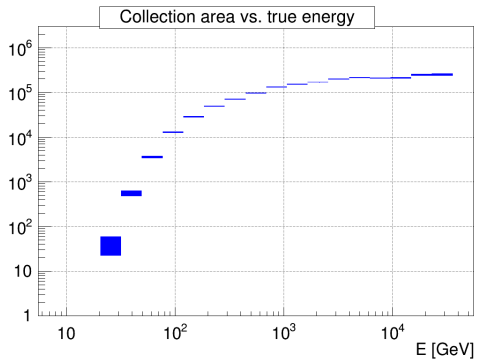

(a) LUT Collection area

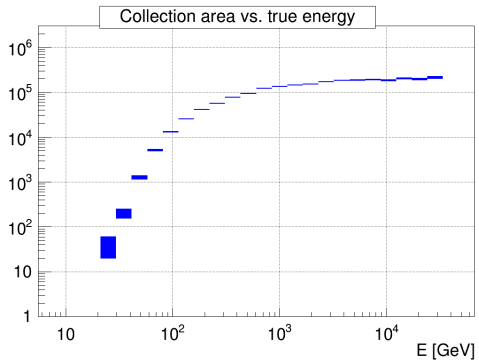

(b) RF Collection area

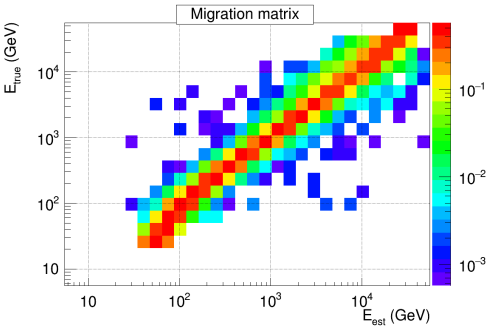

(c) LUT Migration matrix

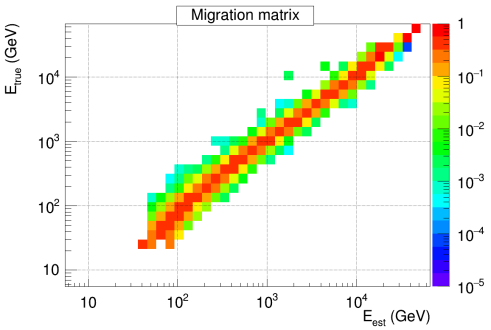

(d) RF Migration matrix

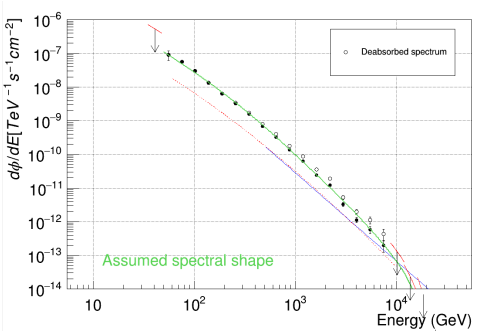

(e) LUT Energy spectrum

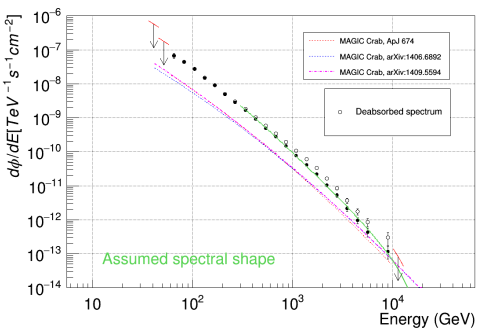

(f) RF Energy spectrum

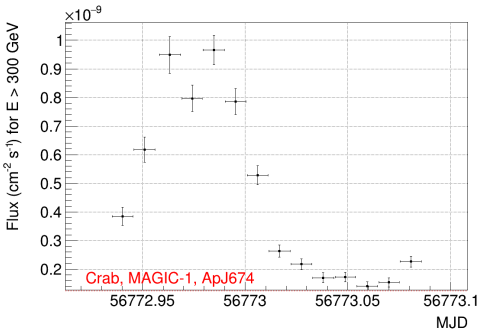

(g) LUT Lightcurve

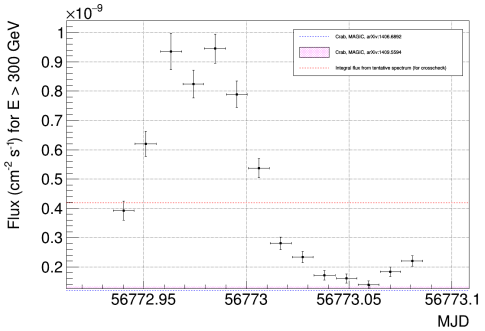

(h) RF Lightcurve

Figure 5.8: Comparison of analysis plots. Left side for the LUT energy reconstruction (From top to bottom: Collection area, energy migration matrix, energy spectral distribution and lightcurve. Right side presents the same plots for the RF energy reconstruction case.)

information of the reconstructed energy and the arrival time of every photon composing the data set.

This section presents two of the three analysis methods used in this thesis to extract any potential energy-dependent delay in the Mrk421 flare data: The PV and the SMM analyses. These method make use only of the photon list to study LIV.

For the more complex ML analysis, we need to describe the instrumental effects on the data and any other effect during photon propagation, as the EBL absorption. The additional ingredients needed for the LIV ML analysis and how to introduce them in the analysis are exposed in Section 5.6.

The final products of MARS are saved in ROOT files that contain histograms, arrays, functions and more complex data structures. To extract the photon list, a code in C++ has been developed by the author that uses the ROOT libraries.

This code extracts the arrival time and reconstructed energy of all events in the camera FoV and selects the events belonging to the ON and OFF observation regions by obtaining the source position from the data and performing a cut in θ^2 and in *hadronnes*. The values of such cuts are extracted from the MARS output file such that the events are the same ones used to compute high level analysis products as the lightcurve or the spectrum. The code is general and can be used to extract the events for any other type of analysis apart from LIV. Moreover, it can estimate the number of OFF events using the two different methods available for wobble mode observations: "Background from wobble partner" or "Simultaneous background" (the two methods are described in Appendix B) and can deal with any amount of OFF regions.

As an example, the energy distribution of the events obtained from the RF analysis is shown in Figure 5.9. In this case, the background is estimated using the "Simultaneous background" technique and the number of OFF regions is 3.

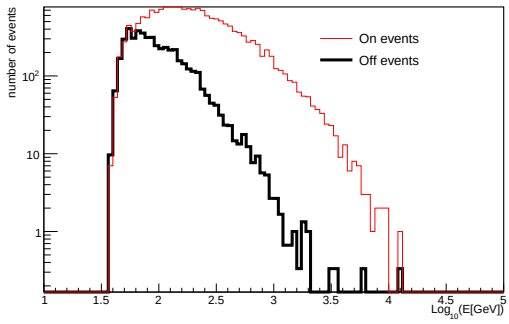

Figure 5.9: Energy distribution of the Mrk 421 2014 flare for RF analysis case.

Once the photon list is extracted, we should also choose an effective energy threshold, or lower cut on reconstructed energy, for the analysis[1]. From the LIV point of view, the lower energy cut should allow us to distinguish between gamma-ray events and hadronic events, such that a value around 100 GeV seems reasonable (see right plot of Figure 5.9), where the energy distributions of both populations start to differ. However, due to the zenith variation during the observation, the effective energy threshold requires a stronger cut, that affects greatly the number of available events, hence the statistical power of the LIV analysis. Therefore, we calculate carefully the effective energy threshold by using the MC simulated

[1] Although the standard energy threshold for MAGIC is $\sim$ 50 GeV, the impossibility to discriminate background events from images whose size is below a certain value, increases the effective energy threshold, that depends on the zenith and the background cuts applied in the data reduction.

Effective energy threshold	
Zenith range(°)	Energy Threshold (GeV)
5-35	68.8
35-50	110.2
5-50	71.8

Table 5.7: Analysis energy threshold estimated from MC simulated gamma-ray events.

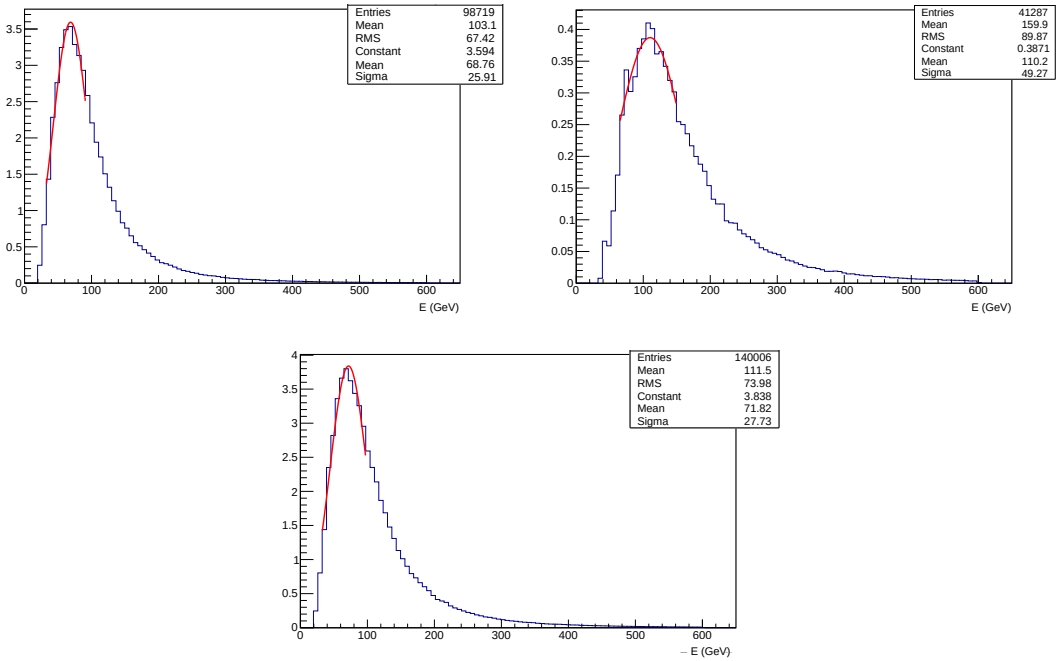

Figure 5.10: Effective energy threshold for different zenith ranges. From left to right and up to down: 5°-35°, 35°-50° and 5°-50°. A Gaussian fit has been made to the fit the data close to the peak and its mean used as estimator for the energy threshold.

gamma-ray sample, applying the analysis background rejection cuts and convoluting with the assumed spectrum (Figures 5.8e and 5.8f for the LUT and RF cases). The effective energy threshold is defined as the peak of the resulting distribution of simulated gamma-ray energies. The process has been repeated for the complete MC zenith range and after dividing the range in 5°-35° and 35°-50°. The resulting plots are shown in Figure 5.10 and the estimated energy threshold values in Table 5.7.

In order to be conservative, we decided to use a lower energy cut of 120 GeV and reject any event whose reconstructed energy is below that value for the LIV analysis. A new code is developed to cut the photon list according to this cut, convert the arrival time from MJD to seconds and bin the events in energy and time, in the later case in a custom histogram that respects the empty time gaps between wobbles, re-scaling the time of the events to the beginning of the first wobble time. The time bin size has been chosen to contain at least 10 events in the smallest bins in order to ensure that the Poissonian fluctuations in bin entries can be approximated by Gaussian fluctuations. Figure 5.11 shows the resulting time and energy histograms for the RF analysis case and for the ON and OFF regions, and Table 5.8 shows the time slots of the wobble periods. These gaps are not relevant for PV and SMM analyses that do not require to define an event time distribution, however they should be taken into account for the ML analysis (see Section 5.6).

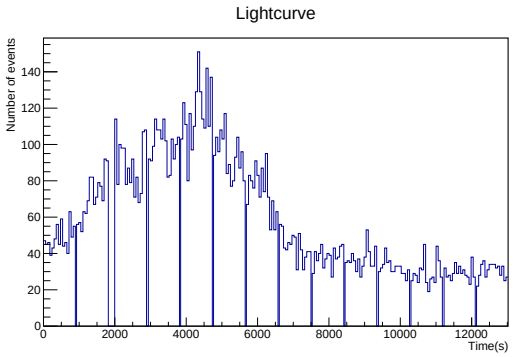

(a) Time distribution ON region

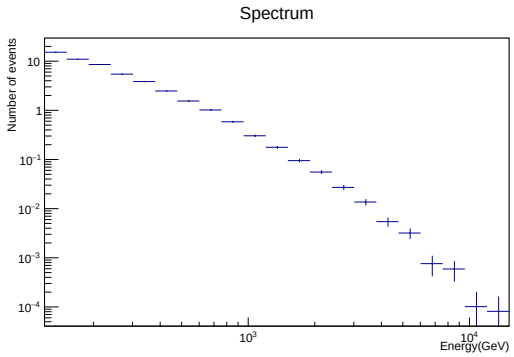

(b) Energy distribution ON region

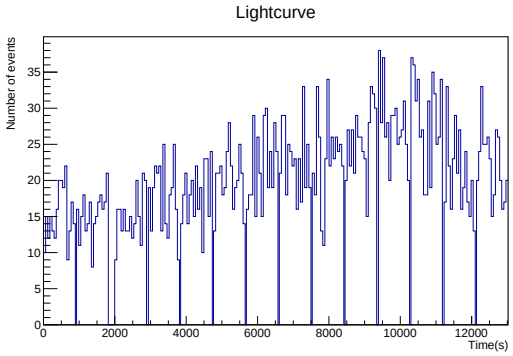

(c) Time distribution OFF region

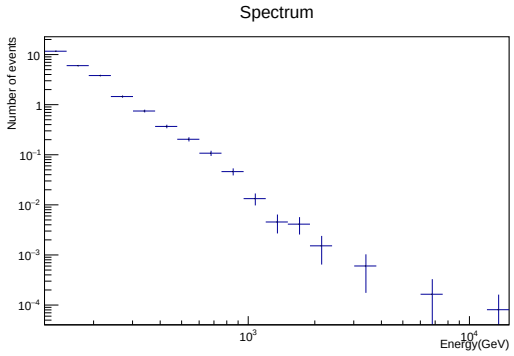

(d) Energy distribution OFF region

Figure 5.11: Time and energy event distributions in the ON (upper plots) and the OFF (bottom plots) camera regions, after applying the low energy cut.

Wobbles of the observation		
Wobble	Start time (s)	End time (s)
W1	0	893
W2	926	1816
W3	1996	2887
W4	2938	3811
W5	3844	4731
W6	4766	5653
W7	5686	6573
W8	6609	7496
W9	7531	8416
W10	8451	9338
W11	9387	10258
W12	10298	11178
W13	11226	12100
W14	12137	13020

Table 5.8: Time duration of the wobbles of the observation, re-scaled to the beggining of the first wobble.

5.5.1 Pair View analysis

For the extraction of the time-lag using PV analysis, we have developed a code that computes the ratio $l_{i>j(n)}$ (Equation 3.20) for every possible event pair in the photon list. The process is performed for the linear and quadratic cases.

Before applying the method on the data, we created 10^3 randomized data sets in order to define the CIs of the τ parameter. The sets are built by randomizing the energies and arrival times of the events in the ON region in order to remove any potential energy-dependent dispersion. We generated several hundreds of randomized sets in order to study the statistical uncertainties. Figure 5.12 shows the resulting distribution of $l_{i>j(n)}$ when applying the PV method to one randomized data set, for the linear and the quadratic case. From every of these analyses, we obtained a $\hat{\tau}$, defined as the maximum of such distribution (see section 3.6.1).

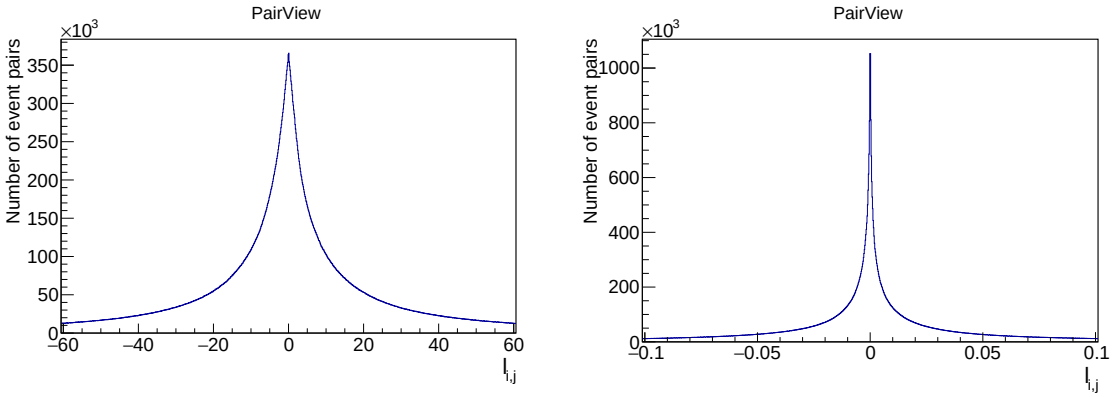

Figure 5.12: Resulting distribution of the parameter $l_{i>j(n)}$ of the PairView method to a randomized data set for the linear(left) and the quadratic (right) case.

The distribution of the $\hat{\tau}$ values obtained after applying the PV analysis to all the randomized data sets is normalized and used as PDFs of the τ error. Moreover, the quantiles of this distribution are computed in order to produce the lower and upper limits for the analysis result of the real data as indicated in Equation 3.24. The resulting error PDFs and their corresponding quantiles for one-sided 90% and two-sided 95% CL are shown in Figure 5.13, left side for the linear case and right side for the quadratic case.

Finally, the results of the application of the PV analysis over the data, its upper limits and the limits obtained in the QG energy scale are presented in Table 5.9.

PV analysis results		
	Linear case (s/GeV)	**Quadratic case (s/GeV^2)**
$\hat{\tau}$	-0.044	$3.460{\cdot}10^{-5}$
UL	0.041	$2.694{\cdot}10^{-4}$
LL	-0.121	$-3.196{\cdot}10^{-4}$
E_{QGsub} (GeV)	$3.285{\cdot}10^{17}$	$8.681{\cdot}10^{9}$
E_{QGsup} (GeV)	$1.117{\cdot}10^{17}$	$7.971{\cdot}10^{9}$

Table 5.9: QG scale results for the linear and quadratic case for the PV analysis.

The PV analysis gives average results with respect to previous analysis. While in the linear case, the results improve slightly the ones obtained with Mrk 501 flare in 2005, it stays one order of magnitude below the ones obtained in the quadratic case. However, the Mrk 501 results were obtained with ML

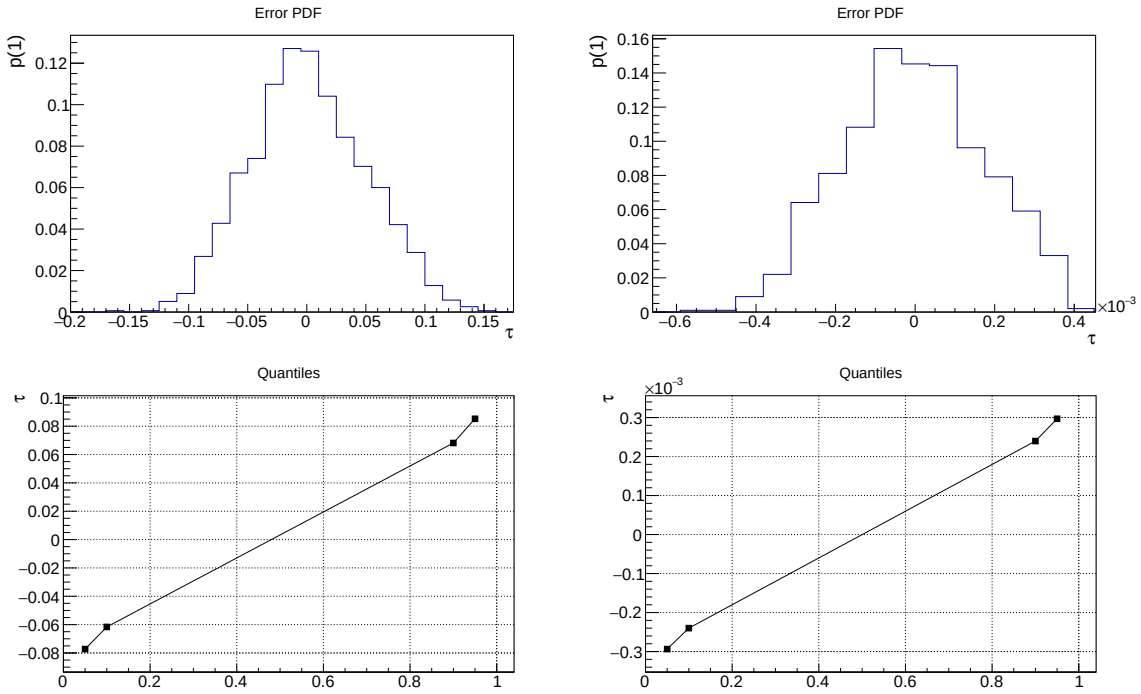

Figure 5.13: PDF of the errors and corresponding quantiles for the application of the PV analysis for the linear case (left plot) and the quadratic case (right plot). On the top, the normalized distribution of $\hat{\tau}$ after applying the PV analysis to 10^3 randomized data set, the bottom figure show the quantiles when integrating 5%, 10%, 90% and 95%of the above distributions.

analysis taking into account many other effects. As in other results obtained using the PV analysis [275], the limits on the QG scale are not very symmetrical, with a factor 3 difference in the linear case. The PV analysis also does not take into account the energy resolution, requires a binning of the result and maybe is a too simplistic analysis method for a complex flare as the one we are considering, hence it would require further analysis on its application and the effect on the considered assumptions.

5.5.2 SMM analysis

For the SMM analysis, exposed in Section 3.6.2, we produced 10^3 randomized data sets in the same way as for the PV analysis. Each of these sets is divided in two groups, LE and HE, trying to maximize difference in the mean energy between both groups while ensuring similar statistics. Table 5.10 summarizes the properties of such data groups, and Figure 5.14 shows the two groups time distributions, its CDFs and their comparison for one realization of the SMM analysis over a randomized set of data.

SMM analysis	
Energy cut (GeV)	250
LE events	6014
HE events	6504
LE mean energy (GeV)	175.2
HE mean energy (GeV)	664.4

Table 5.10: Characteristics of the HE and LE data sub-sets used for the SMM analysis.

In this analysis, we use α as LIV parameter, that is related to the τ parameter, used in the PV analysis,

as

$$\alpha = \frac{M_P}{M_{QG}} = \frac{M_P\,\tau}{l(z)H_0}, \tag{5.7}$$

that is the same parameter used for the ML analysis. From every application of the SMM analysis to a randomized data set, we obtained the value of $\hat{\alpha}$, that minimizes the Kolmogorov distance between the CDFs of the time distributions of the HE and LE event groups, as explained in section 3.6.2.

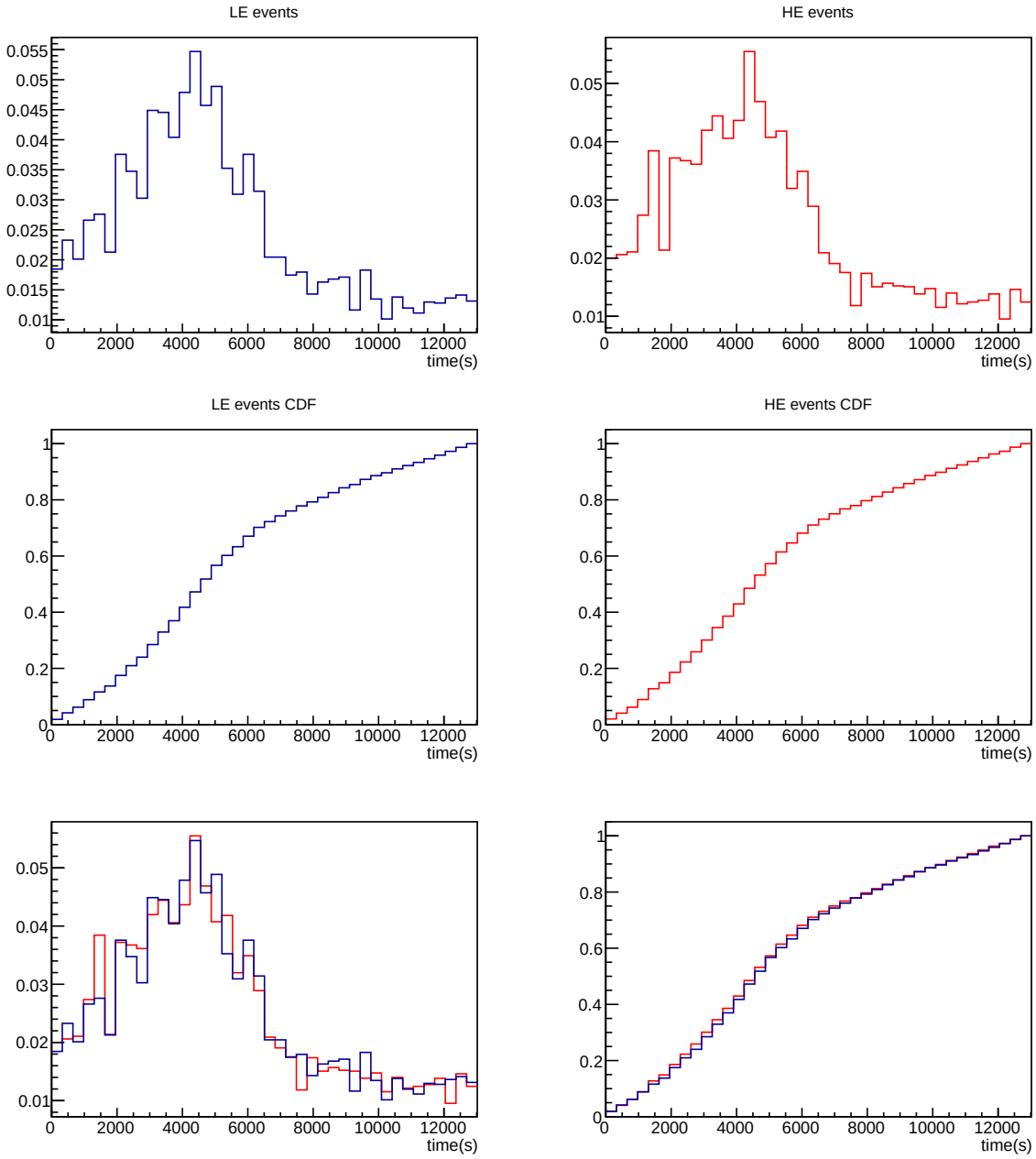

Figure 5.14: Resulting time distributions and CDFs of the two event (HE and LE) groups for the application of the SMM method to a randomized data set.

In order to compute the CI of the result once the analysis is applied to data, the distribution of $\hat{\alpha}$ obtained after the application of the SMM analysis to all the randomized data sets is normalized and the 0.5, 0.1, 0.9 and 0.95 quantiles are calculated in order to compute one-sided 90% CL and side-sided 95% CL, as in the PV case. Figure 5.15 shows such distribution and its quantiles for the linear and quadratic

case. The final results of applying the SMM analysis over the data are collected in Table 5.11.

SMM analysis results		
	Linear case	**Quadratic case**
$\hat{\alpha}$	883.000	1.280
UL	1166.517	1.468
LL	644.483	1.131
E_{QGsub} (GeV)	$1.029 \cdot 10^{16}$	$1.107 \cdot 10^{11}$
E_{QGsup} (GeV)	$1.861 \cdot 10^{16}$	$1.262 \cdot 10^{11}$

Table 5.11: QG scale results for the linear and quadratic case for the SMM analysis.

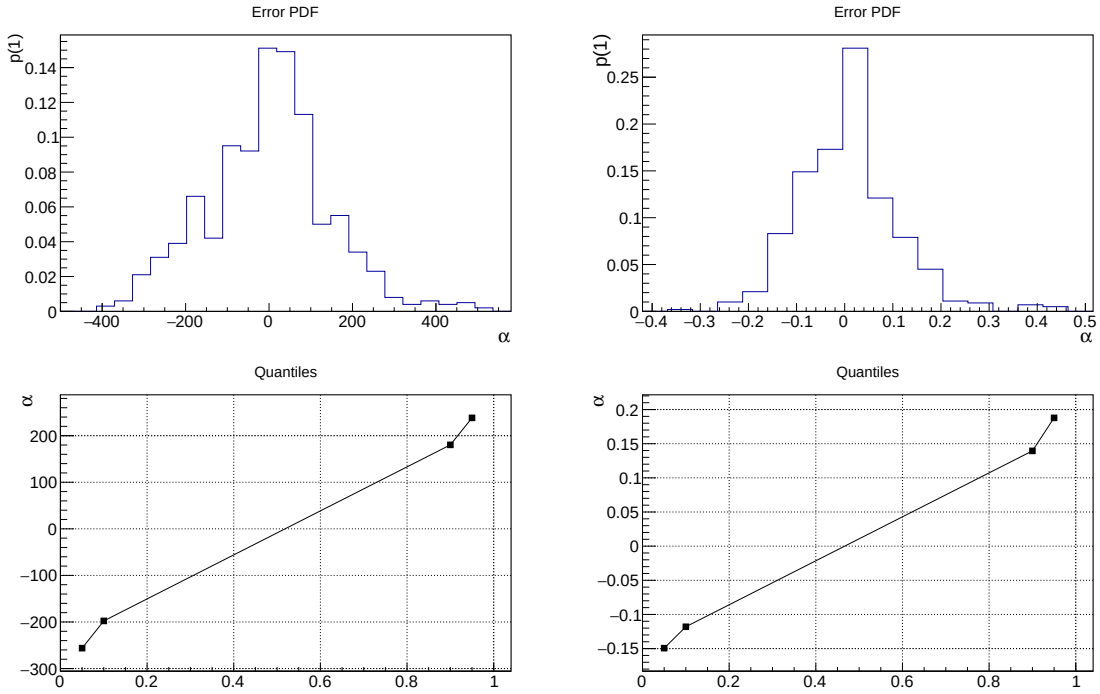

Figure 5.15: PDF of the errors and corresponding quantiles for the application of the SMM analysis for the linear case (left plot) and the quadratic case (right plot).

One can see that the SMM analysis gives worse results for the linear case, that do not reach the ones obtained for the Mrk 501 flare. However, due to the amount of events and the large energy range that allow a difference in the average energy between the LE and the HE groups of more than 500 GeV, the limit in the quadratic case are among the best ones obtained up to date with GRBs (see Figure 3.4). This analysis deals better with the fact that the energy resolution is not perfect but presents some problems with burst asymmetry and requires a binning of the data for the analysis. For this reason, we consider the results more robust than the ones obtained by PV analysis but we prefer the use of the Likelihood analysis for the final results, due to the amount of information that can be used and its better performance for complex time structures.

5.6 Maximum Likelihood analysis

The Likelihood function is the product of the PDFs of each event in the data set, considered independent from one another. Such PDFs indicate the probability of detecting an event of measured energy E and measured time t and are calculated with the expected time and energy distributions of the events in the data set as well as all effects altering such distributions. The LIV effect is described through a parameter (see Section 3.6.3) called α, that is related to the QG energy scale, for the linear and quadratic cases, as

$$\alpha(n=1) = \frac{M_P}{E_{QG1}} \quad \alpha(n=2) = \frac{3}{2}\frac{M_P}{E^2_{QG2}}, \tag{5.8}$$

such that the expected LIV time-lag can be generally described as

$$\Delta t_n = \xi \frac{z}{H_0}\frac{\Delta E^n_s}{M_P} \cdot \alpha, \tag{5.9}$$

where $n = 1, 2$ corresponds to the linear and quadratic cases, respectively. The parameter ξ has a positive (negative) unity value for the subliminal (superluminal) scenario.

The final PDF of a specific event is a normalized combination of its PDF as a gamma-ray event and its PDF as a background event, as provided by Equation 3.31. The normalizations of the signal and background PDFs (N_b and $N_\gamma(\alpha)$) are extracted by integrating these PDFs in the chosen range of reconstructed energies $[E_{min}, E_{max}]$ and reconstructed times $[t_{min}, t_{max}]$, shown in Section 5.6.1.

The background events are not considered to be affected by LIV, such that the background PDF can be directly defined as:

$$\frac{dP}{dEdt}_b = \Gamma(E) \cdot F(t), \tag{5.10}$$

where $\Gamma(E)$ is the measured spectral energy distribution of the OFF regions and $F(t)$ its lightcurve. Most LIV analyses [273, 270] consider $F(t)$ a flat distribution, however in our data set the amount of background increases towards the end of the observation, due to the zenith variation during the observation of the Mrk 421 flare. This information is contained in $F(t)$, whose parametrization follows the same methods used for the ON data time parametrization. Such methods are exposed in Section 5.7.

The PDF for the gamma-ray events is the one defined by Equation 3.29 with a couple of extra components:

$$\frac{dP}{dEdt} = \int_0^\infty \Gamma(E_s)C(E_s,t)G(E-E_s,\sigma_E(E_s))T(E_s,z)F(t-D(E_s,\alpha,z))W(t)dE_s. \tag{5.11}$$

$T(E_s, t)$ indicates the EBL transmission effect as a function of the true energy of the event and the source distance. If affects the observed energy distribution of the events. Even though Mrk421 is a close-by source (z=0.031), this effect must be taken into account since we reach energies of several tens of TeV. $W(t)$ contains the information of the wobble gaps, despite it does not affect the PDF value of the events, it should be taken into account when computing the normalization. In this chapter, we will use E when referring to the reconstructed energy of the events and E_s for the their unknown true energy.

The next sections describe the ingredients that compose the gamma-ray PDF − with the exception of the lightcurve − and their parametrization for the analysis. The parts of the background PDF are detailed in Section 5.6.6. The time template parametrization, due to its complexity, is explained in a separate section (Section 5.7).

Likelihood analysis	
Energy range (LUT/RF)(GeV)	120 - 30000/ 120 - 50000
Time range (s)	0 - 13020

Table 5.12: Time and reconstructed energy ranges for the ML analysis. LUT refers to the analysis with worse energy resolution based on LUTs, whereas RF denotes the energy reconstruction with improved resolution.

5.6.1 Time and energy range

In the case of the observation of Mrk421 in 2014, the flare is mostly contained inside the observation window with an appreciable gamma-ray baseline (Figure 5.11a) at the end of the observation. Due to the large time-lag expected for the most energetic events of the sample, we decided to directly take the complete observation window to correctly parametrize the flare − whose position is expected to be shifted as a function of energy due to LIV − and the baseline with the largest amount of data available. The presence of 30 TeV events, which may suffer a serious time lag for the LIV scenarios investigated here, forces us to parametrize the time template also outside of the observation window. The procedure followed for that extrapolation are shown in Section 5.7.

For the reconstructed energy range and since LIV is directly proportional to energy or its square, we use a lower cut in reconstructed energy at the energy threshold (120 GeV) while preserving all the most energetic events.

The time and energy ranges for the ML analysis are summarized in Table 5.12.

5.6.2 Collection area

The collection area ($C(E_s, t)$ in Equation 5.11) indicates the acceptance of the instrument as a function of the true energy of events and its changes with time. The collection area is computed as part of the MARS analysis pipeline using MC simulations (see Section 4.5.7), so that it can be directly extracted from the analysis output. We consider here the collection area constant in time and convolute it with the intrinsic spectrum (see Section 5.6.4) and the EBL effect in order to lead to the reconstructed energy PDF. The resulting collection areas for the LUT and RF analyses are shown in Figures 5.8a and 5.8b, respectively.

5.6.3 Energy resolution and bias

The instrumental effects on the reconstruction of the energy of events, introduced in the ML analysis with the function $G(E - E_s, \sigma(Es))$, see Equation 5.11, show the probability of deviations of the reconstructed energy from the true energy of events. Such deviations are studied in the MARS analysis pipeline by comparing the reconstructed and the true energy of simulated MC gamma-ray events. This code produces the energy Migration Matrix (shown for the LUT and the RF analyses in Figures 5.8c and 5.8d, respectively), which can be directly extracted from the analysis output and parametrized to describe the function $G(E - E_s, \sigma(Es))$. This experimental effect can be parametrized by the so-called energy bias, which accounts for the mean difference between the true and the reconstructed energy value, and the energy resolution, which accounts for the dispersion of the reconstructed energies of events of a same true energy around its mean value. Both parameters can be obtained from the distribution of the quantity $\Delta E/E$, computed for every MC simulated gamma-ray event, where ΔE is the difference between true and the reconstructed energy of the events, while E is its reconstructed energy.

In the case of the ML analysis, $\Delta E/E$ must be obtained as a function of the true energy E_s, in order to apply it to the simulated events produced to test our ML analysis' sensitivity. The reconstructed energy of each simulated event is then obtained from the probability distribution of the reconstructed energies at the simulated true energy. This distribution can be parametrized with a single Gaussian or a more complex function, as we explain below. The simulation details are explained in Section 5.6.8.

On the other hand, the PDFs that compose the Likelihood function, predict the probability to originate from a true energy of an event as a function of its reconstructed energy E. Therefore, in order to evaluate all the possible E_s of a specific event, we must also know the parametrization of the energy bias and resolution as a function of E.

The distribution $\Delta E/E$ is obtained from the MARS output as 2-dimensional histograms, one depending on E and another on E_s (see Figure 5.16). A possible way to parametrize $\Delta E/E$ is by fitting a Gaussian to every energy bin (from the projection of the histogram for every E and E_s bin), as shown in the left plot of Figure 5.17. However, the Gaussian does not fit well the distribution due to tails at both sides. These tails are known features in the energy reconstruction of IACTs. Their impact seems to be reduced when converting the energies to the logarithm of energy, but the quality of the fit does not improve in a significant way. However, by fitting a double Gaussian, the fit quality becomes much better since, one of the Gaussians can fit the main peak with a smaller width and the second one takes care of the tails adopting a bigger width with a smaller amplitude.

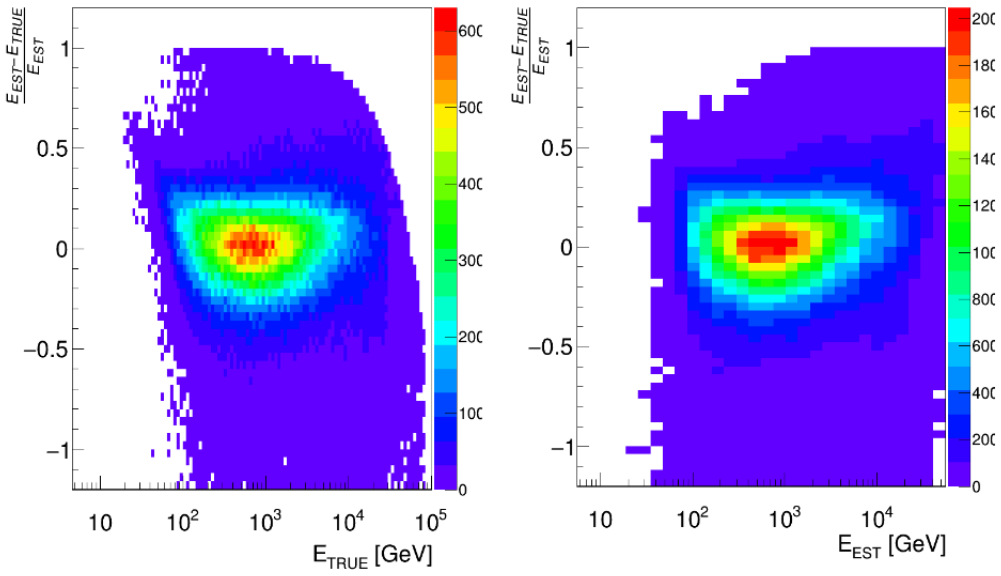

Figure 5.16: Energy migration as a function of the true energy of the MC simulated events (left) and as a function of their reconstructed energy (right).

The impact of using single of double Gaussians to describe the energy migration has been analyzed for the RF and the LUT analyses, and both show similar improvements when describing the effect with two Gaussians. The parameters of the single and double Gaussian fits for both analyses and for $E_s \sim 1$TeV are shown in Table 5.13, while a graphical example of a fit in linear energy scale for one and two Gaussians and in logarithm scale for one Gaussian is shown in Figure 5.17 for the RF case. Moreover, an example of the $G(E - E_s, \sigma(Es))$ shape for an event of 1 TeV energy, using one or two Gaussian parameterization can be seen in Figure 5.21b.

Energy resolution at 1 TeV				
Parametrization	LUT analysis		RF analysis	
	σ_1	σ_2	σ_1	σ_2
1 Gaussian	0.18	-	0.13	-
2 Gaussians	0.13	0.21	0.11	0.19

Table 5.13: Energy migration parameters at 1 TeV energy for different parametrizations of the instrumental effect.

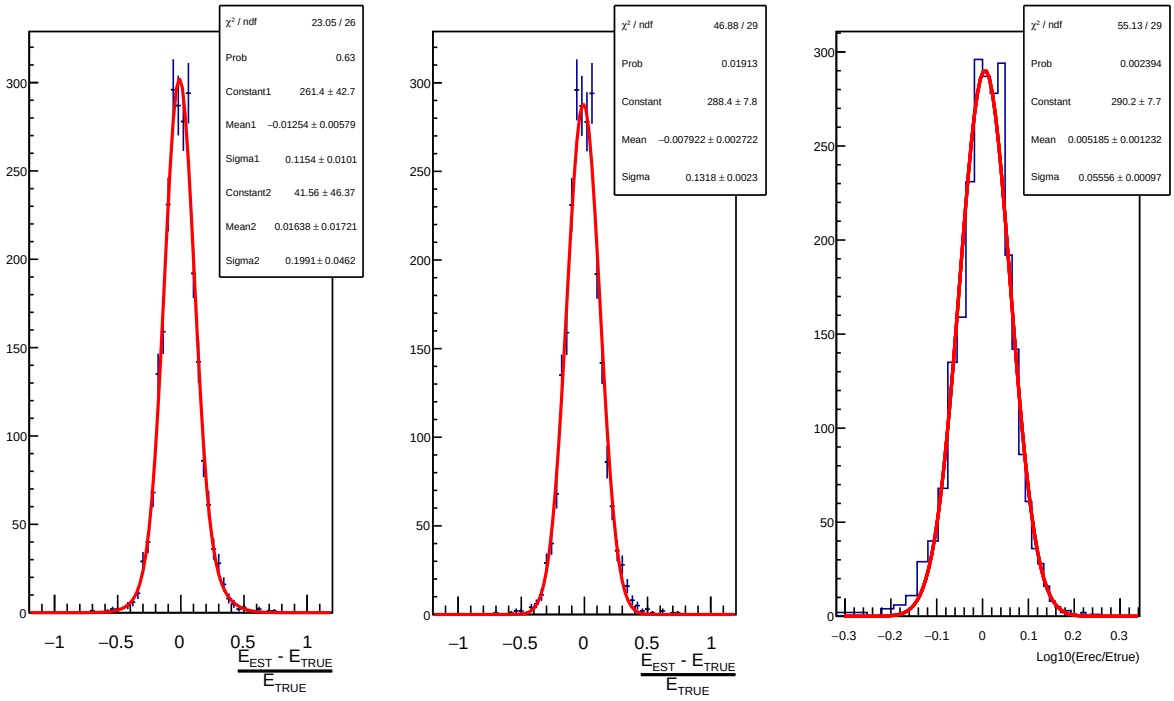

Figure 5.17: Fit results in linear energy using two Gaussian (left), one Gaussian (center), and fit in logarithmic energy to a single Gaussian (right). One can see that the χ^2 of the fit square of the fit improves greatly when applying a double Gauss fit in comparison with the other two cases.

5.6.4 Energy spectrum

The energy distribution is obtained differently for the signal and background, since LIV is assumed to affect only gamma-ray events from the source.

For gamma-ray events, we need to estimate the intrinsic spectrum with the use of a forward-unfolding algorithm (see Section 4.5.8) of the measured spectrum, such that we take into account the instrumental effects and the EBL absorption during propagation. The estimated intrinsic spectrum after the unfolding procedure can be obtained directly from the analysis output. In the case of the Mrk421 2014 flare, the intrinsic spectrum can be described by a log parabola,

$$\Gamma(E_s) = c \left(\frac{E_s}{E_0}\right)^{\Gamma - \beta^2 \cdot \log_{10}(E_s/E_0)}, \tag{5.12}$$

whose parameters, for the LUT and RF cases, are listed in Table 5.14. The intrinsic energy distribution obtained from the RF analysis is shown in Figure 5.18.

For the hadronic events, we take directly the measured energy spectrum and use it to compose the PDF of the background events. Since we are working with measured energy, there is no need for the

Parameters	LUT analysis	RF analysis
E_0 (GeV)	364	367
c	$1.4^{+0.025}_{-0.024} \cdot 10^{-9}$	$1.3^{+0.024}_{-0.024} \cdot 10^{-9}$
Γ	$-2.5^{+0.015}_{-0.015}$	$-2.5^{+0.015}_{-0.015}$
β	$0.57^{+0.027}_{-0.026}$	$0.56^{+0.024}_{-0.025}$
χ^2/NDF	$36/22$	$17/20$

Table 5.14: Parameters of the log parabola assumed as intrinsic spectrum for the Mrk421 2014 flare.

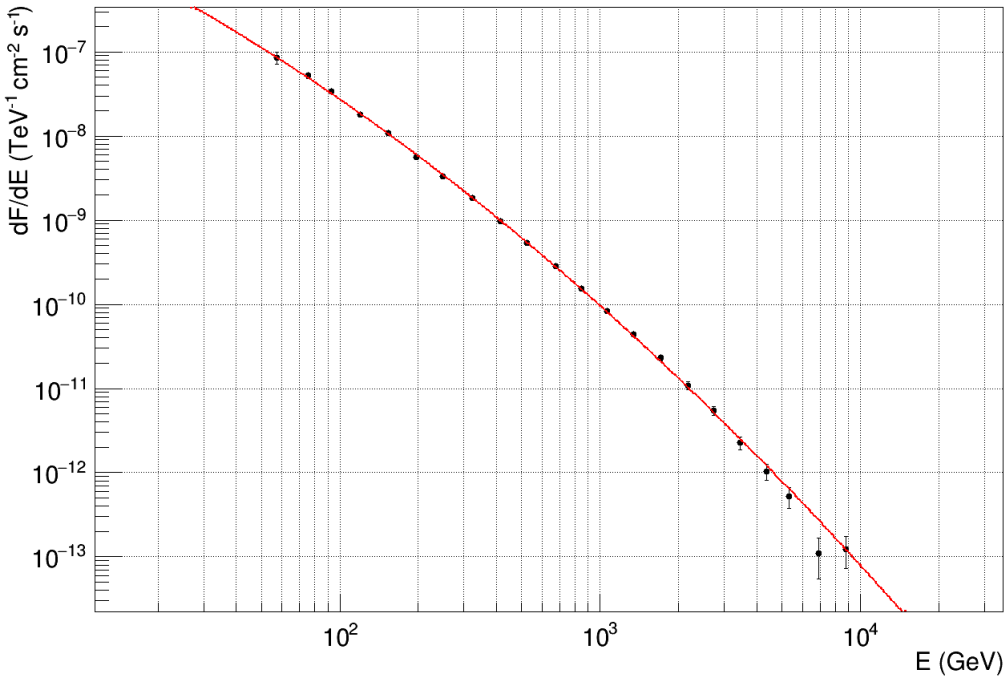

Figure 5.18: Intrinsic spectrum after forward-unfolding for the Mrk 421 2014 flare.

integral over E_s indicated in Equation 3.29. The energy distribution of the hadronic events for the RF analysis is shown in Figure 5.19.

5.6.5 EBL absorption

The effect of the EBL absorption ($T(E_s, z)$ in Equation 5.11) can be obtained from tables from published analyses that indicate the gamma-ray transmission as a function of redshift and the true energy. By using this table for the specific redshift of the source, we obtain the transmission as a function of the true energy, that can be applied directly to the intrinsic spectrum in the PDF. The transmission value, using the Dominguez EBL model [220], as a function of the true energy for the redshift of Mrk421 is shown in Figure 5.20.

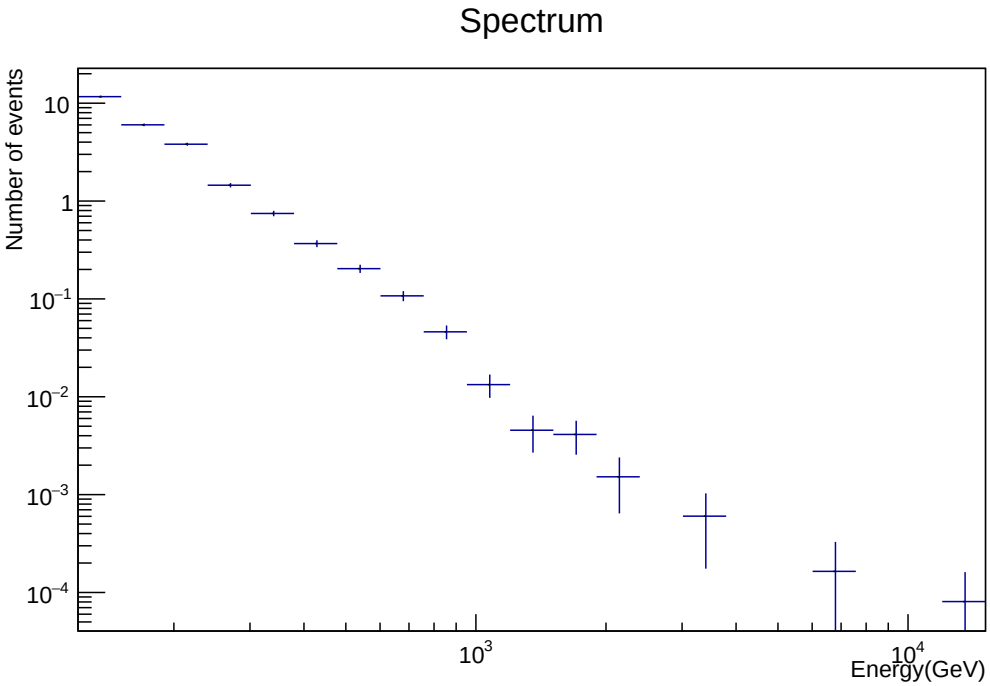

Figure 5.19: Measured energy distribution of the hadronic events in the OFF region for the RF analysis case.

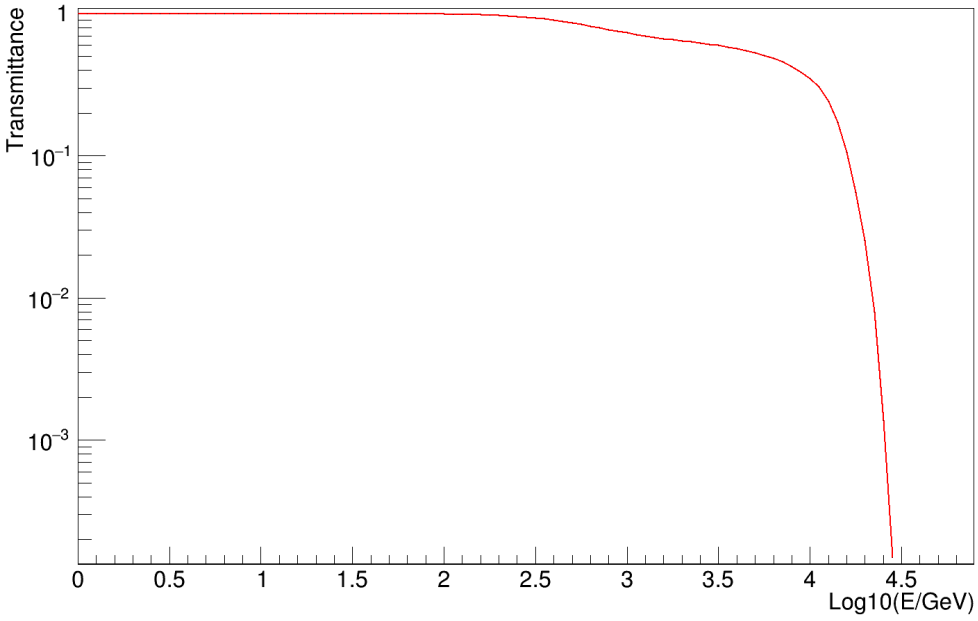

Figure 5.20: EBL transmission effect as a function of energy for Mrk421 redshift.

5.6.6 Background events

The background events' measured energies and arrival times are taken directly from the high-level products of the MARS analysis. Even though they are not directly used in the ML analysis, they allow us to estimate the energy and time distribution of the background events contained in the ON region, used to construct the background events PDF (Equation 5.10), and the proportion between gamma rays and background in that region.

For this reason, the RF analysis that uses three OFF regions to estimate the background, increases the statistics and allows for a better determination of those distributions, even though the resulting templates must be re-scaled to preserve the signal-to-background ratio correctly.

In the background PDF of Equation 5.10, as hadronic energy template, we use the linear interpolation of the binned distribution of the reconstructed energies of the events (Figure 5.19). We do not need to extract the intrinsic spectrum through an unfolding procedure since we expect no LIV effect on hadrons. For the time distribution, we apply the same method as used for the time parametrization of the signal time template (Section 5.7) to account for the zenith effect.

5.6.7 Light curve

The definition of a template ($F(t)$ in Equation 5.11) for the flare time-dependent emission is one of the key parts of this ML analysis. LIV effects are expected to shift the function by a different amount for every event energy (factor $D(E_s, \alpha, z)$ in Equation 5.11). Up to now, most ML analyses have defined such a template by using a function fitted to the binned time distribution of the ON events [270, 273, 269, 289] in some cases considering only events of the lowest energies to minimize the possible impact of LIV on the template. The Mrk421 flare is the longest (>3h) flare used to study LIV up to date and it seems to present variability on smaller times scales. Additionally, the number of events is so high, that the time gaps between the observation wobbles have a serious impact on the results and need to be taken into account in the template definition, since they are an instrumental effect while the template defines the emission at the source. For these reasons, the definition of a time template for this flare has supposed several challenges. Section 5.7 describes in detail the methods used to resolve these and the resulting time templates introduction in the ML analysis.

5.6.8 Simulations for Likelihood

In order to test the performance of the analysis before its application to real data, we produce simulated data sets that share as many aspects as possible with the real data and are produced using the same templates as the ones that are later used in the ML analysis.

The simulation code generates simulated events at the source, with their intrinsic time and energy distributions and apply the different propagation and instrumental effects on the simulated events, to obtain the measured time and energy distributions. Also the total number of events follows the ones of the real data.

In order the simulate the energy distribution, we take the intrinsic energy spectrum provided by the forward unfolding and convolute it with the collection area and the EBL transmission, as indicated in Figure 5.21a. The resulting template is used to simulate the true energy of the events that is smeared later using the corresponding energy dispersion, defined as a Gaussian or a double Gaussian. Both options are exemplified in Figure 5.21b for a 1 TeV event. An example of the simulated energy distribution, compared with the real data energy distribution is shown in Figure 5.22a.

On the other hand, for the different complex time templates, explained in the next section, we do not need to apply instrumental effects because the MAGIC time resolution is orders of magnitude better than any possible LIV effects searched in this work. Instead, we introduce a possible LIV time-lag in order to see if the ML code is able to reconstruct it correctly. The lag is added to the event time after its simulation. For the time simulation, we use the MC technique called "hit-or-miss" [321], which generates

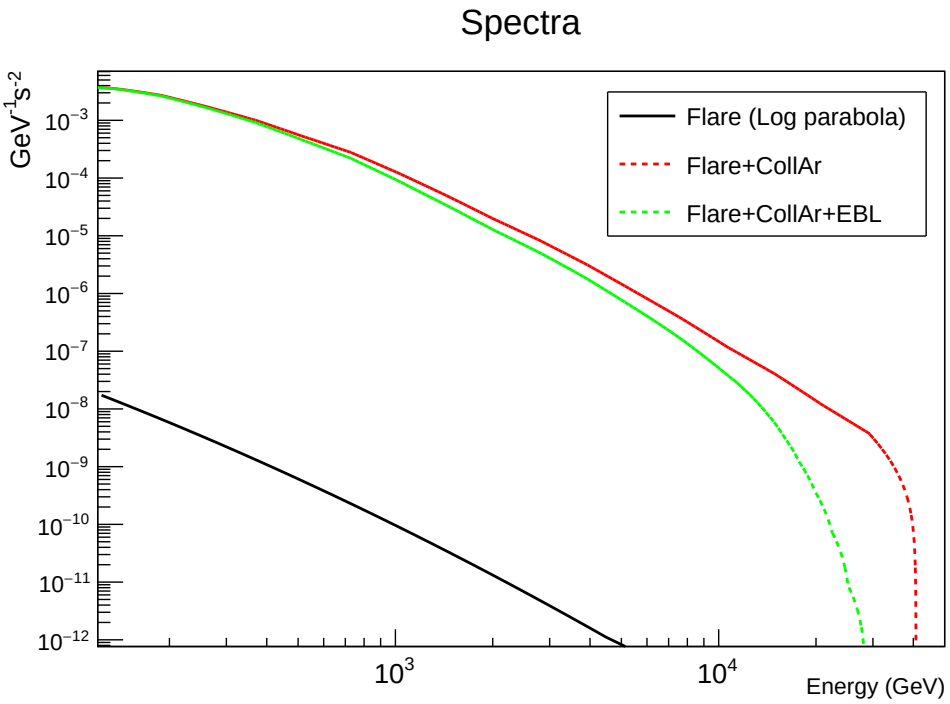

(a) Intrinsic spectrum convoluted with the MAGIC collection area and the EBL transmittance for redshift z=0.031. The intrinsic spectrum, expressed in GeV^{-1} m^{-2}s^{-1}, is also shown for comparison purposes. The black line shows the intrinsic spectrum. The red dotted line shown the convolution of the intrinsic spectrum and the collection area. The green dotted line shows the convolution of the latter with the EBL absorption effect.

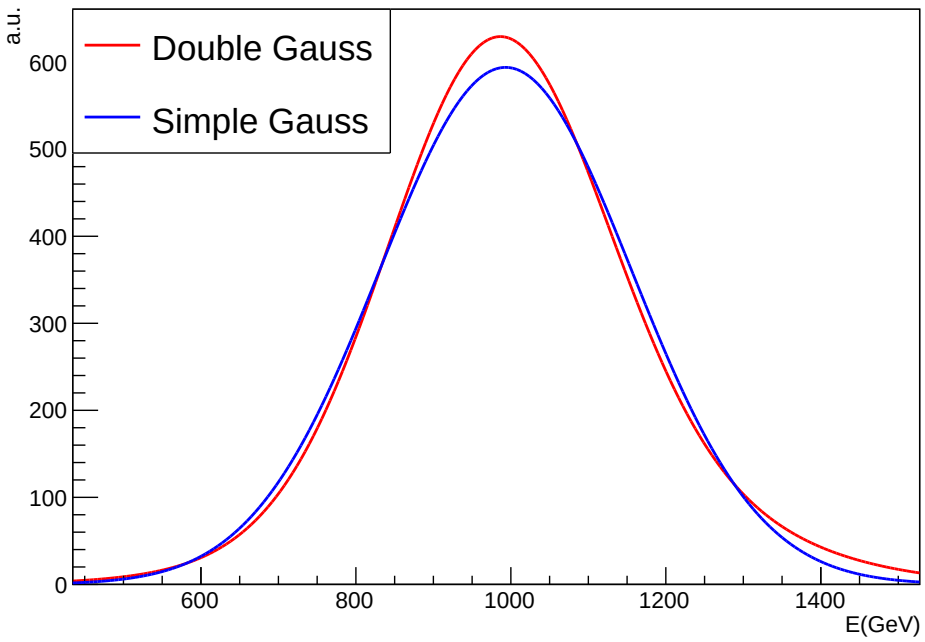

(b) Energy dispersion PDF for a 1 TeV event, modelled with one or two Gaussian functions.

Figure 5.21: Instrumental and physical effects applied to the simulated energy distribution.

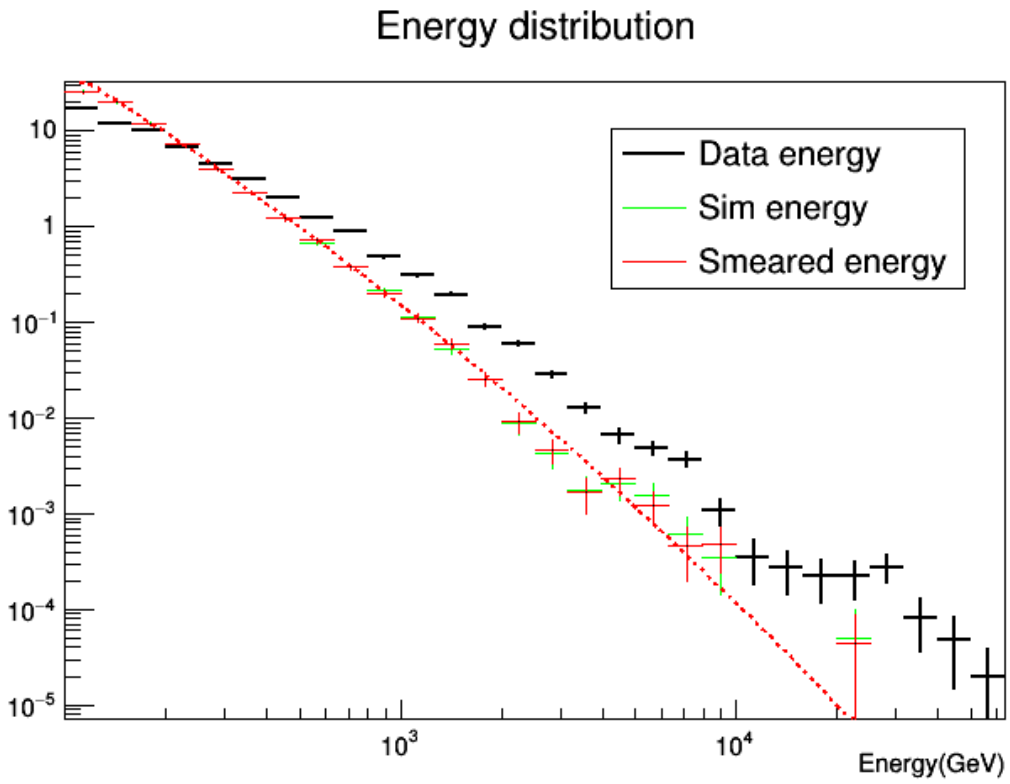

(a) Simulated true and reconstructed energy distributions, before and after applying the effect of energy dispersion, compared with the reconstructed energy distribution from real data.

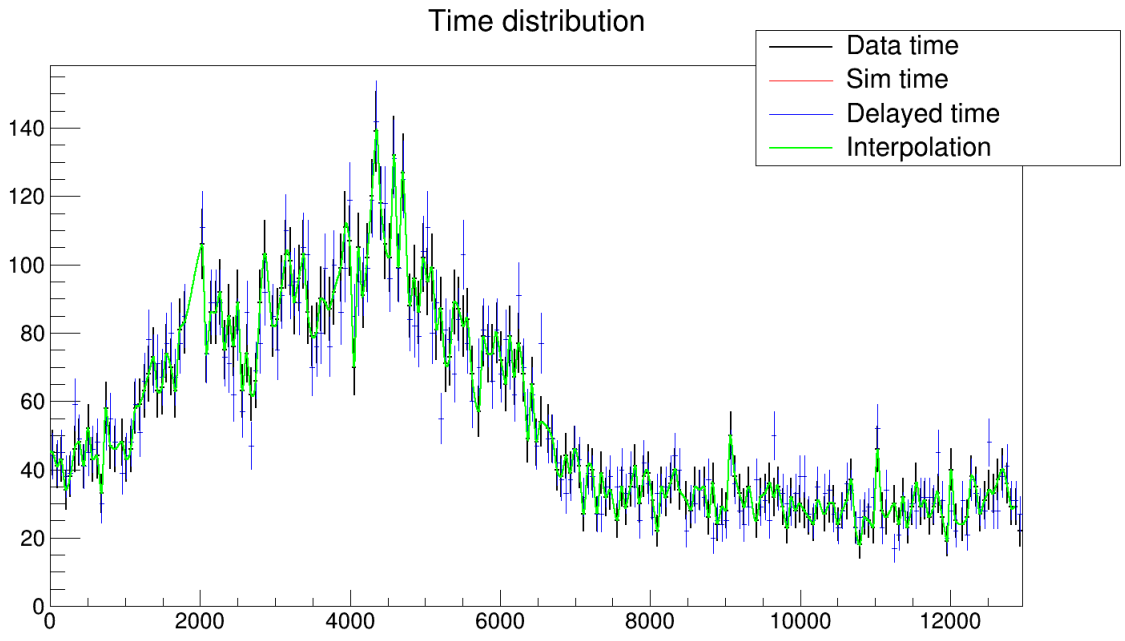

(b) Simulated time distribution compared with the data time distribution. Since there is no LIV delay injected, the simulated and the delayed time distributions are the same.

Figure 5.22: Time and energy simulated events distribution

random points in a bounded rectangle and counts the simulated "hits" or points that are inside the area of the function we want to simulate. This technique allows to reproduce better more complex templates, but requires longer simulation times. An example of the simulated time distribution with no time-lag, compared to the real data time distribution is shown in Figure 5.22b. In this example, due to the absence of delay, the event distribution tagged as "Sim time" is the same as the one tagged as "Delayed time" such that only the latter is visible on the plot.

The simulation code also takes into account the wobble gaps and allows to introduce the background events that are simulated directly from their measured energy template (see Figure 5.19) and their time template, modelled following the same methods as for the signal events. The number of simulated background events follows the signal-to-background ratio obtained by analyzing the number of events in the ON and OFF regions of the data.

5.7 Defining a complex lightcurve template for the Likelihood.

An important feature of the Mrk 421 flare, due to its duration and the large amount of events that compose it, is the clear presence of time gaps with a complete lack of events that correspond to the change from one wobble to another during the observation (see Table 5.8). These gaps should be taken into account to define the intrinsic time template of the data, introduced in the PDF ($F(t - D(E_s, E_{QGn}, z))$ in Equation 5.11). The wobble gaps' location in time will remain fixed no matter the value of the tested LIV parameter, whereas the rest of the time template will be shifted according to the effect produced by the test LIV parameter during the fitting procedure.

No matter if the methods to define the time template are binned or unbinned, these wobble gaps must be taken into account inside the Likelihood as the rest of instrumental effects, including the correct normalization of the PDFs of the events.

Additionally, the time template must be defined also outside of the chosen analysis time window, that in our case corresponds to the observation window. During the fit procedure to the data, the tested LIV parameter α will take different values, producing different LIV time-lags ($D(E_s, \alpha, z)$)). Such time-lags $-$ that can be large for very energetic events $-$ shift the time template. This way, a given event with arrival time t will be evaluated at another time, given by $t - D(E_s, E_{QGn}, z)$. Therefore, for the low-energy events close to the observation edges or the very-high-energy events, it is probable that the evaluation time lies outside the observation window chosen for the real data. Technically, this does not represent a big concern when dealing with functions obtained from fits to data, since they can be easily extrapolated outside their regime, however,it requires more study for alternative method of defining the time template. Anyway, for any method, such extrapolation must be treated as an assumption, with its corresponding systematic uncertainties.

5.7.1 Fit to the light curve

Our first trial to define a time template, commonly used in LIV studies [270, 269], was to fit directly the binned distribution of the events' arrival times. First, we constructed a custom histogram respecting the wobble gaps. This histogram bin width was chosen to be one minute, since we expect variability on time scales of minutes in AGN flares and all the bins contained at least 15 events in the less luminous part of the flare in order to preserve statistics of a size where the Poissonian fluctuations can be approximated by

Gaussian ones. Secondly, we produced a code to perform a custom fit taking into account the wobble gaps. For that, we consider Poissonian fluctuations in the number of events in each bin, defined a model function $f(t, \hat{v})$ and fit it to the histogram using a binned Likelihood:

$$\mathcal{L}(\vec{v}) = \sum_{bin=1}^{Nbins} \frac{f_b^{n_b} e^{-f_b}}{n_b!}, \tag{5.13}$$

,

where n_b is the measured number of events contained in the bin and f_b its expectation value, computed as:

$$f_b = \int_{width_b} f(t, \vec{v}) dt. \tag{5.14}$$

The function $f(t, \vec{v})$ is a continuous parametrization of the shape and height of the whole histogram, parametrized by a set of parameters $\vec{v}$. The Likelihood fit gives, as a result, the set of parameters $\vec{v}$ that fit the parametrization best to the histogram data.

Fixing the parameters to the values obtained in the fit, we tested the quality of the fit with a χ^2-test that compares the real bin contents $-$ only for the full bins $-$ with the ones predicted according to:

$$\chi^2 = \sum_{bin=1}^{Nbins} \frac{(n_b - f_b)^2}{f_b} \tag{5.15}$$

and $NDF = Nbins - Nparameters + 1$.

As first parametrization, we defined $f(t, \vec{v})$ as a simple Gaussian and as an asymmetric Gaussian function, obtaining a better fit for the second case, shown together wit the fit residuals in Figure 5.23.

However, these simple functions do not incorporate any possible internal variation of the flare (so-called "sub-flares"), very relevant for the sensitivity of the method to LIV. Consequently, we tried to deconvolute the functions into a series of Gaussians. To do so, we added subsequently more Gaussian functions to the fit, which improved the fit quality, indicating that the data was better described with a more complex parametrization, as shown in Figure 5.24. In order to initialize the positions of the newly added Gaussian functions, we performed several fits sliding that newly added Gaussian function along the time window to finally initialize it at the position where the final fit quality comes out best. Once the new Gaussian has been fixed at that location, we add another Gaussian and restart the process. During every fit, all the parameters of all the Gaussians are free and refitted, in order to account for possible correlations. The quality of the fit improved until it did not converge anymore. However, the p-values reached were still unsatisfactory, thus the difference between the fit function and the data histogram were statistically significant (p-value < 0.05), as reflected in Table 5.15. Usually the fit function parameters are later treated as nuisance parameters in the Likelihood fit together with the LIV parameter [270, 273], not possible in this case (the addition of the extra LIV parameter) if the fitting function reaches very high complexity. Unfortunately, so far, there was not a physical model providing a suitable fit function to such a complex light curve, and particularly no one based on a series of Gaussian functions, even though it is the usual, most used and simplest model. Additionally, we do not know whether the possible sub-flares can be described by Gaussians, since previous flares have shown asymmetries in the structures of the sub-flares [269]. Having asymmetric sub-flares would mean a even more complex parametrization of our lightcurve. For these reasons, we tried to look for other alternatives to define the emission time template.

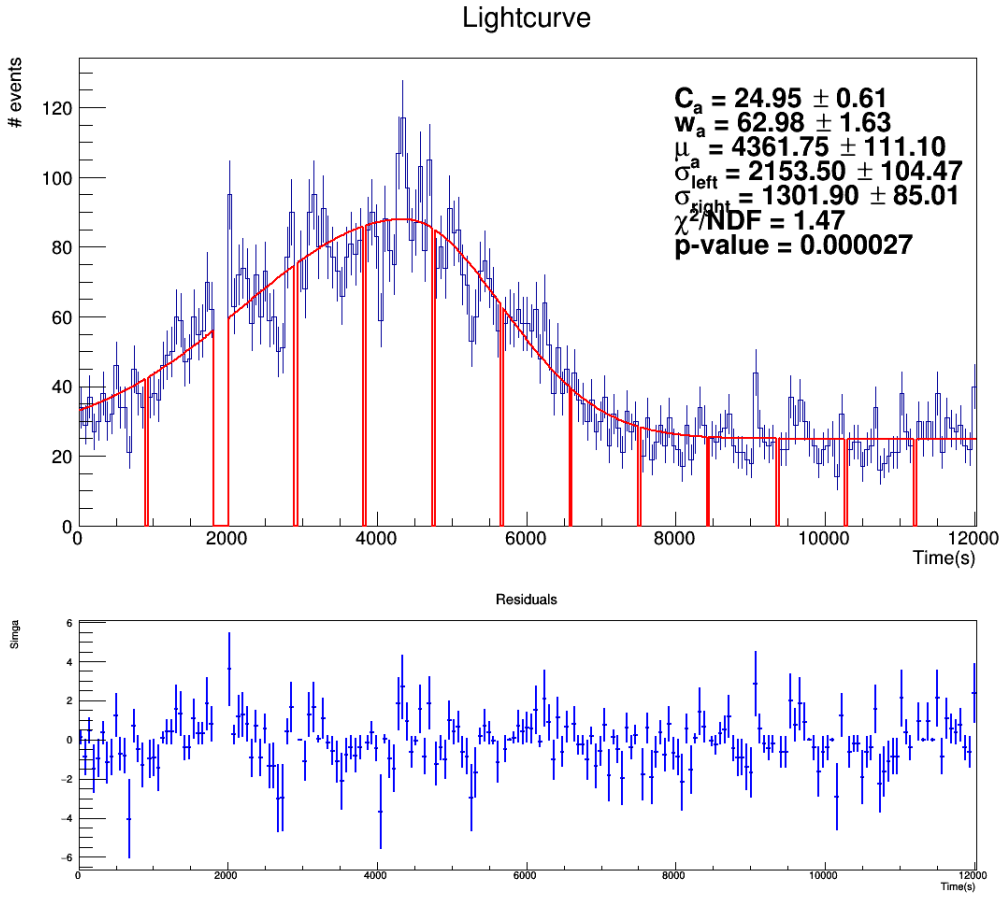

Figure 5.23: Fit of the time distribution using a binned Likelihood and an asymmetric Gaussian as parametrization.

LC fit with binned Likelihood			
Number of Gaussians	Parameters	χ^2/NDF	p-value
0	5	1.47	$2.7 \cdot 10^{-5}$
1	8	1.36	$8.1 \cdot 10^{-4}$
2	11	1.30	$4.4 \cdot 10^{-3}$
3	14	1.25	$1.3 \cdot 10^{-2}$
4	17	1.20	$3.7 \cdot 10^{-2}$

Table 5.15: Quality of the fit to the event time distribution using a custom binned Likelihood based in a decomposition into summed Gaussians.

5.7.2 Interpolation of the binned light curve

Instead of defining a shape for the time template by fitting a specific function, we can let the time distribution define its own shape, by interpolating directly the binned time distribution of the data.

The mathematical procedure used to fit the time-wise PDF to the data, called MIGRAD [322], is based on the variation of the derivatives of such PDF function with respect to its different parameters, in the sense that both the function describing the time template and its first derivative must be continuous through the entire time rage. For this reason, a linear interpolation, that consists of straight lines between data points, resulting in a continuous function with a discontinuous derivative, is not well suited in this case. We must also take into account that the empty histogram bins reflecting wobble gaps must not be used in the interpolation, such that the distance between data points increases in these cases and the

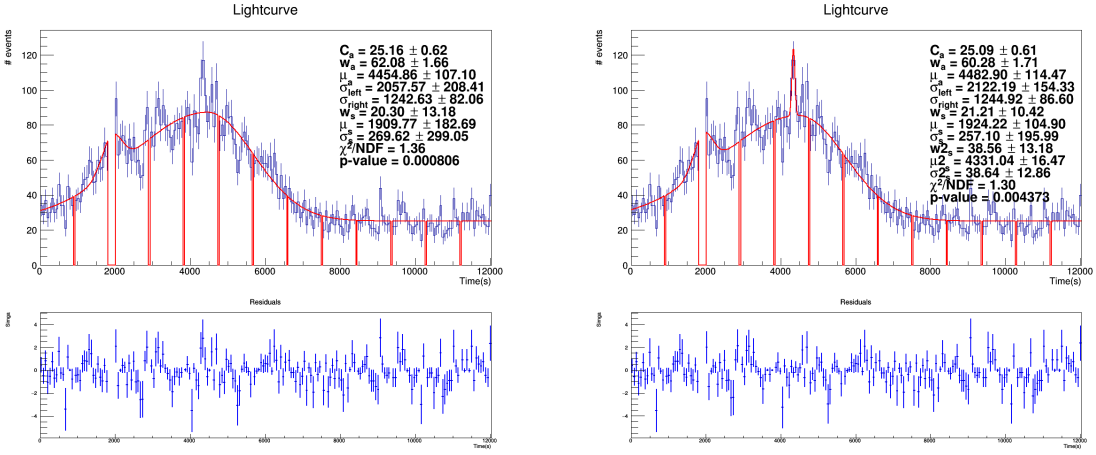

(a) One extra Gauss function **(b)** Two extra Gauss functions

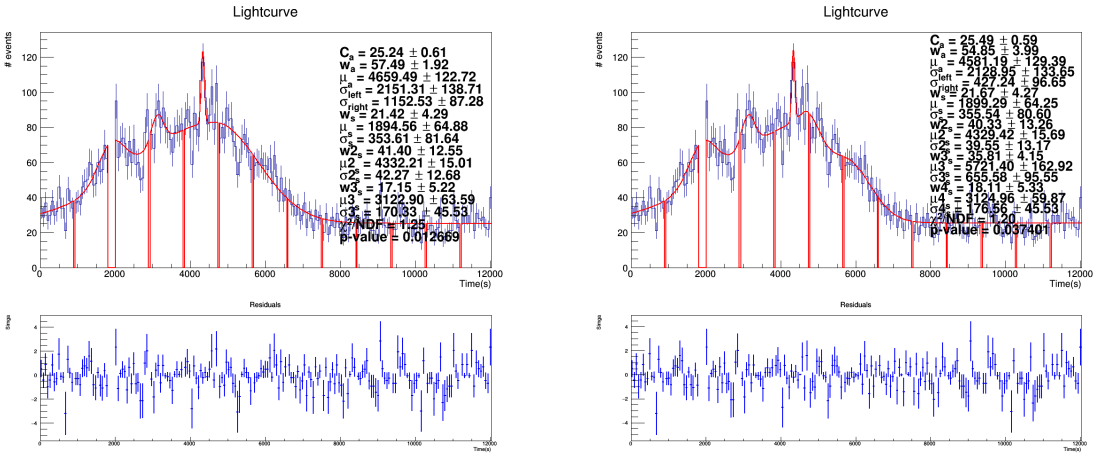

(c) Three extra Gauss functions **(d)** Four extra Gauss functions

Figure 5.24: Fit of the time distribution adding extra Gaussian functions to the initial asymmetric Gauss.

interpolation function must remain stable.

In order to obtain a smooth interpolation, continuous and with a continuous first derivative, we made use of a cubic spline, whose interpolation function is a third-degree piece-wise polynomial function, with matching first and second derivatives at the supplied data points. The second derivative is chosen to be zero at the first and last point.

The Akima method is a special case of cubic interpolation, also based on piece-wise polynomials, but which differs by the conditions imposed at the data points. In this method, the interpolation function is a cubic polynomial whose coefficients are fixed between every pair of successive data points by the condition that the function passes through the points with specified slopes. These slopes are determined by a "local" procedure: the slope at a given data point being a weighted average of the slopes of the line segments connecting that point with those on either side [323]. This extra condition makes the interpolation more stable to outliers and changes of the distance between data points. [2]

We applied both cubic interpolations to the data and analyzed their behaviour close to the wobble gaps, as seen in a zoomed section of the flare shown in Figure 5.25. The cubic interpolation creates an

[2] http://www.jive.nl/jivewiki/lib/exe/fetch.php?media=expres:fabric:interpolation.pdf

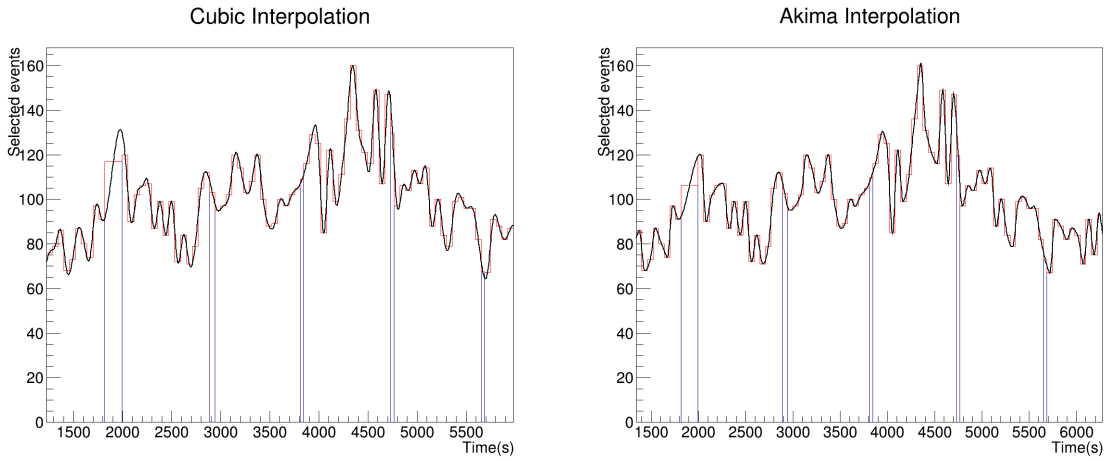

Figure 5.25: Zoomed section of the Mrk 421 2014 flare with a cubic interpolation (left) and a cubic Akima interpolation (right).

artificial excess of events close to the histogram holes (see e.g. around 2000 s in Figure 5.25). Therefore, we chose the Akima interpolation to construct a time template from the data histogram.

To define the time template outside the observation window, due to the lack of data points, we made use of the simple asymmetric Gaussian fit explained in the past section (Figure 5.23). Figure 5.26 shows the final interpolation and its corresponding Gaussian extrapolation at the window edges. Furthermore, in order to ensure a smooth transition between the interpolation and its corresponding extrapolation, an extra point was added to the original interpolation that connects with a "fake" data point located on the Gaussian curve. In the absence of this smooth link, the time PDF presents a "jump" at the two transition points.

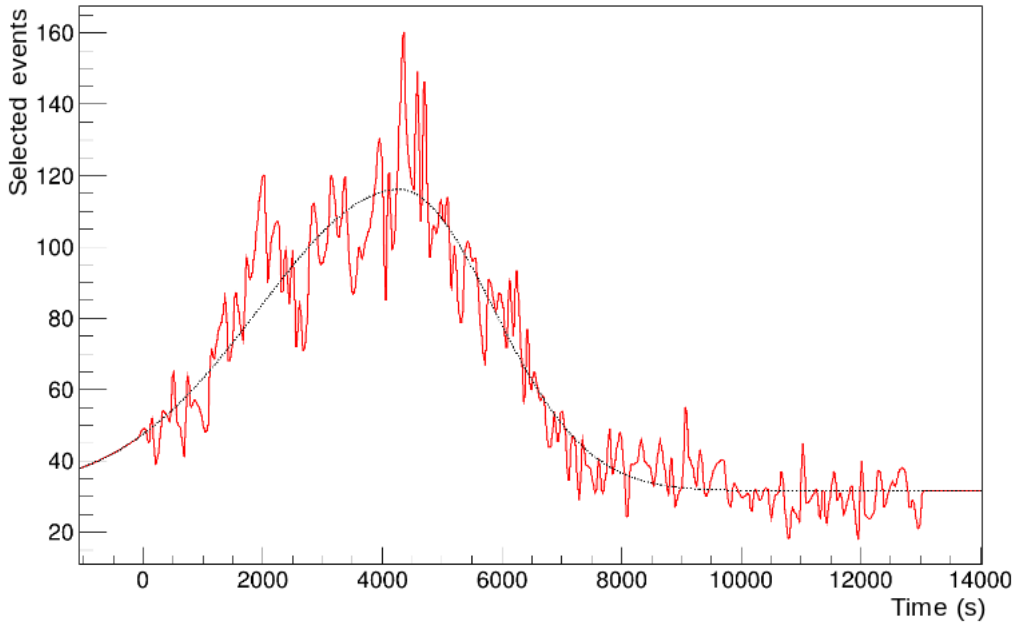

Figure 5.26: Data time histogram with one-minute bin width. The red line shows the smooth function produced by the Akima interpolation. The black dotted curve indicates the asymmetric Gaussian function used to produce an extrapolation of the time template outside the observation window.

In order to test the sensitivity of the ML analysis with this time template, we use it, together with all the ingredients exposed in Section 5.6, to produce 300 simulated data sets and apply the ML analysis

	LUT analysis		RF analysis	
Parameter	**Linear**	**Quadratic**	**Linear**	**Quadratic**
α	0.27±0.37	-1.28±0.83	0.04±0.27	-0.04±0.17
UL	10.57	7.93	7.79	3.82
LL	-10.56	-15.01	-7.99	-3.51
E_{QG} (GeV) ($\xi = +1$)	$1.11 \cdot 10^{18}$	$5.24 \cdot 10^{10}$	$1.54 \cdot 10^{18}$	$6.80 \cdot 10^{10}$
E_{QG} (GeV) ($\xi = -1$)	$1.11 \cdot 10^{18}$	$3.63 \cdot 10^{10}$	$1.53 \cdot 10^{18}$	$7.09 \cdot 10^{10}$

Table 5.16: Expected sensitivity for the linear and quadratic case in the LUT and RF analysis cases.

over them, where the PDFs are built using the same templates. We consider simulated data sets with no time-lag injected and take the simplified case of no background events. The resulting distribution of $\hat{\alpha}$ parameters from every analysis is shown in Figure 5.27 for the linear and the quadratic case, respectively. Table 5.16 shows the expectation value of $\hat{\alpha}$, obtained from a Gaussian fit to the distribution of retrieved $\hat{\alpha}$ values, their Upper Limit (UL) and Lower Limit (LL), and hypothetical constraints on the QG energy scale, for the linear and quadratic scenarios, and the subluminal and superluminal cases. The analyses have been applied on two different simulation sets, based on both analysis (RF and LUT) in order to quantify the effect of the improvement of the energy resolution. In both cases, the energy migration has been parametrized using a double Gaussian function.

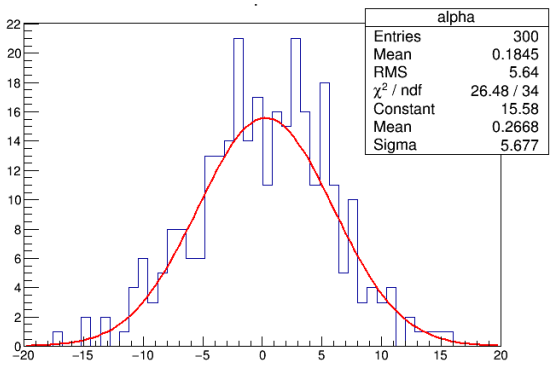

(a) Linear case, LUT analysis

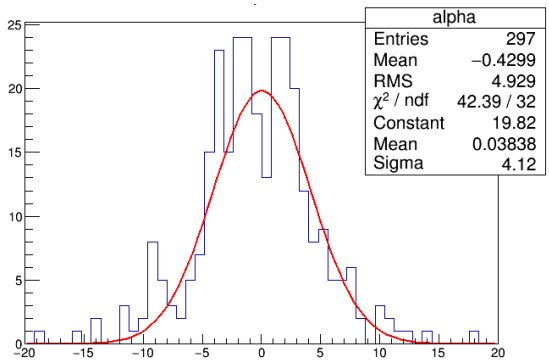

(b) Linear case, RF analysis

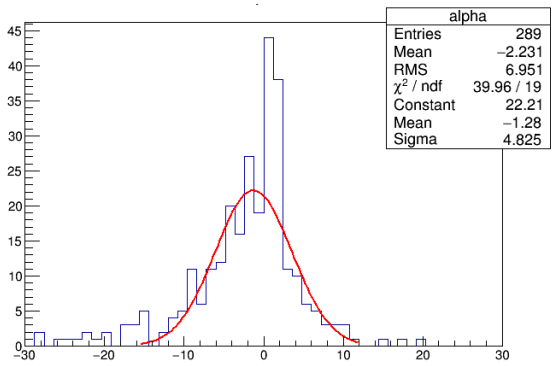

(c) Quadratic case, LUT analysis

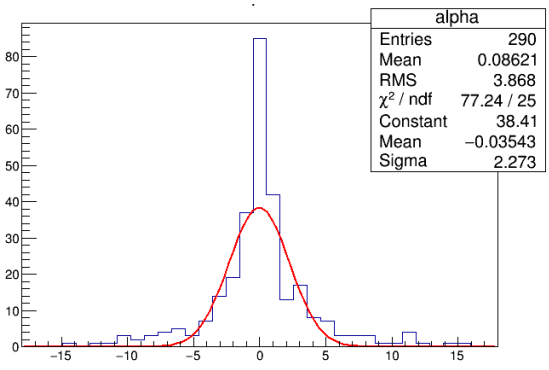

(d) Quadratic case, RF analysis

Figure 5.27: Resulting $\hat{\alpha}$ distributions for the linear and the quadratic case, using as time template an Akima interpolation over a histogram of 1 minute bin width. The red line shows a Gaussian fit to the distributions, whose mean parameter value is used to define the final value for $\hat{\alpha}$, shown in Table 5.16.

From the results, we can conclude that an improvement in the energy resolution, obtained by using RF instead of LUT for the energy estimation, translates into an improvement of the expected sensitivity to detect LIV. This can be seen directly with the distributions in Figure 5.27, where the dispersion in the results − reflected in the RMS parameter − is wider for the LUT analysis, in both the linear and the quadratic scenarios. For the linear case, the dispersion of results decreases by 37%, and the expected sensitivity improves a factor 1.4; while for the quadratic case, the dispersion decreases more than 50%, leading to a sensitivity improvement of up to a factor 2 in the superluminal case.

Nevertheless, in both cases, the distributions of $\hat{\alpha}$ for the quadratic scenario do not fit well a Gaussian function (see e.g. the bottom plots in Figure 5.27), indicating that the likelihood is not always well-behaved. We find the presence of two kinds of likelihood curves, the parabolic-shaped ones and the ones not presenting a parabolic shape, that we have called "pathologic" curves.

We performed a profound study to understand the origin of such pathologic curves. First, we checked that the simulated data sets reproduced correctly the data. For this purpose, we simulated a large statistical sample (10^6 events) and performed a χ^2-test energy and time distribution of the simulated events with respect to the templates used to generate them. The χ^2-test yielded a χ^2/NDF of 1.10, corresponding to a p-value of 0.15, thus showing that the events were correctly simulated. Additionally, we performed several tests inside the ML analysis code, as modifying the energy interval of the events used in the fit or including a larger number of events in such fit, taking profit of the large simulated data set. Based on all these tests, we could hypothesize that the pathologic curves are an expected feature due to two factors: the complexity of the lightcurve template and the lack of statistics in the energy range around tens of TeV.

In order to confirm our hypothesis, we studied the contribution to the total Likelihood function ($\mathcal{L}$) of the individual PDFs of the highest energy events in a simulated data set. In such PDFs (see the two cases shown in Figure 5.28a), it can be observed that the PDF shape follows the shape of the lightcurve template in the corresponding time interval where the event was evaluated, which depends itself on the interval of tested values for the alpha parameter and the value of the arrival time of the event. This phenomenon is graphically shown in Figure 5.28a for two simulated events of very-high energy. These irregular contributions to the likelihood function from the most energetic events, make an irregular final Likelihood curve. However, by restricting the most energetic events to contribute to the fit (with the corresponding loss of sensitivity) or increasing the statistical power by adding more events, such that the irregular contributions of the VHE events compensate each other, we recover the expected parabolic Likelihood curve (see Figure 5.28b).

In conclusion, the pathologic curves are also expected to appear in the LIV analyses using data from the next generation of Cherenkov telescopes (CTA), since the improvement in sensitivity will allow us to observe much more detailed flux features of the sources, leading to complex time templates as in our case. However, the bigger collection area of the CTA array will allow to detect a higher number of VHE events, making the effect of the lack of statistics not so critical for the Likelihood curves as in this case.

The fact that the Likelihood curves are not completely parabolic goes along with the $\hat{\alpha}$ distributions not following a precise Gaussian shape, especially in the quadratic case. Therefore, to estimate the sensitivity, we make use of the distributions of and LLs andULs obtained from each analyzed simulation set, instead of the dispersion of reconstructed $\hat{\alpha}$ values. The LL and UL values shown in Tables 5.16 and 5.17 are the mean values of such distributions. Moreover, the non-parabolic curves force a correction of the coverage to define the CI, when applying the analysis to the data (see Section 5.9).

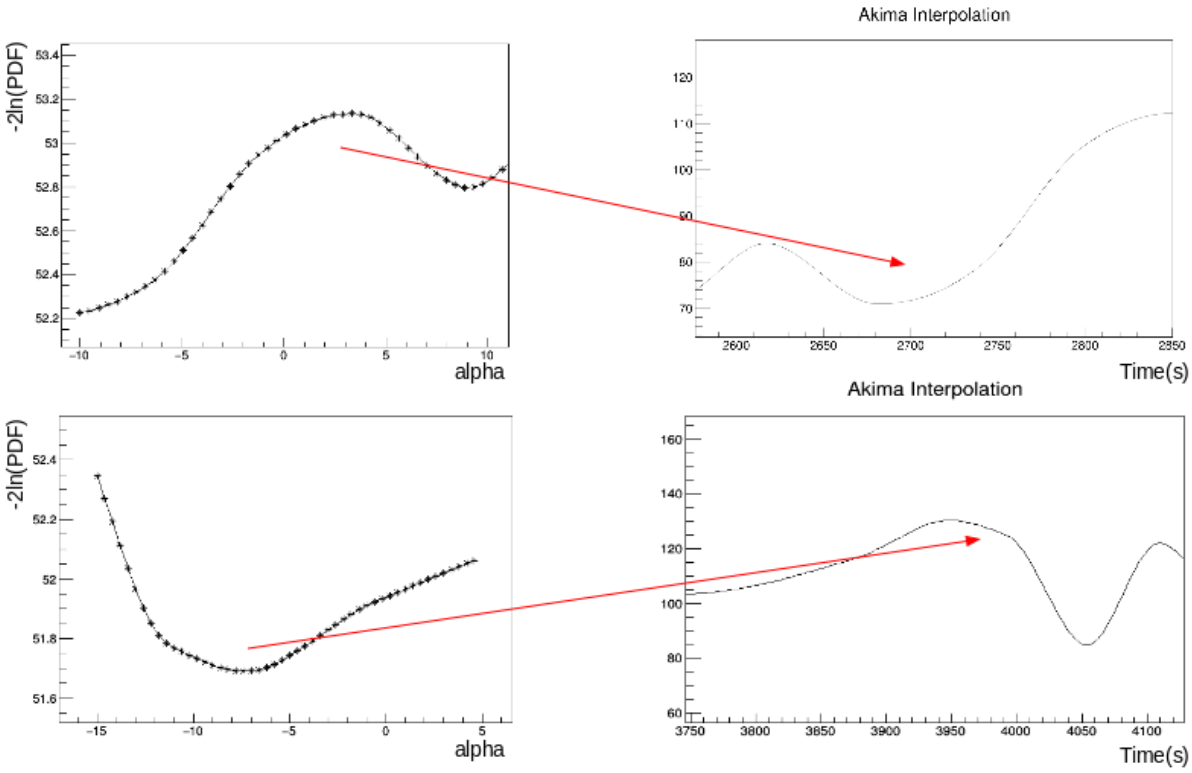

(a) PDF contribution of two very energetic events of a simulated data set for an α range (left plots) and the section of the time template where those events have been evaluated for that α range (right plots).

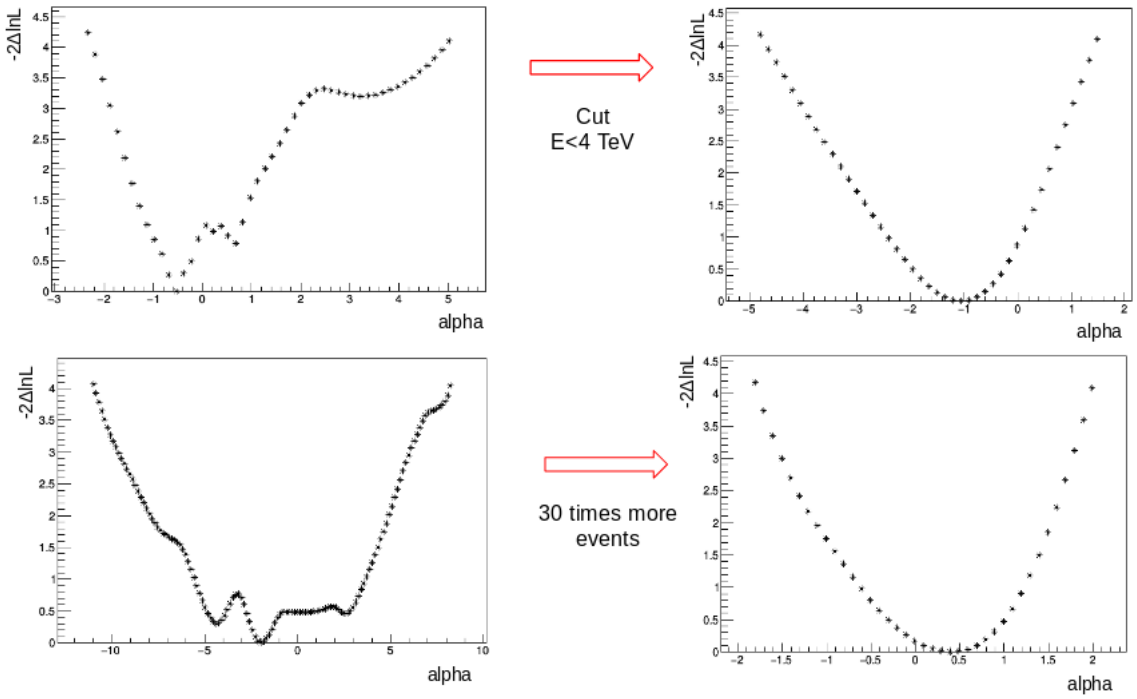

(b) Likelihood curves resulting from a ML analysis of 2 different simulated data sets (left plots) and their evolution when reducing the energy of the events used in the fit (upper right plot) and when including more events in the fit (bottom right plot).

Figure 5.28: Study of the factors producing pathologic likelihood curves.

Interpolation from 3 min bins		
Parameter	**Linear**	**Quadratic**
α	0.80±0.88	0.40±0.46
UL	34.2	16.6
LL	-32.3	-14.2
E_{QG} (GeV) ($\xi = +1$)	$3.5 \cdot 10^{17}$	$3.2 \cdot 10^{10}$
E_{QG} (GeV) ($\xi = -1$)	$3.7 \cdot 10^{17}$	$3.5 \cdot 10^{10}$

Table 5.17: Expected sensitivity for the linear and quadratic case using as time template an Akima interpolation over a histogram of 3 minutes bin width.

The effect produced by the election of a complex template makes the analyzer wonder if the light curve binning is the optimal one and how to judge if the flare's internal variability has been correctly taken into account. Therefore, we decided to evaluate the effect of an increase in the binning from 1 to 3 minutes, compute its corresponding interpolation and extrapolation, produce the simulation sets and apply the analysis on them. From now on, we base the simulation sets on the RF analysis to take profit from the improvement in sensitivity given by the improvement in the energy resolution. The resulting $\hat{\alpha}$ distributions and the QG energy limits for this 3 minutes case are shown in Figure 5.29 and Table 5.17.

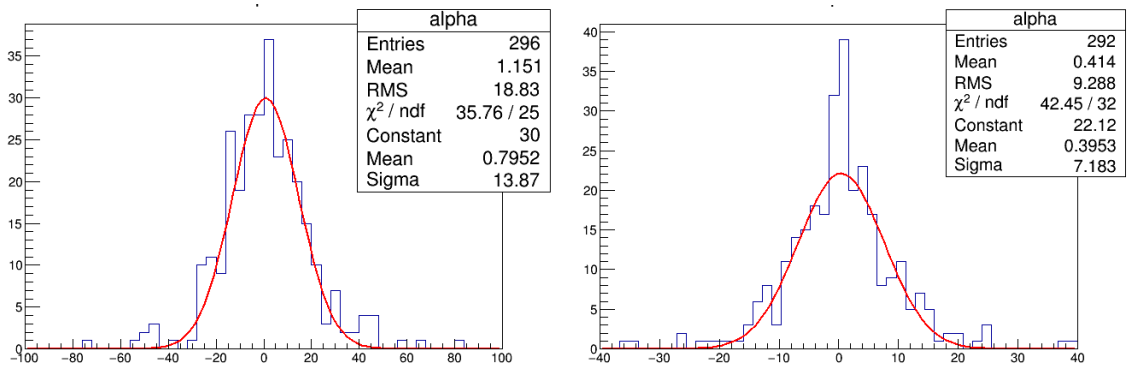

Figure 5.29: $\hat{\alpha}$ distribution for the linear (left) and the quadratic (right) case when using as time template an Akima interpolation over a histogram of 3 minutes bin width. The red line shows a Gaussian fit to the distributions in order to obtain the $\hat{\alpha}$ values of Table 5.17.

In this case, the increase of the bin size has a big impact on the expected sensitivity, since any possible variability on time scales of less than 3 minutes will be hidden. The expected energy scale limit for the linear scenario is worse by a factor 3 while in the quadratic case, it worsens by a factor 2. It is expected that the quadratic case is less affected since it depends more on the energy than on the time variability. The distribution of $\hat{\alpha}$ values is still incompatible with a Gaussian, due to the pathologic curves, but the ξ^2 is better than in the 1 minute case, as it can be seen in the quality of the Gaussian fit shown the right plot of Figure 5.29.

As a conclusion, the choice of the binning is relevant for the expected sensitivity. Moreover, it is difficult to find a right criterion to choose a specific time binning for the data, apart from the knowledge that AGN flares are expected to present variability on minutes time scales for the MAGIC sensitivity. However, we are dealing with an extremely flaring period, among the strongest emissions detected by MAGIC so far, and applying the known criteria from other flares might make us loose information. For this reason, we decided to try out one more strategy of defining the lightcurve template, based on an unbinned method in order to let the data itself define its time template.

5.7.3 Event-wise Kernel Density Estimation

In order avoid the problems associated with defining a time template with a fit − that entails a lack of knowledge of physics to define a model for the fitting function − or to use directly an interpolation of the data histogram, due to the binning effects on the final expected sensitivity, we tried one more method for the time template, called the Kernel Density Estimation (KDE).

The notion of KDE developed from the asymptotic limit of the Averaged Shifted Histograms (ASH) [324], a technique to reduce the binning effect of traditional histograms, that produces a family of N histograms, shifted respect to each other, and consider the parent distribution as the average of such a family. In the limit $N \to \infty$, ASH is equivalent to placing a triangular shaped KDE about each data point [325].

The general kernel estimate of the parent distribution is given by

$$f_0(x) = \frac{1}{nh} \sum_{i=1}^{n} K\left(\frac{x - t_i}{h}\right), \tag{5.16}$$

where n is the size of the data set, t_i are the data points and h is the smoothing parameter, also called bandwidth. The estimate f_0 is bin-independent regardless of the choice of K, that is in charge of spreading out the contribution of each data point in our estimate of the parent distribution. For this reason, a natural choice for K is a Gaussian with $\mu = 0$ and $\sigma = 1$:

$$K(x) = \frac{1}{\sqrt{2\pi}} e^{-x^2/2}. \tag{5.17}$$

Furthermore, Gaussian kernels are positive, differentiable and well-behaved.

The bandwidth sets the scale of the kernel and is completely specified by our data set. For large amount ($n \to \infty$) of normally distributed data [325], the mean integrated squared error of f_0 is minimized when [290]

$$h* = \left(\frac{4}{3}\right)^{1/5} \sigma n^{-1/5}. \tag{5.18}$$

However, data rarely distribute normally and the optimal bandwidth $h*$ is unknown, as happens in our case. The KDE method works directly on the events, for this reason, it is sensitive to the artificial wobble gaps that produce empty intervals inside the data. It is also sensitive to the time window edges, where the number of events drops to zero due to the observation limit, in a non-smoothly way. For this reason, before applying this method, we generate fake events inside the wobble gaps using the information of the expected events in those time gaps from the interpolation obtained in the past section. Additionally, we generate extra events outside the observation window, using the asymmetric Gaussian fit, in order to define the KDE template there for the later ML analysis. The final complete time histogram of events is shown in Figure 5.30.

The application of the KDE method to our final data events using different ρ factors, defined as,

$$\rho = \sqrt{\frac{\sigma_{local}}{\sigma}}, \tag{5.19}$$

produces very different time templates, appreciable by eye, as shown in Figure 5.30, for a small and a large values of ρ. The effect of ρ is to adjust the sigma value from its typical value of unity when the local

structure of the data σ_{local} is orders of magnitude smaller than the standard deviation of the flare σ, which would be our case, if indeed there is internal variability of the flare.

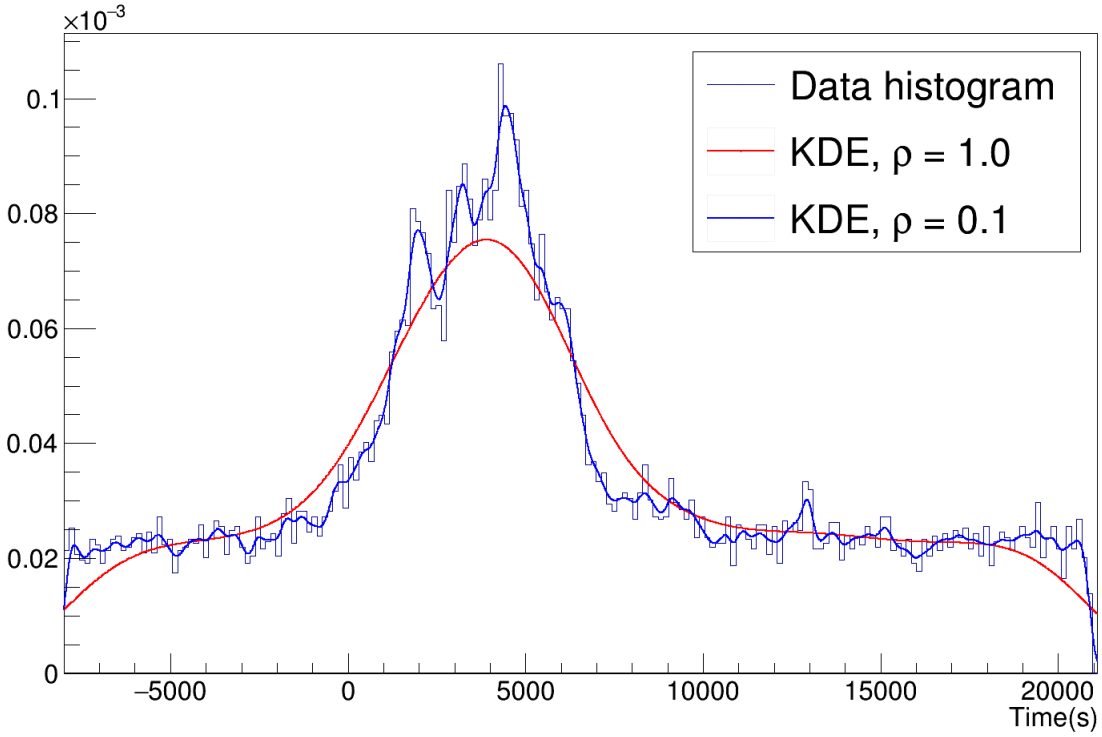

Figure 5.30: Data distribution and its KDE interpolations, for two different ρ values. Only the events are used to define the template, the histogram is also plotted for comparison. The time window has been expanded at both sides in order to avoid the border effects due to the KDE.

To avoid additional variablity in the time template introduced by the KDE, we decided to choose a value for ρ (smoothing parameter) based on the results of applying the method on the OFF data, which is expected to be smooth. Higher values of ρ produce ever smoother time templates and it is not clear where to stop and accept the residual deviation from flatness linearity (see Figure 5.31a). Moreover, our OFF time distribution is not flat, due to the zenith and stereo observation effects so which makes it even more difficult to evaluate the match of the KDE with expectation.

Therefore, to evaluate the KDE impact on a known parent distribution, we generate a large number of events (10^6) following a flat distribution and test the effect of applying the KDE with a ρ factor from 0.2 to 0.8. The results, shown in Figure 5.31b, show that the KDE is able to create visually appreciable variations with amplitudes of >1% even for such a large data set and big values of the ρ parameter. For this reason, deciding on a smoothing parameter based on the OFF distribution with more than seven times less statistics than the ON data might make us overestimate the variability of the flare.

As a final test to choose a smoothing parameter, we simulate again a flat distribution, this time with the same number of events as our ON data sample, create a KDE template ($f(t)$) and estimate the template variation using a parameter called Noise Estimator (NE), defined as

$$NE = \frac{f(t)_{max} - f(t)_{min}}{f(t)_{averaged}}, \tag{5.20}$$

where $f(t)_{max}$ and $f(t)_{min}$ are the maximum and minimum value of the template function found in the full time interval, while $f(t)_{averaged}$ is the mean value of the template function in such a time interval.

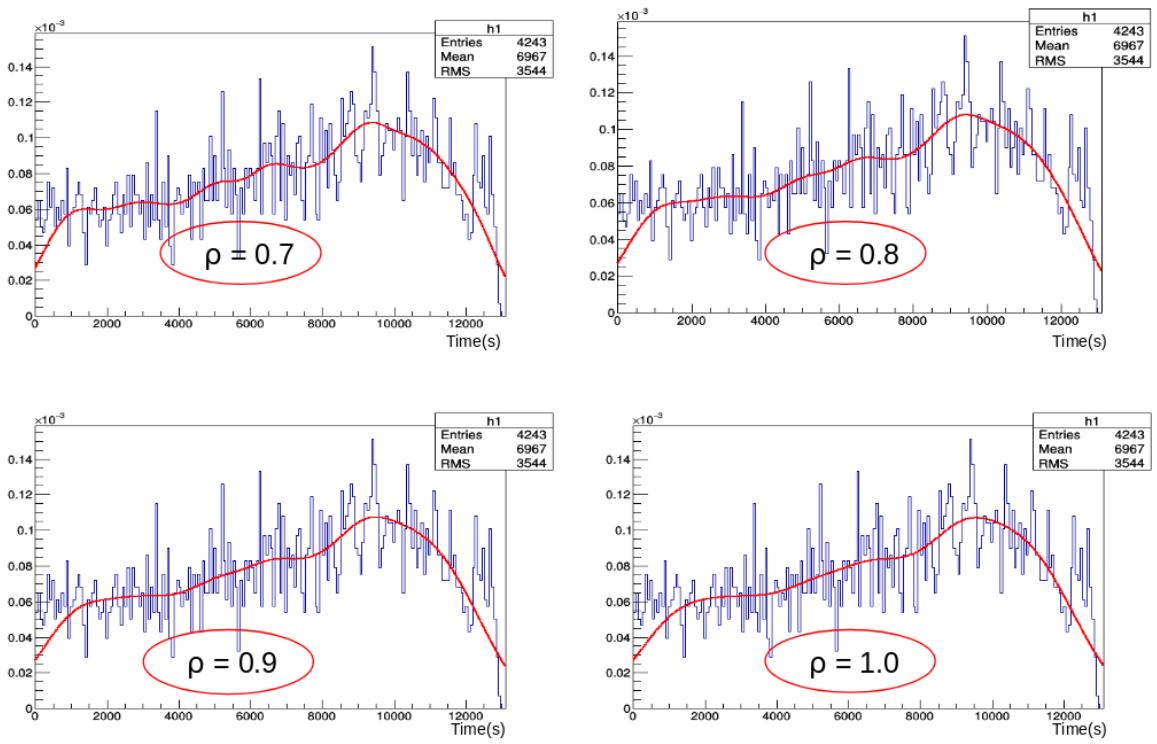

(a) Resulting KDE templates for the OFF data for different ρ parameters.

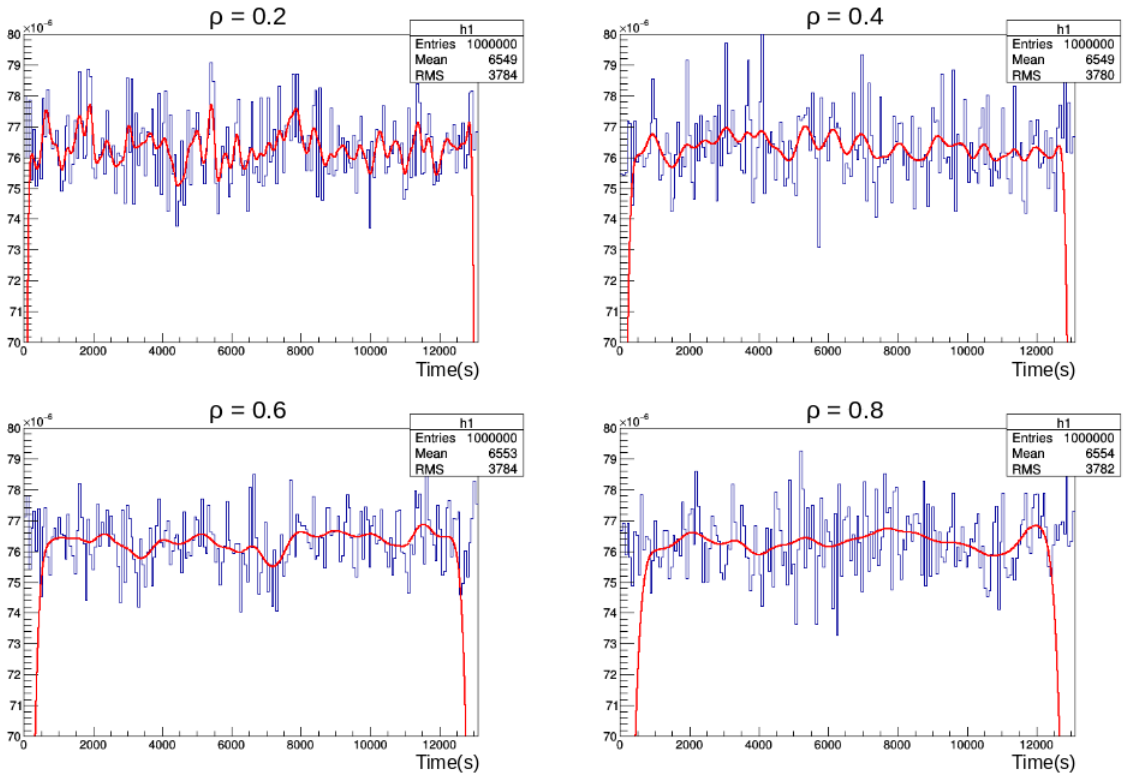

(b) KDE templates for the 10^6 simulated events following a flat distribution for different ρ parameters. The y-axis has been re-scaled to show the scale of the variations.

Figure 5.31: Study of the effect of varying the ρ smoothing parameter on the KDE template.

The procedure is repeated for 500 simulated sets for each ρ value. Figure 5.32 shows the results of the test, where the error bars show the 1σ standard deviations.

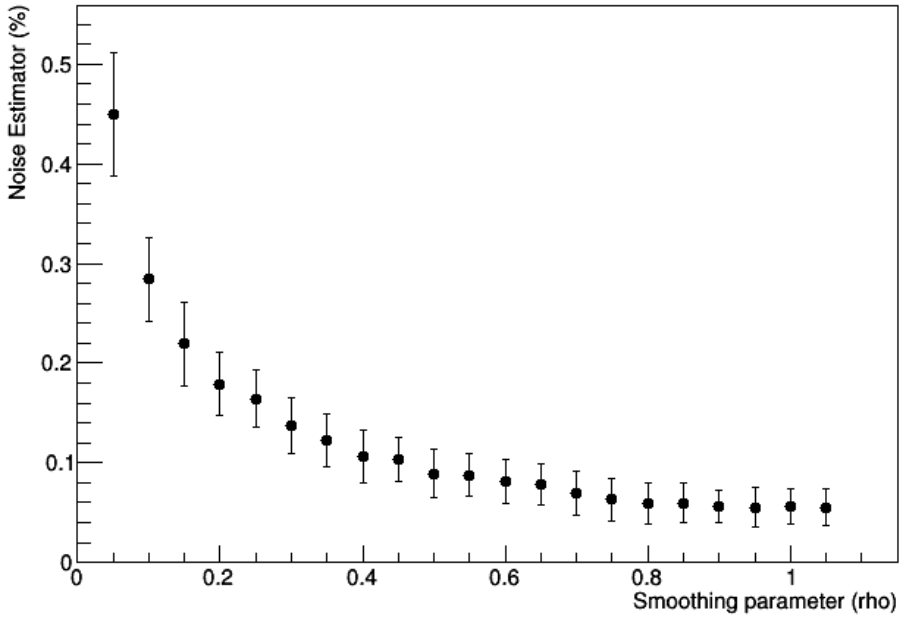

Figure 5.32: Noise estimator test results.

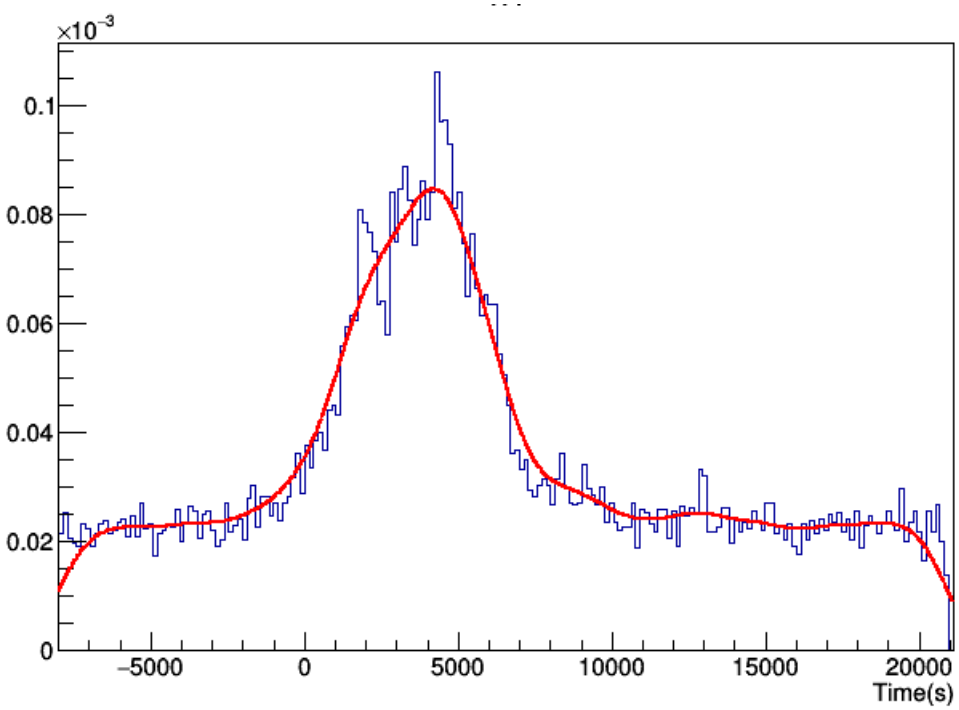

Figure 5.33: Final KDE interpolation with $\rho = 0.5$. The data histogram is also plotted for comparison. The time window has been expanded at both sides in order to avoid the border effects due to the KDE.

From the test, we can conclude that for ρ values smaller than 0.5, the method produces an additional variation amplitude with respect to the expected flat distribution larger than 10%, given our specific number of events. On the other hand, for ρ values larger than 0.8, the fluctuations produced by the KDE

KDE template with $\rho = 0.5$		
Parameter	**Linear**	**Quadratic**
α	-4.6±3.8	-1.2±1.0
UL	116.3	31.4
LL	-124.2	-40.0
E_{QG} (GeV) ($s_{\pm} = +1$)	$1.1 \cdot 10^{17}$	$2.4 \cdot 10^{10}$
E_{QG} (GeV) ($s_{\pm} = -1$)	$9.3 \cdot 10^{16}$	$2.1 \cdot 10^{10}$

Table 5.18: Expected sensitivity for the linear and quadratic cases using as time template a KDE with $\rho = 0.5$.

method fall below 7%, as shown in Figure 5.32. We found a 10% statistical fluctuation amplitude for the template acceptable and we created our time template using $\rho = 0.5$, taking into account the variations introduced by the KDE as an additional statistical uncertainty when computing the expected QG energy scale.

The expected sensitivity using the KDE template, when applied over 500 simulated data sets, is presented in Table 5.18. The distribution of α values obtained from all the analyses is shown in Figure 5.7.3.

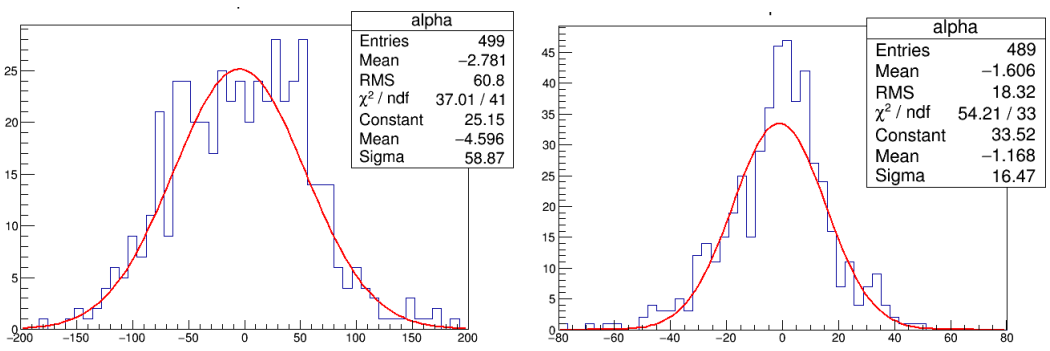

Figure 5.34: α distribution for the linear (left) and the quadratic (right) case when using the KDE method with $\rho = 0.5$ to define the time template. The red line shows a Gaussian fit to the distributions, used to obtain the $\hat{\alpha}$ values of Table 5.18.

The results obtained with the KDE template lie slightly below the ones obtained with the interpolation method over a 3 minutes bin histogram (see Table 5.17). Therefore, we conclude that probably the selection of the smoothing parameter is not the most optimal one, and might neglect any possible variability in the strongest sectors of the flare. The KDE method was used before for ToF studies with GRBs [275], but no detailed information about the chosen smoothing parameter was provided there. Moreover, the α parameter distributions do not show the expected Gaussian shape, probably due to the influence of these issues associated with the KDE that require further research. The quadratic scenario still shows a contribution from the pathologic curves, shown in the bad quality of the Gaussian fit (see Figure) but the effect is smaller than in the interpolation cases shown in previous section.

This method presents hence two disadvantages: first, as we have seen, there is a dependence on the smoothing parameters that probably must be studied further; secondly, the smoothing parameter acts on the whole data set, in a way that the bandwidth is constant along the observation window. Since our flare is very variable, with a flare structure superimposed over a flat background, a variable smoothing parameter may fit better in this case, but this will require further work to propagate the impact of such a variable bandwidth and its evolution along the time window when applying the template in the ML

analysis and it is out of scope of this thesis.

For this reason, even though the KDE code used to create the above mentioned time templates allows a variable bandwidth, its variability cannot be controlled by the user, and we decided to discard the KDE. Finally, we tried one last method to estimate the time template of our data, adapted to the more variable parts of the flare in a controlled way.

5.7.4 Interpolation with adaptive binning

Due to the rapid variability shown by our source, computing the time template for the data based on fixed time bins, as presented in Section 5.7.2, or a smoothing procedure with a fixed parameter, as in Section 5.7.3, is not optimal in this case. Based on the method to produce light curves used by X-ray observatories, already used in very rapid gamma-ray flares [316], we binned our data in bins containing a fixed number of ON events, after removing empty periods between wobbles.

Since the number of background events in the ON region, estimated from the hadronic events detected in the OFF regions, is always more than 7 times smaller than the number of total events in the ON region, we decided to make bins of 9 ON events, such that the significance of individual points in the defined lightcurve is close to 3σ. The final time template for the ML analysis is composed by bins showing dN/dt, where N is 9 events and dt depends on the flare variability, becoming as small as 1.8 seconds for the most variable sectors of the flare. Both histograms, the one composed of fixed events bins and the one used as time template, are shown in Figure 5.35.

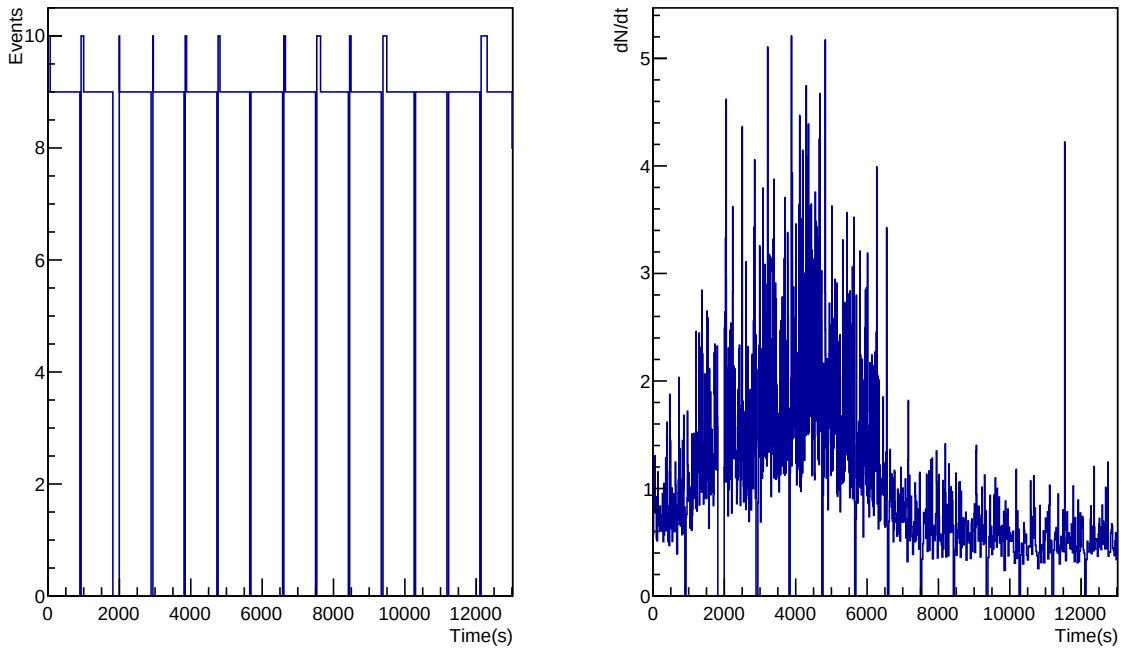

Figure 5.35: Histograms from binned 9 events. Left: Data histogram containing 9 ON events per bin. Right: Histogram showing dN/dt, use as time template for the ML analysis.

Even though we are working again with binned data, now we can establish a good criterion for the bin width based on precision of the lightcurve points, that let the flare statistics determine the bin size. However, the choice of a specific number of events per bin has an associated Poissonian fluctuation,

Interpolation template with 9 ON events						
	No Background case		**With Poisson**		**With background**	
Parameter	**Linear**	**Quadratic**	**Linear**	**Quadratic**	**Linear**	**Quadratic**
α	0.014±0.0070	-0.00012±0.0017	0.0068±0.013	-0.0064±0.0040	0.0016±0.0078	-0.0015±0.0029
σ	0.15±0.0081	0.036±0.0028	0.230±0.0022	0.064±0.0038	0.233±0.0083	0.070±0.0041
UL	0.32	0.11	0.33	0.097	0.34	0.12
LL	-0.30	-0.11	-0.31	-0.12	-0.33	-0.13
E_{QG} (GeV)	$3.9 \cdot 10^{19}$	$5.0 \cdot 10^{11}$	$2.6 \cdot 10^{19}$	$3.8 \cdot 10^{11}$	$2.6 \cdot 10^{19}$	$3.6 \cdot 10^{11}$

Table 5.19: Expected sensitivity for the linear and quadratic cases using as time template an Akima interpolation over a histogram of 9ON events.

that should be correctly propagated in the ML analysis in order to account for the additional statistical uncertainty due to the chosen template.

In order to use the template inside the ML analysis, we make use of the Akima interpolation introduced in Section 5.7.2, as well as its corresponding extrapolation obtained with the asymmetric Gaussian fit. The final template is shown in Figure 5.36a.

The effect of the Poisson fluctuations of the template itself in each bin was studied by modifying every bin content of the original histogram, applying random Poissonian fluctuations, before performing the interpolation again. This way, the time template was modified for every simulation analysis. Figure 5.36b shows an example of the change between the original template and a template used in one of the iterations.

In order to study the effect of such Poissonian fluctuations, we produced 500 simulated data sets and applied the ML analysis on them, first without including any Poissonian fluctuation, and later after including them. Figure 5.37 shows the $\hat{\alpha}$ distribution for both cases, for the linear and quadratic scenario, respectively. These distributions are fitted with Gaussian functions in order to obtain the values presented in Table 5.19.

To fully test the sensitivity of the model, we included also the background events contribution and performed a final test with 10^3 simulated data samples. In this case, the Poissonian fluctuation were already included. The resulting $\hat{\alpha}$ distributions are shown in Figure 5.38 and exposed in Table 5.19, together with the case of no-background.

The effect of a fluctuated time template is reflected in a bigger dispersion of the distribution of the reconstructed $\hat{\alpha}$ parameter, estimated by the width of the Gaussian fit in Figure 5.37, whose values are shown in the second row of Table 5.19. The dispersion grows by a factor 1.6 for the linear scenario and up to 1.8 for the quadratic one. Despite the effect on the dispersion, we can appreciate that the Poissonian fluctuations have a negligible effect on the upper limits. Those limits are computed evaluating the Likelihood at $-2 \ln \Delta\mathcal{L} = 4$ in order to obtain a two-sided 95% CL. If the Likelihood was well-behaved, we would expect that the upper limits obtain a value twice as big as the dispersion, a true statement before applying the Poisson fluctuations. The fact that the dispersion increases but the upper limits are only hardly affected, means that the introduction of the statistical effect produces a loss of the parabolic shape of the Likelihood such that the coverage is modified. Therefore, we need a coverage correction, when applying the method to real data (see Section 5.9). However, for a first estimate of the expected QG energy scale, we will use directly the dispersion value as

$$\alpha_{final} = \alpha + 2\sigma_{stat}, \tag{5.21}$$

where σ_{stat} is the width from the Gaussian fit shown in Table 5.19. We can see that the impact of the fluctuations of the time template translates into a worsening of the expected QG energy scale by a factor

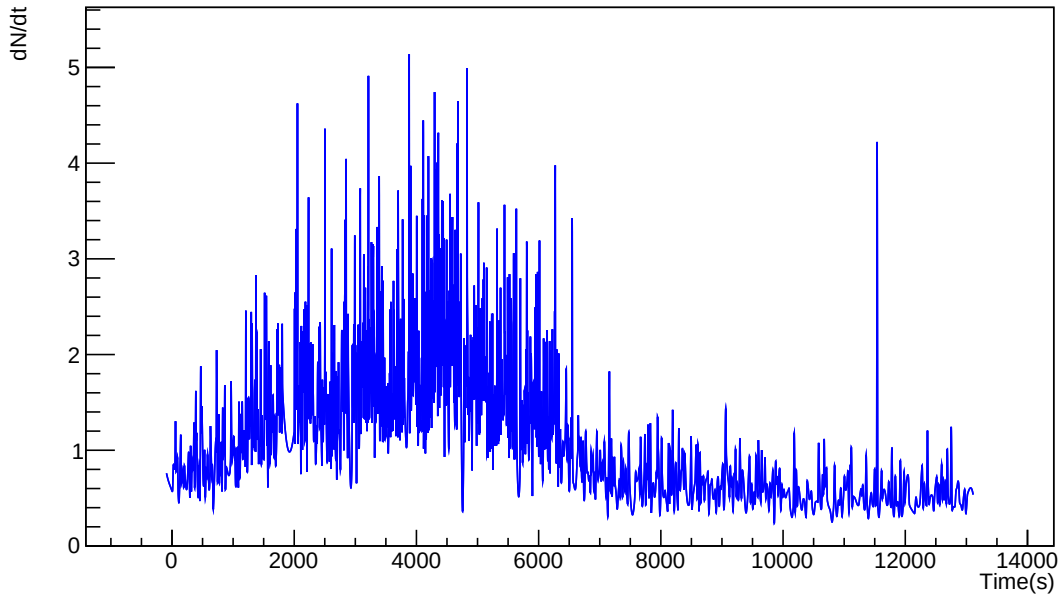

(a) Final interpolation with 9ON event bins.

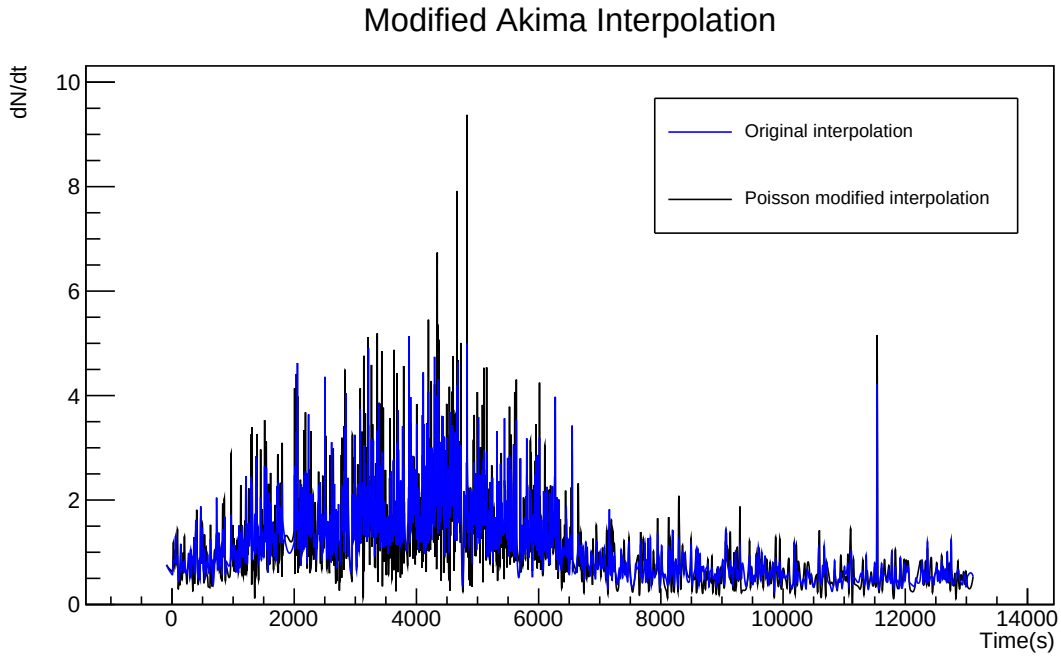

(b) Modified interpolation with 9ON event bins.

Figure 5.36: Upper part: Resulting interpolation obtained from a histogram built with 9 events per bin. Lower part: Modified interpolation before and after applying Poisson fluctuations to the previous template.

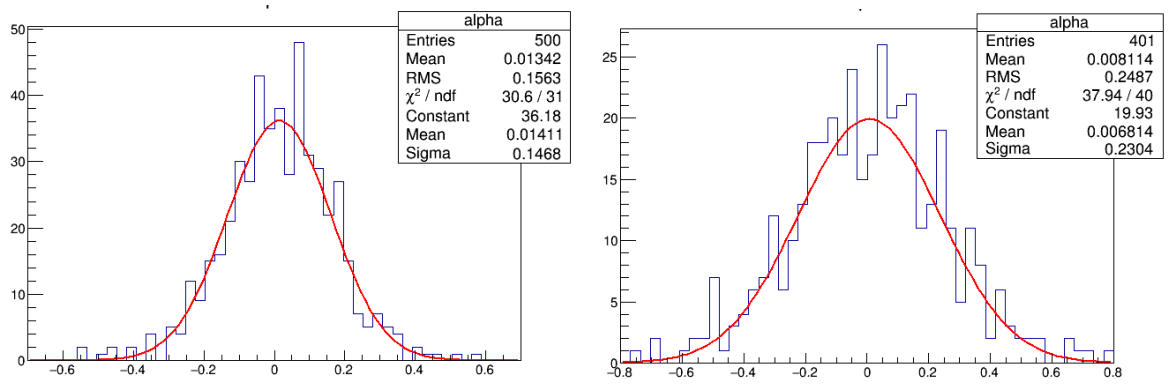

(a) $\hat{\alpha}$ distribution using the 9ON events time template for the linear scenario. On the left, the Poisson fluctuations are not include. On the right, with Poisson distribution included.

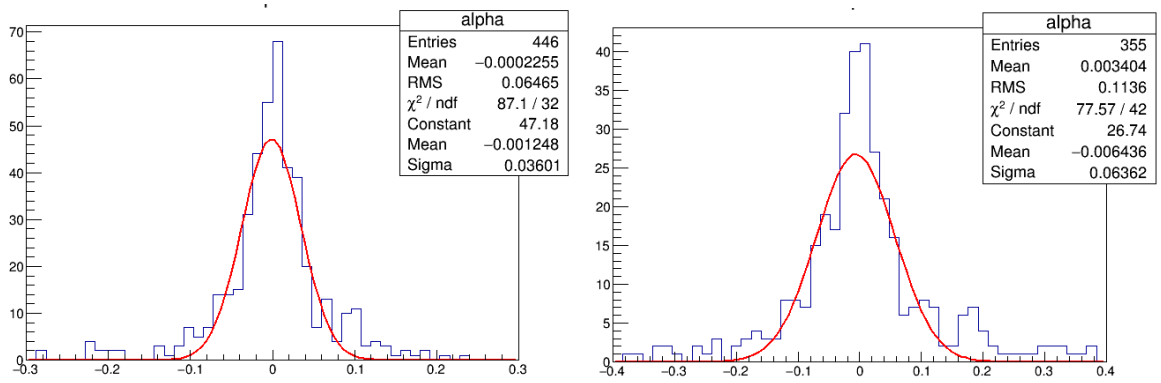

(b) $\hat{\alpha}$ distribution using the 9ON events time template for the quadratic scenario. On the left, the Poisson fluctuations are not included. On the right, with Poisson fluctuations included.

Figure 5.37: Effect of introducing Poissonian fluctuations inside the ML analysis. Upper plots: linear scenario. Lower plots: quadratic scenario.

1.5 in the linear case and 1.3 in the quadratic case, respectively.

The template used for the background contains also 9 events per bin, and uses the Akima interpolation. It requires no extrapolation though, since the hadronic background is assumed not to be affected by LIV. The additional introduction of the background events does not have a relevant impact, as was expected in this case, due to the large signal-to-background ratio. The effect on the dispersion is less than 1% in the linear case and around 9% for the quadratic case. The energy scale does not change for the linear case and shows a 5% worsening in the quadratic case.

The introduction of the Poissonian fluctuations almost doubles the statistical uncertainty associated to the result obtained by the ML analysis. Therefore, we decided to study if the size of the binning was too small and how would the situation change, if we defined our histogram with another number of ON events per bin. We increased the significance required per lightcurve point and discover an unexpected feature: the inclusion of Poisson fluctuations creates an even bigger effect for larger bins, such that the additional statistical uncertainty introduced by it is larger than the initial statistical uncertainty provided by the ML analysis without Poissonian fluctuations. After studying the likelihood curves obtained by the analysis of the different simulated data sets, we discovered that the Poissonian fluctuations produce an increase in the number of pathologic curves, and that the previously noted increase in the statistical uncertainty

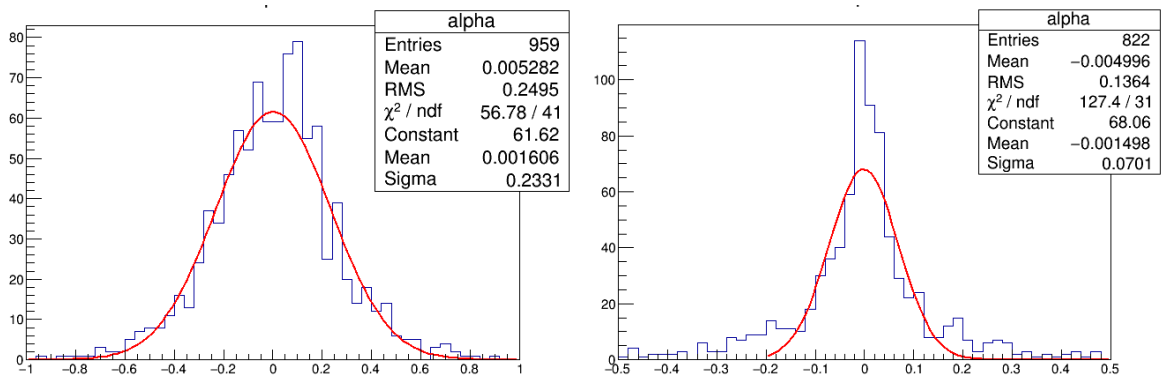

Figure 5.38: Distribution of the results after applying the ML analysis over 10^3 simulations, including Poisson fluctuations and background events. The time template contains 9 events per bin. The number of entries is slightly smaller than 10^3 since not all the ML fits converge.

was a combination of these two factors. Additionally, the increase of pathologic curves deforms the $\hat{\alpha}$ distributions, especially in the quadratic case. For this reason, fitting Gaussian functions to the $\hat{\alpha}$ distributions does not allow us to estimate correctly the effect of the two combined factors. Consequently, to test the effect for different bin sizes, we used two alternative robust statistical estimators, instead of the σ parameter provided by the Gaussian fit.

The first estimator is called Median Absolute Deviation (MAD). MAD is a robust measure of the variability of a sample of quantitative data. It is defined as the median (med) of the absolute deviations from the data median ($med_j x_j$):

$$MAD = med|x_i - med_j x_j|. \tag{5.22}$$

MAD is a robust scale estimator, first promoted by Hampel [326]. This estimator is simple and easy to compute. Its high sturdiness makes it ideal for screening outliers in the data. However, the MAD measures how far away the results are from a central value, so that it does not deal so well with asymmetric distributions. Hence we used an additional robust estimator as a cross check. Such estimator, called S_n has been introduced as an alternative to MAD in [327], it is defined as

$$S_n = med\{med_j|x_i - x_j|\}. \tag{5.23}$$

The S_n estimator computes the median of every difference between data members, and then compute the median of all such medians. This estimator has not a central reference value, but it looks directly for a typical distance between results, such that it is still valid for asymmetric distributions. Both estimators are based on the collection of results and not on its binned distribution, as was the case of the Gaussian fit.

The results for the different number of events per bin are shown in Table 5.20, where $\sigma_{Poisson}$ shows the statistical effect due to the Poisson fluctuations and is computed as

$$\sigma_{Poisson} = \sqrt{\sigma_2^2 - \sigma_1^2}, \tag{5.24}$$

with σ_1 shows the dispersion in the results before applying the Poisson fluctuations (estimated with MAD and S_n) and σ_2 is the dispersion after such fluctuations. The results are also shown graphically for both estimators in Figure 5.39 as a function of the number of events per bin.

From Figure 5.39, we can conclude that both statistical estimators give similar results. They differ slightly more for larger bins, but show the same evolution of the statistical uncertainty.

Study of the Poisson fluctuation effects							
		MAD			Sn		
Events	Type	σ_1	σ_2	σ_{Poi}	σ_1	σ_2	σ_{Poi}
4	Linear	0.034	0.055	0.043	0.035	0.057	0.045
4	Quadratic	0.0073	0.014	0.012	0.0083	0.016	0.014
9	Linear	0.15	0.21	0.15	0.15	0.21	0.15
9	Quadratic	0.036	0.051	0.036	0.040	0.057	0.041
16	Linear	0.37	0.55	0.40	0.38	0.55	0.39
16	Quadratic	0.10	0.18	0.15	0.11	0.19	0.15
25	Linear	0.65	0.96	0.70	0.70	1.05	0.79
25	Quadratic	0.20	0.32	0.25	0.21	0.36	0.29
36	Linear	1.34	1.86	1.29	1.70	2.25	1.29
36	Quadratic	0.51	0.72	0.51	0.63	0.87	0.60
100	Linear	5.30	7.07	4.68	5.48	7.23	4.72
100	Quadratic	2.73	3.48	2.16	2.67	3.37	2.05

Table 5.20: Study of the effect of introducing Poisson fluctuations inside the ML analysis, using as time template a histogram with different number of events per bin.

From Table 5.20, we can conclude that the additional statistical effect provided by the Poisson fluctuations is not so big in the 9ON case, since the light curve is so peaky that all the low-energy and high-energy events have irregular contributions to the Likelihood (as the ones shown in Figure 5.28a), that compensate each other, leading to parabolic Likelihood curves. For smaller bins, as the 4 events case, the likelihood seems well-behaved but the Poissonian fluctuations completely dominate the statistical uncertainty. On the other hand, as the bin size increases, only the high-energy events maintain irregular contributions such that the likelihood becomes pathologic. Moreover, the Poisson fluctuations boost such effect. This statement can be clearly seen in Figure 5.40 for the quadratic case of 16 ON events per bin, where the contribution of pathologic curves reaches a maximum. In this case, the peak located at $\alpha = 0$ decreases from a value of $\sim$145 to $\sim$125 after the addition of the Poisson fluctuations while the non-Gaussian tails increase, indicating that the number of pathologic curves has increased.

From $\approx$ 36 events per bin on, the additional dispersion of reconstructed $\hat{\alpha}$ values, caused by the introduction of the Poissonian fluctuations, does not dominate the total statistical uncertainty anymore, corresponding to 6 sigma significance per lightcurve point. We decided to choose such binning for our final template for two reasons: first, the pathologic curves are not completely avoidable, but we do not want our final result to be dominated by them; second, going to even larger bins (as the 100 events case) does not decrease in a relevant amount the Poissonian dispersion and entails a sacrifice of the sensitivity of the method (directly related to σ_1), due to the possible masking of the internal flare variability.

The final template can be seen in Figure 5.41, together with one realization of the Poissonian fluctuations added. The $\hat{\alpha}$ distributions before and after adding Poissonian fluctuations are shown in Figure 5.42 for the linear and quadratic scenario. The corresponding sensitivity to the QG energy scale is shown in Table 5.21, computed from the dispersion given by the S_n estimator, obtained from the distributions of the results shown in Figure 5.42.

From Table 5.21, we cross check the loss of coverage due to the pathologic curves, that will be studied and corrected during the application to the data, in Section 5.9.

Once we know the statistical uncertainty associated to the chosen time template and before applying the analysis to real data, we develop a detailed study of the different systematic uncertainties.

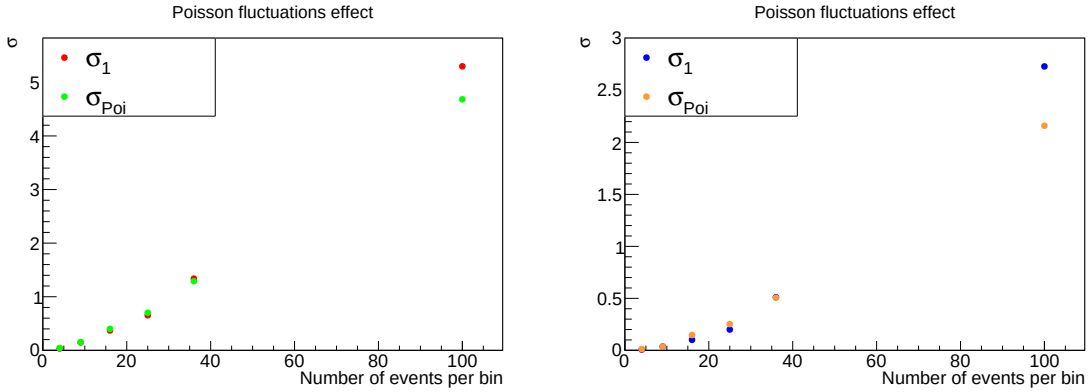

(a) Dispersions of the $\hat{\alpha}$ distributions, estimated with the parameter MAD. Left: linear scenario. Right: quadratic scenario.

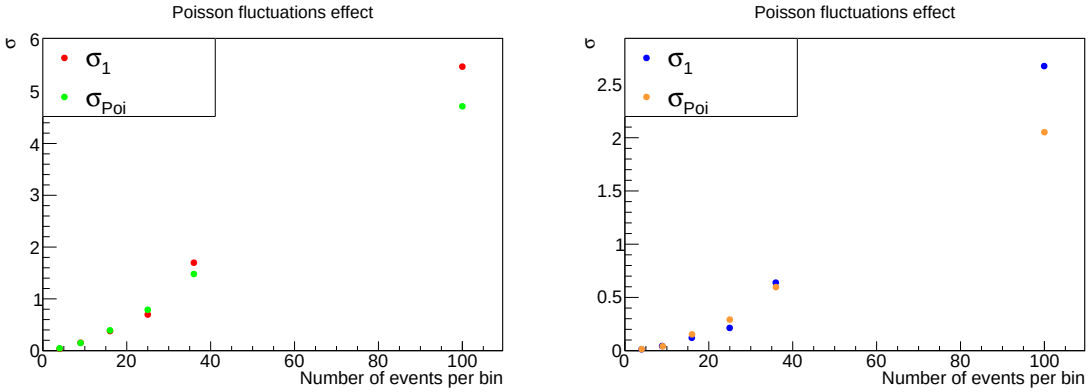

(b) Dispersions of the $\hat{\alpha}$ distributions, estimated with the parameter Sn. Left: linear scenario. Right: quadratic scenario.

Figure 5.39: Graphical view of the impact of the additional statistical uncertainty due to the introduction of Poisson fluctuation in the ML analysis. σ_1 refers to the statistical dispersion before applying the Poissonian fluctuations and σ_{Poi} is calculated with Equation 5.24

	Interpolation template with 36 ON events	
Parameter	**Linear**	**Quadratic**
α	0.050	-0.0045
S_n	2.25	0.87
UL	2.83	0.86
LL	-2.73	-1.06
E_{QG} (GeV)	$2.7 \cdot 10^{18}$	$1.0 \cdot 10^{11}$

Table 5.21: Expected sensitivity for the linear and quadratic cases using an Akima interpolation from a histogram of 36 ON events as time template .

5.8 Likelihood systematics study

Due to the complexity of the lightcurve, we did not include nuisance parameters in the event PDF to study the systematic uncertainties, as it has been done for other LIV analyses in MAGIC [270, 273]. Instead, we study them by using simulated data sets, a strategy followed in other ML analyses [269, 289]. For such a study, we modify several parameters in the simulated data sets, apply the ML analysis to them and study the effect on the dispersion of results, as done with the Poissonian fluctuations. The different considered

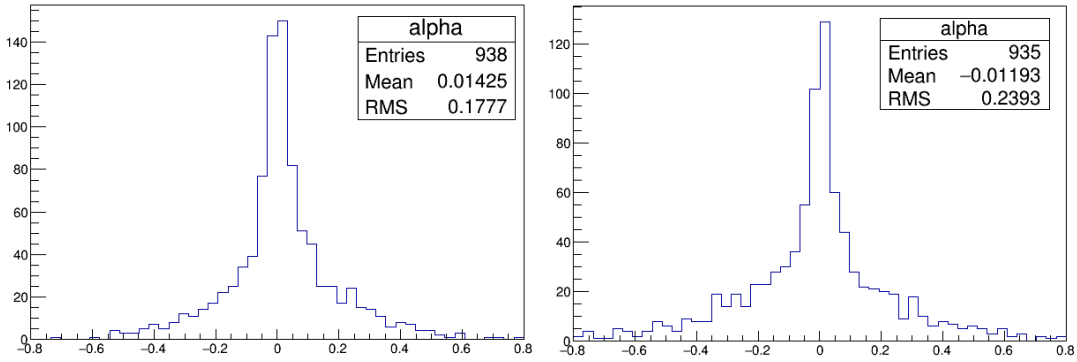

Figure 5.40: Distribution of the reconstructed $\hat{\alpha}$ values after applying the ML analysis to 10^3 simulations, including background events and using a time template with 16 events per bin, for the quadratic scenario. Left: no Poisson fluctuations added to the time template. Right: with Poissonian fluctuations included.

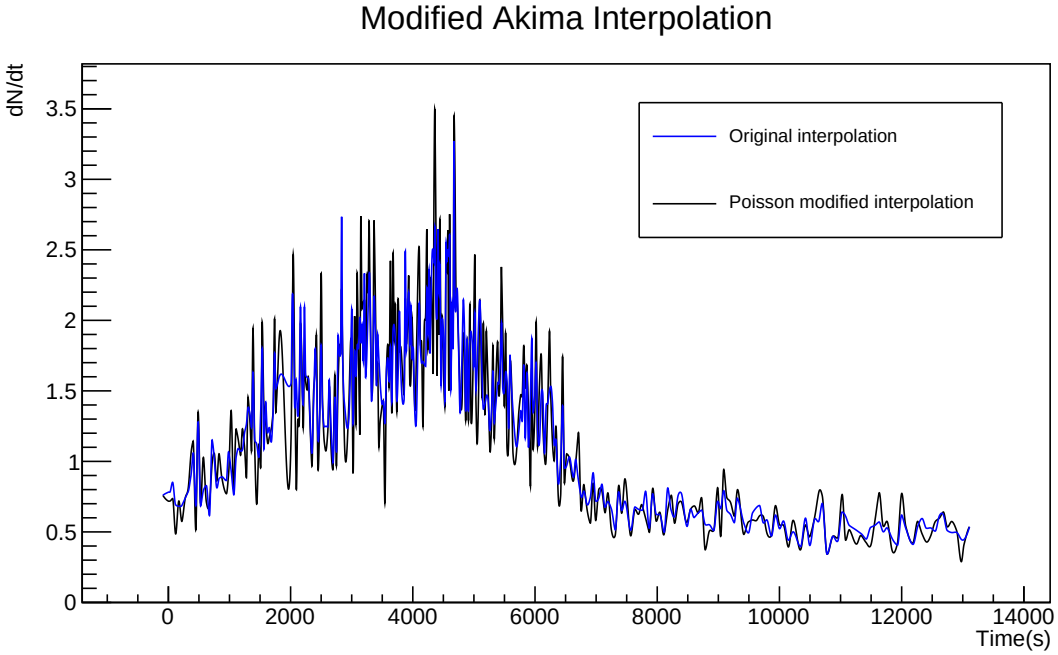

Figure 5.41: Original and modified interpolation with 36 ON event bins.

uncertainties, summarized in Table 5.22, are:

- **Spectrum uncertainties**. The parameters of the function defining the signal energy spectrum are varied within their uncertainties for every simulated data set. The effect of each parameter was studied separately, but we have used later the one with the biggest impact, to be conservative.
- **Energy scale instrumental uncertainty**. The MAGIC systematic uncertainty in the determination of the global energy scale is 15% [311]. We shifted the energy of the simulated events by this amount in both directions and studied its effect on the reconstructed $\hat{\alpha}$ values.
- **Extrapolation associated uncertainty**. We studied the effect of the extrapolation applied to the time template outside the observation window by using a flat extrapolation in its place.
- **Background energy template uncertainty**. We tested the effect of the change of binning in the energy template used for the hadronic events.

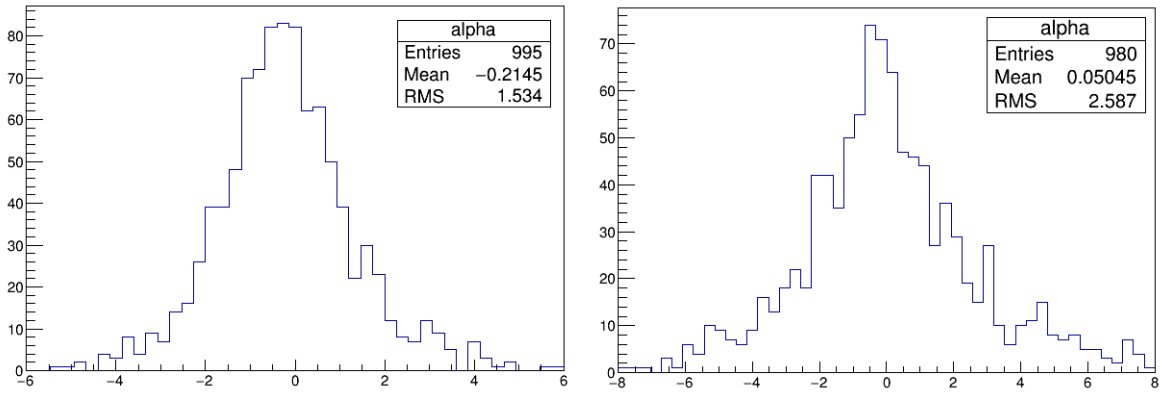

(a) Linear scenario. On the left and right, without and with Poisson fluctuations, respectively.

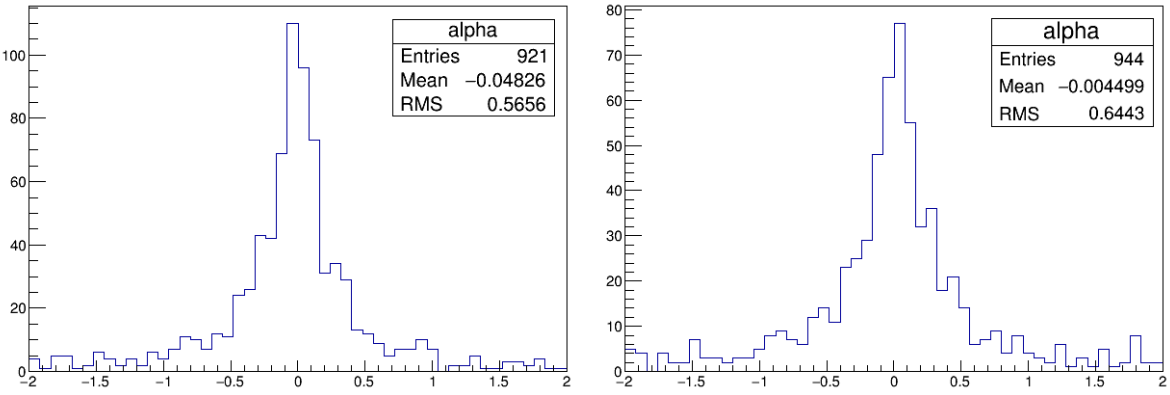

(b) Quadratic scenario. On the left and right, without and with Poisson fluctuations, respectively.

Figure 5.42: $\hat{\alpha}$ distributions for a time template with 36 ON events per bin with and without including Poisson fluctuations. Upper part: Linear scenario. Lower part: quadratic scenario.

Study of systematic uncertainties		
Systematic effect	**Size**(E_{QG1})	**Size**(E_{QG2})
Spectrum uncertainties	< 6%	< 4%
Energy scale	< 10%	< 20%
Extrapolation uncertainty	< 1%	< 1%
Background estimation	< 5%	3%
Total	12.7%	20.6%

Table 5.22: List of studied systematic uncertainties

In order to estimate the effect of all these factors, we made use of the robust statistical estimators introduced in the past section.

The bigger impact is produced when shifting the energy of events in order to apply the MAGIC energy scale uncertainty. It affects the results specially in the quadratic case when shifting the energy to lower values. Such effect is expected since it entails a loss of sensitivity and thus a worse reconstruction of the injected lag, leading to a bigger dispersion of results. The change on the parameters of the spectrum does not produced a big impact, the slope parameter (Γ in Equation 5.12) is the one dominating the uncertainty. This slope of the spectrum directly relates with the amount of high-energy events, such that we expect its effect to be bigger. On the other hand, the extrapolation shape, that could present some effect since the flare's location is close to the observation window edge, shows almost no impact on the results when

comparing it with the a flat extrapolation. Finally the effect on the binning used for the background energy template has also a small effect, yet bigger than the extrapolation. The background events, due to their small amount, have a small impact on the analysis dispersion (see Section 5.7.4), as so has a change in their energy template.

We assumed that all the systematic uncertainties are uncorrelated, such that we add them up quadratically to obtain the final uncertainty shown in Table 5.22 for the linear and quadratic scenarios, respectively. For this analysis, we obtain a 12.7% for the linear and 20.6% for the quadratic case.

5.9 Likelihood analysis results

Before applying the analysis to the real data, we study the loss of coverage using the $\hat{\alpha}$ distributions obtained after the introduction of the Poissonian fluctuation. For that, we normalize these distributions and integrate them between the UL and LL values obtained (exposed in Table 5.21). If the Likelihood function was well-behaved, that is, it follows a χ^2 distribution, we must obtain a value close to 0.95, since the upper limits were supposed to provide a two-sized 95% CI. In our case, however, the integral gives us smaller values in both linear and quadratic cases. In order to correct the upper limits, we compute the quantiles of the $\hat{\alpha}$ distributions (see Figure 5.43), in an equivalent way as for the PV and SMM analyses, and obtain the corrected upper and lower limits. As a result, we calculate a correction factor that must be applied to the original LL and UL (shown in Table 5.21), to recover the desired coverage. The results are summarized in Table 5.23.

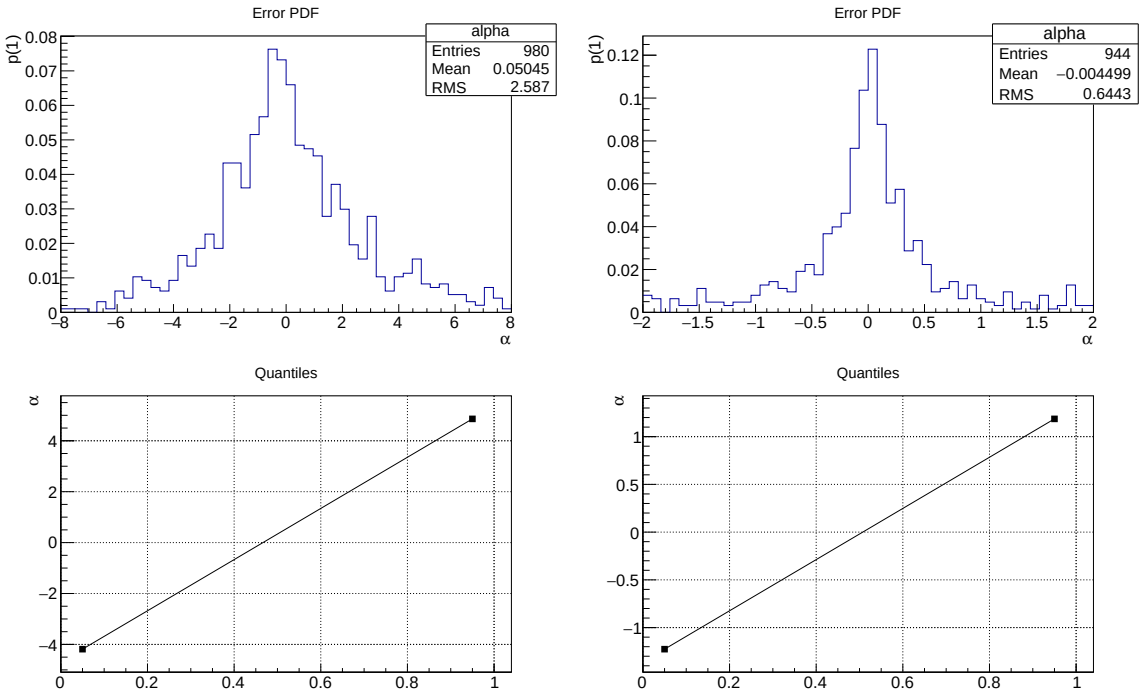

Figure 5.43: Computation of the $\hat{\alpha}$ distributions quantiles.

There are other methods to correct the loss of coverage. For example, using a parametrization of the $\hat{\alpha}$ distributions, as performed for the MAGIC LIV analysis of the Crab Pulsar [273].

Once the correction factors for the limits are known, we applied the method to the data. The resulting Likelihood curves are shown in Figure 5.44 and the corrected values for the minimum and upper limits are

Correction of coverage					
Type	**Coverage**	**New UL**	**UL factor**	**New LL**	**LL factor**
Linear	0.76	4.86	1.72	-4.19	1.53
Quadratic	0.88	1.19	1.38	-1.23	1.15

Table 5.23: New sensitivity estimates of $\hat{\alpha}$, obtained after the coverage correction and the corresponding correction factors.

ML parameters		
Parameter	**Linear**	**Quadratic**
α	-0.47	-0.03
UL	1.94	0.57
LL	-5.07	-1.16

Table 5.24: Likelihood curve minimum and upper limits obtained from the real data. The coverage correction factors are included.

ML analysis results over data		
Case	**No systematics**	**Including systematics**
Linear scenario: $E_{QG1}(GeV)$		
$\xi = +1$	$6.2 \cdot 10^{18}$	$5.4 \cdot 10^{18}$
$\xi = -1$	$2.4 \cdot 10^{18}$	$2.1 \cdot 10^{18}$
Quadratic scenario: $E_{QG2}(GeV)$		
$\xi = +1$	$1.8 \cdot 10^{11}$	$1.4 \cdot 10^{11}$
$\xi = -1$	$1.2 \cdot 10^{11}$	$9.9 \cdot 10^{10}$

Table 5.25: 95% CL limits from the ML analysis, without and with the systematic uncertainties. The coverage correction is included here.

collected in Table 5.24. The limits on the energy scale for the subluminal and superluminal cases, without and with systematics uncertainties, are finally presented in Table 5.25.

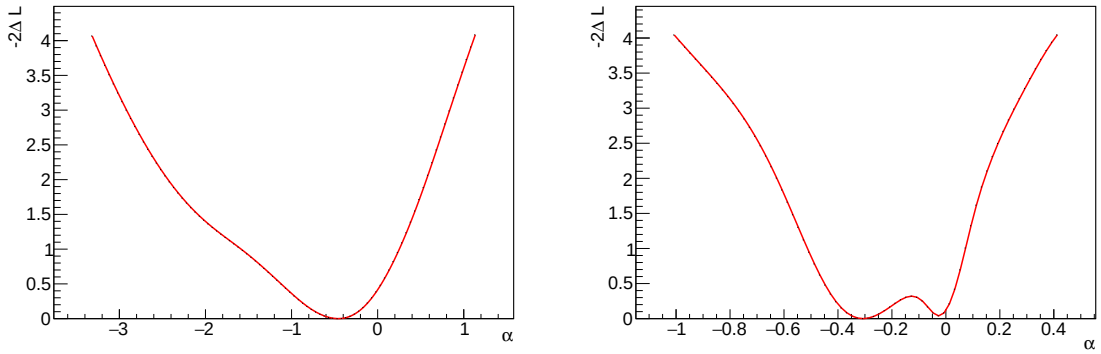

Figure 5.44: Likelihood curve obtained with the 36 ON events template for real data.

From the obtained results, one can see that the ML analysis method is able to greatly improve the results obtained with the alternative simpler methods, namely PV and SMM. In the PV case, the results for the linear scenario were one order of magnitude below this one, while for the quadratic case the limits were two orders worse. For the SMM case, the linear scenario result lies two orders of magnitude below the results of the ML method, while the quadratic case results coincide with the ones obtained with the ML. Probably, an optimized binning as the one used for the ML analysis could further improve the limits

for the SMM analysis. In any case, the better use of additional information, as well as the optimized time template, is expected to translate in an improvement of results for the ML case.

The Likelihood curves in Figure 5.44 present pathologic behaviour in both the linear and the quadratic scenarios. In the linear case, this translates into asymmetric limits that lead to a significant difference of a factor 3 between the limits obtained for the subluminal and superluminal cases. In the quadratic case, one can observe a second minimum, that anyway does not affect much the asymmetry of the limits. This quadratic curve is a good example for the possible case, where the lack of well-behavedness of the Likelihood leads to an increase of the 1σ dispersion, while the upper and lower limits remain approximately constant (see e.q. Table 5.19). In this case, the 2σ limits, given by evaluating $-2\Delta L = 4$, would be practically not affected if the number of minima increases.

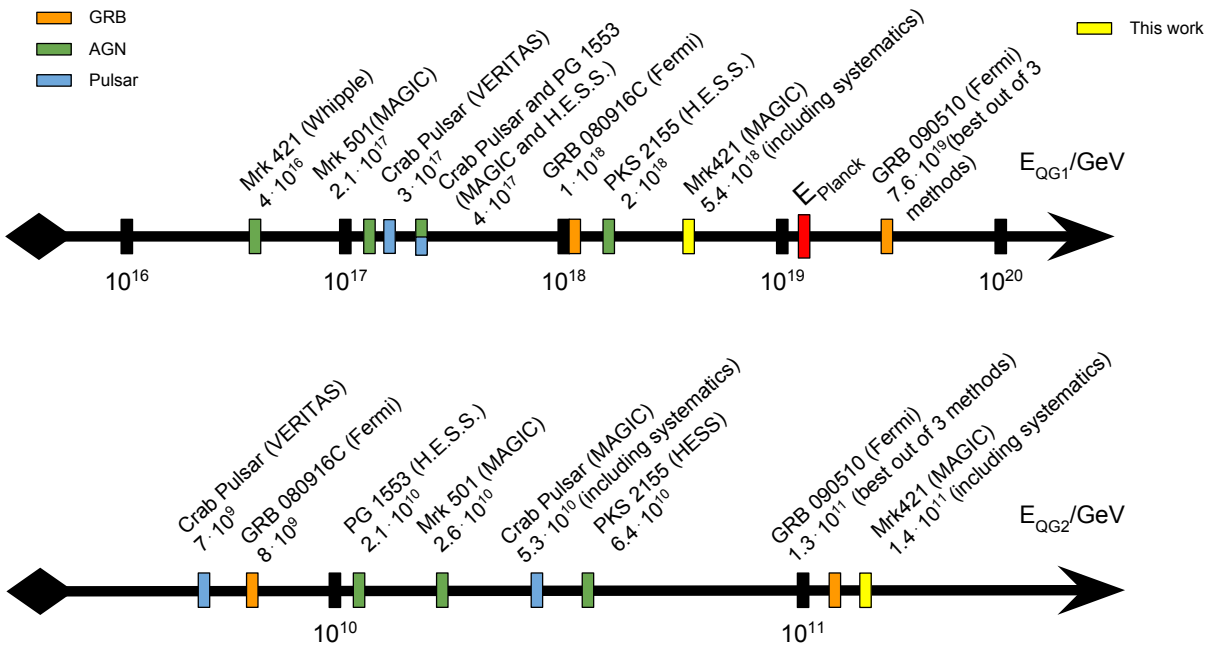

Figure 5.45: Limits on the photon LIV energy scale for the linear (upper part) and the quadratic (lower part) case, including the ones obtained in this work.

Our new limits improve previous constraints obtained from AGN flares (see Figure 5.45), especially for the quadratic case. In the linear case, the limits improve the ones obtained by the PKS 2155 flare observed by H.E.S.S. [269] by a factor of 2 for the subluminal case. Moreover, the linear case improves by an order of magnitude the previous results obtained by MAGIC using the AGN flare of Mrk501 in 2009 [270]. Nevertheless, the obtained results are still one order of magnitude below the current best constraints, obtained with the GRB090510 [275]. However, the limits in [275] do not incorporate the additional systematic uncertainty of 10% due to instrumental effects, claimed by them and require the application of a trial factor, since the limit claimed in the abstract was obtained by selecting, for each case separately, the best of three statistical methods applied over the same data. In the quadratic case, the results improved the ones by the PKS 2155 flare as well by a factor of 2 and the ones obtained by MAGIC with Mrk501 by almost a factor of 4. In this scenario, the results improved even the limits claimed with the GRB090510, in the subluminal and superluminal cases. If we consider only their ML case (see Table 6 in [273]), our subluminal limit is better by an order of magnitude.

In conclusion, we have shown results for a very special flare case. It was composed of a very large amount of events reaching very-high energies, such that an improvement for the limits in the quadratic LIV case was expected. However, it was a very long flare and the source distance was not ideal. We have nevertheless proven that, after profiting from the flare large statistics and a profound study of the possible parametrization for the flare time template, we are able to improve current limits, at the price of having to deal with new effects as the pathological likelihood curves, in our ML analysis.

Chapter 6

LIV Consortium

The LIV Consortium is a collaboration established by a group of scientists belonging to the H.E.S.S., MAGIC and VERITAS collaborations in order to share expertise and data to work together for a joint analysis to study LIV.

This chapter gives an introduction to the group, its members and its goals in Section 6.1, continues with the first trial of a joint LIV analysis in Section 6.2 and finishes with the results of such analysis using simulations of published data detected by the three instruments in Section 6.3.

6.1 Introduction to the collaboration

The LIV Consortium is a team of experts belonging to the H.E.S.S., MAGIC and VERITAS collaborations that share data and look for common protocols for the scientific study of LIV using VHE gamma-ray data from different source types as AGNs, Pulsars and GRBs, with the goal of improving individual results and perform global analysis with different instruments, different sources and more redshift points, reducing therefore the systematic and statistical uncertainties.

The cooperation agreement is stated as an official *Memorandum of Understanding* signed by the Spokespersons of MAGIC and VERITAS and by the Observatory Director of H.E.S.S..

6.1.1 Members

This section describes the 12 members that composed the LIV Consortium by the time the results showed in this thesis were produced.

- H.E.S.S. members
  - Cedric Perennes, Laboratoire de Physique Nucléaire et de Hautes Energies (LPNHE), Paris, France.
  - Julien Bolmont, Laboratoire de Physique Nucléaire et de Hautes Energies (LPNHE), Paris, France.
  - Agnieszka Jacholkowska, Laboratoire de Physique Nucléaire et de Hautes Energies (LPNHE), Paris, France.
  - Robert M. Wagner, Stockholms universitet, Sweden.

- MAGIC members
  - Leyre Nogués, Institut de Física d'Altes Energies (IFAE), Barcelona, Spain.
  - Markus Gaug, Universitat Autònoma de Barcelona and IEEC-CERES, Barcelona, Spain.
  - Manel Martinez, Institut de Física d'Altes Energies (IFAE), Barcelona, Spain.
  - John E. Ward, Institut de Física d'Altes Energies (IFAE), Barcelona, Spain.
- VERITAS members
  - Tony T.Y. Lin, McGill University, Montreal, Canada.
  - Alasdair E. Gent, Georgia Tech, Atlanta, U.S.A.
  - A. Nepomuk Otte, Georgia Tech, Atlanta, U.S.A.
  - Benjamin Zitzer, McGill University, Montreal, Canada.

The group of people composing the LIV Consortium is expected to be temporal and its members can be replaced at any time by the collaboration nominating them, under the condition that the number of experts per collaboration does not exceed 4 people.

Inside every collaboration, the nominated experts compose a Working Group that, only within it, shares data from other collaborations for LIV studies.

In order to become part of the LIV Consortium, the members have agreed previously on several points as objectives, forms of cooperation, confidentiality, property rights or publication procedures.

6.1.2 Objectives and Scope

The objective of the agreement was to establish a framework for the cooperation between different collaborations in order to pursue a combined LIV study.

The shared data provided by each collaboration consists of the individual photon lists of each source observation, that includes reconstructed energy and time of every event, as well as the Instrument Response Functions (IRFs) that indicate the impact of the instruments on the detected data. The different members then agree on protocols to analyze the shared data in order to extract the LIV information.

The data of the shared sources must already be published by the individual collaborations and must belong to any of the three groups: Flaring AGNs, VHE Pulsar or GRBs whenever detected in VHE.

The purpose of the collaboration is to improve the sensitivity of LIV studies and to further extend constraints on various models by combining the different sources detected by the different instruments in a single LIV analysis. The combination of different sources improves the statistical power of published studies, reducing the statistical uncertainties. Moreover, using different kinds of sources, we reduce intrinsic effects and minimize systematic uncertainties related to each individual measurement. Finally, the predicted linear dependence of the LIV effects, once detected, on the source redshift allows to discard hypothesis of the source emission intrinsic time-lags which are in principle redshift independent.

6.2 First LIV combined analysis

In this section, the LIV analysis method for the time-lag determination and the procedure of the source combination are presented and discussed, followed, in the next section, by the results obtained from simulations of the existing published data for the different sources detected by the three different experiments.

6.2.1 Analysis methodology

All the source observations considered for combination in the first LIV Consortium work use the ML method for the extractions of the QG limits. Compared with alternative methods developed in the literature (see Section 3.6), the ML method allows an optimal use of the information contained in the data and allows a straightforward combination of the results from the different observatories. Either in the individual or the combined analysis, the aim of the ML method is to find the value of the LIV estimator that maximizes the likelihood function.

In practice, the concept behind the ML analysis has already been applied by the different observatories and the different source types [270, 269, 289, 273, 275]. Nevertheless, there are fundamental differences: Some observatories use unbinned data while others use binned data. Also, sometimes the ML fit is multi-parametric, where some quantities are treated as nuisance parameters and profiled to propagate their uncertainty, whereas in others is uni-parametric combined with Monte Carlo simulations to estimate the uncertainties in the possible additional parameters. Furthermore, when dealing with sources that have flares (as AGNs) the photon PDF is based of the γ ray arrival time while, for periodic emissions (as Pulsars), it uses the γ ray arrival phase instead.

Here, in order to achieve a combined analysis, all observatories deliver their likelihood functions for the different sources, previously agreed to be uni-parametric, with a common LIV parameter, such that the different likelihoods can be combined into a single likelihood L_{Comb} allowing a joint parameter estimation

$$\mathcal{L}_{Comb}(\lambda) = \prod_{i=1}^{Nsource} L_i(\lambda) \;\longrightarrow\; -2\ln(\mathcal{L}_{Comb}(\lambda)) = -2\sum_{i=1}^{Nsource} \ln(\mathcal{L}_i(\lambda)), \tag{6.1}$$

where λ is the common LIV estimator. To combine different sources from different experiments, the common estimator must be redshift independent.

Once the individual measurements are combined into a single likelihood curve as a function of the LIV parameter, CLs for either a measurement, if the minimum of $-2\ln(\mathcal{L}_{Comb}(\lambda))$ is significantly different from the LI hypothesis, or single-sided CLs can be easily extracted from the χ^2-statistics table [295]. In the results presented in Section 6.3, one-sided 95% CLs are extracted from the point at which $-2\ln(\mathcal{L}_{Comb}(\lambda)) = 2.71$.

6.2.2 Source simulation

The individual sources combined in this first LIV Consortium work are three AGN flares − the Mrk 501 2005 flare detected by MAGIC [328], the PG 1553+113 2012 flare detected by H.E.S.S. [329] and the PKS 2155-304 2006 flare detected by H.E.S.S. [330] − and VHE radiation from the Crab Pulsar detected by VERITAS [331]. The individual simulation settings are summarized in Table 6.1. The first two terms, linear and quadratic in energy in formula 3.2, were considered for the simulation and later analysis.

For testing LIV, and hence the corresponding QG models, we generated simulated data sets constructed from the parametrization of published observational data from the sources mentioned above.

Event true energies and arrival times are generated from the parametrized spectra and lightcurves for each source. The number of simulated events also follows the real data. Possible LIV time-lag effects ($\Delta t \propto E^n$) are added, as required for the linear or quadratic models. IRFs are used to model detection probability and reconstructed energy for each event. Only signal events are considered, except for the

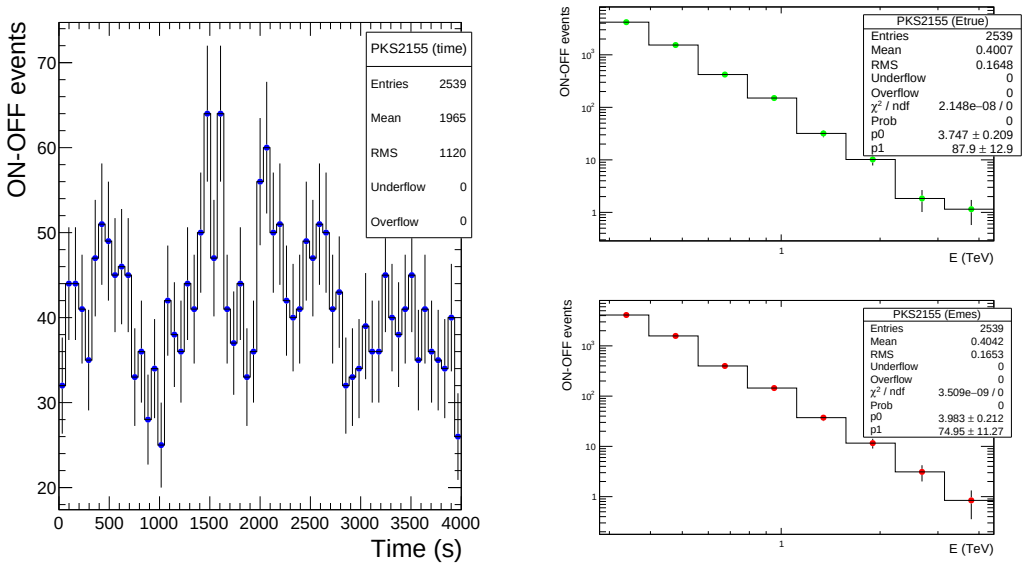

Figure 6.1: Simulated PKS 2155-304 data. Left: time distribution, right: energy distribution (Upper panel, true energy, lower panel, reconstructed energy).

Simulation settings						
Source	Energy Range (TeV)	Time Range	Spectral shape	Lightcurve	Energy resolution	Number of events
PG 1553+113	0.4 - 0.8	0 - 8000 s	PL (Index = 4.8)	Double Gauss	10%	180
Mrk501	0.25 - 11	0 - 1531 s	PL (Index = 2.2)	Simple Gauss	22%	800
PKS 2155-304	0.28 - 4	0 - 4000 s	PL (Index = 3.46)	5 Asymmetric Gauss	10%	2800
Crab Pulsar	0.12 - 7	0 - 1 phase	PL (Index = 3 for signal, 3.5 for bkg)	Double Gauss + Baseline	10%	860000

Table 6.1: Simulation settings for the individual sources.

case of the Crab pulsar, where the background contribution is significantly relevant. For each source, 10^3 measurements are simulated to be used for analysis.

The Monte Carlo (MC) simulation data is analyzed to show that the spectra and lightcurves are compatible with the original data. As an example, Figure 6.1 shows the simulated time and energy distributions for the PKS 2155-304 flare.

6.3 Results on LIV and QG limits

As discussed in Chapter 3, the expected energy-dependent time lag for photons $\Delta t/\Delta E^n$ can be related to E_{QGn} as

$$\frac{\Delta t_n}{\Delta E^n} \simeq s_{\pm}\,\frac{n+1}{2\,H_0}\,\frac{1}{E^n_{QG}}\int_0^z \frac{(1+z')^n}{\sqrt{\Omega_m\,(1+z')^3+\Omega_\Lambda}}\,dz' = s_{\pm}\,\frac{n+1}{2\,H_0}\,\frac{1}{E^n_{QG}}\kappa(z), \tag{6.2}$$

being Ω_m and Ω_Λ the standard cosmological parameters [248].

Limits on $\Delta t/\Delta E^n$ provide an estimation of E_{QGn} at one-sided 95% CLs. Equation 6.2 takes into account the expansion of the universe and was used for the QG limit calculations in the cases $n = 1, 2$, with the parameter $\kappa(z)$ being referred to $\kappa_l(z)$ for the linear and $\kappa_q(z)$ for the quadratic case.

The estimator λ is defined as

$$\lambda = \frac{\Delta t_n}{\Delta E^n \kappa(z)} = \frac{1}{E^n_{QG} H_0}, \tag{6.3}$$

Parameter	PKS 2155	Mrk 501	PG 1553	Crab Pulsar	Combination
λ_{best} (s/TeV)	-4.5±2.6	4.9±5.6	-11.3±13.4	-5.4±4.7	-2.37±2.2
1σ CL (s/TeV)	84.6±2.1	168.6±4.4	412.0±9.7	146.0±3.8	67.6±1.6
λ_{LL} (s/TeV)	-154.9	-296.6	-687.7	-254.2	-118.2
RMS$_{LL}$ (s/TeV)	88.8	169.9	414.5	150.4	67.52
λ_{UL} (s/TeV)	142.5	299.5	658.6	244.7	117.8
RMS$_{UL}$ (s/TeV)	83.72	171.6	421.4	151.3	66.1

Table 6.2: Linear case: best λ values and one-sigma 95% CL Upper Limits on λ for each source and combination. The standard deviations and RMS values for the limits are also shown

Parameter	PKS 2155	Mrk 501	PG 1553	Crab Pulsar	Combination
λ_{best} (s/TeV^2)	1.3±1.9	-0.8±1.1	1.0±17.5	3.8±6.4	-0.6±0.9
1σ CL (s/TeV^2)	59.8±1.7	31.85±1.0	533.7±13.2	189.5±5.6	26.7±0.7
λ_{LL} (s/TeV^2)	-104.4	-59.2	-912.1	-326.6	-49.5
RMS$_{LL}$ (s/TeV^2)	69.2	33.2	542.1	351.0	28.9
λ_{UL} (s/TeV^2)	100.0	56.8	921.1	354.2	48.1
RMS$_{UL}$ (s/TeV^2)	67.9	34.1	554.2	355.0	28.0

Table 6.3: Quadratic case: best λ values and one-sigma 95% CLs Upper Limits on λ for each source and combination. The standard deviations and RMS values for the limits are also shown.

and allows a simultaneous analysis of sources with different redshifts (opposite to $\Delta t/\Delta E^n$, which is redshift dependent). A study of the precision of the estimated parameter λ with representative MC simulations of the sources mentioned in the previous section is the main aim of the first LIV combined analysis.

In order to obtain an estimation of the attainable precision, no initial time-lag has been injected in the simulated data samples. The analysis of each source as well as their combination provided the best fit value for the parameter λ, as well as one-sided 95% CLs. The distributions of λ and CLs were built with 10^3 realizations allowing to evaluate the statistical probability to obtain a given result. As no systematic effects have been introduced in the likelihood fits, both λ and CLs present Gaussian behavior as seen in Figure 6.2. Later, these statistical uncertainties with the systematic ones are added in quadrature when calculating the E_{QGn} limits.

The combined results for $n = 1, 2$ and their Gaussian fits are exposed in Figure 6.2. Tables 6.2 and 6.3 summarize the mean fit values, standard deviations and CLs for λ, for the individual and combined cases and for the linear and quadratic model, respectively. It should be noted that independently of the source redshift, the reconstructed mean values of the time-delay reproduce well the initial value of time-lag equal to zero within slightly more than 1 σ deviation in the linear case and less than than 1 σ deviation in the quadratic case. Thus no systematic shift is introduced by the method in use. Furthermore, a comparison of the results for each source and their combination is shown in Figure 6.3.

The hypothetical limits on E_{QGn} are collected in Table 6.4 and graphically represented in Figure 6.4. These limits were computed considering both statistical and systematic uncertainties; the systematic uncertainty is conservatively taken to be equal to the statistical error in this study.

As the main conclusion, the limits improve with the combination procedure. Still, one can observe that in the linear case the results are strongly dominated by PKS 2155-304, less relevant for the quadratic

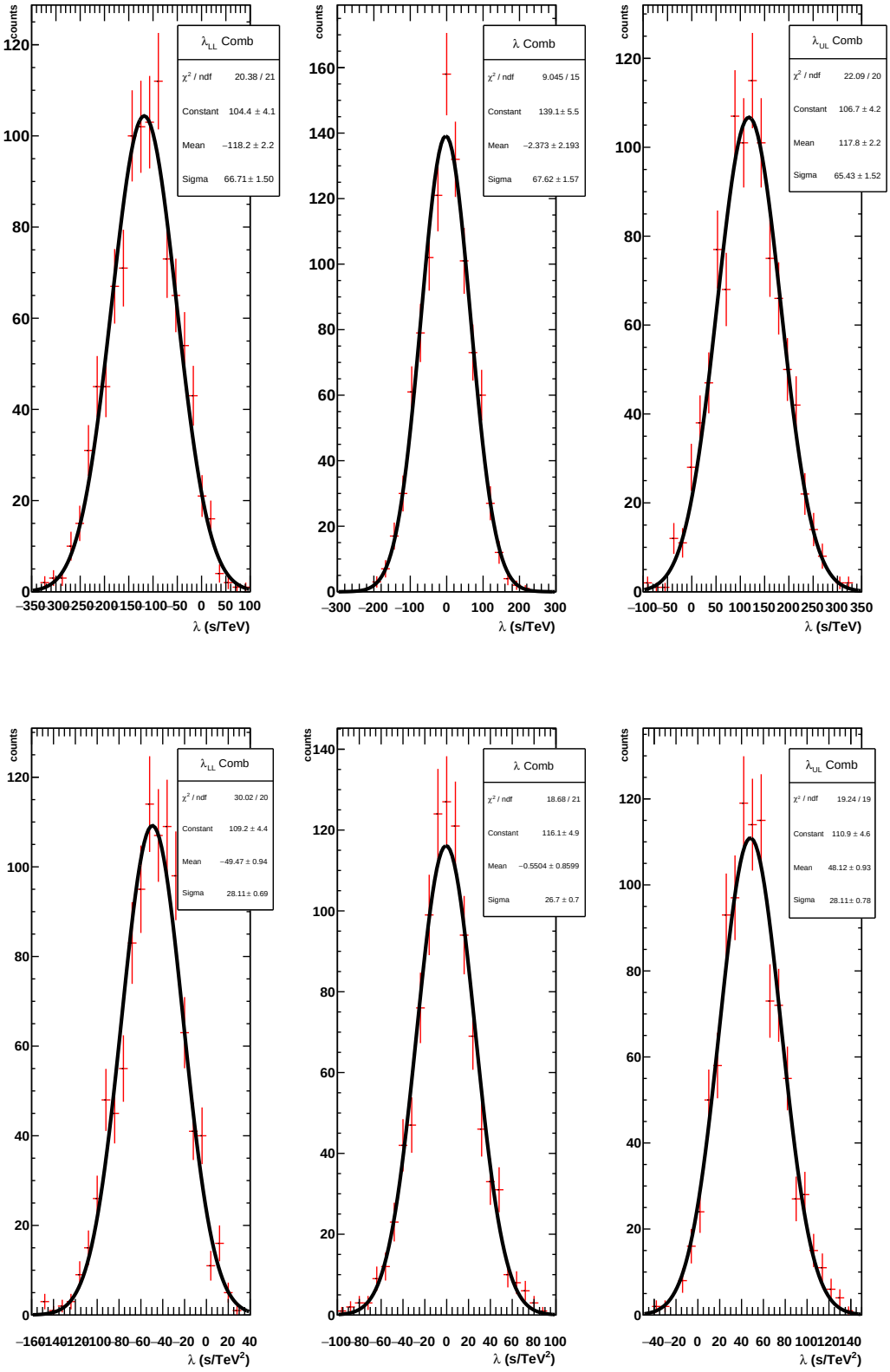

Figure 6.2: Distributions of the best λ values for the combined analysis, up: linear case, down: quadratic case. The curves represent the Gaussian fits to the distributions. The Constant parameter is related to the number of simulations used for the study. The Mean parameters are used to compute the values of λ_{best}, λ_{UL} and λ_{LL} shown in Tables 6.2 and 6.3 with their errors for the 10^3 simulations. The Sigma parameters express the variance or dispersion in the results, also shown in Tables 6.2 and 6.3.

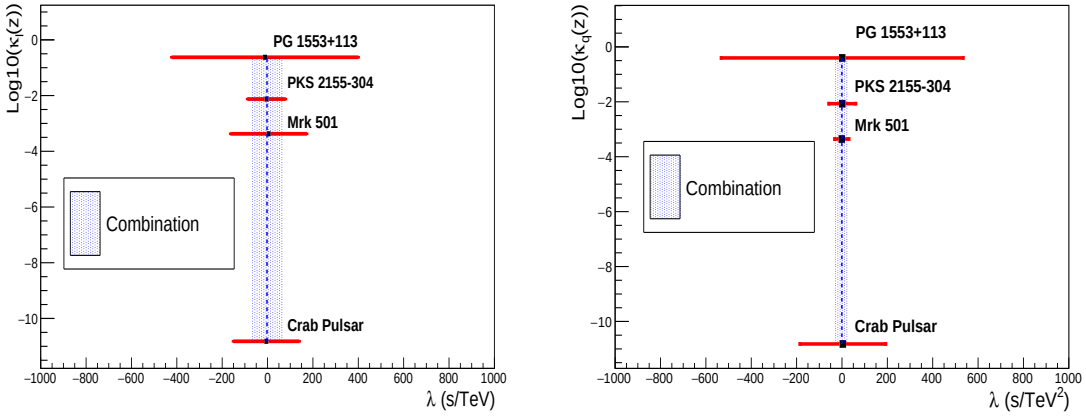

Figure 6.3: Hypothetical mean best λ values and standard deviations (x-axis) for each source and their combination, as a function of the redshift-dependent $\kappa(z)$ parameter (y-axis). Left - linear case, right - quadratic case. The values were obtained from Gaussian fits to the distributions of reconstructed λs.

Source	$E_{QG\_linear}(10^{18}GeV)$	$E_{QG\_Quadratic}(10^{10}GeV)$	Redshift
PKS 2155	1.86	6.20	0.116
Mrk 501	0.91	8.57	0.034
PG 1553	0.38	2.08	0.5
Crab Pulsar	1.07	4.14	2kpc
Combination	2.31	9.34	-

Table 6.4: One-sided 95% CL upper limits on the QG energy scale for the linear and quadratic case, for each source and their combination.

case, where Mrk 501 provides already an outstanding result. In the quadratic case, a 26% improvement is obtained with the combination, and a 10% in the linear case, respectively. The source PG 1553+113 provides important results at very-high-redshift even if contributing at a lower level to the combination, however extending redshift range closer to those found with GRBs [275]. The Crab Pulsar does not contribute to the redshift range, but instead, by increasing importantly the number of events. In the future, more sources will be added to this study leading to a larger extension of the redshift range and available events.

6.3.1 Conclusions and prospects

The LIV Consortium constitutes the first inter-experiment working group in VHE gamma-ray astronomy, consisting of members of the H.E.S.S., MAGIC and VERITAS collaborations. The joint ML analysis allows the measurements from different sources from several different instruments to be combined in a relatively straightforward manner. Simulations generated with inputs from published source observations have been used to show that a more sensitive search for LIV through time-of-flight measurements can be performed than any individual search on a single target or instrument.

As a second project, the LIV Consortium is currently investigating the systematic effects on the measurements and including them directly into the combined likelihood curve. Moreover, the number of candidates for the combined study is increasing as the new flares, as the one presented in Chapter 5, are ready to be incorporated. The benefits of the above presented combined method can be used for all

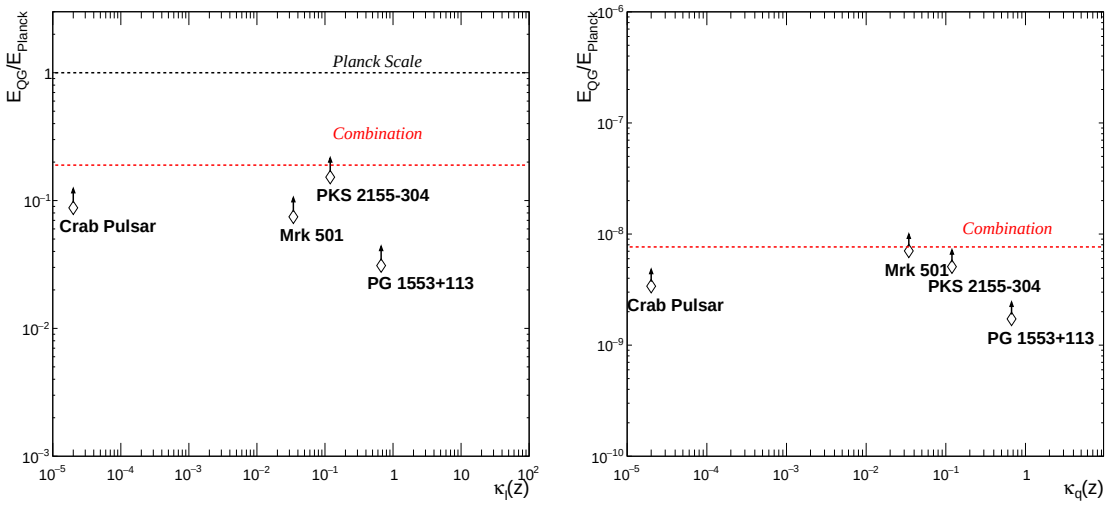

Figure 6.4: Lower limits on E_{QGn} as a function of the redshift-dependent parameter $\kappa(z)$. Sub-luminal case considered. On the left, the linear case and, on the right, the quadratic case. $E_{Planck} = 1.22 \cdot 10^{19}$ GeV.

existing and future gamma-ray experiments, including the upcoming Cherenkov Telescope Array (CTA) [332].

Summary and Conclusions

The first chapters of this thesis were dedicated to offer a general overview of the physics framework used to develop the main topic of this work: Experimental tests of Lorentz Invariance Violation (LIV) with the Time-of-Flight technique using very energetic gamma-ray radiation from different kinds of astrophysical sources. Chapters 5 and 6 described the original research to the field by this thesis, first with a single source observed by MAGIC and later whitin a collaboration of IACTs analyzing a combined set of sources. Appendix A is devoted to the personal contribution of the author to the construction of a new IACT, namely the first LST.

LIV is one of the expected consequences of the case that the gravitational field presents a quantum behaviour. Such effect, predicted by several theories and parametrized in different ways, is proportional to some function of the energy of the particles and to the distance they have travelled. This thesis reports on a study of LIV with the MAGIC telescopes, observing very high energy gamma-ray radiation from a fast varying signal produced by an Active Galactic Nucleus (AGN). The results obtained are preceded by a process of selection of suitable AGN flares among the ones detected by MAGIC. For such a selection, together with technical help from the MAGIC data center, we created a database containing all the flares detected by MAGIC since 2005. That database is now finished and used by the MAGIC collaboration members to select sources for any kind of study. In our case, the selected candidate was a flare from the blazar Mrk 421, detected on April 24, 2014. The flare is composed of more than 12000 gamma-ray events, distributed over 3 hours of observation and reaching energies of more than 30 TeV. This candidate constitutes the longest and most powerful flare used for LIV studies up to date, with a 7 Crab Units (C.U.) flux in its strongest periods. The analysis of the data was modified with respect to the previous standard of the MAGIC collaboration, in order to introduce a better energy estimation, based on Random Forest (RF) decision trees, which translated into an improvement of the energy resolution and hence the sensitivity to LIV. For the LIV study presented in this thesis, we used the Time-of-Flight technique that searches for energy-dependent time delays between photons. First, we applied two simpler analysis approaches, called PairView (PV) and Sharpness-Maximization Method (SMM), that use only the energy and arrival time of the detected gamma-ray events, but do not take into account other experimental effects. No significant energy-dependent delay due to LIV was detected with these methods and we could set upper limits on the expected energy scale for Quantum Gravity (QG) of $E_{QG1} > 3.3 \cdot 10^{17}$ GeV and $E_{QG2} > 1.1 \cdot 10^{11}$ GeV for the linear and quadratic scenarios, respectively. Secondly, we have studied such energy-dependent delays using a more complex analysis based on the Maximum Likelihood (ML) technique. The ML analysis is also an event-wise method that additionally allows to exploit any other

available information as the experimental and propagation effects of the detected photons. The thesis has described the extraction, parametrization and introduction of all available information from the flare within the ML analysis. We performed a profound study of the time template parameterization for this flare, difficulted by the possible presence of internal variability and its long duration. We discarded the otherwise common strategy of using a pre-defined function fitted to the lightcurve. Moreover we have studied, but later discarded, the method of an interpolation of the data histogram with fixed time binning, and the Kernel Density Estimation (KDE) method. Finally, we selected an interpolation of a variable binned histogram, in order to maximally exploit the information in our flare statistics. Such binning has been defined by requiring a given Poissonian detection significance in every lightcurve bin. The Poissonian fluctuations associated to each bin were studied independently with simulations. With such an adapted time template, no significant LIV time delays were found. We were then able to set upper limits on the QG energy scale that are among the most constraining obtained by any IACT up to date. For the linear scenario, we obtained $E_{QG1} > 5.4 \cdot 10^{18}$ GeV, yielding more than a factor two improvement with respect to previous limits set with AGN flares. The limits obtained with GRBs still remain one order of magnitude above ours. In this linear scenario, the source distance plays an important role such that it was already expected that constraints from GRBs were stronger than those from AGNs, located at closer distances. In the quadratic scenario, however, due to the importance of the energy, our limits are the most constraining ones obtained so far, setting a limit on the QG energy scale of $E_{QG2} > 1.4 \cdot 10^{11}$ GeV. Apart from this improvement, our analysis shows a new approach to define a time template parametrization for ML analyses, adapted for long flares with high number of events and shows the consequences of such a choice. This work paves the way for the analysis of future LIV candidates detected with CTA, because, due to its improvement in sensitivity and energy reconstruction, the features found in our source are expected to be common in future detections by CTA.

The second result of this thesis comes from the first combined LIV analysis using different kinds of sources detected by distinct experiments. Such an analysis has been developed in the framework of the LIV Consortium, a collaboration between all current ground-based IACT experiments (MAGIC, H.E.S.S. and VERITAS). The analysis made use of simulated data sets, based on the published time and energy parametrizations of the different sources, provided by the corresponding experiments. The analysis method is again the ML, adapted to combine sources located at different distances. From the analysis outcome, we were able to prove that a combined analysis can set constraints on the QG energy scale that surpass the ones obtained for individual sources. Such results, $E_{QG1} > 2.3 \cdot 10^{18}$ GeV and $E_{QG2} > 9.3 \cdot 10^{10}$ GeV for the linear and quadratic scenario, respectively, present an improvement of 26% and 10% with respect to the best individual results, but do not yet include the previously presented flare of Mrk 421. Consequently, we could show that combining several sources leads to improvements in the study of LIV, as well as greatly reducing the importance of intrinsic source effects at the same time. The predicted increase of the amount of sources included in this study, as the number of detected suitable sources, the distance range and the increase of the number of events will lead to a further improvement of the sensitivity to LIV. The start of operation of CTA will surely speed up this process.

The study of the LIV effect with MAGIC and the rest of IACTs will continue in the coming years. The detection of new suitable sources and their combination will surely boost the sensitivity even further. A hypothetical detection of such an effect would set a revolution at the experimental and theoretical level that could completely change our current understanding of gravity, allowing us to approach the goal of a

unified theory.

Conclusiones

Los primeros capítulos de esta tesis están dedicados a ofrecer un resumen general del marco físico en el que se desarrolla el tema de este trabajo: la búsqueda experimental de la ruptura de la invarianza Lorentz con la técnica "Tiempo de Vuelo", haciendo uso de radiación gamma de alta energía, proveniente de diferentes tipos de fuentes astrofísicas. Los capítulos 5 y 6 describen el trabajo original de investigación esta tesis como contribución aportada a la ciencia. Dicho trabajo hace uso, primero, de una sola fuente detectada por los telescopios MAGIC, y segundo, de un conjunto de fuentes detectadas por todos los telescopios terrestres Cherenkov, trabajo desarrollado en colaboración con dichos telescopios. El anexo A describe la contribución personal del autor en la construcción del telescopio LST, el primero de los que compondrá el nuevo observatorio "Cherenkov Telescope Array".

Se espera que la ruptura de la invarianza Lorentz sea una consecuencia física si el campo gravitatorio presenta un comportamiento cuántico. Este efecto, predicho por múltiples teorías y parametrizado de diversas formas, afecta a las partículas en proporción a su energía y a la distancia que han recorrido. Esta tesis recoge un estudio sobre la ruptura de invarianza Lorentz con los telescopios MAGIC, mediante radiación gamma muy energética. Los resultados obtenidos están precedidos de un proceso de selección de emisiones adecuadas para el estudio, entre todas las emisiones procedentes de galaxias lejanas detectadas por MAGIC. Para dicha selección, contando con ayuda técnica, se ha creado una base de datos que contiene todas las emisiones de dichas características detectadas por MAGIC desde 2005. Esta base de datos está terminada y los miembros de MAGIC hacen uso de ella para la selección de emisiones para diversos tipos de estudios. En nuestro caso, la emisión seleccionada procedía de la galaxia Mrk421 y se detectó el 24 de Abril de 2014. Esta emisión se compone de más de 12000 eventos, distribuidos a lo largo de 3 horas de observación y con energías que alcanzan los 30 TeV. Esta emisión constituye la más fuerte y extensa utilizada para estudios de ruptura de la invarianza Lorentz, con un flujo de 7 "Crab Units" (C.U., el flujo de la Nebula del Cangrejo se utiliza para comparar la fuerza en la emisión de otras fuentes en astronomía de rayos gamma), en su sección más fuerte. El análisis original de los datos se modificó para basar la reconstrucción de la energía de los fotones en el método llamado "Random Forest", que supuso una mejora en la resolución de la energía y, consecuentemente, en la sensibilidad para la detección de la ruptura de la invarianza Lorentz. Para el estudio de dicha ruptura, empleando la técnica "Tiempo de vuelo", se hizo uso de dos métodos de análisis simples − llamados "PairView" y "Sharpness Maximization" − que requieren únicamente la información sobre la energía y el tiempo de llegada de los fotones. Con dichos métodos, no se pudo encontrar un retraso temporal en el tiempo de llegada de los fotonoes debido a la ruptura de invarianza Lorentz con suficiente significancia. Sin embargo, pudieron ponerse límites en

la escala de energía esperada para Gravedad Cuántica: $E_{QG1} > 3.3 \cdot 10^{17}$ GeV y $E_{QG2} > 1.1 \cdot 10^{11}$ GeV para el caso linear y cuadrático, respectivamente. En segundo lugar, se han estudiado estos retrasos con un método de análisis más complejo, llamado "Maximum Likelihood". Este método hace uso de toda la información disponible sobre los efectos instrumentales o de propagación que afectan a los fotones, además de sus energías y tiempo de llegada. En la tesis se detalla la extracción y parametrización de todos los efectos mencionados, para introducirlos en el análisis. En particular, se hizo un minucioso estudio sobre la parametrización de la distribución temporal de los fotones, necesario por la longitud de la emisión y la posible presencia de variabilidad interna. Como resultado de este estudio, se descartaron ciertas parametrizaciones como el ajuste de una función al histograma de datos o la interpolación de dicho histograma con barras de amplitud fija. Finalmente, se escogió como parametrización la interpolación del histograma mencionado anteriormente pero con barras de amplitud variable, dependientes del número de eventos de la emisión, para poder hacer el mejor uso de la amplia estadística ofrecida por nuestra emisión. La amplitud de dichas barras se ha calculado para obtener una significancia concreta en cada barra del histograma. Además, se han estudiado, mediante datos simulados, las fluctuaciones de Poisson asociadas a dichas barras. Con esta parametrización adaptada a nuestro caso, tampoco ha podido hallarse un retraso temporal en el tiempo de llegada de los fotones con suficiente significancia. Sin embargo, se han puesto límites en la escala de energía para Gravedad Cuántica que superan a los límites anteriores obtenidos por otros telescopios terrestres Cherenkov. En el caso lineal, se obtiene $E_{QG1} > 5.39 \cdot 10^{18}$ GeV, que presenta una mejora de un factor 2 respecto a otros límites conseguidos mediante emisiones de galaxias lejanas. Pese a esto, los límites obtenidos usando "Explosiones de rayos gamma" ("Gamma Ray Bursts" en inglés), se sitúan todavía un orden de magnitud por encima de los nuestros. Este hecho se esperaba puesto que, en el caso lineal, la distancia de las fuentes tiene un papel principal y las galaxias lejanas están más próximas que las "Explosiones de rayos gamma", por lo que los fotones han viajado una distancia menor. Por otra parte, en el caso cuadrático el papel clave lo desarrolla la energía de los fotones, por lo que nuestro límite $E_{QG2} > 1.4 \cdot 10^{11}$ supera todos límites establecidos hasta la fecha. Aparte de estas mejoras en los resultados, nuestro método introduce una nueva forma de parametrización para el "Maximum Likelihood" análisis y muestra las consecuencias de dicha parametrización. El análisis mostrado en esta tesis puede servir de guía para futuros análisis que busquen ruptura de la invarianza Lorentz con fuentes detectadas por el observatorio "Chrenkov Telescope Array", puesto que su mejora en sensibilidad y reconstrucción de la energía, hará que estas fuentes compartan muchas características con la que hemos empleado en nuestro caso.

El segundo resultado presentado en esta tesis procede de un estudio combinado de diversas fuentes de varios tipos detectadas por diferentes experimentos para la búsqueda de la ruptura de invariancia Lorentz. Este análisis combinado se ha desarrollado dentro del "LIV Consortium", una colaboración entre todos los telescopios terrestres Cherenkov activos a nivel mundial. Para dicho análisis, se ha hecho uso de datos simulados, basados en las características energéticas y temporales de los datos reales detectados por los telescopios, proporcionadas por ellos mismos. El método de análisis empleado es "Maximum Likelihood", adaptado para lidiar con fuentes situadas a diferentes distancias. De los resultados del análisis, hemos podido probar que el análisis de la combinación de un conjunto de fuentes proporciona unos límites en la escala de energía de Gravedad Cuántica que superan a los obtenidos con fuentes individuales. Dichos resultados, $E_{QG1} > 2.3 \cdot 10^{18}$ GeV para el caso lineal y $E_{QG2} > 9.3 \cdot 10^{10}$ GeV para el caso cuadrático, mejoran los obtenidos de forma individual en un 26% y 10%, respectivamente. Este estudio combinado

no incluye la emisión de Mrk 421 presentada anteriormente. Como consecuencia, hemos visto que la combinación de fuentes supone una mejora en el estudio de la ruptura de la invarianza Lorentz, así como una disminución de los efectos temporales intrínsecos asociados a las fuentes. El número de fuentes empleadas en este análisis está predicho que crezca, lo que se traduciría en un mayor número de fotones, provenientes de un mayor numero de distancias diferentes, lo que aseguraría una mejora en la sensibilidad del análisis. El comienzo del funcionamiento del observatorio "Cherenkov Telescope Array" acelerará este proceso.

El estudio de la ruptura de la invarianza Lorentz con los telescopios MAGIC así como con el resto de telescopios y satélites continuará en los próximos años. La detección de nuevas emisiones adecuadas para este estudio y su posterior combinación desembocará en una mejora de la sensibilidad que pueda desembarcar en una detección del efecto. La hipotética detección de la ruptura de la invariancia Lorentz supondría una revolución a nivel teórico y experimental que llevaría a un cambio completo de nuestro concepto actual de la gravedad, permitiéndonos acercarnos al objetivo de la "Teoría del todo".

Appendix A

Contribution to the Cherenkov Telescope Array: level-0 and level-1 trigger calibrations of the Large-Sized Telescope camera

Among the different telescope sizes that will compose each of the two arrays of the new gamma-ray observatory called Cherenkov Telescope Array (CTA), one in the Southern (Chile) and one in the Northern hemisphere (Canary Islands, Spain), the Large-Sized Telescopes (LSTs) will be the largest ones. There will be 4 LSTs in the central region of each of the two arrays.

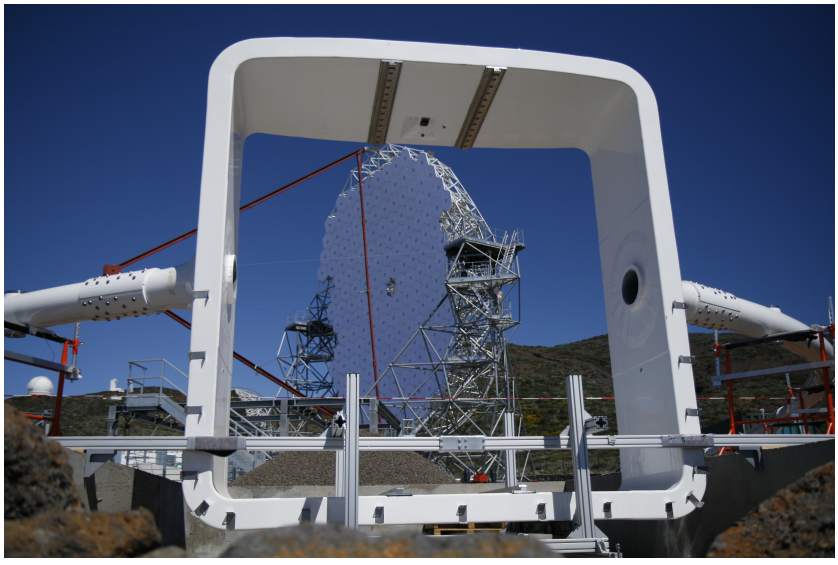

Figure A.1: Front part: Arc and supporting structure for the camera, mounted but still not installed on the telescope. Back part: Current view of drive structure of the LST prototype, with the mirrors already installed and a dummy camera structure (in red), used for the mirror installation. Credit: Dr.P.Peñil

At the moment of writing of this thesis, the construction of the first LST for the Northern location was in an advanced state, while the telescope drive structure, the mirrors and the arc supporting the camera were already installed at the Canary Island of La Palma (see Figure A.1), the full camera was at the

IFAE workshop, in Barcelona, to test and verify the different subsystems and their communication and response (see Figure A.3). The camera was sent to La Palma at the end of July 2018 for the telescope to be inaugurated, according to schedule, in October 2018, with a commissioning period lasting up to mid-2019. The main goal of this first prototype is to verify the design parameters of the structure and the camera.

This chapter focuses on this first telescope prototype, with a brief overview of the whole instrument and later on one of the parts of the telescope camera, its trigger system. The different calibrations designed to achieve a homogeneous spatial and temporal response of the trigger system will be exposed in detail and their structure and launching procedure explained. The chapter aims to show the design and indications to use such calibrations as well as their reason-to-be.

A.1 Introduction to the Large-Sized Telescope

The construction of the first LST telescope was carried out by the *"LST consortium"*, composed of more than 100 scientists from 10 different countries, with Spain among them. The telescope will cover the unique low energy region of CTA, between 20 and 150 GeV.

At such low energies, gamma rays produce a small amount of Cherenkov light, requiring telescopes with large mirror surface in order to be able to capture such faint signals.

Required energy range	Above few tens of GeV
Number of telescopes (per array)	4
Optical design	Parabolic
Reflector diameter	23 m
Effective mirror area	370 m^2
Focal length	28 m
Total weight	103 tons
Field of view	4.5°
Number of camera pixels	1855
Pixel size	0.1°
LST Array trigger rate	24 Gb/s
Positioning time	<30 s
Pointing precision	<14 arcseconds

Table A.1: LST prototype specifications.

With a structure similar to the MAGIC telescopes (described in Chapter 4), the LST is an alt-azimuth telescope (see Figure A.2), with a 23 m diameter parabolic reflective mirror surface. The reflective surface of 400 m^2, is supported by a tubular structure of reinforced carbon fiber and steel tubes. The Cherenkov light is collected and focused by the mirrors onto the camera, where it is converted to electrical signals by photomultiplier tubes. Later on, these signals are processed by dedicated electronics. The main design parameters of this telescope can be found in Table A.1.

The LST will stand 45 m tall and weigh around 100 tonnes, with a large but light camera. However, it will be extremely swift, with the goal to be able to re-position within 20 seconds, in order to catch VHE transient events, as GRBs. A more detailed description of the telescope can be found in [333].

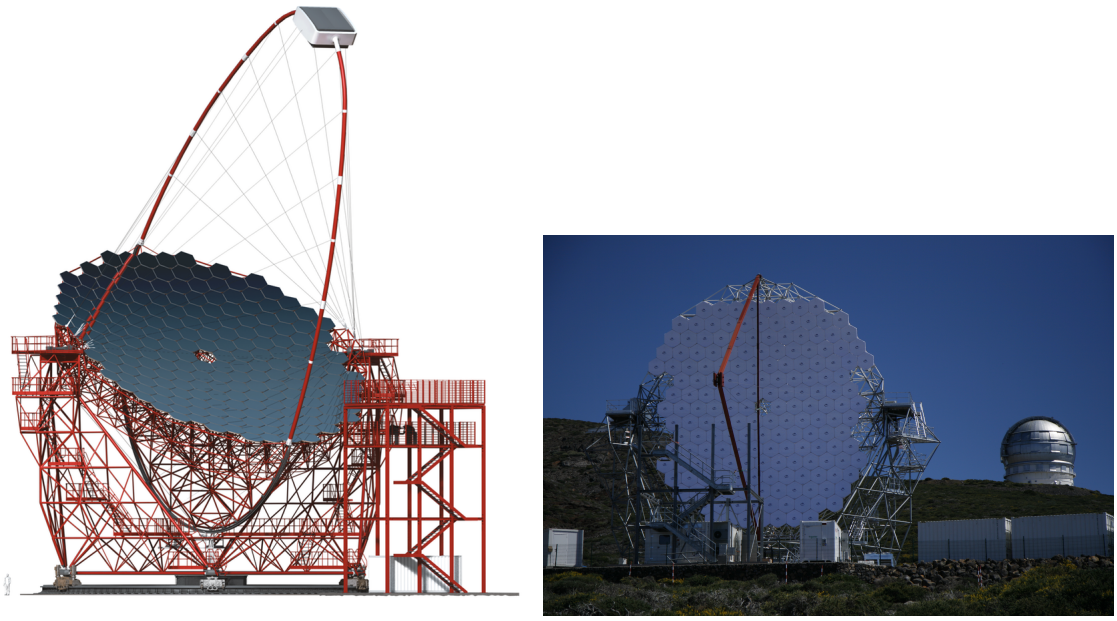

Figure A.2: Left: Illustration of the LST telescope with the main assemblies. Right: Current status of the LST prototype, on the background, the GTC telescope. Credit: Dr.P.Peñil.

A.2 Large-Sized Telescope camera

The LST camera is light, with a weight of less than two tons. It is composed of a total of 1855 PMTs, grouped into 265 modules named clusters, that are easy to access and maintain (see Figure A.3). The clusters are composed by groups of 7 pixels. For every pixel, the PMT, with a maximum quantum efficiency of 42 %, converts the Cherenkov light to electrical signals and is equipped with a light concentrator, in order to lose a minimal amount of light due to the space between pixels.

The camera has a total FoV of about 4.5° and has been designed for maximum compactness and lowest weight, cost and power consumption while keeping optimal performance at low energies. Each pixel incorporates a photosensor as well as the corresponding readout and trigger electronics, based on the Domino Ring Sampler Version 4 (DRS4) chip [305], currently in use by the MAGIC telescopes.

The trigger strategy is based on the shower topology and the temporal evolution of the Cherenkov signal recorded in the camera, by searching extremely short but compact shower images. Moreover, the LST cameras are interconnected in order to form an on-line coincidence trigger between the telescopes, to decrease the probability of accidental triggers. The next section will treat in detail the pixel-level and cluster-level trigger.

A.3 Camera Trigger system

The trigger strategy, followed by IACT cameras, consists on looking for gamma-ray signals contained in a relatively small region of the camera and detected within a few nanoseconds time window. Such a strategy aims to reduce the accidental triggers due the NSB, while preserving the trigger efficiency for gamma rays .

The LST trigger system, designed to decide whether an event stems for a gamma-ray shower and should be recorded or not, counts with two trigger schemes defined as "Majority" and "Sum" trigger,

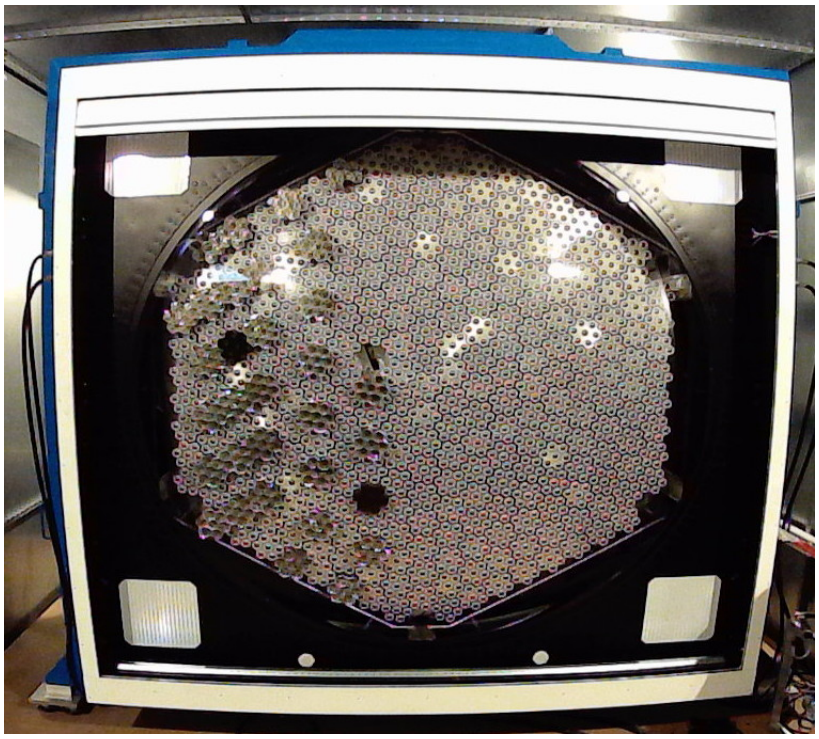

Figure A.3: Picture of the camera at the IFAE workshop during the test period. Most of the clusters are mounted, some of them with the light concentrators on top. Credit: IFAE.

detailed in the next section.

Moreover, the LST trigger relies on the above-mentioned 7-pixels clustering of the camera, defining the trigger regions as different combinations of the signals from each cluster and its neighbours (see Figure A.4).

In the case of the LSTs, with the aim of improving the sensitivity to the faint showers caused by low-energy gamma rays , the different LST telescopes share their trigger information to implement a hardware stereo trigger scheme.

A.4 Trigger structure

This section exposes the three stages that compose the trigger structure. Each module counts with its own trigger electronics, connected with the signal coming from other neighbouring modules. Figure A.4 shows the neighbouring signals arriving at the central cluster trigger with black lines.

The first stage, called L0-level trigger (from now on L0 trigger), collects the analog signals coming from the different pixels and combines them into a single output, that depends on the trigger scheme in use. Such output is moved to the second stage, called L1-level trigger (from now on L1 trigger). At this level, the analog combination of pixel signals coming from that module or from any other neighbouring module or a combination of the latter, is examined.

The L1 stage takes the decision to trigger the camera if the final combined signal exceeds a given threshold. The decision is propagated to the third stage, the Trigger Interface Board (TIB). According to the camera state and the possible coincidences with neighbouring LSTs, the TIB generates a stereo event trigger, sending it back to the modules, so that the readout process can start.

This section will not go further in detail about the TIB, a device to manage the different trigger and timing signals between LSTs. Further information can be found in [334].

A.4.1 L0-level trigger

In a given module, the L0 trigger receives the signals from the 7 channels or pixels composing such module. Those signals can be configured by adjusting several parameters – delay lines, pixel gain, etc. (see Section A.6) – before being added together. Their combination is then replicated 6 times and sent to the different L1 triggers: one located in that same module and the rest in the neighbouring ones. The replicated signals are received by the three adders of the L1 triggers (more details in Section A.4.2). The reason to replicate the L0 signals and to use three adders at L1 level is to have a full coverage and a correct superposition of the cluster signals for the different trigger patterns. Figure A.4 shows the modules in yellow, with the central module showing the neighbouring L0 arriving signals with black lines and the L0 produced signals, replicated and distributed to the neighbours, with red lines.

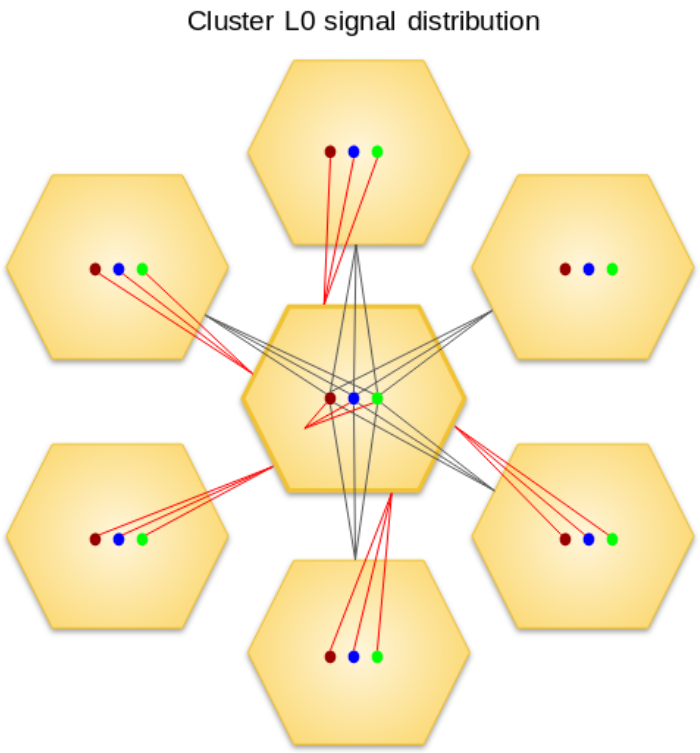

Figure A.4: Diagram of L0 signal distribution among neighbouring clusters. The three central points represent the three adders at L1 level. The black lines indicate the L0 neighbours' signals that arrive at the adders of the central cluster. The red lines indicate the L0 signal produced at the central cluster, that is copied and sent to its own adders and to the neighbouring clusters' adders.

The L0 level counts with two trigger schemes, in order to possibly apply two alternative trigger concepts: Majority and Sum Trigger.

Majority Trigger

The Majority trigger compares the signal from each pixel with a threshold (DTL0 from now on). If the signal amplitude is greater than DTL0, a squared pulse is generated, with a fixed amplitude of 100 mV and

a width that corresponds to the time-over-threshold (see Figure A.5). The DTL0 value can be configured to be different for every pixel. This discrimination process is repeated for the seven pixels and the resulting squared pulses are added such that the resulting signal has an amplitude proportional to the number of pixel signals above their corresponding DTL0. Such resulting signal is then sent to the L1 level.

Both trigger schemes count with an attenuation circuit (see Section A.4.1), that allows for a gain adjustment of the pixel signal (see Figure A.6).

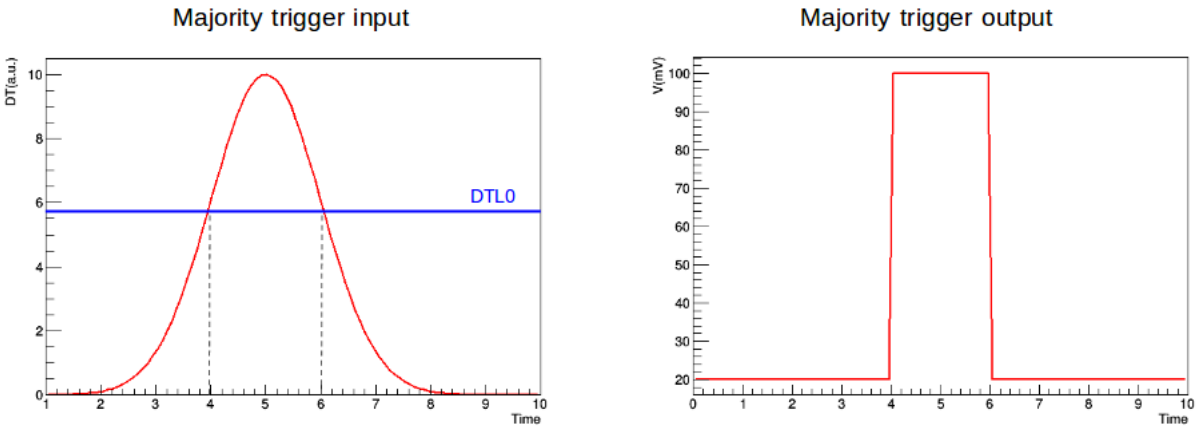

Figure A.5: Simplified representation of the input and output pixel signals with the Majority trigger scheme. On the left, the analog input signal that surpasses the DTL0 threshold value between 4 and 6 ns, in this graphical example. On the right, the produced output, corresponding to a squared digital pulse with an amplitude of 100 mV and a width from 4 to 6 ns, that corresponds to the time-over-threshold interval of the input analog signal.

Sum Trigger

The Sum trigger directly adds the analog signals coming from the pixels and sends the summed signal to the L1 trigger. Before the addition, the signal from each pixel goes through an attenuator and clipping circuit (see Figure A.6).

The attenuator circuit allows to equalize the amplitude of the signals from the different pixels by applying an attenuating factor, leading to an equalization precision at the 5% level. This circuit is used for the gain calibration of the pixels (see Section A.6.1). Such calibration goal is to ensure that the contribution of each pixel to the L1 trigger is the same. While the attenuation circuit is used to calibrate the Sum trigger scheme, the threshold level at L0 is used to calibrate the Majority trigger scheme (see Section A.6.1).

The clipping circuit removes the part of the signal greater than a given reference voltage value, in order to limit the influence of after-pulses from the PMTs [335]. This circuit reason-to-be and its use for the clipping pixel calibration are exposed in Section A.6.1.

The clipping and attenuator circuits configuration allows to reduce the pixel contribution to the trigger line to zero, in order to remove noisy pixels from the trigger pattern.

A.4.2 L1-level trigger

The L1 trigger system has three input points – A, B and C – called adders. Each of them can be configured in order to receive up to 6 L0 signals coming from the same module and its adjacent clusters.

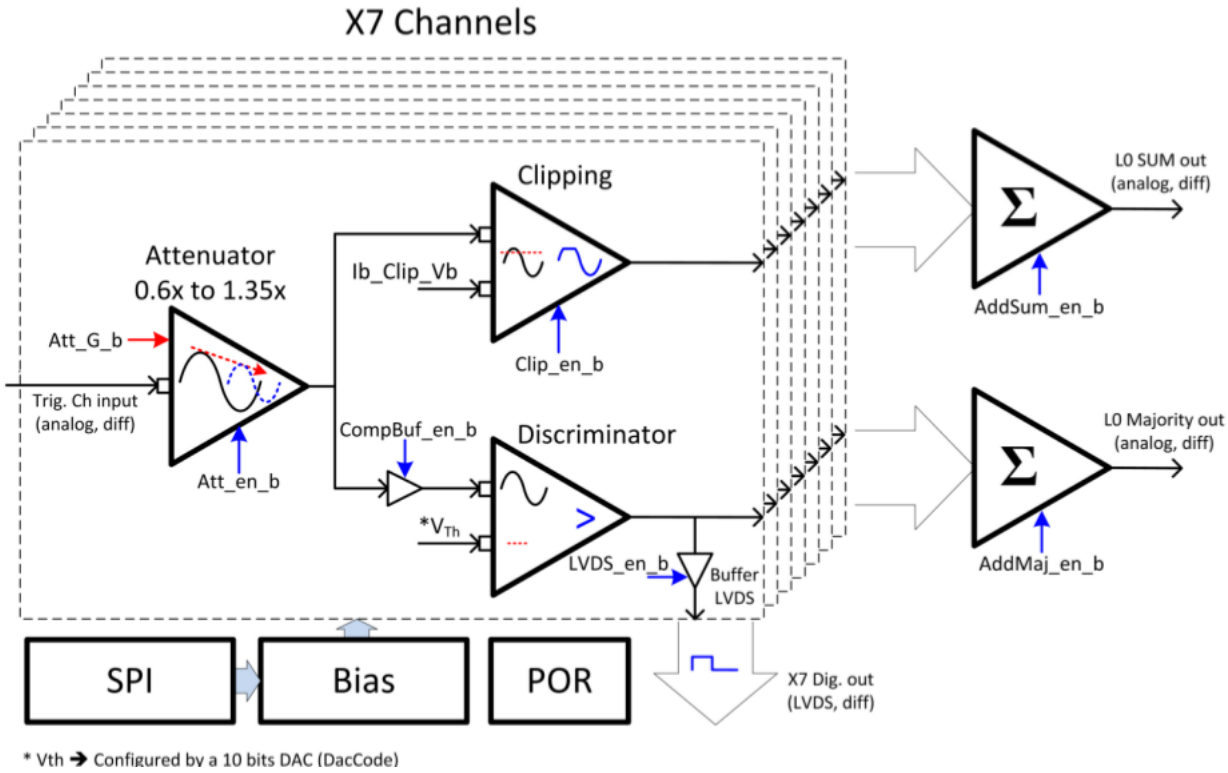

Figure A.6: Diagram of the two L0 trigger schemes. On the left, the attenuator, clipping and discriminator circuits, whose effect is applied individually for every pixel signal. On the right, the output signal from the L0, the upper one for the Sum trigger case, the lower one for the Majority trigger case.

The analog L0 signals are summed in the adders A, B and C (see Figure A.7) and compared with a threshold level (DTL1 from now on). The DTL1 is configurable and different for every adder. If, in any of the adders, the summed signal lies above the DTL1 level, the L1 sends a trigger signal to the TIB to trigger the camera.

Depending on the L0 trigger scheme, the L1 trigger decides if there are more than a certain number of pixels above the DTL0 in a region of the camera (Majority), or if the addition of the pixel signals in this region is greater than DTL1 (Sum).

The trigger strategy has 3 different configurable patterns that look for coincidence between 2, 3 or 4 clusters, corresponding to 14, 21 or 28 pixels. Since all the clusters count with a L1 trigger level, it is possible to cover simultaneously all possible combinations of 2, 3 or 4 compact clusters in the whole camera, and fully trigger overlapping regions are guaranteed. For any selected operation mode (2, 3 or 4) there are never more than 3 sums required, so that the trigger strategy can be performed in a cost-effective way with only 3 adders per L1 level, each of them summing 2, 3 or 4 L0 signals. Inside the adders, the different L0 signals are combined and sent to the discriminators (see Figure A.7), whose DTL1 threshold is configurable for every adder. The outputs of the three discriminators are combined in two OR logic gates, that provide two differential trigger outputs which will be distributed throughout the camera, in order to activate the readout of all the clusters.

The TIB collects the trigger signals generated by each L1, and provide it to the DAQ systems, in order to start the readout process. As in the case of MAGIC, in order to read only a part of the analog memory (the region-of-interest, RoI), the trigger pulse arrival time to the different clusters should be as similar

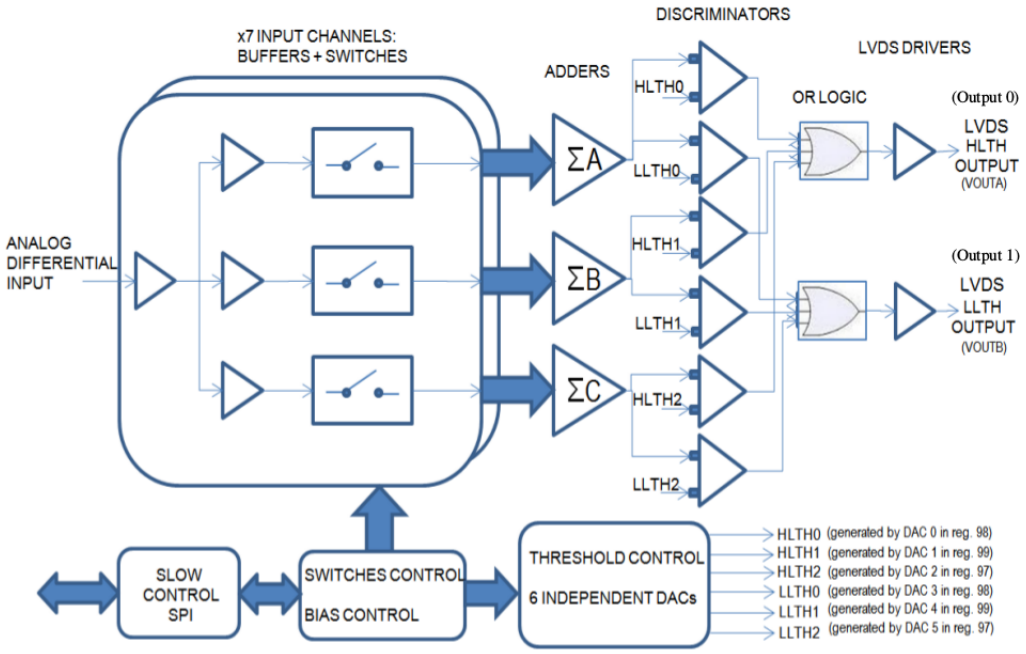

Figure A.7: Block diagram of the L1 trigger.

as possible and stable with respect to the L1 trigger generation time in the datataking. The "Backplane calibration" equalizes the times of the reception of the L1 trigger and the transmission to the DAQ systems, taking into account the position of the modules inside the camera.

A.5 The need for trigger calibrations

When detecting a signal, the trigger system must have an homogeneous and simultaneous response along the camera, with special focus on the trigger pattern regions. For this purpose, we need to calibrate the system to equalize the signals at both L0 and L1 levels, previous requirement before the above-mentioned Backplane calibration. In order to calibrate the trigger system, the camera must be homogeneously illuminated by a signal of known frequency.

The PMTs at every pixel have slightly different gain and transit time for the incoming signals. These differences must be corrected since the trigger strategy relies on a small time window − expecting photon superposition from the gamma-ray shower in less than a few ns − and on a homogeneous response of the trigger lines. At the L0 level, the trigger calibrations correct these PMT effects and make the signals from each pixel to be simultaneous in time and to have an equal contribution in amplitude when arriving at the L1 level. However, depending on the L1 level these signals are sent to (which may be at the same module or at a neighbouring one), their amplitudes will be slightly different, due to small variations in the hardware elements and a different attenuation along the path. Therefore, the best method to equalize the signals is by averaging their different amplitudes in all their reachable L1 level paths, or comparing the results between two clusters and re-scaling the signal parameters according to that difference. Moreover, the arrival time of the L0 signals at the L1 would be different, since the paths to the different neighbours have not exactly equal length. The comparison between clusters is necessary such that all clusters have a same reference in time and amplitude and the difference between them can be adjusted. Following these

ideas, some calibration results at L0 level should be cross-checked or compared with the surrounding clusters, giving place to the so-called inter-cluster L0 calibrations.

At L1 level, the reception and transmission of L1 pulses by the TIB must be asynchronous. The minimum value of the latency in the TIB is the time needed to carry out the transmission of the L1 signal from one cluster to another. The transmission times are calibrated by the Backplane calibration such that all are equalized to the minimum latency. Before equalizing the L1 trigger, the L0 must already be calibrated. Furthermore, a characterization of the L1 level is required in order to understand the response of the L1 trigger adders for the different L0 inputs signals reaching each adder and its relation with the amplitude of the injected signals.

A.6 Trigger calibrations

This section describes in detail the calibrations developed as part of this thesis work for the L0 and L1 triggers, including the reason-to-be behind each calibration, the calibration inputs, their expected results and their configurable settings. The Backplane calibration is not part of this work. This section composes the first detailed documentation about the calibration codes and one of its goals is to provide some guidance for future calibration users.

The calibrations use the concept of rate instead of amplitude of the injected signal. The rate indicates the number of triggered signals per unit of time. The rate is defined as the number of triggered pulses per second using units of frequency, for example 300 Hz, or equivalently, 300 pulses per second. A signal is "triggered" when its amplitude is greater than a specific voltage value, called DT, that is configurable for every trigger level. The L0 level has a DT per pixel, called DTL0, and the L1 has a DT per adder, called DTL1.

The rate value is directly related to the input signal amplitude and the value of the DT. As an example, Figures A.8 and A.9, show the evolution in the value of the output rate as a function of the DTL0 value applied. The example is given for a pulsed signal of specific amplitude, in this case DTL0_3. Such injected pulses are not perfect Gaussian peaks but present smalls perturbations on their base due to electronic noise. This noise is present even without an injected signal.

In Figure A.8, with a time window of one second and two injected pulses $-$ that corresponds to an injected rate of 2 Hz $-$, the relation between the value of the DTL0 and the output rate can be appreciated. If the value of DTL0 is too low (DTL0_1), located inside the noise region, the number of peaks surpassing the threshold due the perturbations is very high and the output rate will be much higher than the injected rate (DTL0_1 peak in Figure A.9).

If the DTL0 has a value such that only the injected pulses surpass it (DTL0_2), the number of triggered pulses is equal to the number of injected pulses and the output rate is equal to the injected rate, as shown in Figure A.9. When the DTL0 value lies around the injected pulse amplitude (DTL0_3), only a ratio of the injected pulses will be triggered and the output rate will decrease as the DTL0 increases beyond the injected signal amplitude. The slope of the transition follows a error function. The DTL0_3 line in Figure A.9 indicates the DTL0 value for which the output rate is 50% of the injected rate, 1 Hz in this example. Finally, if the DLT0 value is above the injected pulse amplitude (DTL0_4), no signal will surpass it and the rate would be 0 (DTL0_1 line in Figure A.9). The selection of a very high DTL0 value, for the Majority scheme, reduces the pixel signal contribution to the trigger line to 0.

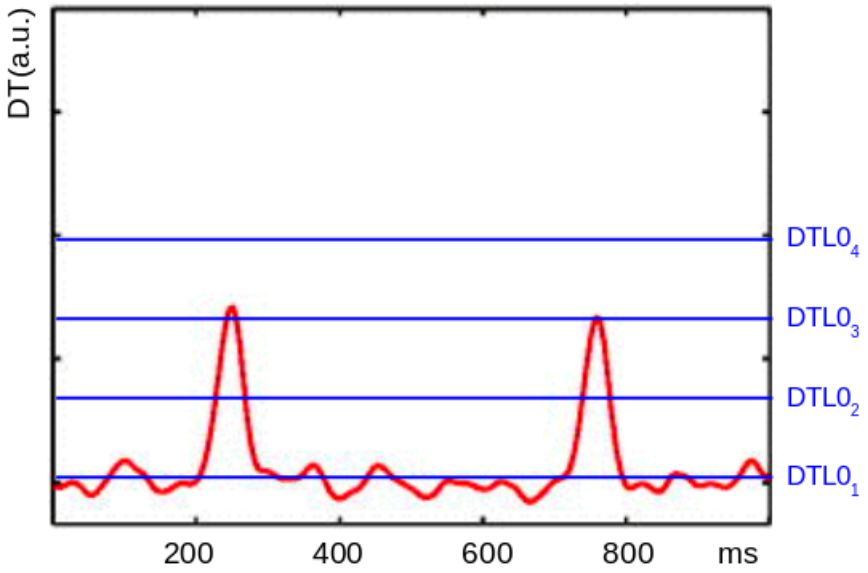

Figure A.8: Graphical representation of the DTL0 threshold effect on injected signal pulses.

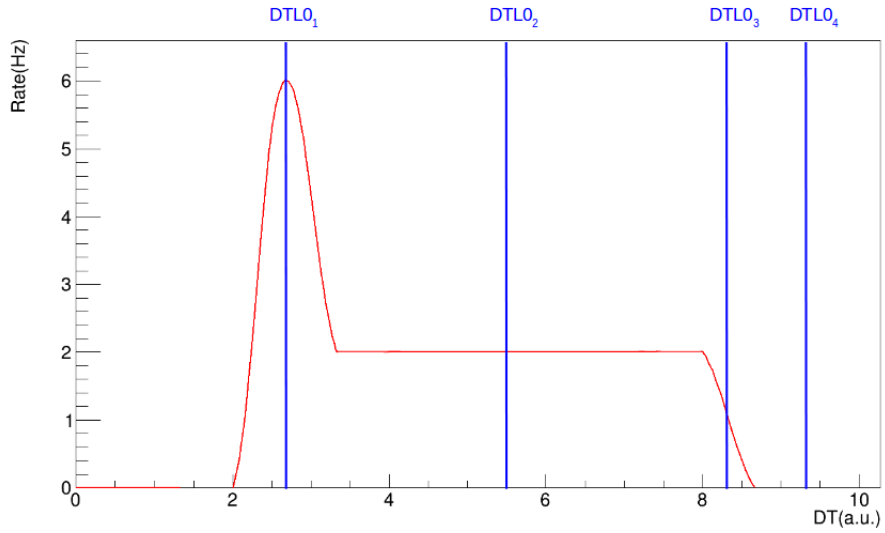

Figure A.9: Graphical representation of the output rate of a injected signal as a function of the DT applied at L0 level. For graphical purposes, the rate peak due to electronic noise is drawn inside the window, but usually its value is orders of magnitude bigger than the signal rate value.

This graphical example describes the L0 level when the Majority trigger scheme is used, and also the L1 level. In the Sum trigger scheme, the L0 signals are not compared with any threshold at L0 level, only later at L1 level their addition is compared with the DLT1.

The calibration algorithms make use of the output rate value, at L0 or L1 level, in order to decide the next step to take in the calibration procedure.

A.6.1 L0 level calibrations

The L0 calibrations or pixel-level calibrations aim to equalize the signals coming from the different pixels in a cluster so that their contribution to L1 is equal − same amplitude at L1 level − and their arrival to L1 level is simultaneous.

For this purpose, the calibrations find the right values of the configurable parameters of the pixels. Such pixel parameters are:

- DTL0 threshold level for each pixel. Obtained by the DTL0 calibration.
- Delay line followed by the pixel signal. Obtained by the delay calibration.
- Gain value applied to the pixel signal in the attenuation circuit (Sum trigger scheme). Obtained by the gain calibration.
- Clipping value applied to the pixel signal in the clipping circuit (Sum trigger scheme). Obtained by the clipping calibration.

Setting the same values of these parameters for all pixels will not assure a homogeneous response due to slight differences in the hardware components. The calibrations will find the right parameter values for each individual pixel and these values will be set in the camera configuration before starting data taking.

The LST camera is modular, allowing to run calibrations simultaneously in parallel using threads over several clusters (see Section A.7.3). The number of threads are controlled internally to optimize the computing resources.

Baseline calibration

This calibration computes the noise region of a given pixel, thus the DTL0 range of values where the output rate is much higher than the injected rate (see Figure A.9). During the telescopes operation, the DLT0 value should always lie above the noise region in order not to spoil the input signal.

The pixel noise is not related to the input signal, so that this calibration can be launched even when there is not an injected signal. The calibration result is the DTL0 value corresponding to the middle point of the noise region (DTN in Figure A.10), computed as the central value between the noise region edges (DTNl and DTNr). This calibration only requires one input:

- **Input 1:** *"injected_rate"*. The introduced value should correspond to the rate of the injected signal (Green line in Figure A.10). In case there is no injected signal, the input value should be set to 0.

The calibration procedure for every pixel − schematically shown in Figure A.11 − is as follows: It starts setting the central value of the allowed range of DTL0 values and reading the rate at L0 level.

If this rate is smaller than the input *"injected_rate"*, such DTL0 lies outside the noise region. In this case the calibration changes the DTL0 value in small steps to the left and to the right simultaneously until finding a DTL0 value for which the rate is higher than the *"injected_rate"*, meaning that such DTL0 value lies inside the noise region.

On the other hand, if in the first rate reading the output rate value is higher than the *"injected_rate"*, the DTL0 is already inside the noise region and the first search is skipped.

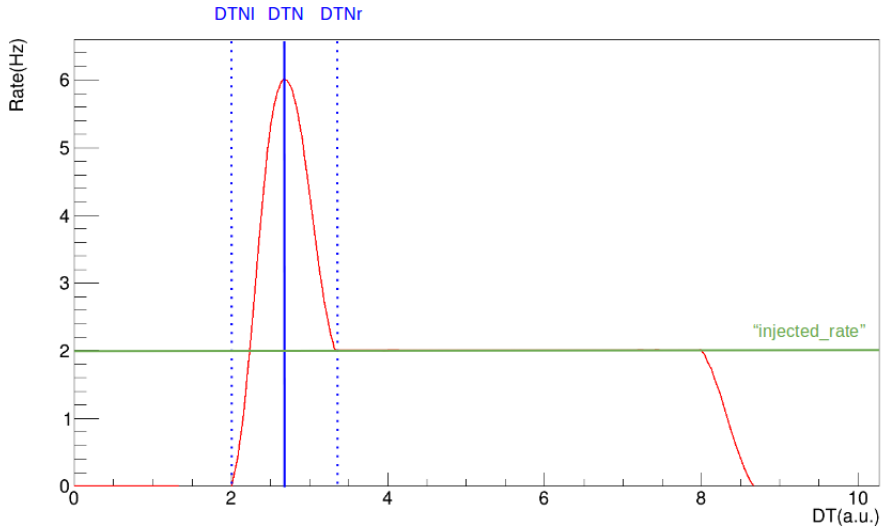

Figure A.10: Graphical result of the Baseline calibration.

Once inside the noise region, the calibration moves the DTL0 value to the left (decrease) and the right (increase) and reads the L0 rate, until the rate value is smaller than the *"injected_rate"* and the edges DTNl and DTNr are found. Once the edges are established, the middle point DTN is computed with:

$$DTN = DTNl + \frac{DTNr - DTNl}{2}. \tag{A.1}$$

Conceptually, the location of the noise region should not depend on the configuration of the pixel. However, its extension does depend on the attenuation value applied to the pixel and the value of the HV applied to the PMTs. This calibration should be the first one launched in order to find the DLT0 working region for the rest of the calibrations, that will be situated above the noise region.

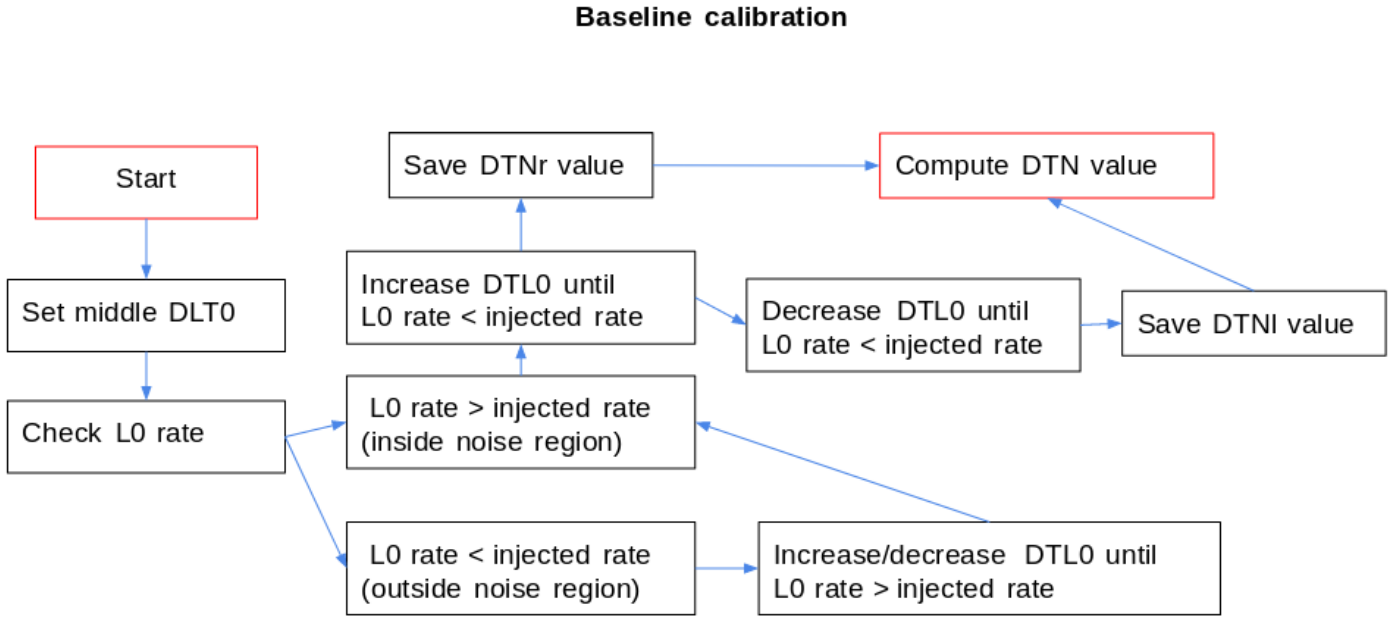

Figure A.11: Graphical scheme of the Baseline calibration procedure.

DTL0 calibration

The DTL0 calibration finds the value of the DTL0 corresponding to an output rate whose value is a given percentage of the input rate. In order to achieve this, the DTL0 calibration develops a binary search between the center of the noise region (DTN in Figure A.12) and the maximum possible value of the DTL0. This calibration requires two input values:

- **Input 1:** *"injected_rate"*. This input indicates the rate on the injected signal.
- **Input 2:** *"ratio"*. This input refers to the percentage of the input rate the calibration must look for.

From these two inputs, the calibration returns the DTL0 value whose rate value is *"injected_rate"* × *"ratio"*. As an example, the black point in Figure A.12, indicates the result of a DTL0 calibration with a *"ratio"* value of 0.5 and *"injected_rate"* of 2, so that the required rate for the calibration is 1.

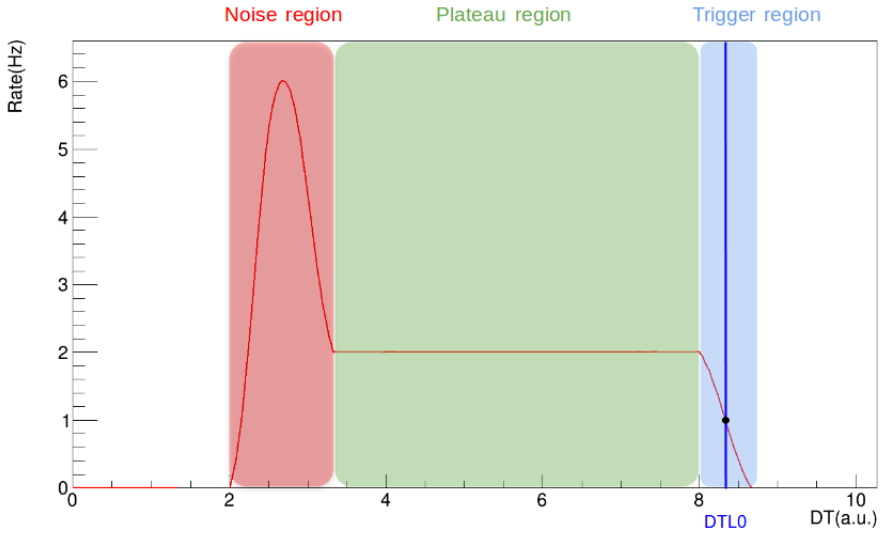

Figure A.12: Graphical example of the result of a DTL0 calibration with *"ratio"* = 0.5 and *"injected_rate"* = 2.

The calibration procedure (schematic view in Figure A.13) consists of a binary search, an algorithm that searches the position of a target value in an ordered interval of values. The binary search, also known as half-search algorithm, compares the target value to the middle element in the interval; if they are unequal, the half in which the target cannot lie is eliminated and the search continues on the remaining half until it is successful. Figure A.14 shows graphically the procedure of the binary search at the L0 level. In reality, the DTL0_{target}, corresponding to a *"injected_rate"* × *"ratio"* output rate, is unknown. During the binary search steps, we take the middle DTL0 value in the interval and measure the rate: if the rate is larger than *"injected_rate"* × *"ratio"*, we are in the plateau region, and the binary search continues with the right half, otherwise, it stays in the left half.

The use of a binary search assures that the number of steps are minimum − as well as the required calibration time − and the precision of the result is maximum, is the sense that it goes as close as possible (allowed by the variable size) to the real target value.

After the DLT0 calibration, we can assure that the response of the different pixels for a given input signal is equal at L0 level. By setting the DTL0 values found by the calibrations in every pixel, all of them would present a rate close to the *"injected_rate"* times the *"ratio"*.

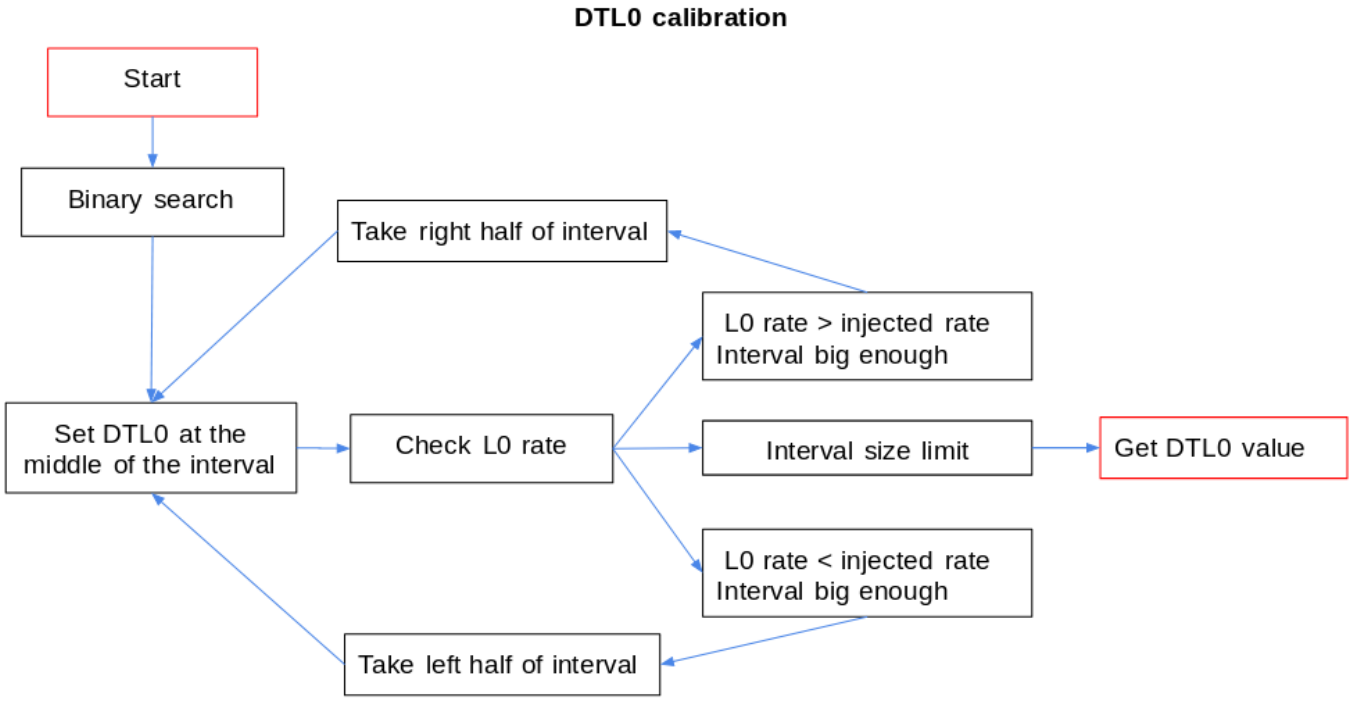

Figure A.13: Graphical scheme of the DTL0 calibration procedure.

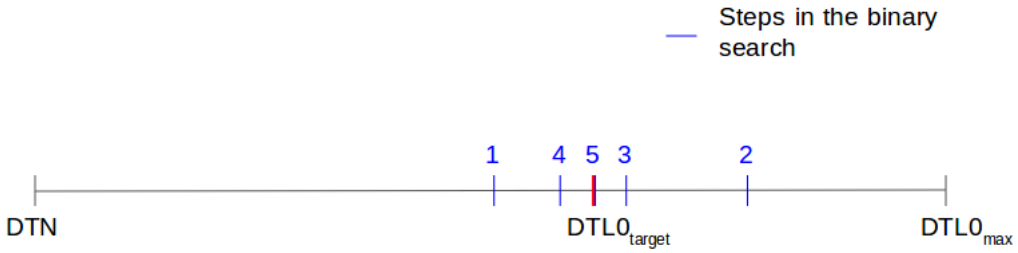

Figure A.14: Graphical example of the DTL0 binary search.

Pixel Delay calibration

Each pixel counts with a PMT that converts the detected Cherenkov light into an amplified electrical signal by using a number of dynodes. The incident Cherenkov photons produce an electron current by the photoelectric effect on the photocatode that is amplified at every dynode. However, PMTs are not all identical and and gains at each dynode vary from PMT to PMT. This is compensated by applying HVs matched to achieve a similar overall gain at each pixel (the so-called "flat-fielding"). This leads, however, to different transit times of the signals in the different pixels, producing delays between such signals that affect the correct operation of the trigger system, crucial to find trigger coincidences correctly. In order to correct these delays, the signals between pixels must be cross-calibrated, in the sense that one is taken as a reference and the others are equalized in time in concordance with it.

The delay calibration compensates the delays of signals from different pixels in a cluster by adding an extra delay to the less retarded ones, such that all arrive simultaneously at L1. This additional delay is achieved by sending the signals through circuits of different length, that add from 0 to 5.75 ns delay,

where the difference in delay between the circuits is 0.25 ns.

The delay calibration is carried out pixel by pixel, by taking another pixel as reference, sent though a medium length channel of 3ns. This calibration must be done for all the pixels in the camera and consists of two levels: The cluster-level, where all the pixels inside a cluster are equalized in time with respect to a reference pixel located on that same cluster; and the inter-cluster level, where the delays of the reference pixels located in different clusters are compared and equalized. The latter is explained in the next section.

Two pixels are involved in this calibration, the one to be adjusted and the one taken as reference. Since we need to receive two signals simultaneously, the calibration works at L1 level, hence it uses the DTL1 value and reads the rate at L1 level during its procedure. Moreover, this calibration must be made for both the Majority and Sum trigger schemes, expecting a similar result for both cases. The initial idea was to use the Majority trigger to get a first preliminary result and then apply the Sum trigger to fine-tune it. However, after the first tests, we realized that the Majority trigger, depending on the DTL0 value set on the pixels, can provide a more precise result than the Sum trigger. For this reason, the procedure can be carried out the other way around, or just launched for each trigger scheme independently.

Furthermore, the delay calibration counts with two different procedures, called "Rate Mode" and "Binary Mode". While one is quicker but gives slightly less precision results, the other gives better precision paying the price of a longer calibration time.

The result of the calibration is the delay that has to be assigned to the adjustable pixel such that its signal arrives at L1 level simultaneously with respect to the reference pixel signal. This calibration has 5 inputs:

- **Input 1:** *"reference_delay"*: This is the value of the delay for the reference pixel in ns. Usually, this input is set to 3ns, such that the adjustable pixel can have both more or less delay.

- **Input 2:** *"reference_neighbour"*: This value indicates if the reference pixel belongs to the same cluster of the adjustable pixel or to another one. Both pixels are in the same cluster if this input is 3, and in different clusters for any other value between 0 and 5. The scheme of the cluster numbering at L1 level is shown in Figure A.15.

- **Input 3:** *"reference_pixel"*: This input indicates which pixel inside the *"reference_neighbour"* will be taken as reference pixel.

- **Input 4:** *"calibration_trigger"*: This variable indicates the trigger scheme used for the calibration. It is a Boolean taking the value 1 for Majority and 0 for Sum trigger.

- **Input 5:** *"calibration_mode"*: This input indicates which of the two procedures is used for the calibration. It is a Boolean and 0 indicates "Rate Mode" while 1 means "Binary mode". The characteristics of the two modes are explained below.

Both delay calibration modes are based on the same idea: they receive the L0 signals from both pixels at L1 level − adder A is used by default − and make these two signals overlap in time. The pixels not involved in the calibration must be turned off by using the clipping and attenuation circuits, or setting the HV of those PMTs to 0. The two signals received at L1 will be analog or squared digital pulses for the Sum or Majority trigger respectively (see Figure A.16). The procedure consists of setting the delay of the reference pixel signal to the *"reference_delay"* value − the value is 1 ns in the example shown in

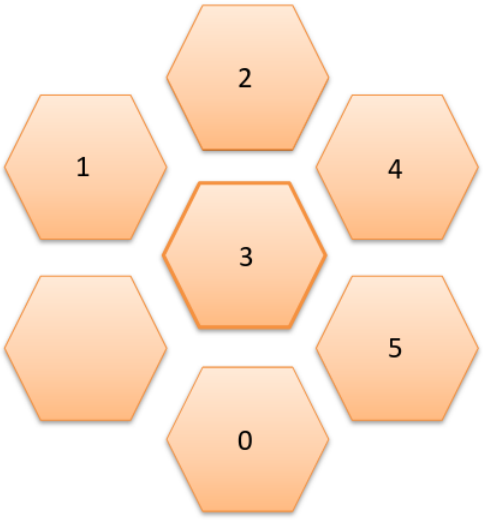

Figure A.15: Cluster numbers at L1 level, from the point of view of the central cluster. The central cluster recognizes itself as number 3, and its neighbours with numbers in the intervals 0-2 and 4-5. One of the surrounding clusters is not able, by hardware reasons, to send its signal to the central cluster (see Figure A.4), so that is does not have a number assigned.

Figure A.16 – and change the delay of the adjustable pixel signal until both signals overlap in time. The difference between the two modes – schematically described in Figure A.20 – is the criterion to decide when the two signals do overlap. While one mode reads the rate at L1 level to take this decision, the other makes binary searches at L1 to see the voltage profile produced by the signals.

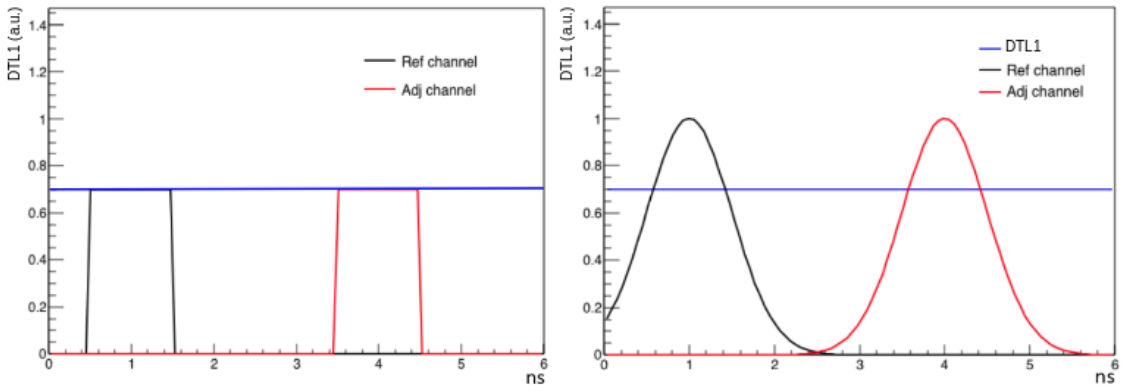

Figure A.16: Graphical view of the L1 level signal when receiving two L0 signals with only one pixel turned on. The trigger scheme used is Majority (left) and Sum trigger (right). The blue line indicates the DTL1 threshold.

- **Delay calibration with Rate mode:** This method reads the rate at L1 to decide when the two pulses overlap in time. Before, an adequate value for the DTL1 must be chosen, usually taken around one and a half times the DTL1 value required for only the reference pixel signal to trigger. The procedure works as follows: First, only the reference pixel signal is allowed to arrive to the L1 level (the rest of pixels are turned off) and a binary search is made to find the DLT1 value corresponding to 50% of the injected rate (DTL1_{ref}), for example, the left plot in Figure A.16 shows the DTL1_{ref} for the Majority case with a blue line. After that, we set a DTL1 level equal to

$1.5\times\text{DTL1}_{ref}$ and allow both the reference and the adjustable pixel signals to reach the L1 level (Figure A.17). While the delay for the reference signal is set to *"reference_delay"*, the adjustable pixel signal is sent through all possible delay paths (from 0 to 5.75 ns) until both signals overlap in time at L1, such that the sum of the two signals will trigger (The sum of the signals is represented in green in Figure A.17). This trigger situation would not happen for one delay value of the adjustable pixel but for a full interval. Therefore, the calibration saves the value of the rate at L1 for every value of the delay of the adjustable pixel, finds the overlap time interval and computes the central point (in an equivalent way as for the baseline calibration, Equation A.1), that is given as the result of the delay calibration. The overlap time interval is considered the time regime where the output rate at L1 is more than 50% of the injected rate. Figure A.18 shows an example of a delay calibration result with rate mode, locating the reference pixel at a *"reference_delay"* of 3 ns, for the Majority and the Sum trigger, where the injected signal has a frequency of 300 Hz. In the Majority case, the signal of the two pixels can be very narrow squared pulses (if the DTL0 is located at the amplitude of the injected signal), such that the overlap time region is narrower, however, the final result, that is the middle point of the overlap region, must be the same for both methods.

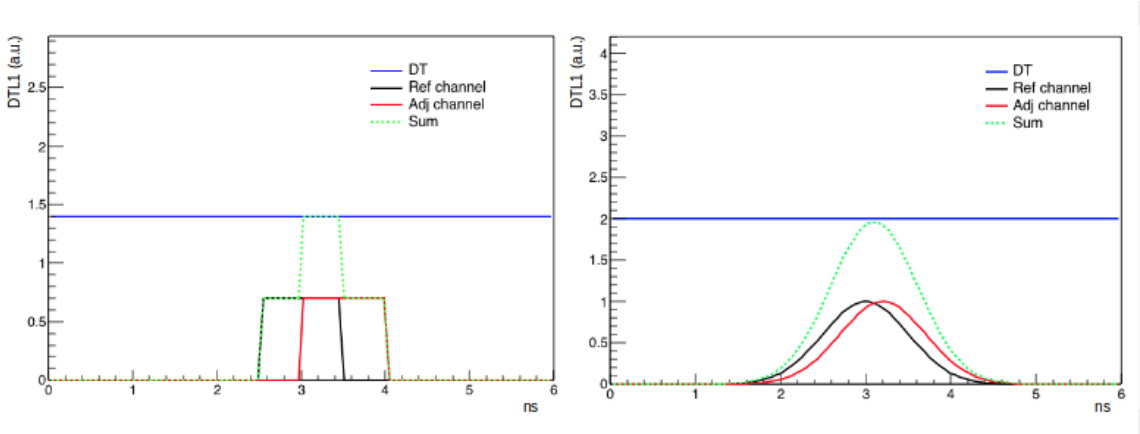

Figure A.17: Graphical representation of two pulses involved in a delay calibration at L1 level, for the Majority (left plot) and the Sum (right plot) schemes. The signal of the reference pixel, located at 3 ns, is shown in black and the adjustable pixel signal in red. The blue line indicates the DTL1 threshold value. The addition of both signals is shown in green. The combined signal will trigger at L1 level when surpassing the chosen DLT1 level.

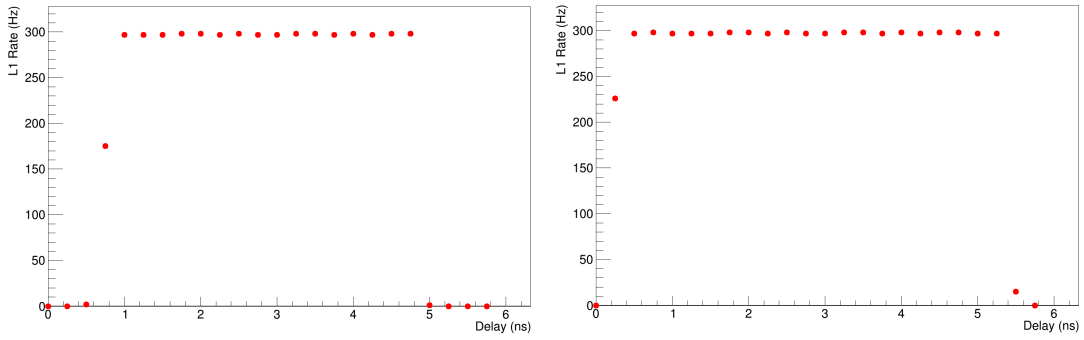

Figure A.18: Example of a graphical representation of the result of a delay calibration when using the Rate Mode, for the Majority (left plot) and the Sum (right plot) trigger schemes. The final result is the middle point of the interval in which the output rate is greater than 50% of the injected rate. The values are obtained from real calibrations.

- **Delay calibration with Binary mode:** This mode is similar to the previous one, but instead of fixing the value of DTL1 to $1.5\times\text{DTL1}_{ref}$, this mode performs a binary search to look for the required value of the DTL1 corresponding to 50% of the injected rate every time the adjustable pixel signal is sent through a different delay path (from 0 to 5.75 ns), while the reference pixel signal is fixed at *"reference_delay"*. This calibration mode saves the value of the DTL1 obtained from the binary search at every value of the delay of the adjustable pixel. Looking at the green dotted lines in Figure A.17, it can be seen that, for the Majority scheme (left plot), the combined green signal shows two DTL1 amplitudes, one pixel amplitude at the sides and a two pixel amplitude in the central overlap region. However, for the Sum scheme (right plot), the combined resulting signal is a smooth Gaussian showing the profile of the overlapping pulses. The result of the delay calibration with binary mode, that shows the DTL1 value versus the delay of the adjustable pixel, gives these same shapes, that are shown in Figure A.19.

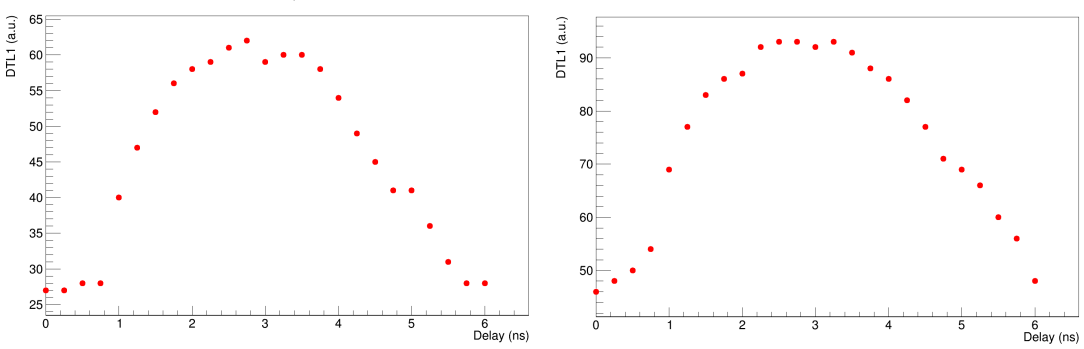

Figure A.19: Example of a graphical representation of the result of a delay calibration when using the Binary Mode, for the Majority (left plot) and the Sum (right plot) trigger schemes. The final result is the middle point of the interval in which the DTL1 value obtained is maximum. In the Sum case, the interval can be composed of a single point. The values are obtained from real calibrations.

The schematic procedure of both delay calibration modes is shown in Figure A.20. From Figures A.18 and A.19, the Rate Mode offer less precision since the overlap region detected is much wider than the one for the Binary. Therefore, if both pixels do not differ much in delay, both methods will offer similar results but, if the difference is delay is wider, as will happen for light pulses − the calibrations shown in the plots were made with electronic pulses −, the Binary Mode is better suited.

Inter-cluster delay calibration

This is not a new calibration, but an extra section of the delay calibration. The inputs, methods and procedures are the same, apart from the *"reference_neighbour"* input value, that must be different from 3. Such value activates an extra section of the delay calibration.

This calibration must be launched once the pixel signals are calibrated inside clusters. The extra procedure, represented in Figure A.21, is as follows: The calibration involves two clusters already calibrated, the calibrated delay values appear in black in Figure A.21. The reference pixel (central pixel) of the adjustable cluster is calibrated with respect to the reference pixel of the reference cluster, using the delay calibration process explained in the previous section. The resulting value, indicated in blue in Figure A.21, shows the relative delay between the two clusters. This relative delay is used to re-scale

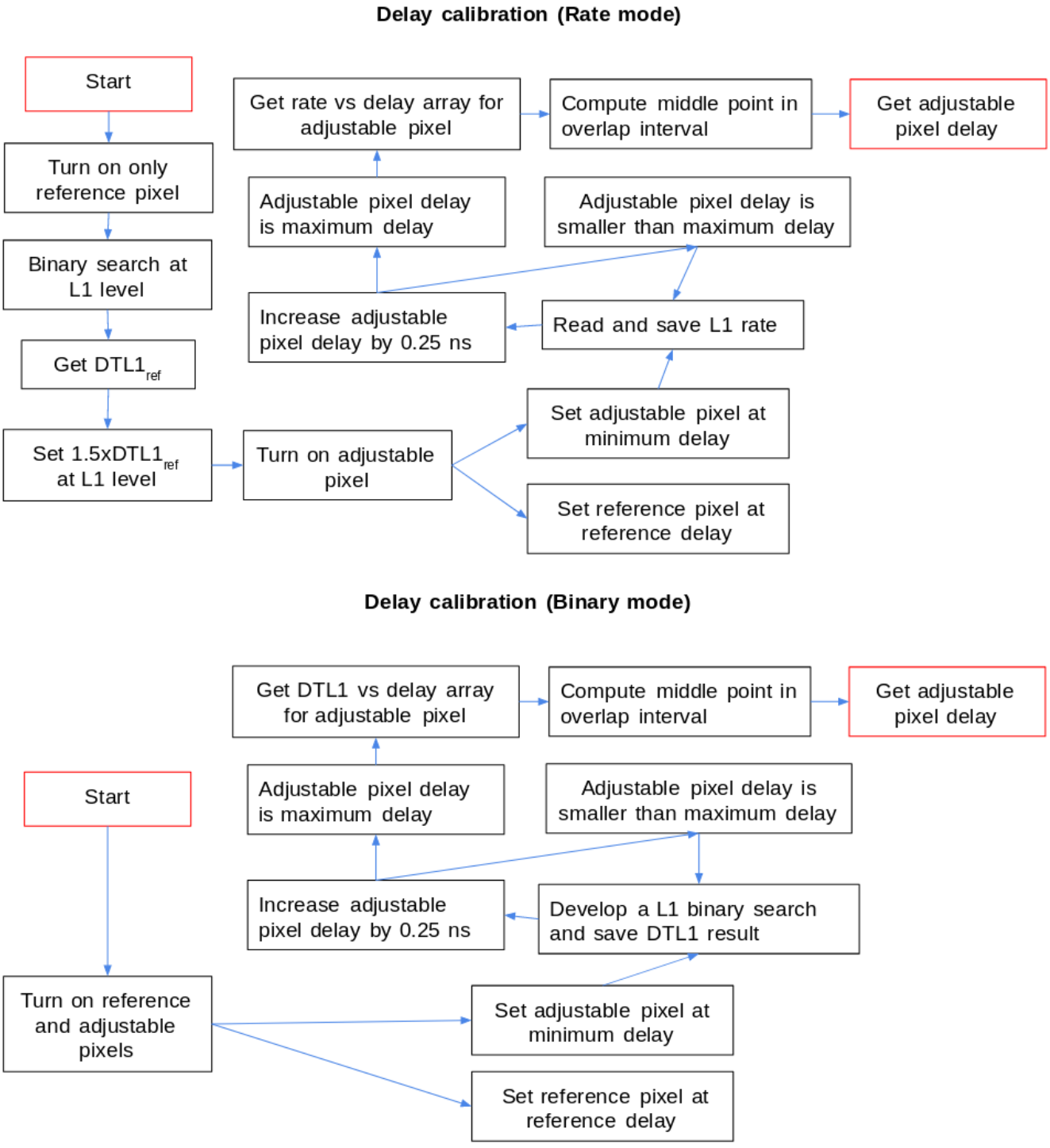

Figure A.20: Graphical scheme of the Delay calibration procedure. On top, the rate mode procedure, on bottom, the binary mode procedure.

the values of the calibrated delays of all the pixels in the adjustable cluster, these corrected values are indicated in red in Figure A.21.

The inter-cluster delay calibration is launched all along the camera in a radial distribution in order to cover the trigger regions as homogeneously as possible. Figure A.22 shows the path to follow for the inter-cluster delay calibrations, taking into account the connections between neighbouring clusters, for the first three rings of the camera.

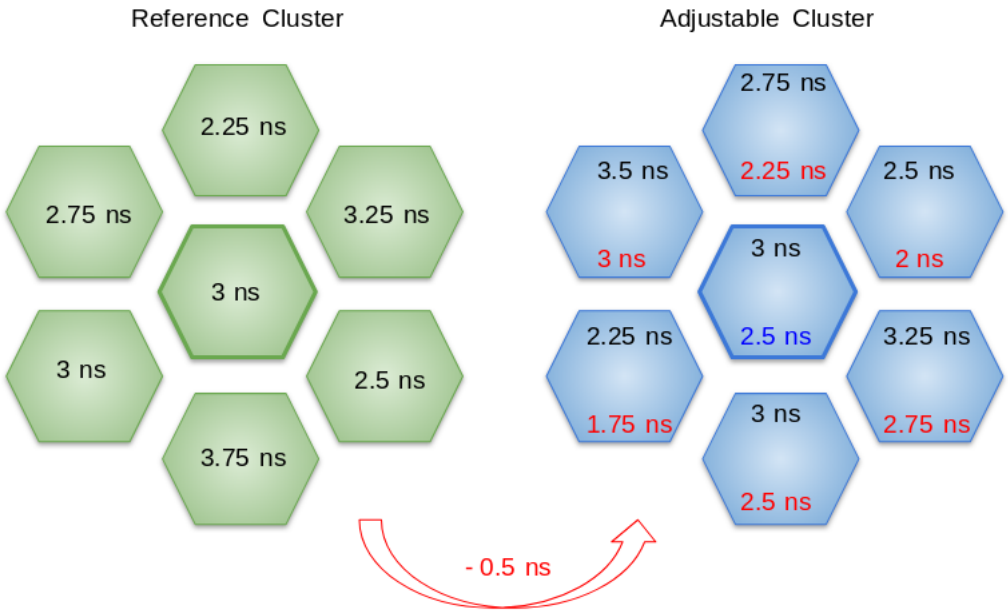

Figure A.21: Graphical representation of the delay re-scaling of an inter-cluster delay calibration.

The inter-cluster delay calibration starts from the central cluster of the camera, taken as the reference cluster to calibrate its neighbours (the blue central ring). The second ring, in orange, is calibrated taking as reference the clusters of the first ring. In the same way, the third ring in green uses the clusters of the second ring as reference clusters. In Figure A.22, the arrows start at the adjustable cluster and point towards the reference cluster. Its corresponding numbers indicate the number of the neighbour cluster used as reference cluster, that is, the value of the *"reference_neighbour"* input.

Pixel Gain calibration

The signal from every pixel travels through circuits that, even tough they are expected to be equal, attenuate them in a slightly different way. In addition, the flat fielding that compensates the HV differences for the different pixels is not perfect. Because of this, the signals from every pixel, that supposedly show equal amplitudes, present differences when arriving at the L1 level.

The gain calibration aims for the contribution of every pixel to the resulting L0 signal sent to L1 level to be the same. In order to do this, the gain calibration makes use of the attenuation circuit in the trigger line, that allows to apply a given gain value to increase or decrease the amplitude of a pixel signal. The decision is taken by comparing the calibrating pixel with another reference pixel, as done for the delay calibration.

Therefore, the gain calibration involves also two pixels, the adjustable and the reference one, that can belong to different clusters, while the rest of the pixels are turned off. This calibration is only made for the Sum trigger scheme.

The gain calibration result depends on the L1 adder used for the calibration. However, we can only set one value for the attenuation of every pixel while the same pixel signal can reach 3×6 different adders. In order to balance out with this, the gain calibration counts with an inter-cluster stage, explained in detail in the next section. The gain calibration inputs are:

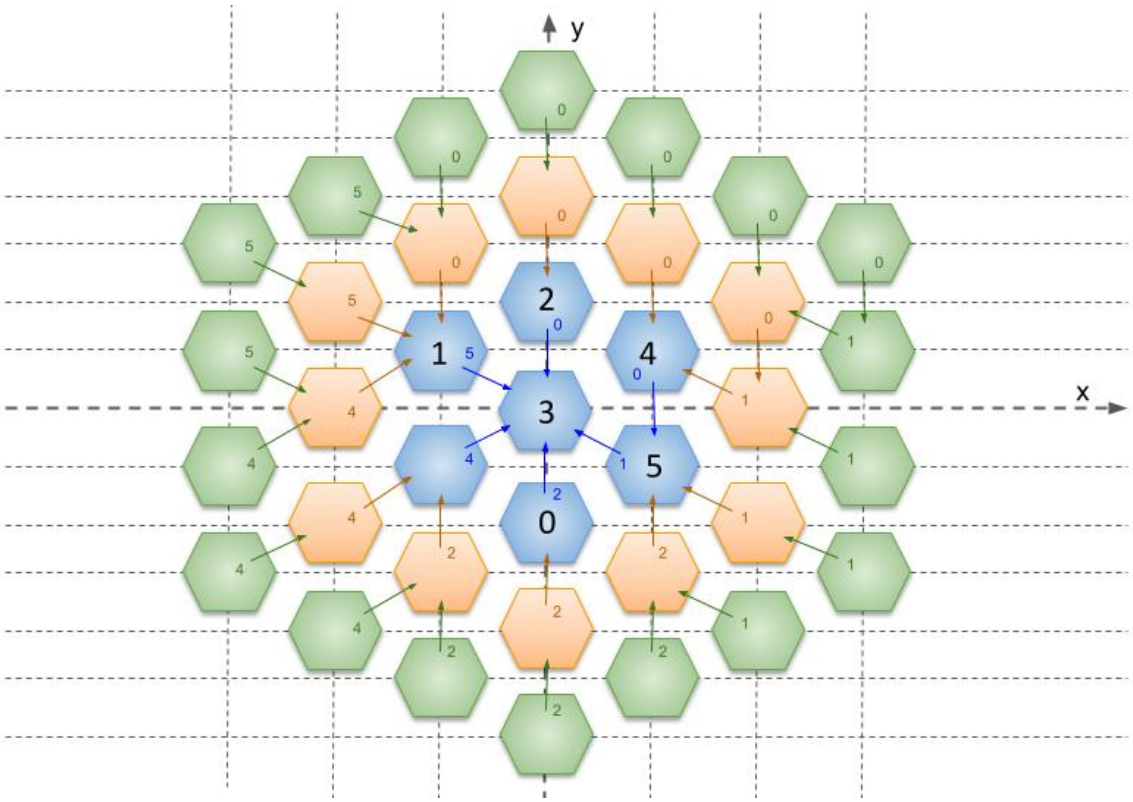

Figure A.22: Distribution of the inter-cluster delay calibrations for the first three rings of the camera (blue, orange and green). The central cluster and its neighbours are indicated with black numbers. The calibration starts at the center of the camera and expands radially.

- **Input 1:** *"reference_gain"*: It represents the value of the gain set for the reference pixel signal. The usual value used in the calibration is the central point of the configurable interval.
- **Input 2:** *"reference_neighbour"*: It indicates the neighbouring cluster whose adder is used in the calibration.
- **Input 3:** *"reference_pixel"*: This input indicates which pixel inside the *"reference_neighbour"* will be taken as reference pixel.

The gain calibration is developed also at L1 level. The procedure − whose scheme in shown in Figure A.24 − is as follows: first only the reference pixel signal is allowed to reach the L1 adder, while the rest of the pixels are turned off. The *"reference_gain"* is applied to this signal and a binary search at L1 is carried out in order to find the DTL1 value whose output rate is half the injected rate ($DTL1_{ref}$). After that, the DTL1 value is fixed to the $DTL1_{ref}$ value, the reference pixel is turned off and the adjustable pixel is turned on. Initially, the *"reference_gain"* is applied to the adjustable signal and the L1 rate is read. If the rate is less than half the injected rate, the amplitude of the adjustable signal is smaller than the amplitude of the reference signal, such that a bigger gain value is applied to the adjustable pixel and the rate is read again. This process is repeated by adding more gain or more attenuation to the adjustable signal until the output rate is half the injected rate (see Figure A.23), meaning that both signals are equalized at L1 level. Inside every cluster, one pixel is chosen as reference and the rest of the pixels are calibrated in relation to it. This reference pixel is the one involved in the next level of the calibration: the inter-cluster gain calibration.

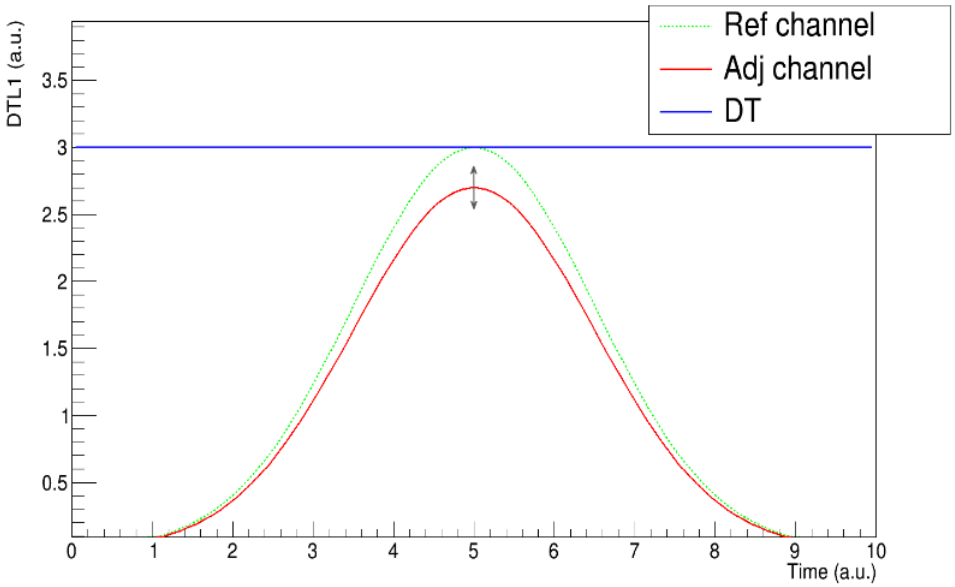

Figure A.23: Graphical scheme of a gain calibration. Even though both signals are not allowed simultaneously at L1, they are shown here for clarification. The blue line indicates the DTL1$_{ref}$ value, computed with the reference signal. In this graphical example, the attenuation for the adjustable signal must be decreased, so that its amplitude increases and reaches the amplitude of the reference signal.

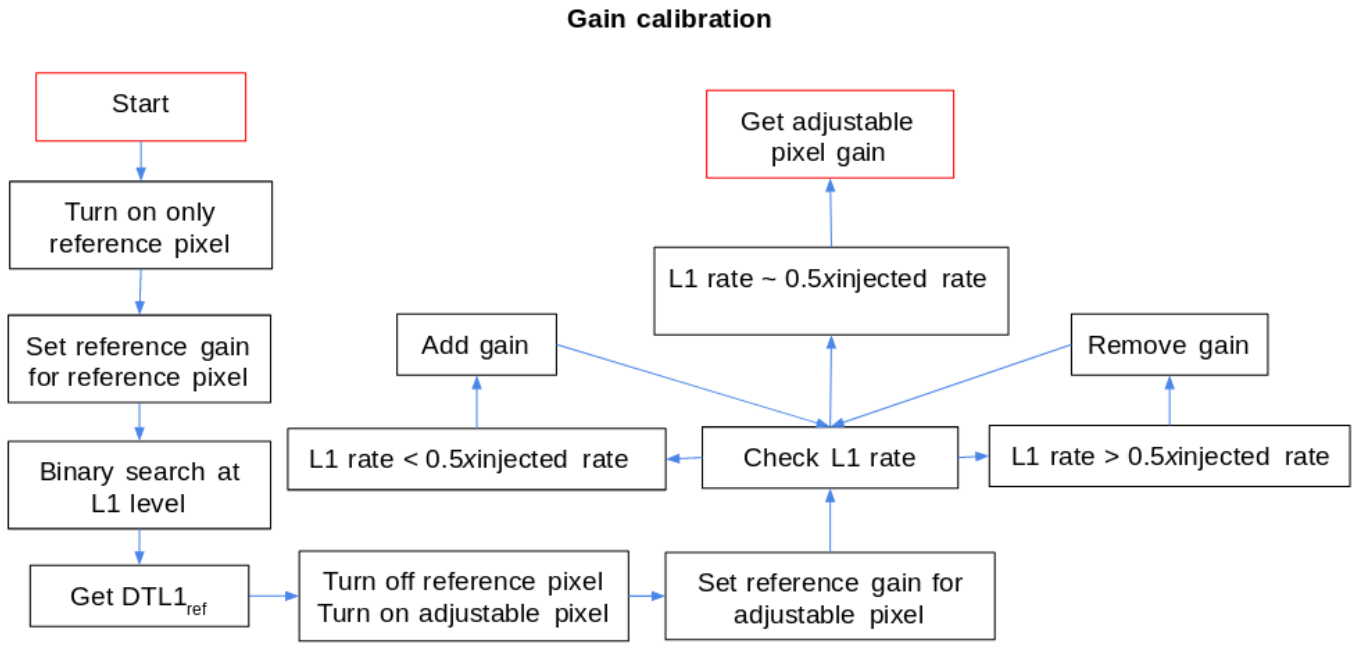

Figure A.24: Graphical scheme of the Gain calibration procedure.

Inter-cluster gain calibration

The inter-cluster gain version corrects for the difference in amplitude of the reference pixel signal from one cluster to another. In every adder, the L0 signal has a slightly different amplitude, however the relation between pixel amplitudes – that is corrected by the gain calibration exposed in previous section – is the same. That is why the delay and gain calibrations only make use of one adder, Adder A, while the L1 calibration (see Section A.6.2) corrects for the differences between the three adders inside the same

module. Thus, the inter-cluster gain calibration compensates differences between a pixel amplitude in all its reachable A adders.

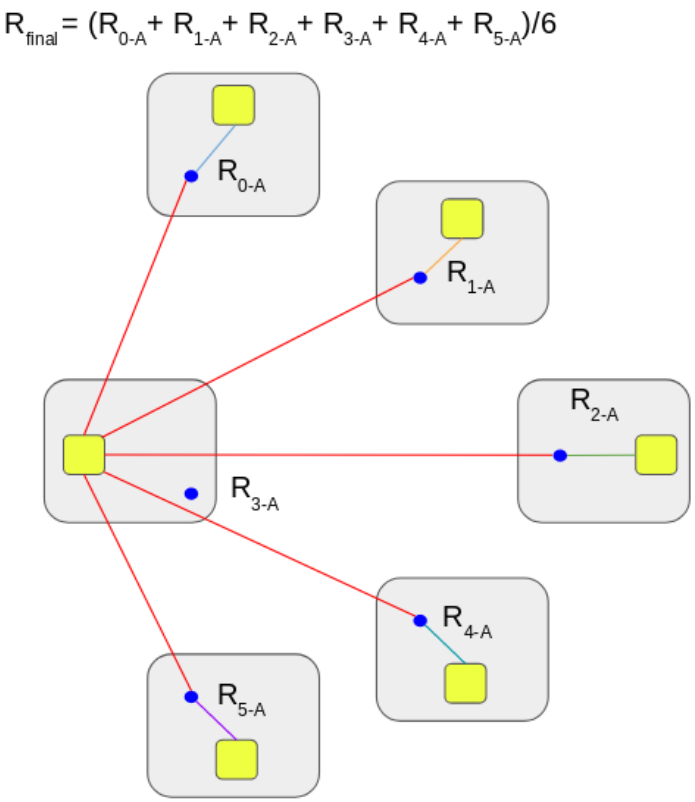

Figure A.25: Graphical scheme of an inter-cluster gain calibration. The grey boxes represent the clusters and the yellow boxes the reference pixel of each cluster. The red lines indicate the signal of the adjustable pixel, sent to the different Adder A (blue dots) located at its different neighbours. The different color lines indicate the signals of the reference pixels of each cluster used in the inter-cluster calibration. The R represents the result from every gain calibration in the different clusters, that are later used to compute the final gain value for the adjustable pixel.

The procedure works as follows: Taking the reference pixel inside an already calibrated cluster, its signal is send to all its reachable L1 levels (its five neighbouring clusters). In each L1 level, a gain calibration is made between this pixel and the reference pixel of such cluster, producing a new gain result for the initial pixel. The initial reference pixel collects six results in total. The final gain result for such pixel is the average of the complete set of results.

At the end, the difference between the initial gain of this reference pixel and the final averaged gain result is added to the rest of the pixels of the cluster the reference pixel belongs to, re-scaling their gain values, in an equivalent way to the one developed by the delay re-scaling, shown in Figure A.21.

The gain and the delay calibration affect the results of each other, since making the signal go through longer of shorter circuits to calibrate the delay, translates into a higher or lower attenuation of the signal during propagation, dis-adjusting the results obtained by the gain calibration. The impact of the delay calibration over the gain calibration is expected to be greater than the other way around, that is why the delay calibration must be launched before, and the gain calibration later. Apart from following this order, an iteration between both calibrations can be performed, until the effects of one calibration results over the other become negligible.

Clipping determination

The clipping circuit installed in the Sum Trigger scheme is used to minimize the effect of afterpulses produced by the PMTs. An afterpulse is produced when the accelerated photo-electron ionizes one of the residual gas molecules inside the PMT tube. The resulting ion hits the photo-catode and produces a new electronic cascade resulting in a pulse that arrives several hundreds of nanoseconds after the main pulse. Every pulse might be followed by an afterpulse and the afterpulse production cannot be predicted. Usually, afterpulses are small, with an amplitude distribution that follows an exponential going from <1 photoelectron to a large amount of photoelectrons. The higher afterpulses can reach or surpass the injected signal amplitude, producing triggers by themselves. Nevertheless, the probability that two PMTs produce an afterpulse simultaneously is very low. The latter is exploited by using a clipping level at L0 before adding the signals coming from different pixels.

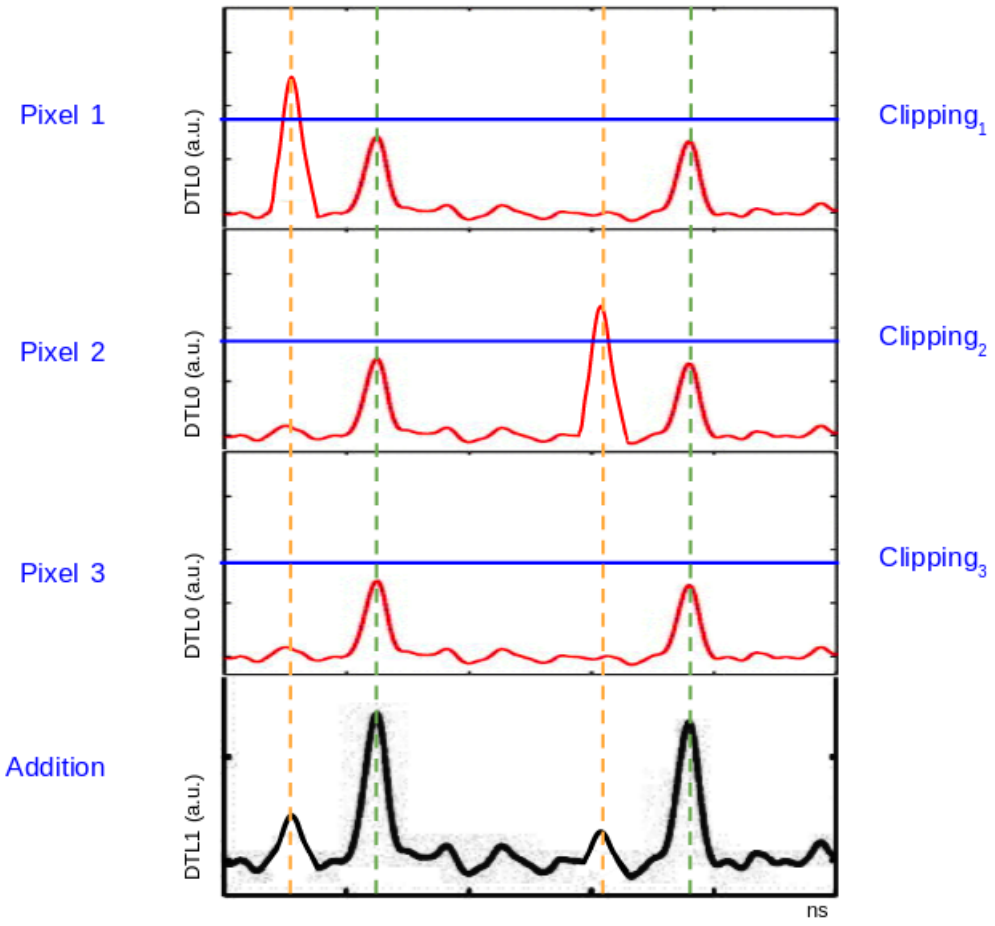

Figure A.26: Graphical example of the signal of three pixels, two of them containing high afterpulses, and the effect of applying a clipping level when the three signals are added in the Sum Trigger scheme.

The clipping circuit removes the part of a pixel signal that lies above a certain reference voltage level, called the clipping level. As seen in Figure A.26, when the pixel signal contains an afterpulse, a cut at an appropriate level will minimize the effect of that afterpulse once all the individual signals are added and sent to the L1 level.

The clipping value in the LST camera is characterized by two parameters, related to the hardware section of the clipping circuit, called the clipping bias and the clipping level. Figure A.27 shows how these two parameters determine the magnitude of the clipping voltage. The clipping algorithms set values

for these parameters. While the clipping determination finds the clipping level that does not affect the injected signal, explained below, the clipping calibration compensates the difference of applying the same clipping value for two different signals, explained in the next section.

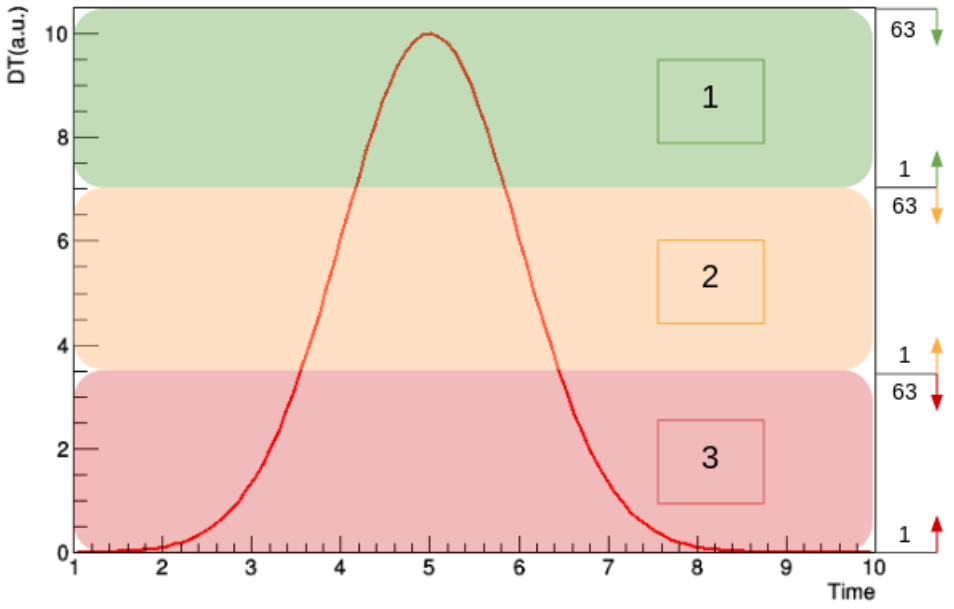

Figure A.27: Clipping regions of the signal, defined by the clipping levels (1,2,3) and the clipping bias (1-63) inside each level. The strongest value that affects the signal most is (3,1), while the softest value, which does not cut the signal, is (1,63).

The clipping determination finds the strongest clipping value that does not affect the signal, or equivalently, that does not cut the injected signal. Its inputs are:

- **Input 1:** *"injection_rate"*: It indicates the input rate of the injected signal.

The procedure, whose scheme is shown in Figure A.28, works as follows: First, the calibration determines at which clipping level (1,2,3 in Figure A.27) the signal is not affected or cut, resulting in an output rate at L1 equal to the injected rate. It tries the two inter-region values – (2,63) and (3,63) in Figure A.27 – and measures the rate at L1 level. If it is lower than the injected rate, it stays in the region above. If the output rate is smaller than the injected rate in (2,63), it means that the signal is affected at some point inside the clipping level 1. After the clipping level is found, the calibration does a binary search inside the bias region (0-63) of the corresponding clipping level, checking the output rate until the correct clipping level is found.

This calibration is repeated for every pixel in every cluster. Before launching the clipping calibration, the delay and gain of the pixels must be calibrated, in order to assure an equal amplitude at L1 that allows us to evaluate only the effect of the clipping value.

Clipping calibration

The clipping calibration compensates the difference when applying a same clipping level to two different pixel signals. This difference is due to the circuit producing the clipping voltage, whose effect can slightly

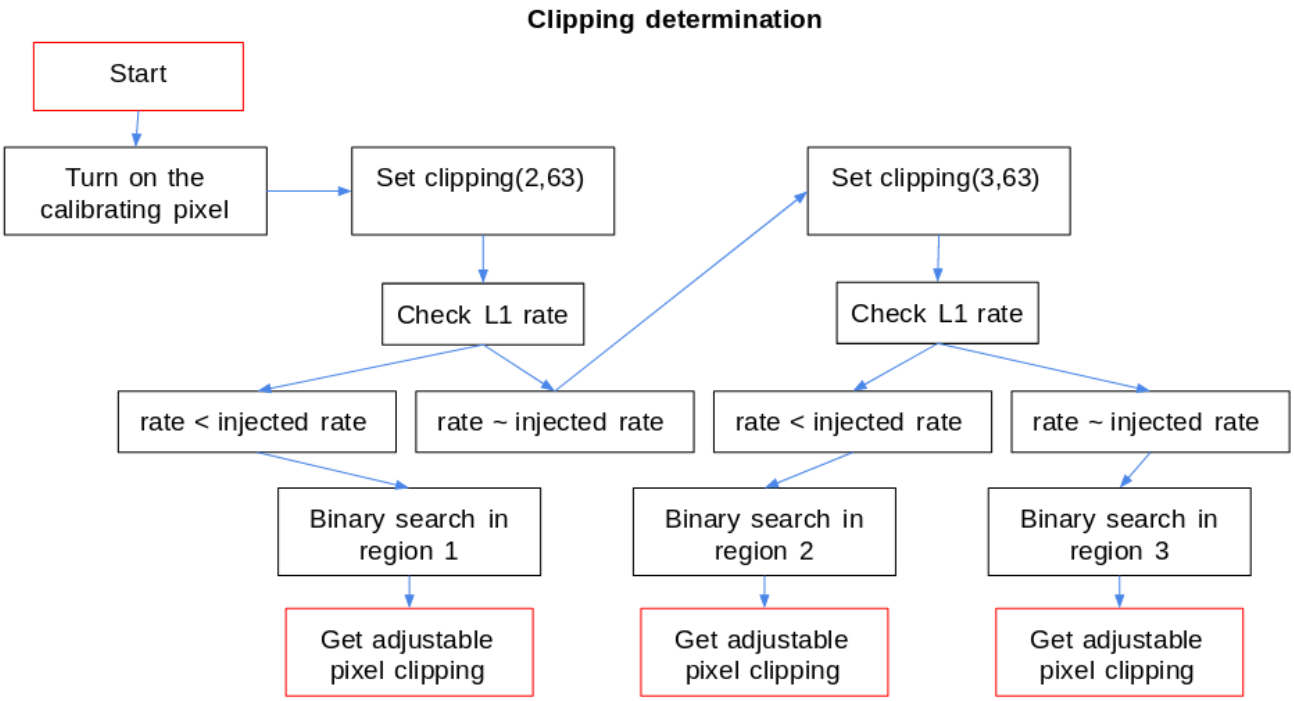

Figure A.28: Graphical scheme of the clipping determination procedure.

differ from pixel to pixel. This calibration assures that, after setting a fixed clipping value, the effect becomes equal for every pixel.

The clipping calibration looks for the difference in the effect with a similar procedure as the one developed by the delay and gain calibrations: by comparing two pixels, the adjustable and the reference pixel. Before launching this calibration, the gain must be calibrated for the pixels involved.

The clipping calibration can be made with pixels of a same cluster or different clusters and counts with the following inputs:

- **Input 1:** *"reference_clip_bias"*: It represents the value of the clipping bias set to the reference pixel signal. The default value used in the calibration is 40, in the center of the allowed interval.
- **Input 2:** *"reference_clip_sel"*: It represents the value of the clipping level set to the reference pixel signal. The usual value used in the calibration is 2, in the center of the allowed interval.
- **Input 3:** *"reference_neighbour"*: It indicates the neighbouring cluster whose adder is used in the calibration.
- **Input 4:** *"reference_pixel"*: This input indicates which pixel inside the *"reference_neighbour"* will be taken as reference pixel.

The procedure for the clipping calibration (Figure A.29) is similar to the one of the gain calibration: It starts allowing only the reference pixel signal to reach the L1 level and sets to it the clipping values *"reference_clip_bias"* and *"reference_clip_sel"*. Then, a L1 binary search is developed to know the required DTL1 level whose output rate is half the injected rate ($DTL1_{ref}$). While keeping this DTL1 value, the reference pixel is turned off and the adjustable pixel turned on, configuring it with the clipping

values *"reference_clip_bias"* and *"reference_clip_sel"*. The L1 rate is measured as, in consequence, the clipping voltage value is increased or decreased until the measured output rate is half the injected rate. This calibration result indicates the difference in the clipping level effect between the reference pixel and the adjustable one. Such that, for a specific clipping value on the reference pixel – i.e. the one obtained by the clipping determination – we know what clipping value we must set to the rest of the pixels to produce the same effect.

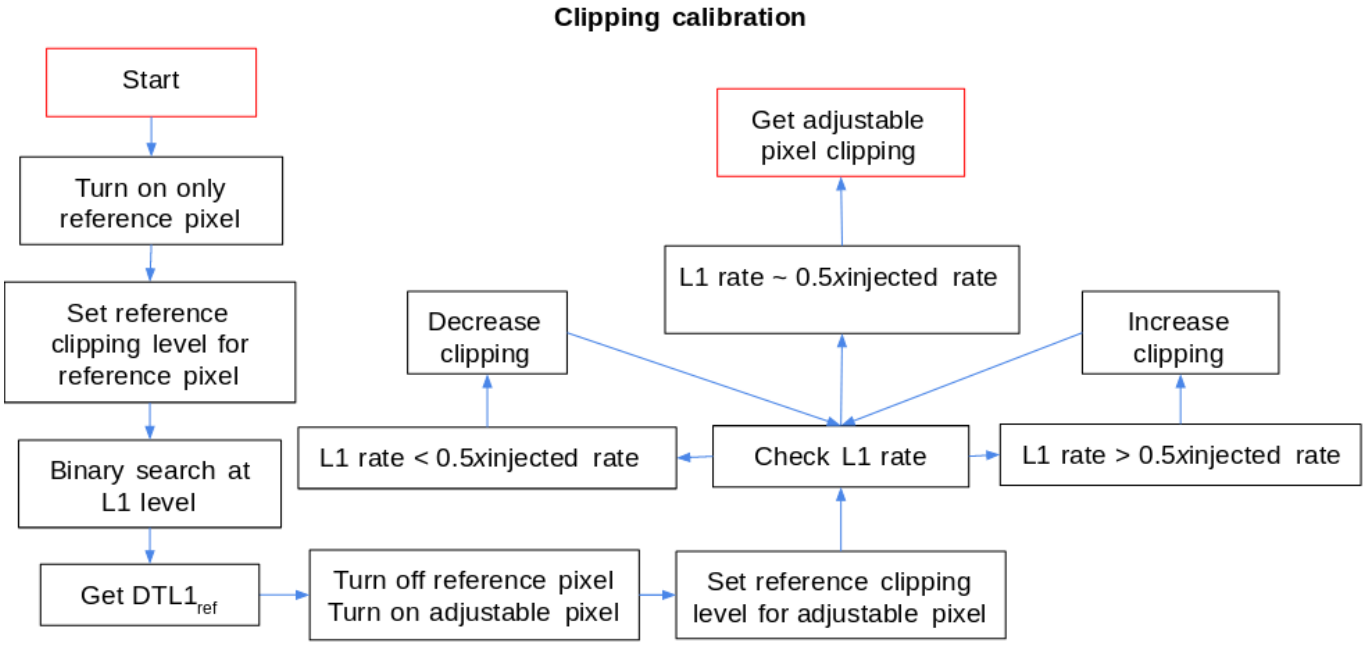

Figure A.29: Graphical scheme of the clipping calibration procedure.

A.6.2 L1 level calibrations

The L1 calibrations deal with the combination of L0 signals arriving at the different adders of the L1 level from different modules. In this level, in contrast to the L0 level, there are no parameters that can be calibrated to equalized all the different inputs in the L1 trigger.

However, the calibrations allow to characterize the differences in the adders of the L1 level in relation to the number of inputs signals and the properties of these signals.

The L1 calibrations fully characterize the L1 level, such that it can be correctly configured prior to the data taking for the different trigger schemes and trigger patterns.

DTL1 calibration

This calibration is equivalent to the DTL0 calibration, but at the L1 level. It sets the DTL1 value to a level where the output rate is 50% of the input rate. In this case, the noise region at L1 is much smaller than the noise region at L0 and is restricted to the few lowest values of DTL1 such that a baseline calibration at L1 is not required.

As in the DTL0 case, the DTL1 calibration develops a binary search (see Figure A.14) at L1 level whose range goes from 0 to 511, that corresponds to voltages from 0 to 1.2V. This calibration can be launched from both trigger schemes: the Majority and the Sum trigger.

The main difference with the DTL0 calibration is the input signal, while the DTL0 deals with the signal of a single pixel, the DTL1 can deal with signals from a single pixel to any combination of pixel, coming from one up to six different clusters. In addition, the DTL1 calibration can be made using any of the 3 adders at L1 level. This results in a bigger number of inputs:

- **Input 1:** *"injection_rate"*: It indicates the rate of the injected signals.
- **Input 2:** *"majority_trigger"*: This input is a Boolean indicating the trigger scheme for the calibration, 1 for Majority and 0 for Sum.
- **Input 3:** *"dac_number"*: This input determines the adder in which the binary search will be developed. The range is 1-3 for A-C respectively.
- **Input 4:** *"check_L0"*: This input is a Boolean that launches a check on the status of the pixels at L0 level. They are turned on and configured with their calibrated L0 parameters or with default ones. This option only acts on the pixels belonging to the module where the calibration is launched, it is more thought to do tests and check that the L0 works correctly and its signal arrives at L1. This option is usually deactivated since the calibration expects signals from more than one module and not necessarily all the pixels must be turned on.

The DTL1 calibration does not configure the adders, thus, it does not configure the clusters sending L0 signals to the different adders. For this reason, the adders must be configured before calling the calibration. The reason behind this is because the rest of calibrations (delay, gain, clipping) call the DTL1 calibration to develop binary searches at L1 level and each of them need special adder configurations, hence the configuration of the adder is in charge of these other calibrations instead of the DTL1 calibration. The only action developed by the DTL1 calibration with the adders is setting the threshold of the two adders not involved in the calibration to their maximum value (511), such that only the adder involved in the calibration allows the transit of the signal.

This calibration is not launched specifically as part of the calibration chain (Section A.6.3), but it is called by most of the calibrations that compose it.

L1 transfer function

The L1 algorithm was proposed by the CIEMAT institute in Madrid [336] [1]. This algorithm characterizes the L1 level by calling the DTL1 calibration for every combination of L0 input signals, modules in the camera and adders in those modules. In addition, the calibration also characterizes the camera for different amplitudes of the injected signal.

The procedure is repeated for each of the three adders and each of the six L0 signals reaching each adder. Also for different L0 signal amplitudes by turning on and off a specific number of pixels.

[1] https://portal.cta-observatory.org/WG/lst/Engineering%20Documents/D-Technical_Documentation/D.06-Drawings_and_Schematics/D.06.03-Camera/Trigger/l1-transfer-function-pseudo-code_draft.pdf

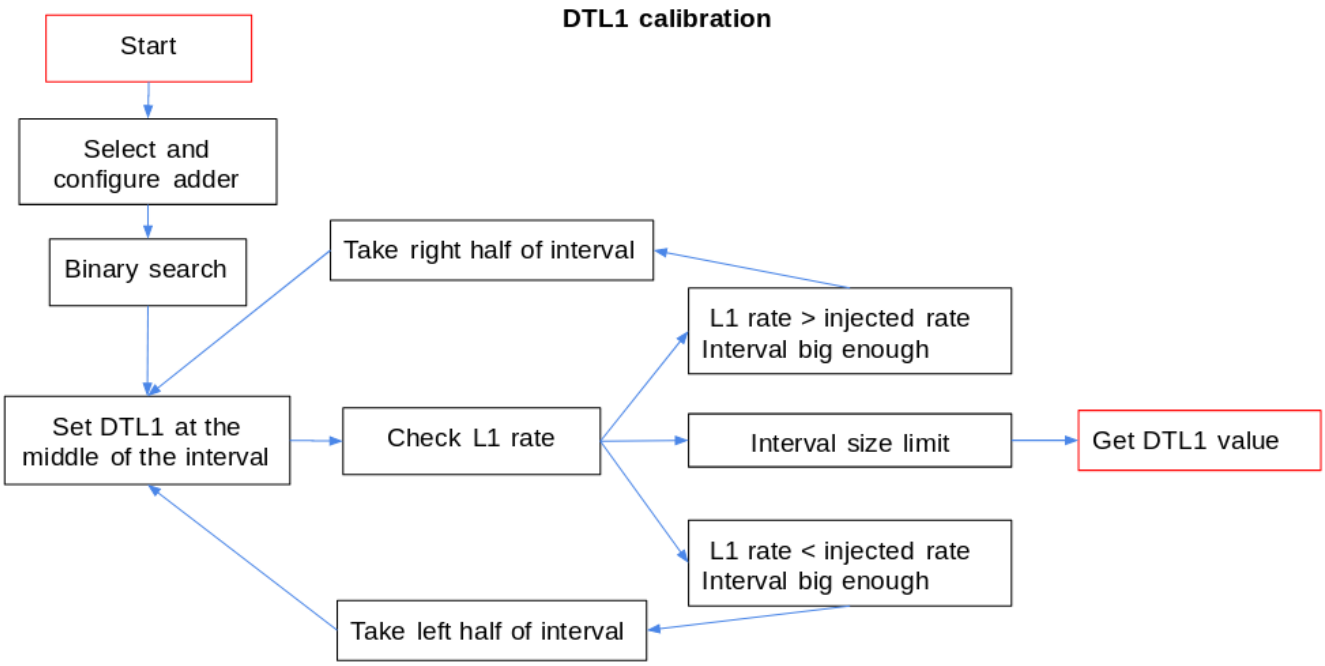

Figure A.30: Graphical scheme of the DTL1 calibration procedure.

Before launching this calibration, the L0 level must be calibrated and the corresponding calibrated parameters must be set to the pixels. In addition, the camera must be uniformly illuminated with a signal of known rate. This calibration counts with 4 inputs:

- **Input 1:** *"injection_rate"*: It indicates the rate of the injected signals.
- **Input 2:** *"majority_trigger"*: This input is a Boolean indicating the trigger scheme for the calibration, 1 for Majority and 0 for Sum.
- **Input 3:** *"dac_number"*: This input determines the adder where the L0 signal arrives.
- **Input 4:** *"neighbour_number"*: This input indicates the module sending the L0 to the corresponding adder. The modules are tagged as indicated in Figure A.15 where 3 means that the L0 comes from the same cluster the adder is located on.

Different pulse amplitudes required for the algorithm are obtained by switching off and on different pixels of the module producing the L0 signal being used in the calibration. For every amount of turned on pixels, a binary search is launched at L1 level, resulting in an output rate of 50% the injected rate.

The L1 transfer function algorithm provides, for that adder and L0 input signal, an array showing the DTL1 calibration results versus the number of turned on pixels (see Figure A.31).

The algorithm is launched inside a loop that goes through all the modules of the camera, all the adders inside those modules and all the L0 signals that can reach those adders, such that all possible combinations are tested and the L1 level is fully characterized. This calibration requires the longest time. In addition, the whole process is repeated for the Majority and Sum triggers, separately.

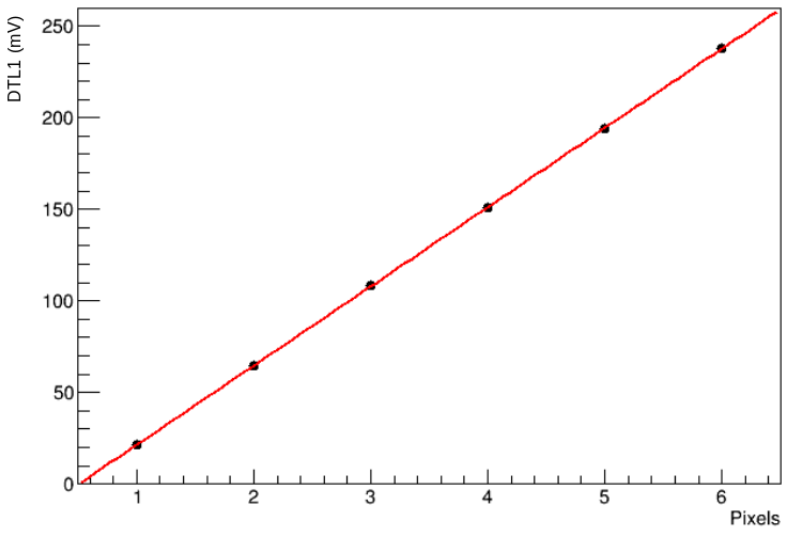

Figure A.31: Transfer function resulting from a single adder and the local L0 signal. The Y axis shows the result of the DTL1 calibrations. The X axis shows the number of pixels enabled to contribute to the L0 signal. Credit: CIEMAT [336]

A.6.3 Calibration order

The calibration musts be launched in a specific order going always from pixel-level to cluster-level and repeating the procedure for both trigger schemes.

Inside the pixel-level, the order of the calibration is also strict and the effect of one calibration on the results of the other ones must be taken into account.

Figure A.32 shows the order of the calibration launches, taking into account the required iterations.

In both trigger schemes, the initial calibration is the baseline calibration, in order to know the working DTL0 region for every pixel, and the DTL0 calibration, that is crucial in the Majority scheme for the signal to reach the L1 level and not so much important in the Sum case, but useful to have an idea about the amplitude of the injected signal. After that, the next calibration is the delay calibration inside the clusters using one pixel as a reference. In the Sum case, the gain is calibrated next, requiring some iterations with the delay calibration until the results of both are stable. In the Sum case, the clipping calibration comes next. Once the individual clusters have all the pixel-level parameters calibrated, the next step is to spread the delay and gain calibrations along the camera via the inter-cluster level calibrations. At the end, the L1 transfer function will characterize the whole camera response.

The current status of the calibration codes and its tests are shown in Section A.8. Some example of the calibration results as well as their required time are exposed in Section A.9.

A.7 Camera software structure

The software in charge of the control of the LST camera is called Camera Control (CaCo). It has been mostly developed at IFAE by Cristobal Pio. CaCo establishes the link between the telescope, the camera and the different subsystems that compose the camera.

CaCo code is written in Java and divided into three main layers:

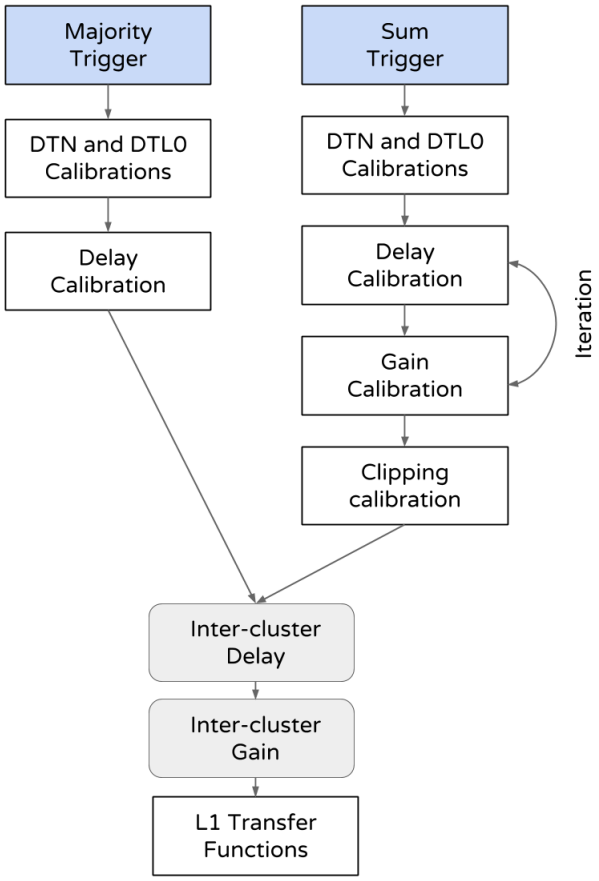

Figure A.32: Graphical scheme of the order of the calibrations launching for every trigger scheme.

- **Export layer:** It exports the camera functionality to the Telescope Control code (top code layer) such that the telescope gets information about the status and operation of the camera.
- **Camera Control Logic:** This layer is the central core of the software. It contains the state machine of the camera, related to the states of every different subsystem. The configuration of the subsystems is done through XML files sent by the camera control.
- **Subsystems access:** This layer communicates with the different subsystems that compose the camera. Using XML files, it can configure and operate the different subsystems (see Figure A.33).

The complete functionality of CaCo can be accessed using an OPC UA Server, where all the subsystems functionality is exported.

In this thesis, we do not go further in detail about the CaCo software but we focus on one of the camera subsystems, called Cluster Control (ClusCo), in which the calibrations mentioned in the last sections are implemented.

A.7.1 Calibrations programs: CaCo, CaCali and ClusCo

ClusCo is the subsystem of the camera in charge of the control of all the clusters and their corresponding pixels. ClusCo is the bottom level code with direct access to the hardware registers. It is written in C++ and developed at ICRR (Japan). ClusCo controls the clusters using methods contained in the low level

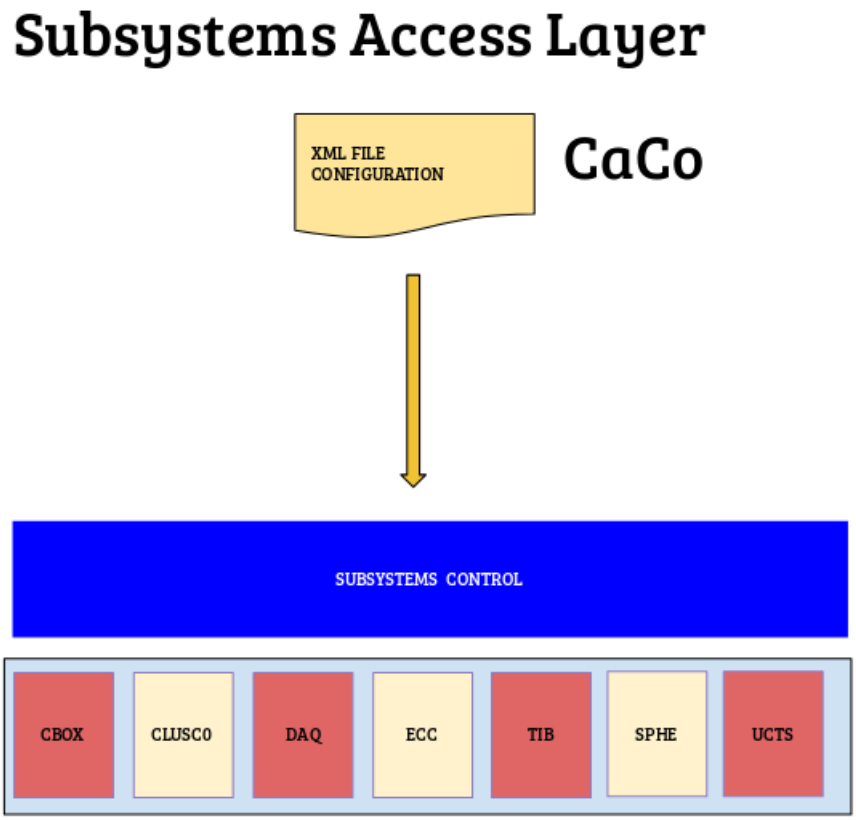

Figure A.33: Graphical scheme of the connection between CaCo and the different camera subsystems. Credit: C.Pio.

access library (See Figure A.34) that acts on the different hardware boards composing the cluster (Dragon Board, Slow Control Board, Backplane Board and Mezzanine Board (L0 and L1 trigger)). Moreover, ClusCo counts with a menu that allows to use such methods in an interactive way or load configuration files in "uic" format. However, ClusCo lacks software logic, in the sense that it does not have a systematic way of controlling the clusters, to calibrate or prepare them for datataking. For this reason a new software layer has been build over ClusCo, developed at IFAE in C++, that acts on the clusters using ClusCo as intermediary. This part of the code allows the connection to CaCo through an OPC UA Server (and a translator layer from C++ to Java) and receives orders from CaCo via XML files that are sent to the hardware through ClusCo. The section of this new code containing the calibrations algorithms is called Camera Calibrations (CaCali).

The calibrations are a collection of C++ codes sending ordered commands to the clusters through ClusCo and reading hardware data through a data structure, shared with ClusCo. Figure A.35 shows graphically the communication between CaCali and ClusCo.

As shown in Figure A.35, the calibrations send their commands, for example set the DT al L0 level, using the setters and getters (Figure A.34) over the data structure. The data structure is an abstract layer that allows to access the data. Such data can be provided by the real hardware but also by a simulator, that can be used for testing the system in the absence of the hardware. When dealing with the real hardware, the data structure refers to the methods developed in the low level access library. ClusCo receives the orders and acts consequently, acting over the hardware via setting the corresponding values or reading

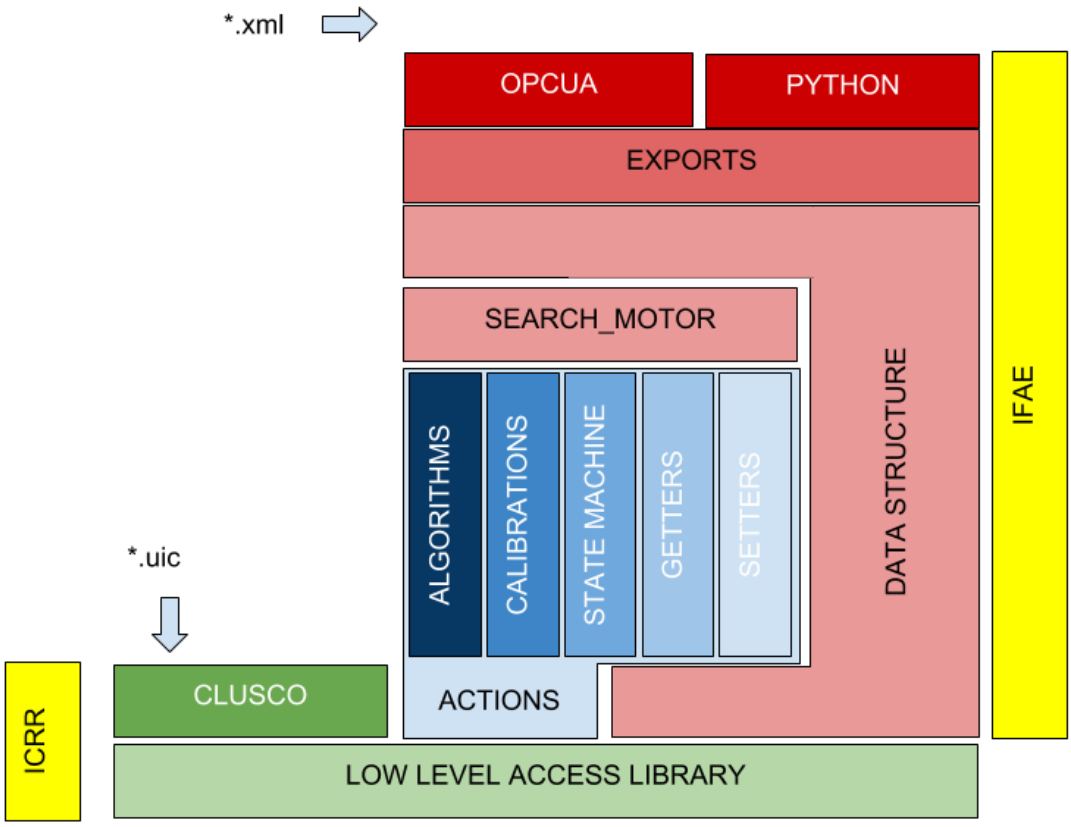

Figure A.34: Graphical scheme of the different layer in the ClusCo subsystem. Credit: C.Pio

the values from the corresponding registers and filling the data structure. When using the simulator, the structure is filled with pre-defined default values. Finally, the calibration codes access the data structure to check if their commands were launched correctly.

This structure was developed to assure a separation between the bottom layer of the code (ClusCo) and the top layers, including CaCali. This is due to the fact that both layers are being developed simultaneously and this structure minimizes the impact and required changes in the top layers when the bottom layer is modified and allows to test the upper layer in the absence of the bottom one.

A.7.2 Calibration structure

The calibration codes are written in C++ in an object-oriented scheme. The algorithms are composed by two classes and one enumerate. The enumerate contains the possible final states of the calibrations (*BEGIN*, *END*, *FAIL*, *NOTFOUND*) and the two classes are called the *Status* class and the *Calibration* class:

- ***Status class*:** This class saves the status and the result of the calibration. It also contains a statement of information, usually explaining the reason behind a failed calibration and the information about

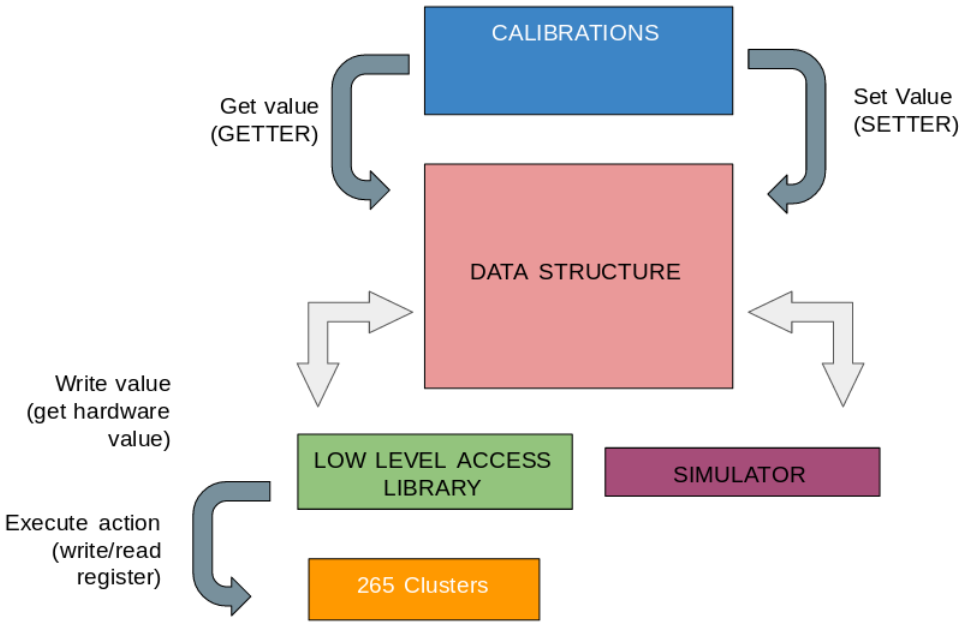

Figure A.35: Graphical scheme of the communication between the calibration codes and the clusters through the ClusCo code level.

the values of the inputs used in the calibration. Therefore, this class allows to check the conditions and status of a given calibration after it has been launched.

- ***Calibration class*:** This class contains the setters for the different inputs of the calibration. It launches the calibration and interacts with the *Status* class to provide the status and the final result. In the case of the delay calibration, this class selects the mode for the calibration and calls the corresponding procedure. The calibration class constitutes the core of the calibration algorithms.

All the calibrations share the same structure, the only difference resides in the Calibration class, where the complete procedure of the specific calibration is coded.

A.7.3 Calibration launches

The calibrations are launched through classes called *Launchers* The *Launchers* receive the information about the calibration type to be launched and the object to be calibrated (a single pixel, a group of pixels, an entire cluster, the whole camera) and check the compatibility between them using discriminators, i.e. they do not allow to launch a cluster calibration like DTL1 over a single pixel. Moreover, they receive the arguments for the inputs and set them into the Calibration class. The *Launchers* control the development timing for the calibrations, that can be launched in serial order − one calibration after another, waiting for one calibration to end before launching the next one − or in parallel, i.e. all calibrations are launched simultaneously, depending on the number of available threads. If the number of threads is smaller than the number of calibrations, the calibrations are divided in groups and every thread launches one of these groups in serial order.

At the final stage, when the camera is completely ready, the *Launchers* will be called via XML files from CaCo, where the XML files are interpreted in the "MOTOR_SEARCH" (see Figure A.34) extracting the information that is provided to the *Launchers*. However, at the present moment and for

testing purposes, the *Launchers* functionality can also be accessed directly creating an object of the class and indicating the corresponding inputs, as shown in Figure A.36.

The calibration inputs do not need to be always introduced, since they count with default values that are applied in case the input values are not provided.

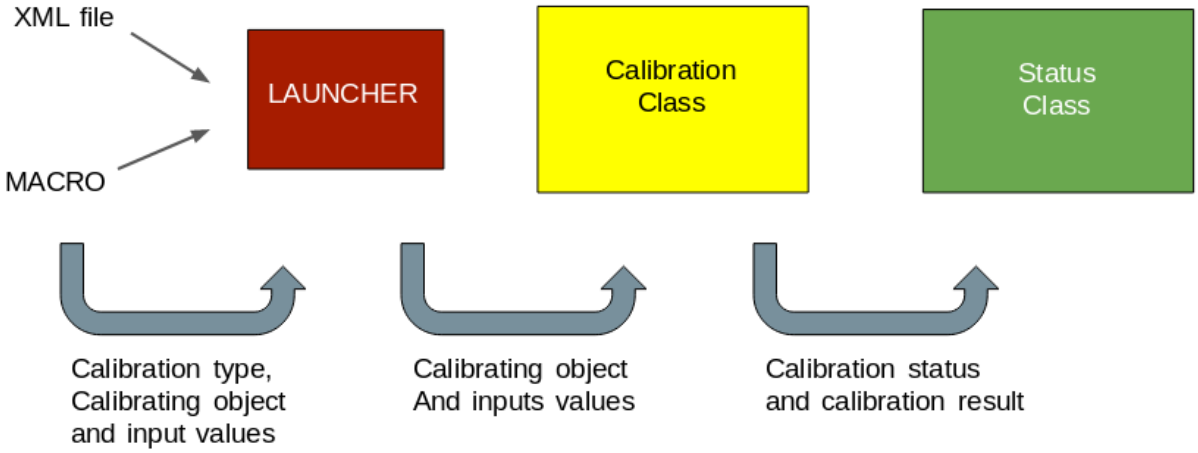

Figure A.36: Graphical description of the procedure followed to launch a specific calibration.

Figure A.37: Picture of the light flasher used for testing the calibrations.

It is important to mention that most of the calibrations require an injected signal in the camera, the *Launchers* are not in charge of injecting a signal, so it must be injected prior to the calibration. This signal must be in the form of light pulses. In the future a subsystem of the camera called Calibration Box will take care of injecting a signal and inform the calibrations about the signal properties (injected rate and injected amplitude), but it is still under development. For this reason, for testing purposes, we currently use an external flasher (see Figure A.37) and introduce the signal properties manually in the calibrations. Another option is to introduce an internal electrical signal, called Test Pulse (TP), with similar properties to the Cherenkov radiation and produced inside the modules right after the PMTs. This signal is very useful for testing purposes since the HV can remain off but it cannot be used for the inter-cluster calibrations since the TP is not simultaneous in all clusters, a condition required for these calibrations. In addition, the PMT transit time and gain effect cannot be corrected by using this electrical signal.

A.8 Current status and perspective

The contribution of this thesis to the trigger calibrations of the LST camera has been based in the design (except for the L1 calibration), production of the codes and tests for all the above explained calibrations, as well as their adaptation in order to interact with the *Launchers*, the Status classes and the ClusCo bottom code layer. Furthermore, the development of tests launching those calibrations via macros and XML files to fully test the correct operation of the codes has been part of the contribution.

At the moment of the writing of this thesis, the individual calibration codes are finished and working correctly on individual modules. All of them has been tested in their intra-cluster version and the Delay and Gain calibrations have also been tested in the inter-cluster version. They have been tested on specific modules of the camera using TP and the external flasher. The Baseline and DTL0 calibration have been test up to 33 modules simultaneously.

However, the complete codes underwent major changes in order to fulfill some new camera requirements, as the use of XML files, that delayed the design process. Additional changes were also required to adapt the calibration codes to changes performed in the ClusCo code layer. Moreover, the initial scheduled time interval for the LST camera to be at IFAE for final testing was reduced and many other important tests (hardware validation, connectivity tests, cluster control tests by ClusCo, etc.) needed to be performed before launching the calibrations. Additionally, the overlap between the writing of this thesis and the whole test period reduced the available time of the author to work on the calibrations tests. Due to all these reasons, the final stable version of the calibrations could only be tested, using TP, in their intra-cluster version and some inter-cluster gain and delay calibration were tested (even though TP is not well suited) to verify the correct performance of the codes, specially focus on the correct configuration of the adders to read signals from different clusters simultaneously. The algorithms that will launch the calibrations along the camera has been already design but are still under development. Therefore, the final test of the calibrations will be done during the commissioning period, as well as the study of their dependency with factors as temperature, humidity, current or NSB. Despite this, the intra- and inter-cluster calibrations are performed by the same code so that a correct operation of the intra-cluster calibration assures a correct operation of its inter-cluster version. One more important issue to study during the commissioning period is if the expansion of the calibrations along the camera produce a homogeneous response of the trigger regions or create any kind of drift towards the outer part of the camera, since that would require a change in the calibration expansion initial plan.

The calibrations do not give a final result, since their results depend on the conditions of the camera and the injected input signal. Even though, it has been tested that the results are reproducible for the same initial conditions. In order to show the correct operation of the calibrations, the next section shows the results of the intra-cluster calibrations over a specific cluster, using a TP as injection signal, and give information about the required time for a calibration over a single pixel and over a complete cluster.

When using the TP, we get rid of the effects due to the PMTs, so that the calibrated quantities (delay, gain, clipping) are expected to be similar to the ones taken as reference. Event though this permits to evaluate the calibrations in a simplified way, the right evaluation is to measure directly this quantities i.e. with an oscilloscope, in order to see directly the signals shape and cross check the calibrations' results.

A.9 Results

First, the initial calibrations applied over single pixels at the beginning of the calibration chain are the Baseline and the DTL0 calibrations. The baseline calibration time differs slightly if the noise region is found at the first trial (34 seconds) or if it has to be found previously (up to 64 seconds). When launched over a complete cluster, were every pixel in the cluster is calibrated simultaneously, the averaged required time is 114s. The results over a cluster a shown in Table A.2.

The DTL0 calibration, due to the binary search, is very quick. It takes 22 seconds for a single pixel and 44 seconds for a whole cluster. Table A.2 shows its results for two different intensities of the TP.

Pixel	DTN	DTL0 (TP gain=25)	DTL0 (TP gain=30)
1	516	618	694
2	498	602	680
3	512	609	698
4	508	612	689
5	518	627	707
6	511	611	692
7	512	612	688

Table A.2: Example of the Baseline and DTL0 calibration results for a specific cluster.

	Majority Trigger		Sum Trigger	
Pixel	Rate Mode	Binary Mode	Rate Mode	Binary Mode
1	3 ns	3 ns	3 ns	3 ns
2	2.5 ns	2.25 ns	2.75 ns	2.75 ns
3	2.75 ns	2.5 ns	2.75 ns	2.5 ns
4	3 ns	3.25 ns	2.75 ns	3.25 ns
5	2.75 ns	2.5 ns	2.75 ns	3.25 ns
6	2.75 ns	3.25 ns	2.75 ns	3.25 ns
7	3 ns	3.25 ns	2.75 ns	3.5 ns

Table A.3: Example of the delay calibration results for a specific cluster, for the Majority and Sum trigger schemes, and for the Rate and Binary modes.

The DTL1 calibration, usually called by the rest of the calibration, takes 18 seconds to perform on one cluster, for any of the two trigger schemes.

The delay calibration required time depends on the mode used. For the "Rate Mode", the calibration time depends on the DTL1$_{ref}$ value, if the value is right for the combined pair of pixels signals, one calibration takes around 68 seconds, however, if it too high, the calibration takes is down until the combined signal of the two pixels triggers and the calibration can take up to 90 seconds. For a complete cluster, the average time required is 7 minutes. In the case of the "Binary Mode", the calibration takes much longer due to the binary search performed for every value of the delay. For an individual pixel, the calibration time is 7 minutes, while for a complete cluster, it takes 43 minutes. An example of the results obtained for the delay calibration, for both trigger schemes and both calibration modes are exposed in Table A.3. For these calibrations, the pixel 1 has been taken as reference, at the delay path of 3 ns.

The gain calibration, using TP is quite quick, since the effect of the PMT is not included. The duration of this calibration for a single pixel takes 28 seconds. When launched for a whole cluster, the required time is 2.9 minutes. Table A.4 summarizes the results of an intra-cluster gain calibration, taking as reference the pixel 1, with a gain of 7.

The clipping calibration takes 30 seconds for a pixel and 3 minutes for a complete cluster. Table A.4 exposes the results of a intra-cluster clipping calibration taking as reference the pixel 1 with clipping bias 20 and the clipping level 2.

The L1 calibration was only tested for one module and one adder and its required time is 2.3 minutes. However, this calibration is repeated many times for all the modules, adders and L0 inputs. The CIEMAT institute did a preliminary expectation of the required time for the complete calibration [336] in 10 hours. However, by parallelizing the DTL1 calibration over the modules, the time could be reduced in, at least, a factor 10. The DTL1 now fulfills this requirement but this calibration could not be tested in its complete

Pixel	Gain	Clipping bias	Clipping level
1	7	20	2
2	7	20	2
3	8	20	2
4	7	20	2
5	7	20	2
6	7	20	2
7	7	20	2

Table A.4: Example of the gain calibration results for a specific cluster.

Number of Pixels	L1 calibration (Majority)	L1 calibration (Sum)
1	50.4 mV	62.4 mV
2	84 mV	175.2 mV
3	132 mV	276 mV
4	177.6 mV	367.2 mV
5	244.8 mV	451.2 mV
6	290.4 mV	525.6 mV
7	338.4 mV	588 mV

Table A.5: Example of L1 transfer function resulting array for the Majority and Sum trigger schemes.

version during the test period at IFAE. An example of the results for one module and one adder and for the Majority and Sum trigger schemes over a cluster, with a TP of gain 25 are shown in Table A.5 and represented graphically in Figure A.38.

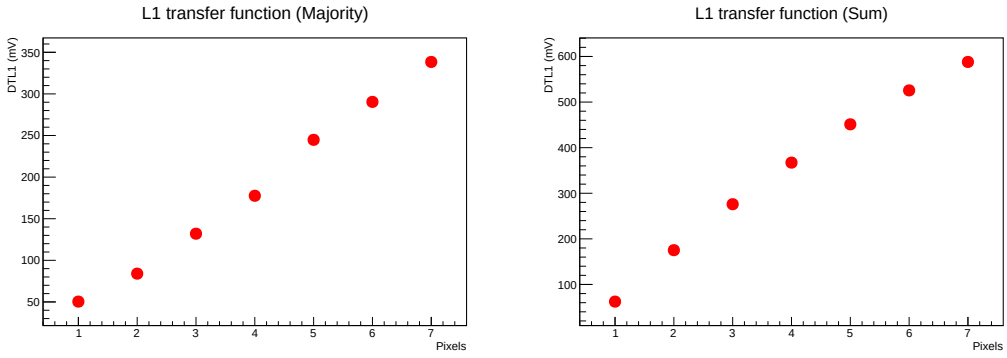

Figure A.38: Resulting array from a L1 transfer calibration, using the Majority and Sum trigger schemes.

As a conclusion, the calibrations related to the amplitude of the pixel signal present less variation with respect to the values taken as reference in the absence of the PMT effects. On the other hand, the delay calibration presents more variability, even though the deviations are never bigger than 0.75 ns with respect to the values taken as reference. In the case of the Sum trigger scheme using Rate Mode, the overlap region is so wide than the calibration is not able to determine correctly the overlap interval central point. Therefore, when working with the Sum trigger, we must use the Binary Mode. This is not the case for the Majority trigger, where the Rate Mode can we used to save time. The L1 transfer function shows a linear relation between the number of turned on pixels and the DTL1 for the Majority trigger, however, in the Sum trigger case, it saturates with large number of turned on pixels. Thus, for the L1 calibration with Sum trigger is recommendable to use a TP gain smaller than 25.

As mentioned before, the codes in charge of expanding the calibration along the camera are under

development so that the time to calibrate a whole cluster, and hence the complete camera, will probably be reduced.

Appendix B

MAGIC background estimation modes

For the wobble mode observation procedure, the number of background events in the ON regions is estimated by comparing the number of observed events around the source of interest (ON region) with the number of recorded events in a nearby region containing no sources (OFF region).

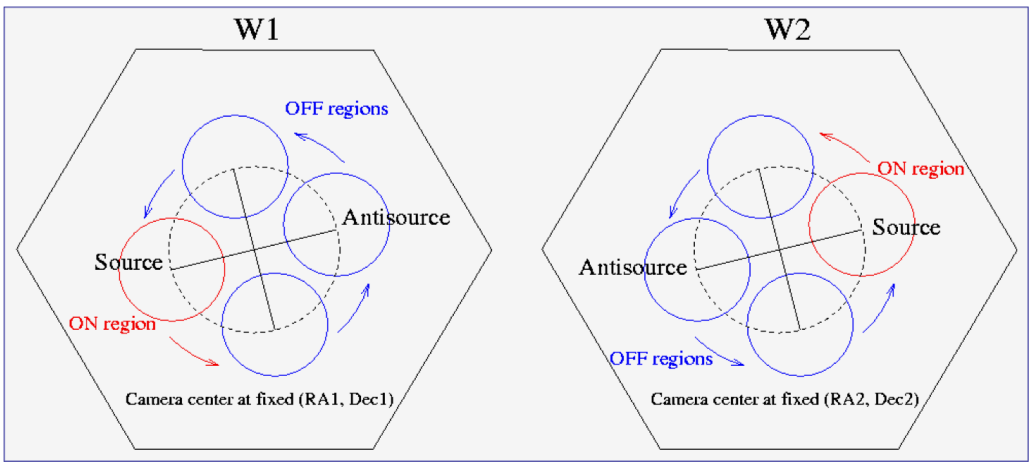

Figure B.1: Graphical description and movement of the source and the OFF regions during a wobble mode observation, for the wobble positions W1 and W2.

Since the mount of the telescopes is alt-azimuthal, during the wobble mode observation, the source will rotate on the camera (see Figure B.1). In this case, the source is not located in a privileged position, in the sense that the best acceptance of the camera is on the center. However, this fact allows to obtain an estimate of the background events by using an "OFF position", located in another region of the camera, for which the acceptance is expected to be the same: for example, the point symmetric to the source position with respect to the center of the camera (sometimes called "anti-source"). Equivalently, other camera regions at the same distance to the camera center can be used as additional OFF positions. This approach, called "simultaneous background", is the simplest way to estimate the background in wobble observations. We simply count the events that are recorded in the OFF regions and then subtract them − after normalization in case of more than one OFF region − from those recorded, in the same period of time, in the ON region.

However, the assumption of equal acceptance of the ON and OFF regions is not completely right. Even though the acceptance mostly depends on the distance to the center of the camera, it is not the only

factor, the different OFF positions are located at slightly different zenith distances and therefore, they are not completely equivalent.

By observing the Figure B.1 the proper OFF for the ON data collected during the wobble pointing W1, would not be obtained during such pointing, but during all the other pointings (W2,W3,W4), because in those, there is always one OFF position which follows approximately the same path through the camera as the the source does in the W1 pointing, for example, in the W2 pointing, such OFF position would be the "anti-source" one. This more complex background estimation approach is called "Off from Wobble partner".

It is hard to say which of the two methods offers a less biased background estimation. Qualitatively speaking, if the observation conditions (detector+atmosphere) are very stable over the observation time, the "Off from Wobble partner" method is better, because it will take care of possible differences in acceptance between the ON and the OFF regions. In case of unstable conditions, then it is better to use the "Simultaneous background" approach, because it will take care of the possible changes in performance over time.

In the case of flares, especially the short ones that consist on very short observations, sometimes with only one wobble, usually the first method is used. In the case of the Mrk 421 flare in 2014 described in Chapter 5, the background estimation was performed using "simultaneous background" since, at the moment of the detection, the camera was homogeneous enough such that the dominant variations were temporal and not spacial.

Glossary

ADC Analog-to-Digital Converter. 99, 100

AGN Active Galactic Nucleus. 3, 56, 61, 63–65, 76, 77, 84, 86, 90, 109, 110, 115, 137, 145, 162, 165–167, 173, 174

AMC Active Mirror Control. 90, 92, 93

BH Black Hole. 58, 61, 62

CaCo Camera Control. 210, 212

CDF Cumulative Distribution Function. 83, 84, 125, 126

CH Counting House. 90, 94, 95, 97

CI Confidence Interval. 81, 84, 87, 124, 126, 143, 160

CL Confidence Level. 81, 84, 87, 124, 126, 152, 167, 169

ClusCo Cluster Control. 211–213

CPT Charge Parity Time. 25, 26, 28, 29, 32

CR Cosmic Ray. 34–36, 41–43, 49, 51, 52, 54, 59, 66, 67, 89

CS Compton scattering. 39, 42

CTA Cherenkov Telescope Array. 5, 7, 20, 54, 56, 57, 76, 77, 143, 174, 181, 182

DAQ Data Acquisition System. 94, 187

DB DataBase. 110, 111, 113–115

DSR Doubly Special Relativity. 27, 29, 30, 70, 71

DT Discriminator Threshold. 96, 189

EAS Extensive Air Showers. 42, 43, 45–47, 50, 53, 54, 89, 95, 101

EBL Extragalactic Background Light. 38, 39, 62–65, 71, 72, 76, 84, 85, 109, 110, 112, 118, 121, 128, 129, 131, 132, 134

EFT Effective Field Theory. 3, 27–32, 69, 71

EHE Extremely High Energy. 35

EM Electromagnetic. 7, 33, 34, 38, 45, 46, 50, 63, 65

FoV field of view. 49, 51–54, 57, 76, 90, 92–94, 121, 183

GR General Relativity. 19, 21–24, 29

GRB Gamma-ray Burst. 3, 8, 32, 49, 65–67, 76–79, 81, 90, 93, 109, 127, 150, 162, 165, 166, 171, 174, 182

H.E.S.S. High Energy Stereoscopic System. 7, 16, 20, 54–57, 60, 62, 66, 72, 78, 80, 84, 87, 89, 162, 165, 167, 171, 174

HAWC High Altitude Water Cherenkov. 52, 74

HE High Energy. 31, 35, 38, 43, 48–50, 59, 60, 62, 64–67, 69, 73, 87, 125–127

HV High Voltage. 94, 192, 194, 195, 200

IACT Imaging Atmospheric Cherenkov Telescope. 7, 12, 30, 45–47, 51, 53–55, 57, 69, 71, 76–78, 82, 89, 90, 98, 118, 130, 173, 174, 183

IC Inverse Compton. 36, 39–41, 60, 61, 64, 66, 67, 75

IPR Individual Pixel Rate. 96

IRF Instrument Response Function. 106, 119, 166, 167

IS interstellar. 58–61, 63, 65

KDE Kernel Density Estimation. 81, 146, 147, 149–151, 174

LAT Large Area Telescope. 7, 43, 49, 50, 59, 60, 64, 65, 67, 76, 78–81

LE Low Energy. 28, 29, 35, 38, 87, 125–127

LI Lorentz Invariance. 26–28, 30, 31, 69, 71–75, 86, 167

LIV Lorentz Invariance Violation. 3, 8, 10, 12, 19–21, 26–32, 36, 63, 69–82, 85–87, 105, 109, 110, 115, 116, 118, 119, 121, 122, 125, 128, 129, 131, 134, 136–138, 143, 154, 157, 160, 162, 163, 165–167, 169, 171, 173, 174

LL Lower Limit. 142, 143

LQG Loop Quantum Gravity. 23–26

LST Large-Sized Telescope. 5, 20, 57, 173, 181–185, 191, 204, 210, 215, 216

LUT Look-Up Table. 8, 93, 104, 118–120, 122, 129–131, 143

MAD Median Absolute Deviation. 155

MAGIC Major Atmospheric Gamma-ray Imaging Cherenkov. 7, 8, 12, 16, 20, 47, 54, 55, 57, 60, 62, 66, 67, 77, 78, 80, 86, 87, 89–99, 102–107, 109–111, 113–119, 121, 134, 145, 157–160, 162, 165–167, 171, 173, 174, 182, 183, 187

MARS MAGIC Analysis and Reconstruction Software. 99, 118, 121, 129, 130, 133

MC Monte Carlo. 12, 87, 98, 99, 102, 105, 106, 118, 121, 122, 129, 134, 169

ML Maximum Likelihood. 13, 82, 84–86, 119, 121, 122, 124, 126, 129, 130, 133, 134, 141, 143, 144, 146, 150–152, 154, 157, 161–163, 167, 173, 174

MW Multi Wavelength. 64

NS Neutron Star. 58–61, 65

NSB Night Sky Background. 54, 93, 100, 183, 216

PDF Probability Density Function. 81, 85, 86, 124, 128–134, 137, 139, 141–143, 157, 167

PMT photomultiplier. 49, 51, 52, 55, 94–96, 98, 183, 186, 188, 192, 194, 195, 204, 215–218

PSF Point Spread Function. 98

PV PairView. 8, 80–82, 84, 121, 122, 124–127, 160, 161, 173

PWN Pulsar Wind Nebula. 32, 59, 61

QED Quantum Electrodynamics. 28

QFT Quantum Field Theory. 19, 21–23, 28

QG Quantum Gravity. 12, 21–26, 28, 69, 77, 80, 85, 109, 124, 125, 128, 142, 145, 150, 152, 156, 167, 168, 173, 174

QM Quantum Mechanics. 22, 25

RF Random Forest. 8, 9, 118–120, 122, 129–131, 133, 143, 173

RMS Root Mean Square. 101

SM Standard Model. 27, 28, 31, 69

SMBH Supermassive Black Hole. 63, 64

SME Standard Model Extension. 28, 30–32, 75

SMM Sharpness-Maximization Method. 82–84, 121, 122, 125–127, 160–162, 173

SN Supernova. 58, 59, 61, 65, 66

SNR Supernova Remnant. 58, 59, 61, 77

SR Special Relativity. 22, 23

SSC Synchrotron Self Compton. 63

ST String Theory. 23–26

SUSY SuperSymmetry. 29, 69

TIB Trigger Interface Board. 184, 185, 187, 189

ToF Time-of-Flight. 12, 69–71, 75–81, 84, 150

TP Test Pulse. 94, 215–218

UHE Ultra High Energy. 35, 41

UL Upper Limit. 142, 143

VERITAS Very Energetic Radiation Imaging Telescope Array System. 7, 16, 20, 54–57, 60, 62, 67, 78, 80, 89, 165–167, 171, 174

VHE Very High Energy. 19, 31, 35, 36, 38–43, 51, 59–66, 69, 76, 89, 109, 111, 116, 143, 165–167, 171, 182

Bibliography

[1] C. D. Hoyle, U. Schmidt, B. R. Heckel, E. G. Adelberger, J. H. Gundlach, D. J. Kapner, and H. E. Swanson. Submillimeter Test of the Gravitational Inverse-Square Law: A Search for "Large" Extra Dimensions. *Physical Review Letters*, 86:1418–1421, February 2001. *Preprint:*hep-ph/0011014.

[2] Jonathan R. Friedman, Vijay Patel, W. Chen, S. K. Tolpygo, and J. E. Lukens. Quantum superposition of distinct macroscopic states. *Nature*, 406:43 EP –, Jul 2000.

[3] Marc H. Goroff and Augusto Sagnotti. The Ultraviolet Behavior of Einstein Gravity. *Nucl. Phys.*, B266:709–736, 1986.

[4] Kenneth Eppley and Eric Hannah. The necessity of quantizing the gravitational field. *Foundations of Physics*, 7(1):51–68, Feb 1977.

[5] C. Moller. Les theories relativistes de la gravitation. *CNRS*, 1962.

[6] L. Rosenfeld. On quantization of fields. *Nuclear Physics*, 40:353 – 356, 1963.

[7] T. W. B. Kibble. Relativistic Models of Nonlinear Quantum Mechanics. *Commun. Math. Phys.*, 64:73–82, 1978.

[8] Roger Penrose. On gravity's role in quantum state reduction. *General Relativity and Gravitation*, 28(5):581–600, May 1996.

[9] G. C. McVittie. An Example of Gravitational Collapse in General Relativity. *ApJ*, 143:682, March 1966.

[10] Roman Jackiw. What good are quantum field theory infinities? In *Mathematical physics 2000*, pages 101–110, 1999. [,101(1999)].

[11] J. B. Hartle and S. W. Hawking. Wave function of the universe. *Phys. Rev. D*, 28:2960–2975, Dec 1983.

[12] S. Deser. General relativity and the divergence problem in quantum field theory. *Rev. Mod. Phys.*, 29:417–423, Jul 1957.

[13] Luis J. Garay. Quantum gravity and minimum length. *Int. J. Mod. Phys.*, A10:145–166, 1995. arXiv:gr-qc/9403008 [gr-qc].

[14] G. Amelino-Camelia. Quantum-Spacetime Phenomenology. *Living Reviews in Relativity*, 16:5, June 2013. arXiv:0806.0339 [gr-qc].

[15] L. Rosenfeld. Zur Quantelung der Wellenfelder. *Annalen der Physik*, 397:113–152, 1930.

[16] M. Fierz and W. Pauli. On relativistic wave equations for particles of arbitrary spin in an electromagnetic field. *Proceedings of the Royal Society of London. Series A, Mathematical and Physical Sciences*, 173(953):211–232, 1939.

[17] B. S. Dewitt. Quantum Theory of Gravity. II. The Manifestly Covariant Theory. *Physical Review*, 162:1195–1239, October 1967.

[18] B. S. Dewitt. Quantum Theory of Gravity. III. Applications of the Covariant Theory. *Physical Review*, 162:1239–1256, October 1967.

[19] L. D. Faddeev and V. N. Popov. Feynman Diagrams for the Yang-Mills Field. *Phys. Lett.*, B25:29–30, 1967. [,325(1967)].

[20] S. Deser and P. van Nieuwenhuizen. One-loop divergences of quantized Einstein-Maxwell fields. *Phys. Rev. D*, 10:401–410, July 1974.

[21] S. Deser and P. van Nieuwenhuizen. Nonrenormalizability of the quantized Dirac-Einstein system. *Phys. Rev. D*, 10:411–420, July 1974.

[22] D. Z. Freedman, P. van Nieuwenhuizen, and S. Ferrara. Progress toward a theory of supergravity. *Phys. Rev. D*, 13:3214–3218, June 1976.

[23] Peter G. Bergmann and Johanna H. M. Brunings. Non-linear field theories ii. canonical equations and quantization. *Rev. Mod. Phys.*, 21:480–487, Jul 1949.

[24] P. G. Bergmann. Introduction of « true observables » into the quantum field equations. *Il Nuovo Cimento (1955-1965)*, 3(6):1177–1185, Jun 1956.

[25] Ezra Newman and Peter G. Bergmann. Observables in singular theories by systematic approximation. *Rev. Mod. Phys.*, 29:443–449, Jul 1957.

[26] Peter G. Bergmann. The canonical formulation of general-relativistic theories: The early years, 1930-1959. In D. Howard and John Stachel, editors, *Einstein and the History of General Relativity*, pages 1–293. Birkhäuser, 1989.

[27] B. S. Dewitt. Quantum Theory of Gravity. I. The Canonical Theory. *Physical Review*, 160:1113–1148, August 1967.

[28] K. Kuchar. Canonical Methods of Quantization. In *Oxford Conference on Quantum Gravity Oxford, England, April 15-19, 1980*, pages 329–376, 1980.

[29] C. J. Isham. Quantum Gravity: An overview. In *Oxford Conference on Quantum Gravity Oxford, England, April 15-19, 1980*, pages 1–62, 1980.

[30] T. Jacobson and L. Smolin. Nonperturbative quantum geometries. *Nuclear Physics B*, 299:295–345, April 1988.

[31] C. Rovelli and L. Smolin. Loop space representation of quantum general relativity. *Nuclear Physics B*, 331:80–152, February 1990.

[32] J. C. Baez. Spin foam models. *Classical and Quantum Gravity*, 15:1827–1858, July 1998. *Preprint:*gr-qc/9709052.

[33] S. W. Hawking. The path integral approach to Quantum Gravity. In *General Relativity: An Einstein Centenary Survey*, pages 746–789. 1980.

[34] R. Penrose. Twistor algebra. *Journal of Mathematical Physics*, 8(2):345–366, 1967. *Preprint:*https://doi.org/10.1063/1.1705200.

[35] A. Connes, M. R. Douglas, and A. Schwarz. Noncommutative geometry and Matrix theory. *Journal of High Energy Physics*, 2:003, February 1998. *Preprint:*hep-th/9711162.

[36] Roger Penrose. On gravity's role in quantum state reduction. *Gen. Rel. Grav.*, 28:581–600, 1996.

[37] C. Rovelli. Notes for a brief history of quantum gravity. *ArXiv General Relativity and Quantum Cosmology e-prints*, June 2000. *Preprint:*gr-qc/0006061.

[38] C. Rovelli. Strings, loops and others: a critical survey of the present approaches to quantum gravity. *ArXiv General Relativity and Quantum Cosmology e-prints*, March 1998. *Preprint:*gr-qc/9803024.

[39] S. Carlip. Quantum gravity: a progress report. *Reports on Progress in Physics*, 64:885–942, August 2001. *Preprint:*gr-qc/0108040.

[40] S. Carlip, D.-W. Chiou, W.-T. Ni, and R. Woodard. Quantum gravity: A brief history of ideas and some prospects. *International Journal of Modern Physics D*, 24:1530028–331, August 2015. arXiv:1507.08194 [gr-qc].

[41] C. Rovelli. Loop Quantum Gravity. *Living Reviews in Relativity*, 1:1, January 1998. *Preprint:*gr-qc/9710008.

[42] L. Smolin. How far are we from the quantum theory of gravity? *ArXiv High Energy Physics - Theory e-prints*, March 2003. *Preprint:*hep-th/0303185.

[43] R. Gambini and J. Pullin. Nonstandard optics from quantum space-time. *Phys. Rev. D*, 59(12):124021, June 1999. *Preprint:*gr-qc/9809038.

[44] J. Alfaro, H. A. Morales-Técotl, and L. F. Urrutia. Quantum Gravity Corrections to Neutrino Propagation. *Physical Review Letters*, 84:2318–2321, March 2000. *Preprint:*gr-qc/9909079.

[45] A. Ashtekar. Introduction to Loop Quantum Gravity and Cosmology. In G. Calcagni, L. Papantonopoulos, G. Siopsis, and N. Tsamis, editors, *Lecture Notes in Physics, Berlin Springer Verlag*, volume 863 of *Lecture Notes in Physics, Berlin Springer Verlag*, page 31, 2013.

[46] L. Freidel, J. Kowalski-Glikman, and L. Smolin. 2+1 gravity and doubly special relativity. *Phys. Rev. D*, 69(4):044001, February 2004. *Preprint:*hep-th/0307085.

[47] L. Smolin. Could deformed special relativity naturally arise from the semiclassical limit of quantum gravity? *ArXiv e-prints*, August 2008. arXiv:0808.3765 [hep-th].

[48] D. V. Ahluwalia. On Reconciling Atmospheric, LSND, and Solar Neutrino-Oscillation Data. *Modern Physics Letters A*, 13:2249–2264, 1998. *Preprint:*hep-ph/9807267.

[49] Hitoshi Murayama and T. Yanagida. LSND, SN1987A, and CPT violation. *Phys. Lett.*, B520:263–268, 2001. arXiv:hep-ph/0010178 [hep-ph].

[50] F. R. Klinkhamer and C. Rupp. Spacetime foam, CPT anomaly, and photon propagation. *Phys. Rev. D*, 70(4):045020, August 2004. *Preprint:*hep-th/0312032.

[51] G. Amelino-Camelia and S. Majid. Waves on Noncommutative Space-Time and Gamma-Ray Bursts. *International Journal of Modern Physics A*, 15:4301–4323, 2000. *Preprint:*hep-th/9907110.

[52] J. Ellis, J. L. Lopez, N. E. Mavromatos, and D. V. Nanopoulos. Precision tests of CPT symmetry and quantum mechanics in the neutral kaon system. *Phys. Rev. D*, 53:3846–3870, April 1996. *Preprint:*hep-ph/9505340.

[53] J. Ellis, N. E. Mavromatos, and D. V. Nanopoulos. String theory modifies quantum mechanics. *Physics Letters B*, 293:37–48, October 1992. *Preprint:*hep-th/9207103.

[54] J. Ellis, N. E. Mavromatos, and D. V. Nanopoulos. A microscopic Liouville arrow of time. *Chaos Solitons and Fractals*, 10:345–363, February 1999. *Preprint:*hep-th/9805120.

[55] S. W. Hawking. The unpredictability of quantum gravity. *Comm. Math. Phys.*, 87(3):395–415, 1982.

[56] G.V. Lavrelashvili, V.A. Rubakov, and P.G. Tinyakov. Particle creation and destruction of quantum coherence by topological change. *Nuclear Physics B*, 299(4):757 – 796, 1988.

[57] Y. Jack Ng, W. A. Christiansen, and H. van Dam. Probing planck-scale physics with extragalactic sources? *The Astrophysical Journal Letters*, 591(2):L87, 2003.

[58] G. Amelino-Camelia. Limits on the Measurability of Space-Time Distances in (the Semiclassical Approximation Of) Quantum Gravity. *Modern Physics Letters A*, 9:3415–3422, 1994. *Preprint:*gr-qc/9603014.

[59] Rodolfo Gambini, Rafael A. Porto, and Jorge Pullin. Realistic clocks, universal decoherence, and the black hole information paradox. *Phys. Rev. Lett.*, 93:240401, Dec 2004.

[60] Ian C. Percival. Quantum space-time fluctuations and primary state diffusion. *Proc. Roy. Soc. Lond.*, A451:503, 1995. arXiv:quant-ph/9508021 [quant-ph].

[61] Ian Percival. Atom interferometry, spacetime and reality. *Physics World*, 10(3):43, 1997.

[62] I. C. Percival and W. T. Strunz. Detection of Spacetime Fluctuations by a Model Matter Interferometer. *Proceedings of the Royal Society of London Series A*, 453:431–446, February 1997. *Preprint:*quant-ph/9607011.

[63] A. Kempf and G. Mangano. Minimal length uncertainty relation and ultraviolet regularization. *Phys. Rev. D*, 55:7909–7920, June 1997. *Preprint:*hep-th/9612084.

[64] A. Błaut, M. Daszkiewicz, J. Kowalski-Glikman, and S. Nowak. Phase spaces of doubly special relativity. *Physics Letters B*, 582:82–85, February 2004. *Preprint:*hep-th/0312045.

[65] Dharam Vir Ahluwalia. Wave particle duality at the Planck scale: Freezing of neutrino oscillations. *Phys. Lett.*, A275:31–35, 2000. arXiv:gr-qc/0002005 [gr-qc].

[66] Andrzej Sitarz. Noncommutative differential calculus on the κ-minkowski space. *Physics Letters B*, 349(1):42 – 48, 1995.

[67] Shahn Majid and Robert Oeckl. Twisting of quantum differentials and¶the planck scale hopf algebra. *Communications in Mathematical Physics*, 205(3):617–655, Sep 1999.

[68] G. Amelino-Camelia. *Doubly-Special Relativity: Facts, Myths and Some Key Open Issues*, pages 123–170. World Scientific Publishing Co, 2010.

[69] Edward Witten. Reflections on the fate of space-time. *Phys. Today*, 49N4:24–30, 1996. [,125(2001)].

[70] G. Amelino-Camelia. Quantum-Gravity Phenomenology. *Modern Physics Letters A*, 17:899–922, 2002. *Preprint:*gr-qc/0204051.

[71] S. W. Hawking. Virtual black holes. *Phys. Rev. D*, 53:3099–3107, March 1996. *Preprint:*hep-th/9510029.

[72] L. J. Garay. Spacetime Foam as a Quantum Thermal Bath. *Physical Review Letters*, 80:2508–2511, March 1998. *Preprint:*gr-qc/9801024.

[73] S. Carlip. Spacetime Foam and the Cosmological Constant. *Physical Review Letters*, 79:4071–4074, November 1997. *Preprint:*gr-qc/9708026.

[74] A. Camacho and D. V. Ahluwalia. Decoherence-Induced Violations of Einstein Equivalence Principle. *International Journal of Modern Physics D*, 10:767–773, 2001. *Preprint:*gr-qc/0107028.

[75] J. Ellis, N. E. Mavromatos, D. V. Nanopoulos, and A. S. Sakharov. Cosmology: Synchrotron radiation and quantum gravity. *Nature*, 428, March 2004. *Preprint:*astro-ph/0309144.

[76] E. Göklü and C. Lämmerzahl. Metric fluctuations and the weak equivalence principle. *Classical and Quantum Gravity*, 25(10):105012, May 2008. arXiv:0801.4553 [gr-qc].

[77] T. Damour and A. M. Polyakov. String theory and gravity. *General Relativity and Gravitation*, 26:1171–1176, December 1994. *Preprint:*gr-qc/9411069.

[78] T. Damour, F. Piazza, and G. Veneziano. Violations of the equivalence principle in a dilaton-runaway scenario. *Phys. Rev. D*, 66(4):046007, August 2002. *Preprint:*hep-th/0205111.

[79] T. Damour. String theory, cosmology and varying constants. *Ap&SS*, 283:445–456, 2003. *Preprint:*gr-qc/0210059.

[80] T. Damour and A. M. Polyakov. The string dilation and a least coupling principle. *Nuclear Physics B*, 423:532–558, July 1994. *Preprint:*hep-th/9401069.

[81] T. Damour, F. Piazza, and G. Veneziano. Runaway Dilaton and Equivalence Principle Violations. *Physical Review Letters*, 89(8):081601, August 2002. *Preprint:*gr-qc/0204094.

[82] V. A. Kostelecký and J. D. Tasson. Matter-gravity couplings and Lorentz violation. *Phys. Rev. D*, 83(1):016013, January 2011. arXiv:1006.4106 [gr-qc].

[83] P. A. M. Dirac. Is there an æther? *Nature*, 168:906 EP –, Nov 1951.

[84] J. D. Bjorken. A dynamical origin for the electromagnetic field. *Annals of Physics*, 24:174–187, October 1963.

[85] Peter R. Phillips. Is the graviton a goldstone boson? *Phys. Rev.*, 146:966–973, Jun 1966.

[86] H.B. Nielsen and Masao Ninomiya. β-function in a non-covariant yang-mills theory. *Nuclear Physics B*, 141(1):153 – 177, 1978.

[87] John Ellis, Mary K. Gaillard, D. V. Nanopoulos, and Serge Rudaz. Uncertainties in the proton lifetime. *Nuclear Physics B*, 176(1):61–99, 12 1980.

[88] A. Zee. Perhaps proton decay violates lorentz invariance. *Phys. Rev. D*, 25:1864–1866, Apr 1982.

[89] On a possible subtraction for the lorentz non-invariant model. *Nuclear Physics B*, 242(2):542 – 546, 1984.

[90] T. Jacobson, S. Liberati, and D. Mattingly. Lorentz violation at high energy: Concepts, phenomena, and astrophysical constraints. *Annals of Physics*, 321:150–196, January 2006. *Preprint:*astro-ph/0505267.

[91] V. Alan Kostelecký and Stuart Samuel. Spontaneous breaking of lorentz symmetry in string theory. *Phys. Rev. D*, 39:683–685, Jan 1989.

[92] G. Amelino-Camelia, J. Ellis, N. E. Mavromatos, D. V. Nanopoulos, and S. Sarkar. Tests of quantum gravity from observations of γ-ray bursts. *Nature*, 393:763–765, June 1998. *Preprint:*astro-ph/9712103.

[93] S. M. Carroll, J. A. Harvey, V. A. Kostelecký, C. D. Lane, and T. Okamoto. Noncommutative Field Theory and Lorentz Violation. *Physical Review Letters*, 87(14):141601, October 2001. *Preprint:*hep-th/0105082.

[94] J. Lukierski, H. Ruegg, and W. J. Zakrzewski. Classical and Quantum Mechanics of Free κ-Relativistic Systems. *Annals of Physics*, 243:90–116, October 1995. *Preprint:*hep-th/9312153.

[95] G. Amelino-Camelia and S. Majid. Waves on Noncommutative Space-Time and Gamma-Ray Bursts. *International Journal of Modern Physics A*, 15:4301–4323, 2000. *Preprint:*hep-th/9907110.

[96] C. P. Burgess, J. M. Cline, E. Filotas, J. Matias, and G. D. Moore. Loop-generated bounds on changes to the graviton dispersion relation. *Journal of High Energy Physics*, 3:043, March 2002. *Preprint:*hep-ph/0201082.

[97] D. Mattingly. Modern Tests of Lorentz Invariance. *Living Reviews in Relativity*, 8:5, September 2005. *Preprint:*gr-qc/0502097.

[98] G. Amelino-Camelia and D. V. Ahluwalia. Relativity in Spacetimes with Short-Distance Structure Governed by an Observer-Independent (Planckian) Length Scale. *International Journal of Modern Physics D*, 11:35–59, 2002. *Preprint:*gr-qc/0012051.

[99] G. Amelino-Camelia. *Doubly-Special Relativity: Facts, Myths and Some Key Open Issues*, pages 123–170. World Scientific Publishing Co, 2010.

[100] S. M. Carroll, J. A. Harvey, V. A. Kostelecký, C. D. Lane, and T. Okamoto. Noncommutative Field Theory and Lorentz Violation. *Physical Review Letters*, 87(14):141601, October 2001. *Preprint:*hep-th/0105082.

[101] C. P. Burgess, J. M. Cline, E. Filotas, J. Matias, and G. D. Moore. Loop-generated bounds on changes to the graviton dispersion relation. *Journal of High Energy Physics*, 3:043, March 2002. *Preprint:*hep-ph/0201082.

[102] D. Colladay and V. A. Kostelecký. Lorentz-violating extension of the standard model. *Phys. Rev. D*, 58(11):116002, December 1998. *Preprint:*hep-ph/9809521.

[103] R. C. Myers and M. Pospelov. Ultraviolet Modifications of Dispersion Relations in Effective Field Theory. *Physical Review Letters*, 90(21):211601, May 2003. *Preprint:*hep-ph/0301124.

[104] J. Collins, A. Perez, D. Sudarsky, L. Urrutia, and H. Vucetich. Lorentz Invariance and Quantum Gravity: An Additional Fine-Tuning Problem? *Physical Review Letters*, 93(19):191301, November 2004. *Preprint:*gr-qc/0403053.

[105] D. Mattingly. Have we tested Lorentz invariance enough? *ArXiv e-prints*, February 2008. arXiv:0802.1561 [gr-qc].

[106] S. G. Nibbelink and M. Pospelov. Lorentz Violation in Supersymmetric Field Theories. *Physical Review Letters*, 94(8):081601, March 2005. *Preprint:*hep-ph/0404271.

[107] P. A. Bolokhov, S. Groot Nibbelink, and M. Pospelov. Lorentz violating supersymmetric quantum electrodynamics. *Phys. Rev. D*, 72(1):015013, July 2005. *Preprint:*hep-ph/0505029.

[108] D. Götz, P. Laurent, S. Antier, S. Covino, P. D'Avanzo, V. D'Elia, and A. Melandri. GRB 140206A: the most distant polarized gamma-ray burst. *MNRAS*, 444:2776–2782, November 2014. arXiv:1408.4121 [astro-ph.HE].

[109] J. R. Ellis, N. E. Mavromatos, and A. S. Sakharov. Synchrotron radiation from the Crab Nebula discriminates between models of space-time foam. *Astroparticle Physics*, 20:669–682, March 2004. *Preprint:*astro-ph/0308403.

[110] V. A. Kostelecký and N. Russell. Data tables for Lorentz and CPT violation. *Reviews of Modern Physics*, 83:11–32, January 2011. arXiv:0801.0287 [hep-ph].

[111] G. Amelino-Camelia, D. Benedetti, F. D'Andrea, and A. Procaccini. Comparison of relativity theories with observer-independent scales of both velocity and length/mass. *Classical and Quantum Gravity*, 20:5353–5370, December 2003. *Preprint:*hep-th/0201245.

[112] J. Kowalski-Glikman and S. Nowak. Non-Commutative Space Time of Doubly Special Relativity Theories. *International Journal of Modern Physics D*, 12:299–315, 2003. *Preprint:*hep-th/0204245.

[113] J. Magueijo and L. Smolin. Lorentz Invariance with an Invariant Energy Scale. *Physical Review Letters*, 88(19):190403, May 2002. *Preprint:*hep-th/0112090.

[114] J. Magueijo and L. Smolin. Generalized Lorentz invariance with an invariant energy scale. *Phys. Rev. D*, 67(4):044017, February 2003. *Preprint:*gr-qc/0207085.

[115] G. Amelino-Camelia. Kinematical Solution of the UHE-Cosmic-Ray Puzzle Without a Preferred Class of Inertial Observers. *International Journal of Modern Physics D*, 12:1211–1226, 2003. *Preprint:*astro-ph/0209232.

[116] J. Lukierski. Relation between quantum κ-Poincar\'{e} framework and Doubly Special Relativity. *ArXiv High Energy Physics - Theory e-prints*, February 2004. *Preprint:*hep-th/0402117.

[117] J. M. Carmona, J. L. Cortés, J. Induráin, and D. Mazón. Quantum noncanonical field theory: Symmetries and interaction. *Phys. Rev. D*, 80(10):105014, November 2009. arXiv:0905.1901 [hep-th].

[118] D. V. Ahluwalia-Khalilova. Operational indistinguishabilty of doubly special relativities from special relativity. *ArXiv General Relativity and Quantum Cosmology e-prints*, December 2002. *Preprint:*gr-qc/0212128.

[119] J. Rembielinski and K. A. Smolinski. Unphysical Predictions of Some Doubly Special Relativity Theories. *ArXiv High Energy Physics - Theory e-prints*, July 2002. *Preprint:*hep-th/0207031.

[120] R. Schützhold and W. G. Unruh. Large-scale nonlocality in "doubly special relativity" with an energy-dependent speed of light. *Soviet Journal of Experimental and Theoretical Physics Letters*, 78:431–435, October 2003. *Preprint:*gr-qc/0308049.

[121] J. Lukierski, H. Ruegg, and W. J. Zakrzewski. Classical and Quantum Mechanics of Free κ-Relativistic Systems. *Annals of Physics*, 243:90–116, October 1995. *Preprint:*hep-th/9312153.

[122] G. Amelino-Camelia, F. Briscese, G. Gubitosi, A. Marcianò, P. Martinetti, and F. Mercati. Noether analysis of the twisted Hopf symmetries of canonical noncommutative spacetimes. *Phys. Rev. D*, 78(2):025005, July 2008. arXiv:0709.4600 [hep-th].

[123] L. Smolin. Could deformed special relativity naturally arise from the semiclassical limit of quantum gravity? *ArXiv e-prints*, August 2008. arXiv:0808.3765 [hep-th].

[124] C. Rovelli. A note on DSR. *ArXiv e-prints*, August 2008. arXiv:0808.3505 [gr-qc].

[125] D. Bear, R. E. Stoner, R. L. Walsworth, V. A. Kostelecký, and C. D. Lane. Limit on Lorentz and CPT Violation of the Neutron Using a Two-Species Noble-Gas Maser. *Physical Review Letters*, 85:5038–5041, December 2000. *Preprint:*physics/0007049.

[126] V. A. Kostelecký and C. D. Lane. Constraints on Lorentz violation from clock-comparison experiments. *Phys. Rev. D*, 60(11):116010, December 1999. *Preprint:*hep-ph/9908504.

[127] F. Canè, D. Bear, D. F. Phillips, M. S. Rosen, C. L. Smallwood, R. E. Stoner, R. L. Walsworth, and V. A. Kostelecký. Bound on Lorentz and CPT Violating Boost Effects for the Neutron. *Physical Review Letters*, 93(23):230801, November 2004. *Preprint:*physics/0309070.

[128] P. Antonini, M. Okhapkin, E. Göklü, and S. Schiller. Test of constancy of speed of light with rotating cryogenic optical resonators. *Phys. Rev. A*, 71(5):050101, May 2005. *Preprint:*gr-qc/0504109.

[129] H. Müller. Testing Lorentz invariance by the use of vacuum and matter filled cavity resonators. *Phys. Rev. D*, 71(4):045004, February 2005. *Preprint:*hep-ph/0412385.

[130] H. Müller, S. Herrmann, A. Saenz, A. Peters, and C. Lämmerzahl. Optical cavity tests of Lorentz invariance for the electron. *Phys. Rev. D*, 68(11):116006, December 2003. *Preprint:*hep-ph/0401016.

[131] P. L. Stanwix, M. E. Tobar, P. Wolf, M. Susli, C. R. Locke, E. N. Ivanov, J. Winterflood, and F. van Kann. Test of Lorentz Invariance in Electrodynamics Using Rotating Cryogenic Sapphire Microwave Oscillators. *Physical Review Letters*, 95(4):040404, July 2005. *Preprint:*hep-ph/0506074.

[132] P. Wolf, S. Bize, A. Clairon, G. Santarelli, M. E. Tobar, and A. N. Luiten. Improved test of Lorentz invariance in electrodynamics. *Phys. Rev. D*, 70(5):051902, September 2004. *Preprint:*hep-ph/0407232.

[133] H. Nguyen. CPT Results from Ktev. In V. A. Kostelecký, editor, *CPT and Lorentz Symmetry*, pages 122–131, February 2002.

[134] B. Schwingenheuer et al. CPT tests in the neutral kaon system. *Phys. Rev. Lett.*, 74:4376–4379, 1995.

[135] A. De Angelis, M. De Maria, M. Antonelli, and M. Dreucci. A search for directional violations of the Lorentz invariance through the study of a possible asymmetry of particle lifetimes. *ArXiv e-prints*, November 2010. arXiv:1011.3720.

[136] Lowell S. Brown and Gerald Gabrielse. Geonium theory: Physics of a single electron or ion in a penning trap. *Rev. Mod. Phys.*, 58:233–311, Jan 1986.

[137] G. Gabrielse, N. S. Bowden, P. Oxley, A. Speck, C. H. Storry, J. N. Tan, M. Wessels, D. Grzonka, W. Oelert, G. Schepers, T. Sefzick, J. Walz, H. Pittner, T. W. Hänsch, and E. A. Hessels. Driven production of cold antihydrogen and the first measured distribution of antihydrogen states. *Phys. Rev. Lett.*, 89:233401, Nov 2002.

[138] R. K. Mittleman, I. I. Ioannou, H. G. Dehmelt, and N. Russell. Bound on CPT and Lorentz symmetry with a trapped electron. *Phys. Rev. Lett.*, 83:2116–2119, 1999.

[139] B. R. HECKEL, , for the Eot Wash Group, and for the Eot Wash Group. *Torsion balance Test of spin coupled forces*, pages 173–180. WORLD SCIENTIFIC, 2011.

[140] L.-S. Hou, W.-T. Ni, and Y.-C. M. Li. Test of Cosmic Spatial Isotropy for Polarized Electrons Using a Rotatable Torsion Balance. *Physical Review Letters*, 90(20):201101, May 2003. *Preprint:*physics/0009012.

[141] L. Maccione, S. Liberati, A. Celotti, J. G. Kirk, and P. Ubertini. γ-ray polarization constraints on Planck scale violations of special relativity. *Phys. Rev. D*, 78(10):103003, November 2008. arXiv:0809.0220.

[142] T. Jacobson, S. Liberati, and D. Mattingly. Threshold effects and Planck scale Lorentz violation: Combined constraints from high energy astrophysics. *Phys. Rev. D*, 67(12):124011, June 2003. *Preprint:*hep-ph/0209264.

[143] V. Baccetti, K. Tate, and M. Visser. Lorentz violating kinematics: threshold theorems. *Journal of High Energy Physics*, 3:87, March 2012. arXiv:1111.6340 [hep-ph].

[144] T. Jacobson, S. Liberati, and D. Mattingly. A strong astrophysical constraint on the violation of special relativity by quantum gravity. *Nature*, 424:1019–1021, August 2003. *Preprint:*astro-ph/0212190.

[145] R. Montemayor and L. F. Urrutia. Synchrotron radiation in Myers Pospelov effective electrodynamics. *Physics Letters B*, 606:86–94, January 2005. *Preprint:*hep-ph/0410143.

[146] R. Montemayor and L. F. Urrutia. Synchrotron radiation in Lorentz-violating electrodynamics: The Myers-Pospelov model. *Phys. Rev. D*, 72(4):045018, August 2005. *Preprint:*hep-ph/0505135.

[147] B. Altschul. Synchrotron and inverse Compton constraints on Lorentz violations for electrons. *Phys. Rev. D*, 74(8):083003, October 2006. *Preprint:*hep-ph/0608332.

[148] L. Maccione, S. Liberati, A. Celotti, and J. G. Kirk. New constraints on Planck-scale Lorentz violation in QED from the Crab Nebula. *J. Cosmology Astropart. Phys.*, 10:013, October 2007. arXiv:0707.2673.

[149] M. S. Longiar. *High Energy Astrophysics,* Cambridge University Press. 1992.

[150] B. Rossi. *Cosmic Rays*. McGraw-Hill Book Company Inc., 1964.

[151] Victor F. Hess. Über Beobachtungen der durchdringenden Strahlung bei sieben Freiballonfahrten. *Phys. Z.*, 13:1084–1091, 1912.

[152] Julian D. G. Krause. *Resolved gamma ray emission of the supernova remnant W51C and HESS J1857+026 obtained with the MAGIC telescopes*. PhD thesis, 2012.

[153] F. A. Aharonian. *Very high energy cosmic gamma radiation : a crucial window on the extreme Universe*. World Scientific Publishing Co, 2004.

[154] W. Heitler. *Quantum theory of radiation*. 1954.

[155] K. S. Cheng and G. E. Romero, editors. *Cosmic Gamma-Ray Sources*, volume 304 of *Astrophysics and Space Science Library*, 2004.

[156] F. A. Aharonian and A. M. Atoyan. Compton scattering of relativistic electrons in compact X-ray sources. *Ap&SS*, 79:321–336, October 1981.

[157] V. L. Ginzburg and S. I. Syrovatskii. *The Origin of Cosmic Rays*. 1964.

[158] A. Y. Prosekin, S. R. Kelner, and F. A. Aharonian. Synchrotron-to-curvature transition regime of radiation of charged particles in a dipole magnetic field. *ArXiv e-prints*, May 2013. arXiv:1305.0783 [astro-ph.HE].

[159] V. L. Ginzburg and S. I. Syrovatskii. Cosmic Magnetobremsstrahlung (synchrotron Radiation). *ARA&A*, 3:297, 1965.

[160] Riccardo Giacconi, Herbert Gursky, Frank R. Paolini, and Bruno B. Rossi. Evidence for x rays from sources outside the solar system. *Phys. Rev. Lett.*, 9:439–443, Dec 1962.

[161] Pierre Auger, P. Ehrenfest, R. Maze, J. Daudin, and Robley A. Fréon. Extensive cosmic-ray showers. *Rev. Mod. Phys.*, 11:288–291, Jul 1939.

[162] P. A. Cherenkov. Visible emission of clean liquids by action of γ radiation. *Doklady Akademii Nauk SSSR*, 2:451+, 1934.

[163] I. M. Frank and I. E. Tamm. Coherent visible radiation of fast electrons passing through matter. *Compt. Rend. Acad. Sci. URSS*, 14(3):109–114, 1937. [Usp. Fiz. Nauk93,no.2,388(1967)].

[164] P.M.S. Blackett. *Phys. Soc. Gassiot Committee Report*, 34, 1948.

[165] W. Galbraith and J. V. Jelley. Light Pulses from the Night Sky associated with Cosmic Rays. *Nature*, 171:349–350, February 1953.

[166] G. Cocconi. *Proc. 6th Int. Cosmic Ray Conf.*, 2:309–311, Moscow, 1960.

[167] T. C. Weekes and K. E. Turver. Gamma-ray astronomy from 10-100 GeV: A new approach. In R. D. Wills and B. Battrick, editors, *Recent Advances in Gamma-Ray Astronomy*, volume 124 of *ESA Special Publication*, July 1977.

[168] A. M. Hillas. Cerenkov light images of EAS produced by primary gamma. *International Cosmic Ray Conference*, 3, August 1985.

[169] T. C. Weekes, M. F. Cawley, D. J. Fegan, K. G. Gibbs, A. M. Hillas, P. W. Kowk, R. C. Lamb, D. A. Lewis, D. Macomb, N. A. Porter, P. T. Reynolds, and G. Vacanti. Observation of TeV gamma rays from the Crab nebula using the atmospheric Cerenkov imaging technique. *ApJ*, 342:379–395, July 1989.

[170] C. E. Fichtel, R. C. Hartman, D. A. Kniffen, and M. Sommer. Gamma-Ray Observations of the Galactic Center and Some Possible Point Sources. *ApJ*, 171:31, January 1972.

[171] J. et al Vasseur. Possible pulsed gamma ray emission above 50 mev from the crab pulsar. *Nature*, 226:534, May 1970.

[172] R. Browning, D. Ramsden, and P. J. Wright. Detection of Pulsed Gamma Radiation from the Crab Nebula. *Nature Physical Science*, 232:99–101, August 1971.

[173] P. et al. Albats. Detection of 10-100 mev gamma rays from the crab nebula pulsar np 0532. *Nature*, 240:221, Nov 1972.

[174] W. L. Kraushaar, G. W. Clark, G. P. Garmire, R. Borken, P. Higbie, V. Leong, and T. Thorsos. High-Energy Cosmic Gamma-Ray Observations from the OSO-3 Satellite. *ApJ*, 177:341, November 1972.

[175] C. E. Fichtel, R. C. Hartman, D. A. Kniffen, D. J. Thompson, H. Ogelman, M. E. Ozel, T. Tumer, and G. F. Bignami. High-energy gamma-ray results from the second small astronomy satellite. *ApJ*, 198:163–182, May 1975.

[176] D. J. Thompson, C. E. Fichtel, D. A. Kniffen, and H. B. Ogelman. SAS-2 high-energy gamma-ray observations of the VELA pulsar. *ApJ*, 200:L79–L82, September 1975.

[177] C. E. Fichtel, G. A. Simpson, and D. J. Thompson. Diffuse gamma radiation. *ApJ*, 222:833–849, June 1978.

[178] B. N. Swanenburg, K. Bennett, G. F. Bignami, R. Buccheri, P. Caraveo, W. Hermsen, G. Kanbach, G. G. Lichti, J. L. Masnou, H. A. Mayer-Hasselwander, J. A. Paul, B. Sacco, L. Scarsi, and R. D. Wills. Second COS B catalog of high-energy gamma-ray sources. *ApJ*, 243:L69–L73, January 1981.

[179] G. F. Bignami, K. Bennett, R. Buccheri, P. A. Caraveo, W. Hermsen, G. Kanbach, G. G. Lichti, J. L. Masnou, H. A. Mayer-Hasselwander, J. A. Paul, B. Sacco, L. Scarsi, B. N. Swanenburg, and R. D. Wills. 3C273 Revisited - Confirmation by Cos-B of High Energy Gamma-Ray Emission. *A&A*, 93:71–75, January 1981.

[180] R. C. et al. Hartman. The Third EGRET Catalog of High-Energy Gamma-Ray Sources. *ApJS*, 123:79–202, July 1999.

[181] D. J. Thompson. Gamma ray astrophysics: the EGRET results. *Reports on Progress in Physics*, 71(11):116901, November 2008. arXiv:0811.0738.

[182] W. B. Atwood, A. A. Abdo, M. Ackermann, W. Althouse, B. Anderson, M. Axelsson, L. Baldini, J. Ballet, D. L. Band, G. Barbiellini, and et al. The Large Area Telescope on the Fermi Gamma-Ray Space Telescope Mission. *ApJ*, 697:1071–1102, June 2009. arXiv:0902.1089 [astro-ph.IM].

[183] Robert Marcus Wagner. *Measurement of Very High Energy Gamma-Ray Emission from Four Blazars Using the MAGIC Telescope and a Comparative Blazar Study*. PhD thesis, Munich, Tech. U., 2006.

[184] W. Heitler. *Quantum theory of radiation*. 1954.

[185] D. J. Thompson. Space detectors for gamma rays (100 MeV-100 GeV): From EGRET to Fermi LAT. *Comptes Rendus Physique*, 16:600–609, August 2015. arXiv:1506.07733 [astro-ph.IM].

[186] Bruno Rossi and Kenneth Greisen. Cosmic-ray theory. *Rev. Mod. Phys.*, 13:240–309, Oct 1941.

[187] W.B Atwood. Gamma large area silicon telescope (glast) applying silicon strip detector technology to the detection of gamma rays in space. *Nuclear Instruments and Methods in Physics Research Section A: Accelerators, Spectrometers, Detectors and Associated Equipment*, 342(1):302 – 307, 1994.

[188] A. Bulgarelli, M. Trifoglio, F. Gianotti, M. Tavani, N. Parmiggiani, V. Fioretti, A. W. Chen, S. Vercellone, C. Pittori, F. Verrecchia, F. Lucarelli, P. Santolamazza, G. Fanari, P. Giommi, D. Beneventano, A. Argan, A. Trois, E. Scalise, F. Longo, A. Pellizzoni, G. Pucella, S. Colafrancesco, V. Conforti, P. Tempesta, M. Cerone, P. Sabatini, G. Annoni, G. Valentini, and L. Salotti. The AGILE Alert System for Gamma-Ray Transients. *ApJ*, 781:19, January 2014. arXiv:1401.3573 [astro-ph.IM].

[189] The Milagro Collaboration. TeV Gamma-Ray Survey of the Northern Hemisphere Sky Using the Milagro Observatory. *ArXiv Astrophysics e-prints*, March 2004. *Preprint:*astro-ph/0403097.

[190] I. Allekotte, A. F. Barbosa, P. Bauleo, C. Bonifazi, B. Civit, C. O. Escobar, B. García, G. Guedes, M. Gómez Berisso, J. L. Harton, M. Healy, M. Kaducak, P. Mantsch, P. O. Mazur, C. Newman-Holmes, I. Pepe, I. Rodriguez-Cabo, H. Salazar, N. Smetniansky-De Grande, D. Warner, and Pierre Auger Collaboration. The surface detector system of the Pierre Auger Observatory. *Nuclear Instruments and Methods in Physics Research A*, 586:409–420, March 2008. arXiv:0712.2832.

[191] S. P. Wakely and D. Horan. `http://tevcat.uchicago.edu/`.

[192] F. Aharonian, J. Buckley, T. Kifune, and G. Sinnis. High energy astrophysics with ground-based gamma ray detectors. *Reports on Progress in Physics*, 71(9):096901, September 2008.

[193] M. G. Baring. Diffusive Shock Acceleration : the Fermi Mechanism. In Y. Giraud-Heraud and J. Tran Thanh van, editors, *Very High Energy Phenomena in the Universe; Moriond Workshop*, page 97, 1997.

[194] A. W. Strong, I. V. Moskalenko, and V. S. Ptuskin. Cosmic-Ray Propagation and Interactions in the Galaxy. *Annual Review of Nuclear and Particle Science*, 57:285–327, November 2007. *Preprint:*astro-ph/0701517.

[195] S. Gabici and F. Aharonian. Gamma-ray emission from young supernova remnants: Hadronic or leptonic? In *European Physical Journal Web of Conferences*, volume 121 of *European Physical Journal Web of Conferences*, page 04001, July 2016.

[196] M. Ackermann et al. A Cocoon of Freshly Accelerated Cosmic Rays Detected by Fermi in the Cygnus Superbubble. *Science*, 334:1103, November 2011.

[197] Ackermann et al. Detection of the Characteristic Pion-Decay Signature in Supernova Remnants. *Science*, 339:807–811, February 2013. arXiv:1302.3307 [astro-ph.HE].

[198] D. R. Lorimer. Binary and Millisecond Pulsars. *Living Reviews in Relativity*, 11, November 2008. arXiv:0811.0762.

[199] D. Michel. Zur theorie der kernspinrelaxation bei einem austausch zwischen zwei bereichen. *Annalen der Physik*, 29(4):365–374, 1973.

[200] J. A. Hinton and W. Hofmann. Teraelectronvolt Astronomy. *ARA&A*, 47:523–565, September 2009. arXiv:1006.5210 [astro-ph.HE].

[201] M. G. Baring. High-energy emission from pulsars: the polar cap scenario. *Advances in Space Research*, 33:552–560, 2004. *Preprint:*astro-ph/0308296.

[202] E. Aliu, others, and MAGIC Collaboration. Observation of Pulsed γ-Rays Above 25 GeV from the Crab Pulsar with MAGIC. *Science*, 322:1221, November 2008. arXiv:0809.2998.

[203] J. Aleksić et al. Phase-resolved energy spectra of the Crab pulsar in the range of 50-400 GeV measured with the MAGIC telescopes. *A&A*, 540:A69, April 2012. arXiv:1109.6124 [astro-ph.HE].

[204] A. Nepomuk Otte and for the VERITAS Collaboration. First Detection of a Pulsar above 100 GeV. *ArXiv e-prints*, November 2011. arXiv:1111.6610 [astro-ph.HE].

[205] J. Arons. Pair creation above pulsar polar caps - Geometrical structure and energetics of slot gaps. *ApJ*, 266:215–241, March 1983.

[206] K. S. Cheng, C. Ho, and M. Ruderman. Energetic radiation from rapidly spinning pulsars. I - Outer magnetosphere gaps. II - VELA and Crab. *ApJ*, 300:500–539, January 1986.

[207] Kouichi Hirotani. Three-dimensional non-vacuum pulsar outer-gap model: Localized acceleration electric field in the higher altitudes. *The Astrophysical Journal Letters*, 798(2):L40, 2015.

[208] A. G. Muslimov and A. K. Harding. Extended Acceleration in Slot Gaps and Pulsar High-Energy Emission. *ApJ*, 588:430–440, May 2003. *Preprint:*astro-ph/0301023.

[209] MAGIC Collaboration. Teraelectronvolt pulsed emission from the Crab Pulsar detected by MAGIC. *A&A*, 585:A133, January 2016. arXiv:1510.07048 [astro-ph.HE].

[210] B. Cerutti, A. Philippov, K. Parfrey, and A. Spitkovsky. Particle acceleration in axisymmetric pulsar current sheets. *MNRAS*, 448:606–619, March 2015. arXiv:1410.3757 [astro-ph.HE].

[211] J. M. Blondin, R. A. Chevalier, and D. M. Frierson. Pulsar Wind Nebulae in Evolved Supernova Remnants. *ApJ*, 563:806–815, December 2001. *Preprint:*astro-ph/0107076.

[212] J. Jeff Hester. The crab nebula: An astrophysical chimera. *Annual Review of Astronomy and Astrophysics*, 46(1):127–155, 2008. *Preprint:*https://doi.org/10.1146/annurev.astro.45.051806.110608.

[213] D. R. Lorimer. Binary and Millisecond Pulsars. *Living Reviews in Relativity*, 11, November 2008. arXiv:0811.0762.

[214] F. A. Aharonian et al. Discovery of a point-like very-high-energy γ-ray source in Monoceros. *A&A*, 469:L1–L4, July 2007. arXiv:0704.0171.

[215] H. E. S. S. Collaboration et al. Discovery of VHE emission towards the Carina arm region with the H.E.S.S. telescope array: HESS J1018-589. *A&A*, 541:A5, May 2012. arXiv:1203.3215 [astro-ph.HE].

[216] HESS Collaboration, A. Abramowski, F. Acero, F. Aharonian, F. Ait Benkhali, A. G. Akhperjanian, E. Angüner, G. Anton, S. Balenderan, A. Balzer, and et al. Discovery of the VHE gamma-ray source HESS J1832-093 in the vicinity of SNR G22.7-0.2. *MNRAS*, 446:1163–1169, January 2015. arXiv:1411.0572 [astro-ph.HE].

[217] A. G. Lyne, B. W. Stappers, M. J. Keith, P. S. Ray, M. Kerr, F. Camilo, and T. J. Johnson. The binary nature of PSR J2032+4127. *MNRAS*, 451:581–587, July 2015. arXiv:1502.01465 [astro-ph.HE].

[218] F. Aharonian, A. G. Akhperjanian, K.-M. Aye, and A. R. Bazer-Bachi. Serendipitous discovery of the unidentified extended TeV γ-ray source HESS J1303-631. *A&A*, 439:1013–1021, September 2005. *Preprint:*astro-ph/0505219.

[219] M. Daniel and CTA Consortium. Lorentz invariance violation with gamma rays. *Nuclear and Particle Physics Proceedings*, 265:314–316, August 2015. arXiv:1501.00824 [astro-ph.HE].

[220] A. Domínguez et al. Extragalactic background light inferred from AEGIS galaxy-SED-type fractions. *MNRAS*, 410:2556–2578, February 2011. arXiv:1007.1459.

[221] A. Franceschini, G. Rodighiero, and M. Vaccari. Extragalactic optical-infrared background radiation, its time evolution and the cosmic photon-photon opacity. *A&A*, 487:837–852, September 2008. arXiv:0805.1841.

[222] A. A. Abdo, M. Ackermann, M. Ajello, L. Baldini, J. Ballet, G. Barbiellini, D. Bastieri, K. Bechtol, R. Bellazzini, B. Berenji, and et al. Fermi Large Area Telescope Observations of Markarian 421: The Missing Piece of its Spectral Energy Distribution. *ApJ*, 736:131, August 2011. arXiv:1106.1348 [astro-ph.HE].

[223] M. Punch, C. W. Akerlof, M. F. Cawley, M. Chantell, D. J. Fegan, S. Fennell, J. A. Gaidos, J. Hagan, A. M. Hillas, Y. Jiang, A. D. Kerrick, R. C. Lamb, M. A. Lawrence, D. A. Lewis, D. I. Meyer, G. Mohanty, K. S. O'Flaherty, P. T. Reynolds, A. C. Rovero, M. S. Schubnell, G. Sembroski, T. C. Weekes, and C. Wilson. Detection of TeV photons from the active galaxy Markarian 421. *Nature*, 358:477, August 1992.

[224] M. Ajello et al. 3FHL: The Third Catalog of Hard Fermi-LAT Sources. *ApJ*, 232:18, October 2017. arXiv:1702.00664 [astro-ph.HE].

[225] A. A. Abdo, M. Ackermann, M. Ajello, A. Allafort, L. Baldini, J. Ballet, G. Barbiellini, M. G. Baring, D. Bastieri, K. Bechtol, and et al. Insights into the High-energy γ-ray Emission of Markarian 501 from Extensive Multifrequency Observations in the Fermi Era. *ApJ*, 727:129, February 2011. arXiv:1011.5260 [astro-ph.HE].

[226] A. U. Abeysekara, S. Archambault, A. Archer, W. Benbow, R. Bird, M. Buchovecky, J. H. Buckley, V. Bugaev, J. V. Cardenzana, M. Cerruti, and et al. A Search for Spectral Hysteresis and Energy-dependent Time Lags from X-Ray and TeV Gamma-Ray Observations of Mrk 421. *ApJ*, 834:2, January 2017. arXiv:1611.04626 [astro-ph.HE].

[227] B. P. Abbott, R. Abbott, T. D. Abbott, F. Acernese, K. Ackley, C. Adams, T. Adams, P. Addesso, R. X. Adhikari, V. B. Adya, and et al. Gravitational Waves and Gamma-Rays from a Binary Neutron Star Merger: GW170817 and GRB 170817A. *ApJ*, 848:L13, October 2017. arXiv:1710.05834 [astro-ph.HE].

[228] S. Dado, A. Dar, and A. De Rújula. The Supernova Associated with GRB 030329. *ApJ*, 594:L89–L92, September 2003. *Preprint:*astro-ph/0304106.

[229] H. Tajima, Fermi LAT Collaboration, and Fermi GBM Collaboration. Fermi Observations of high-energy gamma-ray emissions from GRB 080916C. *ArXiv e-prints*, July 2009. arXiv:0907.0714 [astro-ph.HE].

[230] Katsuaki Asano and Peter Mészáros. Delayed onset of high-energy emissions in leptonic and hadronic models of gamma-ray bursts. *The Astrophysical Journal*, 757(2):115, 2012.

[231] R. Narayan, B. Paczynski, and T. Piran. Gamma-ray bursts as the death throes of massive binary stars. *ApJ*, 395:L83–L86, August 1992. *Preprint:*astro-ph/9204001.

[232] M. J. Rees and P. Meszaros. Relativistic fireballs - Energy conversion and time-scales. *MNRAS*, 258:41P–43P, September 1992.

[233] T. Piran. Gamma-ray bursts and the fireball model. *Phys. Rep.*, 314:575–667, June 1999. *Preprint:*astro-ph/9810256.

[234] R. W. Klebesadel, I. B. Strong, and R. A. Olson. Observations of Gamma-Ray Bursts of Cosmic Origin. *ApJ*, 182:L85, June 1973.

[235] E. Costa, F. Frontera, J. Heise, M. Feroci, J. in't Zand, F. Fiore, M. N. Cinti, D. Dal Fiume, L. Nicastro, M. Orlandini, E. Palazzi, M. Rapisarda#, G. Zavattini, R. Jager, A. Parmar, A. Owens, S. Molendi, G. Cusumano, M. C. Maccarone, S. Giarrusso, A. Coletta, L. A. Antonelli, P. Giommi, J. M. Muller, L. Piro, and R. C. Butler. Discovery of an X-ray afterglow associated with the γ-ray burst of 28 February 1997. *Nature*, 387:783–785, June 1997. *Preprint:*astro-ph/9706065.

[236] B. L. Dingus, J. R. Catelli, and E. J Schneid. EGRET Observations of GeV Emission from Gamma-Ray Bursts. *International Cosmic Ray Conference*, 3:29, 1997.

[237] P. Narayana Bhat, C. A. Meegan, A. von Kienlin, W. S. Paciesas, M. S. Briggs, J. M. Burgess, E. Burns, V. Chaplin, W. H. Cleveland, A. C. Collazzi, V. Connaughton, A. M. Diekmann, G. Fitzpatrick, M. H. Gibby, M. M. Giles, A. M. Goldstein, J. Greiner, P. A. Jenke, R. M. Kippen, C. Kouveliotou, B. Mailyan, S. McBreen, V. Pelassa, R. D. Preece, O. J. Roberts, L. S. Sparke, M. Stanbro, P. Veres, C. A. Wilson-Hodge, S. Xiong, G. Younes, H.-F. Yu, and B. Zhang. The Third Fermi GBM Gamma-Ray Burst Catalog: The First Six Years. *ApJS*, 223:28, April 2016. arXiv:1603.07612 [astro-ph.HE].

[238] MAGIC Collaboration. Magic upper limits on the very high energy emission from gamma-ray bursts. *The Astrophysical Journal*, 667(1):358, 2007.

[239] F. Acero et al. Detection of Gamma Rays from a Starburst Galaxy. *Science*, 326:1080, November 2009. arXiv:0909.4651 [astro-ph.HE].

[240] N. Karlsson and for the VERITAS collaboration. Discovery of VHE Gamma-ray Emission from the Starburst Galaxy M82. *ArXiv e-prints*, December 2009. arXiv:0912.3807 [astro-ph.HE].

[241] A. A. Abdo et al. Detection of Gamma-Ray Emission from the Starburst Galaxies M82 and NGC 253 with the Large Area Telescope on Fermi. *ApJ*, 709:L152–L157, February 2010. arXiv:0911.5327 [astro-ph.HE].

[242] G. Brunetti, T. Venturi, D. Dallacasa, R. Cassano, K. Dolag, S. Giacintucci, and G. Setti. Cosmic Rays and Radio Halos in Galaxy Clusters: New Constraints from Radio Observations. *ApJ*, 670:L5–L8, November 2007. arXiv:0710.0801.

[243] M. Ackermann et al. Gev gamma-ray flux upper limits from clusters of galaxies. *The Astrophysical Journal Letters*, 717(1):L71, 2010.

[244] J. Aleksić et al. Constraining cosmic rays and magnetic fields in the Perseus galaxy cluster with TeV observations by the MAGIC telescopes. *A&A*, 541:A99, May 2012. arXiv:1111.5544 [astro-ph.HE].

[245] G. Amelino-Camelia, J. Ellis, N. E. Mavromatos, D. V. Nanopoulos, and S. Sarkar. Tests of quantum gravity from observations of γ-ray bursts. *Nature*, 393:763–765, June 1998. *Preprint:*astro-ph/9712103.

[246] J. Ellis, K. Farakos, N. E. Mavromatos, V. A. Mitsou, and D. V. Nanopoulos. A Search in Gamma-Ray Burst Data for Nonconstancy of the Velocity of Light. *ApJ*, 535:139–151, May 2000. *Preprint:*astro-ph/9907340.

[247] J. Ellis, N. E. Mavromatos, D. V. Nanopoulos, and A. S. Sakharov. Quantum-gravity analysis of gamma-ray bursts using wavelets. *A&A*, 402:409–424, May 2003. *Preprint:*astro-ph/0210124.

[248] G. Hinshaw, D. Larson, E. Komatsu, D. N. Spergel, C. L. Bennett, J. Dunkley, M. R. Nolta, M. Halpern, R. S. Hill, N. Odegard, L. Page, K. M. Smith, J. L. Weiland, B. Gold, N. Jarosik, A. Kogut, M. Limon, S. S. Meyer, G. S. Tucker, E. Wollack, and E. L. Wright. Nine-year Wilkinson Microwave Anisotropy Probe (WMAP) Observations: Cosmological Parameter Results. *ApJS*, 208:19, October 2013. arXiv:1212.5226.

[249] U. Jacob and T. Piran. Lorentz-violation-induced arrival delays of cosmological particles. *J. Cosmology Astropart. Phys.*, 1:031, January 2008. arXiv:0712.2170.

[250] G. Amelino-Camelia, G. Mandanici, A. Procaccini, and J. Kowalski-Glikman. Phenomenology of Doubly Special Relativity. *International Journal of Modern Physics A*, 20:6007–6037, 2005. *Preprint:*gr-qc/0312124.

[251] J. M. Carmona, J. L. Cortés, and J. J. Relancio. Does a deformation of special relativity imply energy dependent photon time delays? *Classical and Quantum Gravity*, 35(2):025014, January 2018. arXiv:1702.03669 [hep-th].

[252] Robert J. Gould and Gérard P. Schréder. Pair production in photon-photon collisions. *Phys. Rev.*, 155:1404–1407, Mar 1967.

[253] U. Jacob and T. Piran. Inspecting absorption in the spectra of extra-galactic gamma-ray sources for insight into Lorentz invariance violation. *Phys. Rev. D*, 78(12):124010, December 2008. arXiv:0810.1318.

[254] F. Tavecchio and G. Bonnoli. On the detectability of Lorentz invariance violation through anomalies in the multi-TeV γ-ray spectra of blazars. *A&A*, 585:A25, January 2016. arXiv:1510.00980 [astro-ph.HE].

[255] R. C. Gilmore, R. S. Somerville, J. R. Primack, and A. Domínguez. Semi-analytic modelling of the extragalactic background light and consequences for extragalactic gamma-ray spectra. *MNRAS*, 422:3189–3207, June 2012. arXiv:1104.0671.

[256] M. Lorentz and P. Brun. Limits on Lorentz invariance violation at the Planck energy scale from H.E.S.S. spectral analysis of the blazar Mrk 501. In *European Physical Journal Web of Conferences*, volume 136 of *European Physical Journal Web of Conferences*, page 03018, March 2017.

[257] Jonathan Biteau and David A. Williams. The extragalactic background light, the Hubble constant, and anomalies: conclusions from 20 years of TeV gamma-ray observations. *Astrophys. J.*, 812(1):60, 2015. arXiv:1502.04166 [astro-ph.CO].

[258] F. Krennrich et al. Cutoff in the TeV Energy Spectrum of Markarian 421 during Strong Flares in 2001. *ApJ*, 560:L45–L48, October 2001. *Preprint:*astro-ph/0107113.

[259] F. Aharonian et al. Variations of the TeV energy spectrum at different flux levels of Mkn 421 observed with the HEGRA system of Cherenkov telescopes. *A&A*, 393:89–99, October 2002. *Preprint:*astro-ph/0205499.

[260] H. Martínez-Huerta and A. Pérez-Lorenzana. Effects of Lorentz invariance violation on cosmic ray photon emission and gamma ray decay processes. *ArXiv e-prints*, September 2017. arXiv:1709.08247 [astro-ph.HE].

[261] F. Aharonian et al. The Crab Nebula and Pulsar between 500 GeV and 80 TeV: Observations with the HEGRA Stereoscopic Air Cerenkov Telescopes. *ApJ*, 614:897–913, October 2004. *Preprint:*astro-ph/0407118.

[262] H. Martínez-Huerta and A. Pérez-Lorenzana. Restrictions from Lorentz invariance violation on cosmic ray propagation. *Phys. Rev. D*, 95(6):063001, March 2017. arXiv:1610.00047 [astro-ph.HE].

[263] H. Martínez-Huerta and for the HAWC Collaboration. Potential constrains on Lorentz invariance violation from the HAWC TeV gamma-rays. *ArXiv e-prints*, August 2017. arXiv:1708.03384 [astro-ph.HE].

[264] B. Altschul. Limits on Lorentz Violation from Synchrotron and Inverse Compton Sources. *Physical Review Letters*, 96(20):201101, May 2006. *Preprint:*hep-ph/0603138.

[265] A. Reimer. Lorentz invariance under scrutiny of recent high-energy gamma-ray observations. *Nuclear Physics B - Proceedings Supplements*, 203-204:33 – 44, 2010. Masses and Constants. Proceedings of the 48th Internationale Universitätswochen für Theoretische Physik.

[266] P. D'Avanzo. Short gamma-ray bursts: A review. *Journal of High Energy Astrophysics*, 7:73 – 80, 2015. Swift 10 Years of Discovery, a novel approach to Time Domain Astronomy.

[267] A. A. Abdo et al. A limit on the variation of the speed of light arising from quantum gravity effects. *Nature*, 462:331 EP –, Oct 2009.

[268] F. Aharonian, others, and H.E.S.S. Collaboration. Limits on an Energy Dependence of the Speed of Light from a Flare of the Active Galaxy PKS 2155-304. *Physical Review Letters*, 101(17):170402, October 2008. arXiv:0810.3475.

[269] H.E.S.S. Collaboration, A. Abramowski, et al. Search for Lorentz Invariance breaking with a likelihood fit of the PKS 2155-304 flare data taken on MJD 53944. *Astroparticle Physics*, 34:738–747, April 2011. arXiv:1101.3650 [astro-ph.HE].

[270] MAGIC Collaboration, J. Albert, et al. Probing quantum gravity using photons from a flare of the active galactic nucleus Markarian 501 observed by the MAGIC telescope. *Physics Letters B*, 668:253–257, October 2008. arXiv:0708.2889.

[271] O. Blanch, J. Lopez, and M. Martinez. Testing the effective scale of quantum gravity with the next generation of gamma ray telescopes. *Astroparticle Physics*, 19:245–252, May 2003. *Preprint:*astro-ph/0107334.

[272] M. Doro, others, and CTA Consortium. Dark matter and fundamental physics with the Cherenkov Telescope Array. *Astroparticle Physics*, 43:189–214, March 2013. arXiv:1208.5356 [astro-ph.IM].

[273] MAGIC Collaboration, M. L. Ahnen, et al. Constraining Lorentz Invariance Violation Using the Crab Pulsar Emission Observed up to TeV Energies by MAGIC. *ApJS*, 232:9, September 2017. arXiv:1709.00346 [astro-ph.HE].

[274] C. Perennes, H. Sol, and J. Bolmont. Intrinsic time lags in blazar flares and the search of Lorentz Invariance Violation signatures. *ArXiv e-prints*, September 2017. arXiv:1709.04269 [astro-ph.HE].

[275] J. Bolmont, V. Vasileiou, A. Jacholkowska, F. Piron, C. Couturier, J. Granot, F. W. Stecker, J. Cohen-Tanugi, and F. Longo. Lorentz invariance violation: The latest Fermi results and the GRB/ AGN complementarity. *Nucl. Instrum. Meth.*, A742:165–168, 2014.

[276] G. Amelino-Camelia, G. D'Amico, F. Fiore, S. Puccetti, and M. Ronco. In-vacuo-dispersion-like spectral lags in gamma-ray bursts. *ArXiv e-prints*, July 2017. arXiv:1707.02413 [astro-ph.HE].

[277] L. Nogués, T. T. Y Lin, C. Perennes, A. E. Gent, J. Bolmont, M. Gaug, A. Jacholkowska, M. Martinez, A. Nepomuk Otte, R. M. Wagner, J. E. Ward, and B. Zitzer. First combined studies on Lorentz Invariance Violation from observations of astrophysical sources. *ArXiv e-prints*, October 2017. arXiv:1710.08342 [astro-ph.HE].

[278] Bradley E. Schaefer. Severe limits on variations of the speed of light with frequency. *Phys. Rev. Lett.*, 82:4964–4966, Jun 1999.

[279] John R. Ellis, Nick E. Mavromatos, Dimitri V. Nanopoulos, Alexander S. Sakharov, and Edward K. G. Sarkisyan. Robust limits on Lorentz violation from gamma-ray bursts. *Astropart. Phys.*, 25:402–411, 2006. arXiv:0712.2781 [astro-ph], [Erratum: Astropart. Phys.29,158(2008)].

[280] Steven E. Boggs, C. B. Wunderer, K. Hurley, and W. Coburn. Testing lorentz invariance with grb 021206. *The Astrophysical Journal Letters*, 611(2):L77, 2004.

[281] K. S. Cheng and T. Harko. Is there any evidence for extra-dimensions or quantum gravity effects from the delayed MeV GeV photons in GRB 940217? *Astroparticle Physics*, 22:297–305, November 2004. *Preprint:*astro-ph/0407416.

[282] Merab Gogberashvili, Alexander S. Sakharov, and Edward K.G. Sarkisyan. Probing brane-world scenarios with vacuum refraction of light using gamma-ray bursts. *Physics Letters B*, 644(2):179 – 185, 2007.

[283] R. Lamon, N. Produit, and F. Steiner. Study of Lorentz violation in INTEGRAL gamma-ray bursts. *General Relativity and Gravitation*, 40:1731–1743, August 2008. arXiv:0706.4039 [gr-qc].

[284] J. D. Scargle, J. P. Norris, and J. T. Bonnell. On the Problem of Detecting Quantum-Gravity Based Photon Dispersion in Gamma-Ray Bursts. *ArXiv Astrophysics e-prints*, October 2006. *Preprint:*astro-ph/0610571.

[285] M. Martínez and M. Errando. A new approach to study energy-dependent arrival delays on photons from astrophysical sources. *Astroparticle Physics*, 31:226–232, April 2009. arXiv:0803.2120.

[286] Scott Tyler Griffiths. *Exploring the limits of Lorentz Invariance with VERITAS gamma-ray observations of Markarian 421*. PhD thesis, 2015.

[287] A. A. Abdo, M. Ackermann, M. Arimoto, K. Asano, W. B. Atwood, M. Axelsson, L. Baldini, J. Ballet, D. L. Band, G. Barbiellini, and et al. Fermi Observations of High-Energy Gamma-Ray Emission from GRB 080916C. *Science*, 323:1688, March 2009.

[288] A. Nepomuk Otte. Prospects of performing Lorentz invariance tests with VHE emission from pulsars. In *Proceedings, 32nd International Cosmic Ray Conference (ICRC 2011): Beijing, China, August 11-18, 2011*, volume 7, pages 256–259, 2012.

[289] A. Abramowski, F. Aharonian, F. Ait Benkhali, A. G. Akhperjanian, E. O. Angüner, M. Backes, S. Balenderan, A. Balzer, A. Barnacka, Y. Becherini, and et al. The 2012 Flare of PG 1553+113 Seen with H.E.S.S. and Fermi-LAT. *ApJ*, 802:65, March 2015. arXiv:1501.05087 [astro-ph.HE].

[290] K. Cranmer. Kernel estimation in high-energy physics*. *Computer Physics Communications*, 136:198–207, May 2001. *Preprint:*hep-ex/0011057.

[291] G. Amelino-Camelia, G. D'Amico, F. Fiore, S. Puccetti, and M. Ronco. In-vacuo-dispersion-like spectral lags in gamma-ray bursts. *ArXiv e-prints*, July 2017. arXiv:1707.02413 [astro-ph.HE].

[292] Ulisses Barres de Almeida and M. K. Daniel. A Simple Method to Test for Energy-Dependent Dispersion in High Energy Light-Curves of Astrophysical Sources. *Astropart. Phys.*, 35:850–860, 2012. arXiv:1204.2205 [astro-ph.IM].

[293] Jeffrey D. Scargle, Jay P. Norris, and J. T. Bonnell. An algorithm for detecting quantum gravity photon dispersion in gamma-ray bursts: Discan. *The Astrophysical Journal*, 673(2):972, 2008.

[294] John Ellis, Nicholas Harries, Anselmo Meregaglia, André Rubbia, and Alexander S. Sakharov. Probes of lorentz violation in neutrino propagation. *Phys. Rev. D*, 78:033013, Aug 2008.

[295] M. Tanabashi et al. (Particle Data Group). *Phys. Rev. D 98*, 2018.

[296] P. Kaaret. Pulsar radiation and quantum gravity. *A&A*, 345:L32–L34, May 1999. *Preprint:*astro-ph/9903464.

[297] Alba Fernández Barral. *Extreme particle acceleration in microquasar jets and pulsar wind nebulae with the MAGIC telescopes*. PhD thesis, 2017.

[298] Rubén López Coto. *Very-high-energy gamma-ray observations of pulsar wind nebulae and cataclysmic variable stars with MAGIC and development of trigger systems for IACTs*. PhD thesis, 2015.

[299] H. Bartko, F. Goebel, R. Mirzoyan, W. Pimpl, and M. Teshima. Tests of a prototype multiplexed fiber-optic ultra-fast FADC data acquisition system for the MAGIC telescope. *Nuclear Instruments and Methods in Physics Research A*, 548:464–486, August 2005. *Preprint:*astro-ph/0505204.

[300] Joaquim Palacio. *Indirect dark matter searches on the Triangulum-II dwarf spheroidal galaxy and the Perseus galaxy cluster with the MAGIC telescopes*. PhD thesis, 2018.

[301] T. Bretz, D. Dorner, R.M. Wagner, and P. Sawallisch. The drive system of the major atmospheric gamma-ray imaging cherenkov telescope. *Astroparticle Physics*, 31(2):92 – 101, 2009.

[302] D. Borla Tridon, F. Goebel, D. Fink, W. Haberer, J. Hose, C. C. Hsu, T. Jogler, R. Mirzoyan, R. Orito, O. Reimann, P. Sawallisch, J. Schlammer, T. Schweizer, B. Steinke, M. Teshima, and for the MAGIC Collaboration. Performance of the Camera of the MAGIC II Telescope. *ArXiv e-prints*, June 2009. arXiv:0906.5448 [astro-ph.HE].

[303] D. Borla Tridon et al. Performance of the Camera of the MAGIC II Telescope. 2009. arXiv:0906.5448 [astro-ph.HE].

[304] J. R. García, F. Dazzi, D. Häfner, D. Herranz, M. López, M. Mariotti, R. Mirzoyan, D. Nakajima, T. Schweizer, and M. Teshima. Status of the new Sum-Trigger system for the MAGIC telescopes. *ArXiv e-prints*, April 2014. arXiv:1404.4219 [astro-ph.IM].

[305] Julian Sitarek, Markus Gaug, Daniel Mazin, Riccardo Paoletti, and Diego Tescaro. Analysis techniques and performance of the Domino Ring Sampler version 4 based readout for the MAGIC telescopes. *Nucl. Instrum. Meth.*, A723:109–120, 2013. arXiv:1305.1007 [astro-ph.IM].

[306] Juan Cortina, Florian Goebel, and Thomas Schweizer. Technical Performance of the MAGIC Telescopes. 2009. arXiv:0907.1211 [astro-ph.IM].

[307] V.P. Fomin, A.A. Stepanian, R.C. Lamb, D.A. Lewis, M. Punch, and T.C. Weekes. New methods of atmospheric cherenkov imaging for gamma-ray astronomy. i. the false source method. *Astroparticle Physics*, 2(2):137 – 150, 1994.

[308] Daniel Garrido Terrats. *Limits to the violation of Lorentz invariance using the emission of the Crab pulsar at TeV energies, discovered with archival data from the MAGIC telescopes*. PhD thesis, 2015.

[309] P. Majumdar, A. Moralejo, C. Bigongiari, O. Blanch, and D. Sobczynska. Monte Carlo simulation for the MAGIC telescope. *International Cosmic Ray Conference*, 5:203, 2005.

[310] R. Mirzoyan, E. Lorenz, D. Petry, and C. Prosch. On the influence of afterpulsing in pmts on the trigger threshold of multichannel light detectors in self-trigger mode. *Nuclear Instruments and Methods in Physics Research Section A: Accelerators, Spectrometers, Detectors and Associated Equipment*, 387(1):74 – 78, 1997. New Developments in Photodetection.

[311] J. Aleksić et al. The major upgrade of the MAGIC telescopes, Part II: A performance study using observations of the Crab Nebula. *Astroparticle Physics*, 72:76–94, January 2016. arXiv:1409.5594 [astro-ph.IM].

[312] S. Lombardi. Advanced stereoscopic gamma-ray shower analysis with the MAGIC telescopes. *International Cosmic Ray Conference*, 3:266, 2011. arXiv:1109.6195 [astro-ph.IM].

[313] W. Hofmann, I. Jung, A. Konopelko, H. Krawczynski, H. Lampeitl, and G. Pühlhofer. Comparison of techniques to reconstruct vhe gamma-ray showers from multiple stereoscopic cherenkov images. *Astroparticle Physics*, 12(3):135 – 143, 1999.

[314] J. Albert et al. Implementation of the Random Forest method for the Imaging Atmospheric Cherenkov Telescope MAGIC. *Nuclear Instruments and Methods in Physics Research A*, 588:424–432, April 2008. arXiv:0709.3719.

[315] J. Aleksić et al. Search for an extended VHE γ-ray emission from Mrk 421 and Mrk 501 with the MAGIC Telescope. *A&A*, 524:A77, December 2010. arXiv:1004.1093 [astro-ph.HE].

[316] J. Aleksić et al. Black hole lightning due to particle acceleration at subhorizon scales. *Science*, 346:1080–1084, November 2014. arXiv:1412.4936 [astro-ph.HE].

[317] A. J. Barth, L. C. Ho, and W. L. W. Sargent. The Black Hole Masses and Host Galaxies of BL Lacertae Objects. *ApJ*, 583:134–144, January 2003. *Preprint:*astro-ph/0209562.

[318] F. De Paolis, G. Ingrosso, and A. A. Nucita. Astrophysical implications of binary black holes in BL Lacertae objects. *A&A*, 388:470–476, June 2002. *Preprint:*astro-ph/0205092.

[319] X. Chen, S. M. Hu, D. F. Guo, and J. J. Du. Optical variability of Mrk 421. *Ap&SS*, 349:909–917, February 2014.

[320] MAGIC Collaboration. Measurement of the extragalactic background light through magic and fermi-lat gamma-ray observations of blazars (in preparation). 2018.

[321] Harvey Gould, Jan Tobochnik, Wolfgang Christian, and Eric Ayars. An introduction to computer simulation methods: Applications to physical systems, 2nd edition. 74:652–653, 01 2006.

[322] Fred James and Matthias Winkler. MINUIT User's Guide. 2004.

[323] Hiroshi Akima. A new method of interpolation and smooth curve fitting based on local procedures. *J. ACM*, 17(4):589–602, October 1970.

[324] David W. Scott. Averaged shifted histograms: Effective nonparametric density estimators in several dimensions. *Ann. Statist.*, 13(3):1024–1040, 09 1985.

[325] David Scott. *Multivariate Density Estimation: Theory, Practice, and Visualization, Second Edition*, volume 383. 09 1994.

[326] Frank R. Hampel. The influence curve and its role in robust estimation. 69:383–393, 06 1974.

[327] Peter Rousseeuw and Christophe Croux. Alternatives to median absolute deviation. 88:1273 – 1283, 12 1993.

[328] J. Albert et al. Variable VHE gamma-ray emission from Markarian 501. *Astrophys. J.*, 669:862–883, 2007. arXiv:astro-ph/0702008 [astro-ph].

[329] A. Abramowski et al. The 2012 flare of PG 1553+113 seen with H.E.S.S. and Fermi-LAT. *Astrophys. J.*, 802(1):65, 2015. arXiv:1501.05087 [astro-ph.HE].

[330] F. Aharonian. An Exceptional Very High Energy Gamma-Ray Flare of PKS 2155-304. *Astrophys. J.*, 664:L71–L78, 2007. arXiv:0706.0797 [astro-ph].

[331] Thanh Nguyen. Updated Results from VERITAS on the Crab Pulsar. *PoS*, ICRC2015:828, 2016. arXiv:1508.07268 [astro-ph.HE].

[332] M. Actis, G. Agnetta, F. Aharonian, A. Akhperjanian, J. Aleksić, E. Aliu, D. Allan, I. Allekotte, F. Antico, L. A. Antonelli, and et al. Design concepts for the Cherenkov Telescope Array CTA: an advanced facility for ground-based high-energy gamma-ray astronomy. *Experimental Astronomy*, 32:193–316, December 2011. arXiv:1008.3703 [astro-ph.IM].

[333] J. Cortina, M. Teshima, and f. t. CTA Consortium. Status of the Cherenkov Telescope Array's Large Size Telescopes. *ArXiv e-prints*, August 2015. arXiv:1508.06438 [astro-ph.IM].

[334] P. Peñil, L. Ángel Tejedor, J. Abel Barrio, and M. López. A Trigger Interface Board to manage trigger and timing signals in CTA Large-Sized Telescope and Medium-Sized Telescope cameras. *ArXiv e-prints*, September 2017. arXiv:1709.04692 [astro-ph.IM].

[335] Dennis Haefner. Development of a new analog Sum-trigger for the MAGIC experiment with a continuously adjustable analog delay line and automatic calibration. Master's thesis, Munich U., 2010.

[336] C. Delgado, M. Bernardos, and G. Martinez. L1 Transfer function pseudocode. *CTA internal note*, May 2017.